

INSTITUTE OF PHYSICS
SERIES IN MICROSCOPY IN
MATERIALS SCIENCE

**ELECTRON
MICROSCOPY IN
HETEROGENEOUS
CATALYSIS**

P L GAI
E D BOYES

Electron Microscopy in Heterogeneous Catalysis

Series in Microscopy in Materials Science

Series Editors: **B Cantor**
M J Goringe
J A Eades

Other titles in the series

Atlas of Backscattering Kikuchi Diffraction Patterns
D J Dingley, K Z Baba-Kishi and V Randle
ISBN: 0 7503 0212 7

Electron Microscopy of Interfaces in Metals and Alloys
C T Forwood and L M Clarebrough
ISBN: 0 7503 0116 3

The Measurement of Grain Boundary Geometry
V Randle
ISBN: 0 7503 0235 6

Topics in Electron Diffraction and Microscopy of Materials
P Hirsch (ed)
ISBN: 0 7503 0538 X

Characterization of Radiation Damage by Transmission Electron Microscopy
M L Jenkins and M A Kirk
ISBN: 0 7503 0748 X

Forthcoming titles in the series

Nuclear Microbeams in Materials Science
G W Grime

Orientation Imaging Microscopy
D J Dingley, D P Field and S I Wright

Series in Microscopy in Materials Science

Electron Microscopy in Heterogeneous Catalysis

P L Gai†

*DuPont, Central Research and Development,
Wilmington, DE, USA and
University of Delaware, Department of Materials
Science and Engineering, Newark, DE, USA*

E D Boyes†

*DuPont, Central Research and Development,
Wilmington, DE, USA*

*(† Formerly at the University of Cambridge and
University of Oxford)*

IOP

**Institute of Physics Publishing
Bristol and Philadelphia**

© IOP Publishing Ltd 2003

All rights reserved. No part of this publication may be reproduced, stored in a retrieval system or transmitted in any form or by any means, electronic, mechanical, photocopying, recording or otherwise, without the prior permission of the publisher. Multiple copying is permitted in accordance with the terms of licences issued by the Copyright Licensing Agency under the terms of its agreement with Universities UK (UUK).

British Library Cataloguing-in-Publication Data

A catalogue record for this book is available from the British Library.

ISBN 0 7503 0809 5

Library of Congress Cataloging-in-Publication Data are available

Series Editors: **B Cantor**
M J Goringe
J A Eades

Commissioning Editor: Tom Spicer
Production Editor: Simon Laurenson
Production Control: Sarah Plenty
Cover Design: Victoria Le Billon
Marketing: Nicola Newey and Verity Cooke

Published by Institute of Physics Publishing, wholly owned by The Institute of Physics, London

Institute of Physics Publishing, Dirac House, Temple Back, Bristol BS1 6BE, UK

US Office: Institute of Physics Publishing, The Public Ledger Building, Suite 929, 150 South Independence Mall West, Philadelphia, PA 19106, USA

Typeset in L^AT_EX 2_ε by Text 2 Text, Torquay, Devon
Printed in the UK by MPG Books Ltd, Bodmin, Cornwall

Contents

Preface	xi
Acknowledgments	xii
1 An introduction to heterogeneous catalysis	1
1.1 Science and technology of catalysis	1
1.2 Fundamental principles of catalysis: some basic definitions	2
1.3 Electronic configurations and quantum theory	5
1.3.1 Valence electrons: examples of common elements	7
1.4 Chemical bonding	8
1.5 Thermodynamic definitions relevant to catalysis and the role of electron microscopy	9
1.5.1 Energy, enthalpy and entropy	9
1.6 Structure and chemistry of carbons and hydrocarbons	10
1.7 Catalysis and band theory	11
1.7.1 pH scale, Lewis Bronsted acidity and basicity	12
1.7.2 Band theory	12
1.8 Some important structures of solid catalysts	13
1.8.1 Metals and oxides	13
1.8.2 Oxides	13
1.8.3 ReO_3	14
1.8.4 Jahn–Teller distortion	15
1.8.5 Titania (TiO_2) system	15
1.8.6 Rutile (TiO_2) structure	15
1.8.7 Anatase	15
1.8.8 Layer structures	16
1.8.9 Perovskites and pyrochlores	16
1.9 Carbons as supports in catalysis and new forms of carbons with atomic scale building blocks	18
1.9.1 Amorphous carbon, graphite, fullerene and carbon nanotubes (CNT)	18
1.9.2 Nanotubes	20
1.9.3 Carbons and catalytic reactions	20
1.9.4 Choice and design of catalyst supports or carriers	22

1.9.5	Carbon deposits	22
1.9.6	Polymers	24
1.10	Oxides and non-stoichiometry in catalysis and the unique role of electron microscopy	24
1.10.1	Methods of accommodating non-stoichiometry	24
1.10.2	Point defect models	26
1.10.3	Larger deviations from stoichiometry	26
1.10.4	Non-stoichiometry in metallic monoxides	27
1.10.5	Defect elimination: crystallographic shear (CS)	29
1.10.6	Background to earlier work	30
1.10.7	Reaction mechanism	31
1.10.8	Block structures	34
1.10.9	Infinitely adaptive structures	36
1.10.10	Vernier structures	37
1.10.11	Coherent intergrowths	39
1.10.12	Chemical twinning	40
1.10.13	Novel glide shear mechanism in anion-deficient oxides	40
1.11	Catalysis by oxides	41
1.11.1	Non-stoichiometry in oxidation catalysis	41
1.12	Extended defects and crystallographic shear	41
1.12.1	Relevance to oxidation catalysis	41
1.12.2	Distinction between shear mechanisms and defect structures	42
1.12.3	Important issues in oxide catalysis and EM techniques	43
2	Electron microscopy and diffraction in heterogeneous catalysis	45
2.1	Background	45
2.2	Imaging in the TEM	49
2.2.1	Classification of some important defect structures and diffraction contrast in catalysis	49
2.2.2	High-resolution transmission electron microscopy (HRTEM)	52
2.2.3	Development of HRTEM	55
2.2.4	Multi-slice HRTEM image simulations	57
2.2.5	Surface-profile imaging in HRTEM	57
2.3	Chemical composition analysis of catalysts in the EM	58
2.3.1	X-ray spectroscopy in the electron microscope	59
2.4	Electron energy loss spectroscopy	60
2.5	Convergent (or focused) beam electron diffraction	61
2.6	The development of <i>in situ</i> environmental-TEM (ETEM) under controlled reaction environments to probe catalysis at the atomic level	61
2.6.1	Background to <i>in situ</i> ETEM	62
2.6.2	<i>In situ</i> studies of dynamic oxidation catalysis in action under high gas pressures and at operating temperatures	65

2.6.3	Recent advances in <i>in situ</i> atomic-resolution ETEM for probing gas–catalyst reactions at the atomic level	66
2.7	Novel wet-ETEM development for nanoscale studies of liquid–catalyst reactions at operating temperatures	67
2.8	Scanning EM (SEM), cathodoluminescence in catalysis and environmental SEM (ESEM)	70
2.8.1	Recent advances in ultra high-resolution low-voltage FE SEM (HR-LVSEM) and extreme FESEM in catalysis	71
2.8.2	Extreme FESEM	73
2.8.3	Cathodoluminescence in catalysis	74
2.9	Scanning transmission EM (STEM)—recent advances	75
2.9.1	Z contrast and three-dimensional electron tomography	76
2.10	Image processing	77
2.10.1	Charge-coupled devices	77
2.11	Other developments	78
2.11.1	Reflection EM	78
2.11.2	Electron holography	78
2.11.3	Other surface techniques	78
2.12	Parallel chemical studies and correlations with the catalyst microstructure	79
2.12.1	Analysis and characterization of catalyst dispersion and surface areas	79
2.12.2	Physical adsorption	80
2.12.3	Chemisorption	81
2.12.4	Comparison of surface areas with electron microscopy	81
3	Electron microscopy studies of catalysis by oxides	82
3.1	Single and mixed metal oxide systems: redox pathways and anion deficiency	82
3.2	Single metal oxide catalysts: MoO ₃	83
3.3	<i>In situ</i> direct observations of surface defect structures in catalysts under controlled reducing environments and methods for defect analysis	84
3.4	Shear domains and crystallographic shear (CS) planes in catalytic reduction	85
3.4.1	Do CS planes form at catalyst operating temperatures and how quickly do they form?	87
3.4.2	Collapse in the catalyst's structure leading to the formation of CS planes	88
3.4.3	Growth of surface defects: CS planes in catalytic reduction and climb of dislocations	89
3.4.4	Direct observation of dynamic redox processes in C ₃ H ₆ :O ₂ (or air) mixtures: behaviour of surface defect structures	91

3.4.5	Methanol oxidation over MoO ₃	91
3.4.6	V ₂ O ₅ catalysts	92
3.5	Electron microscopy and defect thermodynamics: a new understanding of oxidation catalysis	93
3.5.1	Development of thermodynamics of reacting catalysts based on EM	93
3.5.2	New understanding of defect mechanisms in oxidation catalysis from dynamic electron microscopy	95
3.5.3	Supersaturation leading to a modified mechanism for the formation of CS planes in oxides	97
3.6	The role of defects in catalytic reactions	98
3.6.1	Correlations of the catalyst microstructure with catalytic activity and selectivity	98
3.7	Multi-component (practical) oxide catalysts	101
3.7.1	Bismuth molybdate catalysts	101
3.7.2	Review of crystal structures	102
3.7.3	Experimental procedures	104
3.7.4	Dynamic electron microscopy in controlled environments	104
3.8	Iron molybdates in methanol oxidation reactions	109
3.9	Vanadium phosphate (V–P–O) catalysts for butane oxidation technology: the elucidation of active sites by <i>in situ</i> electron microscopy	110
3.9.1	Synthesis and characterization of VPO catalysts	113
3.10	Examples of other mixed metal oxide systems	125
3.10.1	Heteropolyacids	125
3.10.2	Mixed metal amorphous and spinel phase oxidation catalysts derived from carbonates	127
3.10.3	Ca–Mn–O perovskites	128
3.11	Electronic structure of crystallites and dopant distributions by cathodoluminescence electron microscopy	129
3.11.1	Sb–Sn oxide catalysts and Fe–Sb–O catalysts	129
3.12	Zirconia (ZrO ₂)-based solid-acid catalysts and ceria (CeO ₂) systems	131
3.13	The key role of electron microscopy in the discovery of novel reaction mechanisms in selective oxidation catalysis	131
3.14	Stable silica-based ceramic oxide supports for catalysts: some recent developments	135
3.14.1	Structural principles	136
3.14.2	Nanostructure and microchemistry	138
3.14.3	Stabilization mechanisms	139
4	Catalysis by zeolites and molecular sieves	141
4.1	Structures, acidity and uses of zeolites	141
4.1.1	Shape-selective catalyst	143
4.2	Silicalites and aluminophosphates	144

4.3	Determining three-dimensional structures by ED and HRTEM: MALPO solid acid catalysts	147
5	Catalysis by supported small metal particles	151
5.1	Recent developments	151
5.2	Facile versus structure-sensitive reactions	152
5.3	Preparation and characterization of model and practical metallic catalysts	153
5.3.1	Monometallics: single metals on amorphous alumina	153
5.3.2	Model and practical (real-life) bimetallic systems	154
5.4	Catalytic mechanisms on supported metals	155
5.4.1	Single metal particles	155
5.4.2	Ceramic surfaces	155
5.4.3	Metal–ceramic interface interactions: wetting and interfacial energies	156
5.4.4	Particle nucleation and sintering in supported metal catalysts	157
5.4.5	Particle size distributions (PSD): measurement of dispersion of metal particles on supports	158
5.4.6	Selective gas adsorption or chemisorption	159
5.4.7	Particle migration model and its limitations	160
5.5	Experimental studies by electron microscopy	162
5.5.1	Sintering of Pt/alumina	162
5.5.2	Re-dispersion phenomena	165
5.6	Small particles in HRTEM	166
5.6.1	Supported metal-particle catalysis	166
5.7	Experimental and theoretical developments in small metal-particle catalysis using electron microscopy	167
5.7.1	Detection and surface structure of very small particles by HRTEM	167
5.7.2	Image contrast and visibility of supported small metal catalyst particles in HRTEM	167
5.7.3	Examples of image simulations of supported small particles	168
5.7.4	Theoretical procedures and corrections of spherical aberration	168
5.8	Structure of small metal particles	171
5.8.1	Single crystal particles and multiply twinned particles (MTP)	171
5.9	EM studies of chemical interactions at metal–support interfaces	175
5.10	Metal–support interactions	176
5.10.1	Strong metal–support interactions (SMSI) and electronic structures: <i>In situ</i> atomic resolution ETEM	177
5.11	<i>In situ</i> ETEM studies of metal–irreducible ceramic support interactions	180

5.11.1	Copper/alumina systems in different gas environments	180
5.11.2	Ag/alumina	183
5.11.3	Pd/alumina and thermal sintering	184
5.12	Methanol synthesis and oxidation reactions	188
5.13	Monometallic nanocatalyst systems: copper nanocatalysts supported on silica (Cu/SiO ₂)	188
5.14	Bimetallic or alloy systems: atomic structure and composition	189
5.14.1	Cu–Pd alloy system: structure, phase stability and catalysis	189
5.14.2	Diffuse scattering in essentially perfect B2 catalyst particles and Ewald sphere	192
5.14.3	State of the active catalysts	194
5.14.4	Cu–Ru system	197
5.14.5	Promoted Pt catalysts in pollution control	200
5.14.6	Different synthesis routes and HRTEM of bimetallic systems	201
5.14.7	Wet-ETEM of catalyst–liquid reactions at operating temperatures: catalytic hydrogenation of nitriles in the liquid phase over novel bimetallic nanocatalysts and polymerization	202
5.15	Fischer–Tropsch and Ziegler–Natta catalysts	205
6	Environmental catalysis and catalyst design	206
6.1	Perovskite-based catalysts for environmental pollution control: The role of electron microscopy	206
6.2	High temperature superconducting cuprates (HTSC) as catalysts	207
6.2.1	Lanthanum–copper-oxide-based systems	208
6.2.2	Yttrium–barium–copper oxide systems (Y–Ba–Cu–O)	210
6.2.3	Bismuth–copper–calcium based systems	210
6.3	Hydrodesulfurization (HDS) catalysis	213
6.4	Nanocatalysts in emission control, steam reforming, photocatalysis and fuel cell catalysis	214
6.5	Nanocatalysts for alternatives to chlorofluorocarbons	217
6.6	Concluding remarks	218
	References	221
	Index	230

Preface

Electron Microscopy in Heterogeneous Catalysis describes the unique role electron microscopy plays in the immensely important field of heterogeneous catalysis. It brings together several disciplines, namely surface science, solid state chemistry and physics, materials science, chemical engineering and crystallography. The work described in this monograph exemplifies the many striking advances made by electron microscopy in advancing our understanding and creating advanced catalyst materials and processes. Catalysis plays a pivotal role in national economies and controls more than 90% of the world's chemical manufacturing processes. In many technological processes, catalysts are increasingly nanoscale heterogeneous materials. With growing regulatory guidelines requiring efficient and environmentally compatible catalytic processes for selective hydrocarbon catalysation and for creating new energy sources, it is crucial to have a fundamental understanding of the nanostructure of the catalyst and the mechanisms involved to design novel catalysts and processes. As we show in the following chapters, electron microscopy is playing a direct role in the development of catalytic materials and reactions. Pioneering developments in atomic-resolution environmental transmission electron microscopy (ETEM) for directly probing the catalyst's behaviour during the reaction at the atomic level, wet ETEM for studying catalyst-liquid reactions dynamically at the molecular level, field-emission low-voltage high-resolution scanning electron microscopy (LVHRSEM), atomic-resolution scanning TEM and electron-induced analytical spectroscopic (AES) methods address the fundamental issues of the materials and processes in catalysis. All these techniques are playing a unique role in obtaining insights into active sites, the atomic structure, atomic scale chemistry, point and extended defects and surface reconstruction, the nature of bonding and the electronic structure of the surface and the related subsurface of the catalyst and the mode of operation. These modifications govern the relationships between structure and activity in catalytic reactions and identify the factors that control the activity, selectivity and the activation barrier. New opportunities have evolved in catalysis research as a direct consequence of electron microscopy.

The book will be especially useful for scientists, undergraduates and graduates working in the rapidly expanding field of catalysis research. Looking forward to the future, electron microscopy is set to play an even more important

role in the design of new catalysts and economic routes for creating energy that can meet stringent performance requirements. This will also incorporate a more efficient use of our limited natural resources. We dedicate the book to our parents, Urmila Chandra and Laxman Gai and Douglas and Elizabeth Boyes.

Pratibha L Gai, MSc, PhD (Cambridge), FInstP, FRMS^{1,2}
and **Edward D Boyes**, MSc, PhD (Cambridge), FRMS¹

¹ DuPont, Central Research and Development Laboratories, Experimental Station, Wilmington, DE 19880-0356, USA

² University of Delaware, Department of Materials Science and Engineering, Newark, DE, USA

Acknowledgments

We thank the series editors, Professors Brian Cantor, Michael J Goringe and Alwyn Eades for the invitation to prepare this monograph.

We thank Tom Spicer, Senior Commissioning Editor of the Institute of Physics Publishing (IOPP), Katheryn Cantley, Sally Wride, Sarah Plenty, Nicola Newey, Verity Cooke and Simon Laurenson of the Institute of Physics Publishing for the excellent organizational support and for the successful publication of the monograph.

We thank the following publishers for permission to use some of the figures reproduced in the monograph: Butterworths Publishers, London, UK (figure 2.2); Arnold Publishers, UK (figures 2.4 and 1.10); Marcel-Dekker (figure 2.7(b)); EDP Sciences, France and USA (figures 1.13 and 1.14); Oxford University Press (figure 4.1); NORAN Instruments Inc. USA (figure 1.1), Academic Press and the American Chemical Society.

We thank our many colleagues including, at the University of Cambridge, University of Oxford, DuPont (including L Hanna and K Kourtakis), the University of Delaware, The Royal Institution, UK, Universities of Sydney, Melbourne and the Australian National University, Canberra, Australia, Indian Institute of Science and the Jawaharlal Nehru Centre for Advanced Scientific Research, Bangalore, India, Universite Claude Bernard, France, Universities of Nagoya, Osaka and Tokyo, Japan and Professors J B Goodenough, J Gopalakrishnan, Sir P B Hirsch, A Howie, C Lyman, C N R Rao and Sir John Meurig Thomas for wonderful collaborations.

Professor P L Gai and E D Boyes
USA

Chapter 1

An introduction to heterogeneous catalysis

1.1 Science and technology of catalysis

Catalysis research is central to the science of modern chemical processing, fuel technologies and environmental control. It controls more than 90% of the world's chemical manufacturing processes and is one of the most important technologies in national economies. Modern society as we know it would be impossible without catalysis. In the United States, the United Kingdom and in other major western European nations, catalysis contributes substantially to the GNP. Catalysts owe their importance to their unique properties, namely their ability to selectively catalyse chemical reactions. Solid state heterogeneous catalyst materials such as metal oxides and small metal particles on ceramic oxide substrates or on carbon are the most common. They are typically used with commodity gases and liquid reactants. Selective oxidation catalysis of hydrocarbon feedstocks which converts them to key industrial chemicals, polymers and energy sources is the dominant process. In large industrialized economies such as that of the USA, catalyst technologies can yield annual revenues in the excess of \$1 trillion. The annual cost of manufacturing catalysts is roughly several billion dollars. Generally, the cost of catalysts in a catalytic process is about 0.1% of the product value, making catalysis a highly economical process.

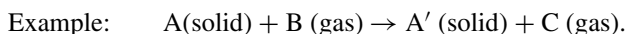
Catalysis is a multidisciplinary science. It is a combination of fundamental and applied science with major contributions from chemistry, physics and material science. Its technological importance lies in the tremendous achievements of this science to give humanity some cheap, highly convenient and outstanding materials. Energy sources, plastics, synthetic fibres, modern building materials, paper products, polymers, pharmaceuticals, agricultural products are just some examples. It is fascinating to note that many of these processes start out in the laboratory with a handful of research scientists experimenting with ideas. These are then transferred to a pilot plant and, if successful, to a full plant. The long-term advantage of this approach is that a new fundamental

scientific knowledge base associated with a catalytic process is often developed. Thus a catalytic process may involve catalyst synthesis, activation, operation micro/nanostructure and compositional data, structure–property correlation, deactivation, regeneration (disposal/recovery issues), patents, all of which deepen our understanding of the intellectual framework and its applications. Insights into catalytic properties, determination of the local surface and subsurface atomic structure, the composition and reactions of catalysts during the actual process, optimization of the synthesis and the design of novel catalysts and catalytic processes have all been pivotal contributions of electron microscopy (EM) to the catalytic sciences. EM also plays a major role in the development of environmentally beneficial catalysts and processes for the safe disposal of deactivated catalysts and byproducts. A large number of unusable catalysts, along with their hazardous byproducts, are currently disposed of in land fill sites.

In heterogeneous catalytic processes, oil and gas feedstocks are normally converted over supported aluminosilicate-based zeolite catalysts and nickel/cobalt/molybdenum/tungsten-based catalysts to produce naphtha and to remove sulfur, respectively. Other products in the conversion are hydrogen and fuel. Naphtha is converted to various products including aromatics, C₄ hydrocarbons, propylene and ethylene, using zeolite-based and supported metal-particle catalysts. Aromatics are, in turn, converted to maleic anhydrides for polyurethane intermediates over oxide catalysts. Oxide catalysts and metal-particle catalysts on supports are used to convert C₄ and other hydrocarbons (e.g. propylene and ethylene) to key industrial chemicals such as butadiene, vinyl chloride and acrylonitrile. The intermediate chemicals are used to manufacture important industrial polymers, plastics, synthetic fibres and so on. Ammonia is converted over metal catalysts to make fertilizers in agricultural businesses. As we describe in this monograph, electron microscopy plays a critical role in the fundamental understanding and creation of materials and processes for catalysis.

1.2 Fundamental principles of catalysis: some basic definitions

Some of the basic concepts and technologies are described here. Catalysis can be divided into two types: (1) homogeneous and (2) heterogeneous reactions. In homogeneous reactions, the reaction occurs between similar species, e.g. liquid–liquid reactions. In heterogeneous reactions, the reaction occurs between different types of species, e.g. gas–solid, liquid–solid and liquid–gas. Many industrial reactions are heterogeneous gas–solid or liquid–solid reactions. We will concentrate first on gas reactions occurring at solid catalyst surfaces:



Such reactions are multi-stage processes and the physical aspects governing them are (Bond 1987, Gates *et al* 1979):

- (1) Diffusion of reactants to the surface of the solid.
- (2) Adsorption/chemisorption at the surface (adsorption of gas molecules occurs on the solid surface because of attractive forces between them). Gas molecules approaching the surface may lose some of their momentum (in the component normal to the surface) and become trapped in the potential well. The energy required to overcome the attractive potential barrier of the surface and the attraction of neighbouring molecules is the heat of adsorption (Van der Waals forces) and several monolayers may be adsorbed. However, if there is some interaction or electron transfer between the gas molecule and the surface (forming, e.g., a surface compound), it is defined as chemisorption. The heat of chemisorption is usually greater than the heat of adsorption. The extent of chemisorption depends upon the specific nature of the solids and gases.
- (3) Reaction.
- (4) Desorption or diffusion of products away from the surface.

Historically, a very convenient and simple definition has existed which describes a catalyst as a material which augments the rate of a chemical reaction without itself being consumed. However, as we demonstrate in the following chapters, in practice, the performance of catalysts is governed by several factors, including its nanostructure, chemistry, surface structure and electronic properties on a fine (atomic) scale. There are formidable problems in the unambiguous identification of the active species responsible for heterogeneous catalysis and catalytic reaction pathways, but they are crucial to understanding the selectivity to produce the desired products and the activity of a catalyst. In many catalytic processes, empirical developments in catalysts and their processes often lead to a loss of activity and present major difficulties in technological applications. A deeper understanding of the nature of the active sites at the catalyst surface, the reaction mechanisms and the factors controlling the activity, the selectivity as well as the activation barrier and the role the surface structure and nanostructure of working catalysts is therefore essential to be able to design high-performance catalysts and clean processes.

Normally, catalytic activity is expressed as the reaction rate per unit area of active surface (expressed as metre^2 per gram) under given conditions. In a chemical reaction, catalytic conversion is defined as the fraction of reactants converted to products and selectivity is a function of the rate of formation of a desired product with respect to the overall conversion of the initial reactants. The reactant molecules transfer to the catalyst surface where adsorption may occur on an 'active site', with possible rearrangement of their bonds leading to a chemical adsorption (chemisorption), gas-catalyst reaction and the subsequent desorption of new species. The active 'site' or 'phase' is of high activity and selectivity for the desired products. Thus, the nature of the active sites is important. In many cases, it is not enough to have just activity. Selectivity to desired products is important and often modifiers or promoters are needed both to improve the

catalytic process and to keep the costs down.

In general, the rate (k) of heterogeneous catalysis in a gas–catalyst (and liquid–catalyst) reaction may be expressed as the product of the rate coefficient k_0 and a function of pressure (or concentration), p , i.e. $k = k_0 f(p)$ where p is the partial pressure of the reactant. k_0 depends on the reaction conditions and may involve reaction steps prior to the first rate-determining step of the reaction. A convenient method for determining k_0 is to use the Arrhenius equation:

$$k_0 = A \exp(-E/RT)$$

where E is the activation energy of the reaction and A is a temperature-dependent parameter. However, since the concentration of the reactant at the catalyst surface may be temperature-dependent, a more general method incorporating the concept of a rate factor known as the turnover frequency (TOF), is used to describe the catalytic activity. TOF is the number of times (n) that a catalytic reaction occurs per catalytic site per unit time under the given reaction conditions of temperature/pressure (concentration) and reactant ratio. TOF is thus simply the measure of catalytic activity expressed by the number of revolutions of the catalytic cycle per second, i.e. $\text{TOF} = \text{number of molecules of a product}/\text{number of active sites} \times \text{time} = (1/S_n)(dn/dt)$, where S_n is the number of active sites. If S_n is unknown, it can be expressed as the total surface area of the catalyst and this enables some estimates of TOF to be derived. For most heterogeneous oxidation reactions which occur in a temperature range 100–500 °C and a pressure of a few bars, TOF is in the range 10^{-2} – 10^2 s^{-1} . TOF is used as a true measure of catalytic activity while the number of observed turnovers before a catalyst is deactivated is the expression for the catalyst's life.

Deactivation of catalysts, or loss of catalytic activity, may be chemical, thermal or mechanical in nature. Chemical effects may arise from a loss of active sites due to the growth of non-active species/phases, poisoning by certain foreign species or from the carbon/hydrocarbon-containing residues from hydrocarbon reactants. Thermal effects may include the sintering of a catalytically active phase leading to the loss of the surface area of the active phase, desegregation effects in multicomponent catalysts or metal–support interactions in supported metal catalysts. Mechanical effects include fouling by coke or carbon deposition on the catalyst. We will discuss these phenomena in subsequent chapters.

The microstructure of surface evolves during the reaction due to changes in the local atomic arrangement at the catalyst's surface leading to defect structures. The defect structures and their role in catalytic reactions are fundamental to how a catalyst functions, its reaction paths and the rate-determining reaction steps but studies on these issues in complex catalysts, especially under dynamic conditions, have so far been limited. Furthermore, the exploitation of dynamic surface processes to design improved catalyst systems remains a challenge. The nature of the active sites on the surfaces and their relationship to defects or phases is extremely important. Here we address some of the most fundamental issues in heterogeneous catalysis: the process of chemical reactions involving

chemical reduction and oxidation and catalyst surface modifications; and the scientific challenge to develop reactions from a laboratory scale to a plant scale economically. Most importantly, we address the role of surface and interface defect structures resulting from oxide and metal catalysts in the following areas: activation of hydrocarbons, fast oxygen diffusion/exchange and the activity of catalysts. We describe the crucial and unique role of electron microscopy and chemical microanalysis in understanding the dynamics at the gas–catalyst interface, in the improvement of known processes and designing new catalytic systems and technologies. The principles of the chemical processes in heterogenous catalysis have been described in Thomas and Thomas (1967, 1997). Some of the fundamental principles applicable to electron microscopy studies of catalysts are highlighted in the following sections.

1.3 Electronic configurations and quantum theory

The general picture of an atom is now well known (Cottrell 1971). It has a nucleus at the centre surrounded by electrons (elementary particles $\sim 10^{-13}$ cm in radius (10^{-8} cm = 1 ångström (Å) = 0.1 nanometre (nm))). The electrons move in orbitals. The nucleus contains positively charged particles (protons) and (except for hydrogen) uncharged neutrons. The number of protons and neutrons in the nucleus of an element are denoted by the atomic numbers Z and N , respectively, with the atomic weight being essentially $Z + N$. The hydrogen atom has the simplest nucleus with a single proton ($Z = 1$). The building blocks of all matter form chemical elements with their own atomic number. The Periodic Table (figure 1.1) is a compilation of the chemical elements known thus far, ordered by their atomic weights, first formulated by Mendeleev (Moeller 1952) and new elements are still being added. In the modern Periodic Table, each element is identified by its atomic number, chemical symbol, chemical name and atomic weight. The table contains both metals and non-metallic elements.

A material consisting of atoms of several elements is called a compound. A description of their nature and properties can be found in Moeller (1952), Cotton and Wilkinson (1970), Issacs (1984) and Nathan (1993). If tightly bound atoms behave like a single entity, this is called a molecule: for example, H_2 with two hydrogen atoms. A chemical compound with an exact integral atomic ratio, for example quartz (silica, SiO_2) with a silicon:oxygen ratio of exactly 1:2, is called a ‘stoichiometric’ compound (with an atomic ratio of 28.09:32 or 47% Si to 53% oxygen). If the ratio deviates from this, the compound becomes ‘non-stoichiometric’. A molecular weight, or ‘mole’, is used to indicate the relative concentrations of the various components in a material or compound and their amounts in grams is equal to the sum of the atomic weights of the components. For example, one mole of water (H_2O) weighs $2(H) + O = 2(1) + 16 = 18$ grams (g). Thus, if the atomic weight of an element is obtained in g, the sample then contains 1 mole of atoms of the element. The atomic mass unit (amu) is

The periodic table is organized into groups and periods. Each element cell contains the following information:

- Atomic Number:** Located at the top left of the cell.
- Symbol:** Located in the center of the cell.
- Element Name:** Located at the bottom of the cell.
- Atomic Weight:** Located at the bottom right of the cell.

Key features of the table include:

- Groups:** Labeled with letters L, A, and A at the bottom of the table.
- Periods:** Numbered 1 through 7 on the left side.
- Block Structure:** The table is divided into s, p, d, and f blocks.
- Special Elements:** Hydrogen (H) and Helium (He) are shown in separate boxes at the top left.

Figure 1.1. Periodic Table: by courtesy of NORAN Instruments Inc.

1/16th of the mass of an oxygen -16 atom and is defined as follows: $1 \text{ amu} = 1.66 \times 10^{-24} \text{ g}$. (The reciprocal is Avogadro's number which defines the number of particles in 1 mole $= 6.03 \times 10^{23}$.) The mass of a proton, a neutron and an electron are 1.0076, 1.0089 and 0.000555 amu, respectively.

Electrons are attracted to protons electrostatically. An atom can exist with more or fewer electrons than its atomic number allows, in which case it becomes either a negative or a positive ion. The electrons rotating around the nucleus are organized in various 'orbitals' as defined by the quantum theory formulated by Bohr, de Broglie, Schrödinger, Dirac and Pauli (Cottrell 1971). Each orbital has a characteristic energy and is assigned two electrons. Bohr's theory of atomic structure consists of electrons in shells K L M N O P Q, defined by a principal quantum number $n = 1-7$ and thus each orbital is characterized by a principal quantum number and a number identifying the maximum number of electrons permitted for that level. The Pauli exclusion principle forbids two electrons to be similar, so the energy levels are divided into subshells, $l = 0, n - 1$, and electrons in subshells or orbitals are characterized as s, p, d and f electrons. For a stable atom, electrons fill the orbitals from the lower energy states—the s-states. The maximum number of electrons in each state (s, p, d, f) are 2, 6, 10 and 14, respectively. $1s^1$ means a single electron in the s-subshell of K and $3d^5$, five electrons in the d-subshell of M etc. The order of energies for a given n are: $s < p < d < f$; s being the lowest energy level.

1.3.1 Valence electrons: examples of common elements

The element hydrogen with atomic number 1 has an electronic configuration of $1s^1$ and a valence subshell of $1s^1$. Therefore, it has common valence of +1 (and also -1 forming metallic hydrides). Similarly, for oxygen: $Z = 8$, the electronic configuration is $1s^2 2s^2 2p^4$ orbitals with a valence subshell $2p^4$ and it therefore has a valence of -2 . From the previous discussion, it is clear that electrons are added to the subshell with the lowest energy until it is full then the subshell at the next energy level is filled, etc. A filled p-type orbital leads to a stable configuration. The inert gases have stable configurations. Other elements accept or lose electrons to achieve stability. This can occur by electrons being shared between atoms. For example, carbon has the electronic configuration $1s^2 2s^2 2p^2$ (Moeller 1952). The orbital of the second electron subshell is $2s^2 2p^2$ and it therefore has four electrons to share. The carbon atom can thus accept four electrons and can also lose four or two, with valences -4 , $+4$ or $+2$, respectively. Gilbert Lewis (1923) presented the first representation of the electronic structure diagram. In his representation, the valence electrons were shown as dots and this is now known as the Lewis diagram. The electronic structure is highly significant in heterogeneous catalysis and EM methods play a crucial role in elucidating the electronic structures of catalysts in catalytic reactions.

1.4 Chemical bonding

An attractive force between two atoms constitutes a chemical bond. However, a repulsive force also exists to separate them at a certain distance. At the equilibrium spacing between two atoms these two forces are equal. The energy and chemical bonding between atoms are defined by quantum mechanics. There are primarily four types of interatomic forces: (a) the Van der Waal force, which represents a weak attractive force between atoms, (b) the covalent bond, (c) the ionic bond and (d) the metallic bond. Stable atoms are neutral (with no electrical charge) and have an equal number of electrons and protons. Atoms can achieve stable configurations by either losing or accepting electrons. For example, the oxygen molecule can be formed by two oxygen atoms sharing electrons and this is called a covalent bond.

In the Periodic Table, metallic elements have excess electrons (Moeller 1952). For example, potassium (K) has $Z = 19$, $1s^2 2s^2 2p^6 3s^2 3p^6 4s^1$. It can lose one electron, and become a positive ion, called a cation, K^+ . Non-metallic elements like oxygen have $Z = 8$, $1s^2 2s^2 2p^4$ and can accept two electrons, and become a negative ion, or anion, O^{2-} . If a pair of elements exchange electrons to achieve a stable configuration by electrostatic attraction (e.g. KCl or NaCl), this is called an ionic bond. The strength of the bond therefore depends on the charge and size of the ions. The ionic radii of many of the elements have been calculated (Shannon 1986): for O^{2-} it is 1.45 Å. Isoelectronic elements contain the same number of electrons in the same orbitals. Covalent bonds can form between atoms of different elements with differing ionization energies and electron affinities. The resulting bond may be asymmetric with electrons concentrated at the more electronegative atom and a mixture of covalent and ionic bonding can exist. The degree of covalent or ionic bonding between two heterogeneous atoms can be determined using Pauli's electronegative tabulations. In an ionic bond, electrons are transferred from an electropositive atom to an electronegative atom and the ions so formed are attracted electrostatically. The balancing repulsive force evolves when the completely filled electron-shells of the ions overlap and electrons are shared. When such an overlap occurs between partially empty shells, a strong covalent or metallic bond can result. The ionic valency is defined as the number of electrons donated or lost to produce an ion of the nearest noble gas electronic structure (Cottrell 1971).

According to these principles, carbon ionization requires the loss of four electrons. In ionization, a coordination complex called a 'ligand' may be formed in which a molecule or an ion donates a pair of electrons to a metal atom and ligands attach to the central ion electrostatically. For example, in $(PtCl_4)^{2-}$ with four Cl^- ions are coordinated with the central Pt^{2+} ion. Such coordination compounds (and the lone pair the electron ligands donate) play a key role in defining the structural properties of metal complexes and ligand field theory has evolved to study their properties.

1.5 Thermodynamic definitions relevant to catalysis and the role of electron microscopy

Thermodynamics is the science of energy. It is of great importance in catalysis as a quantitative tool for understanding and predicting structural properties as we show later. Heterogeneous catalysis involves chemical change due to catalytic reactions. Here we describe such important terms as free energy, enthalpy and entropy of a system which are important in understanding the thermodynamic processes in catalysis and the pivotal role of electron microscopy in elucidating the thermodynamics of reacting catalyts.

Thermodynamic systems are those involving, for example, molecules and atoms. For general reading on thermodynamics, the excellent books by Swalin (1962), Cottrell (1971) and Adams (1974) are recommended. In simple homogeneous systems like gases (H_2 , O_2 etc) their amounts are sufficient to understand the properties. However, in a heterogeneous system, e.g. in a gas–solid interface system, the components can be defined as the phases of a thermodynamic system. If shielded from external forces, the system attains a steady state, called an equilibrium state, where its structure and properties do not change with time. The equilibrium state of a simple system can be defined by various properties at pressure P and volume V and the equation of the state of a perfect gas is given as $PV = RT$ (R is the gas constant and equals 1.986 cal/deg mole). For instance, the volume of a fixed mass of a permanent gas at a fixed low pressure gives the absolute temperature scale (degrees Kelvin (K)) on which ice melts at 273.15 K and water boils at 373.15 K (at 1 atmosphere (atm)). The processes of adsorption and chemisorption are defined by their rates as discussed earlier. Adsorption can be fast with little activation energy; chemisorption requires some activation energy, E (the minimum energy required for the reaction), given by the Arrhenius equation for the rate constant for chemisorption = $A' \exp(-E/RT)$, where A' may be a function of temperature, sticking probability and the number of collisions of the molecule per unit surface area per unit time.

1.5.1 Energy, enthalpy and entropy

Thermodynamics is defined in terms of the energy and enthalpy of a system. The internal energy E is the combination of all the kinetic energies of motion and energies of interaction (potential energies) of the particles in the system. If left alone, this energy is constant. However, when the system interacts with its surrounding environments, it changes energy by transfer of either work (W) or heat (h) and the change in energy is given by $\Delta E = \Delta h - \Delta W$. In most experiments where the pressure is constant, the work δW is performed at pressure P and through a volume change ΔV giving a function of state defined by $H = \Delta E + PV$, where H is called the enthalpy of the system. H is considered as the heat content of the system. It is more convenient to work with compared to

the internal energy. When a chemical reaction takes place at a constant pressure, the heat absorbed is called the heat of reaction, ΔH , which is the change in H during a reaction. In endothermic reactions, heat is absorbed and ΔH is positive; in exothermic reaction, heat is released and ΔH is negative. Thus, a large $-\Delta H$ denotes a strong chemical affinity between reacting species.

Systems involved in reactions are generally in thermal contact with their surrounding environments. To define the equilibrium of a reaction, the term Gibbs free energy is used, which means that, under given conditions, the most stable structure is that with the lowest Gibbs free energy,

$$G = E + PV - TS.$$

If the system can release energy as work, chemical change can occur and the total energy of the system can then be divided as energy which can be released (free energy) and that which is unavailable for release (bound energy). S is the property called entropy (Ellingham 1930, Cottrell 1971). If a system changes slowly from its initial to its final state in steps of equilibrium states, the final state can be independent of the reaction path between the two states; if the process is reversible in which the system absorbs an infinitesimal heat ΔH , the entropy of the system is defined as $\Delta S = \Delta h/T$. The Ellingham diagram summarizes the free-energy data for many elements and compounds. Free energy is released by the combination of a fixed amount, e.g. 1 mole, of the oxidizing agent: $\text{Mg} + 0.5\text{O}_2 \rightarrow \text{MgO}$; ΔG is 144 kcal/mole oxide. Metals generally release free energy during oxidation (Ellingham 1930).

In catalysis by oxides, the properties of the oxides depend greatly on the extent of non-stoichiometry, activity and chemical potential of oxygen. Thus if a vacancy is introduced into the lattice sites, the free energy change ΔG (difference between the defective and initial perfect crystals) is given by $\Delta H_v - T\Delta S$ (ΔH_v is the enthalpy of vacancy formation) and ΔS contains both the configurational and vibrational entropies involved in forming the defect. An equation to describe the loss of an anion forming a doubly and positively charged anion vacancy v' is given by (Sorensen 1981): $2\text{M} + \text{O} \rightarrow v' + 2\text{M} + \frac{1}{2}\text{O}_2$ (where M and O are metal and oxygens in the lattice). We show in chapter 3 that these simple thermodynamic concepts can be further developed by electron microscopy to understand defects and predict the structural properties of complex oxide catalysts.

1.6 Structure and chemistry of carbons and hydrocarbons

Carbon has the electronic configuration $1s^2 2s^2 2p^2$. Carbon atoms make single, double and triple bonds. Carbon also makes some of the simplest organic compounds by linking with hydrogen: these are called hydrocarbons and are of tremendous economic importance since they are integral to petroleum feedstocks and gas. The concepts are described in Moore (1950), Moeller (1952), Bond (1987), Nathan (1993) and Thomas and Thomas (1997). Heterogeneous catalysis

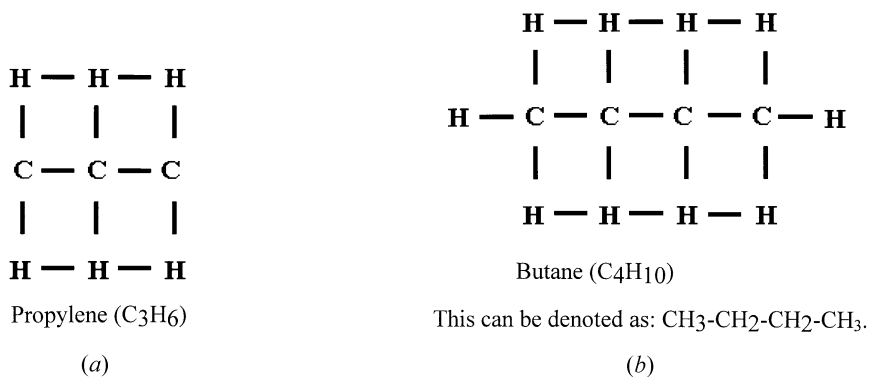


Figure 1.2. Simple organic molecules of (a) propylene, C_3H_6 and (b) butane (C_4H_{10}).

of hydrocarbons essentially deals with the selective oxidation of hydrocarbons. Simple organic (hydrocarbon) molecules like propylene and butane have the structures shown in figures 1.2(a) and (b), respectively.

Two polymorphs with the same molecular composition but different structures are called isomers. Thus the chain of carbon atoms can be unlimited and many new exciting compounds are being synthesized for various applications. In the previous examples, the hydrocarbons where carbons form single bonds are called alkanes (e.g. butane) (which share two electrons). Hydrocarbons forming double bonds (two carbons sharing four electrons) are called alkenes (e.g. ethylene) and those with triple bonds are alkynes. Organic compounds with other elements like oxygen and nitrogen are possible. The common organic compounds are classified as functional groups and are based on alcohols, aldehydes, carboxylic acids and amines. Carbons as catalyst supports are discussed in section 1.9.

1.7 Catalysis and band theory

Why are transition metals and transition-metal oxides so interesting and what makes a good catalyst? The d-character of the metallic bond is, in an empirical way, connected to catalysis and plays a key role (as will be shown in chapter 5). Transition metals are interesting because, in addition to the s and p electrons, their atoms can possess up to nine d-electrons. When the atoms overlap to form solids, the d-orbitals can spread out to form relatively narrow d-bands which are partially full. The s-band is also partially full. These give rise to interesting magnetic and electrical properties. In transition-metal oxides, there are unpaired d-electrons associated with metal ions. Furthermore, the 2p orbital of anions is below the partially filled d-band of cations. The s-orbitals of cations are raised in energy above the d-band, the separation between them, $2p - s$, is the binding energy.

They also are strong and hard with high melting points (MP) and high boiling points (BP). They conduct heat and cold well. Noble metals are less susceptible to acidic effects and corrosion.

1.7.1 pH scale, Lewis Bronsted acidity and basicity

The pH scale, which is logarithmic, is used to define the acidity or alkalinity of a solution (i.e. in terms of the concentration of hydrogen ions (H_{conc}) in solutions (Bond 1987)). To a first approximation, the pH of a solution is defined as $-\log_{10}[H_{\text{conc}}]$. A neutral solution at room temperature (RT) has a pH of 7. Acids have pH values less than this.

Acidity and basicity are defined using Lewis' (1923) principles as follows. A Lewis acid can accept a pair of electrons from a donor substance whereas a base can donate a pair of electrons. A Bronsted acid owes its acidity to the presence of protons (H^+). The Bronsted–Lowry nomenclature follows that acid is a proton donor and base is a proton acceptor. The Bronsted acidity of an oxide or a mixed oxide catalyst is of great importance in catalysis, especially aluminosilicate-zeolite-based catalysts. Aluminosilicates possess strong Bronsted acidity. Acid catalysts facilitate hydrocarbon cracking, isomerization and the reformation of hydrocarbons and are useful in the dehydration of alcohols as we describe in chapter 4. Alkene molecules adsorb at Bronsted sites and reactions proceed by primary carbonium ions (which are organic ions with a positive charge on the C-atom) which are involved in cracking. In reforming processes, hexane and its related compounds are converted to aromatics; an acid catalyst capable of two functions (e.g. hydrogenation and isomerization) is called a 'bi-functional' catalyst.

1.7.2 Band theory

Band theory is useful in the characterization of solids (Coulson 1937, 1961) and has been used to predict the properties of heterogeneous catalysis. Briefly, the band gap is the range of forbidden energies between non-overlapping bands and the band-gap energy characterizes the band structure of a solid. For example, semiconductors are distinguished by the width of the energy gap. This can be understood as follows: the allowable energies of electrons in a crystal are called the energy levels. In crystals with an atomic lattice, the neighbouring nuclei influence the electronic structure and sharp energy levels (e.g. those associated with single atoms) become bands of energy, each band representing specific quantum states. Forbidden bands exist between these bands. Electrons giving rise to chemical bonding constitute a valence band. We show in later chapters that many oxide catalysts are semiconductors and electron microscopy reveals that their band-gap energy can be varied as a function of defect structures resulting from catalytic reactions.

1.8 Some important structures of solid catalysts

The main classes of materials employed as catalysts are metals (generally transition and noble metals), oxides (including transition-metal oxides), transition-metal sulfides and zeolites. In the following sections, we discuss some of the more common structures and chemistry exhibited by catalytic systems.

1.8.1 Metals and oxides

Metals generally have face-centred cubic (fcc), body-centred cubic (bcc) or hexagonal structures. The simplest is fcc. In the bcc structure, if the central atom is different, the lattice is known as a CsCl (cesium chloride) structure. A bcc structure can be considered as two interpenetrating cubic lattices. These are shown schematically in figure 1.3. In catalysis, nanoscopic metallic particles supported on ceramic supports or carbon are employed in many catalytic applications as we show in chapter 5. Increasingly, a combination of two metals (bimetallic) or alloys of two or more metals with special properties are used for specific catalytic applications.

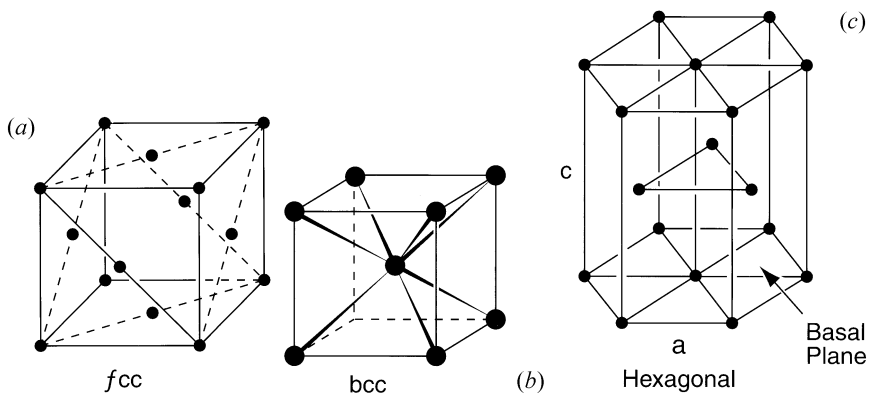


Figure 1.3. Schematic diagrams of (a) the fcc structure, (b) the bcc structure and (c) the hexagonal one.

1.8.2 Oxides

Oxides generally have complex crystal structures. The oxides of composition MO ($M \equiv$ metal) show a wide range of structural types. For example FeO, VO, NiO and MnO oxides have the ionic sodium chloride structure (figure 1.4(a)). Other structural types relevant to catalysis are described here.

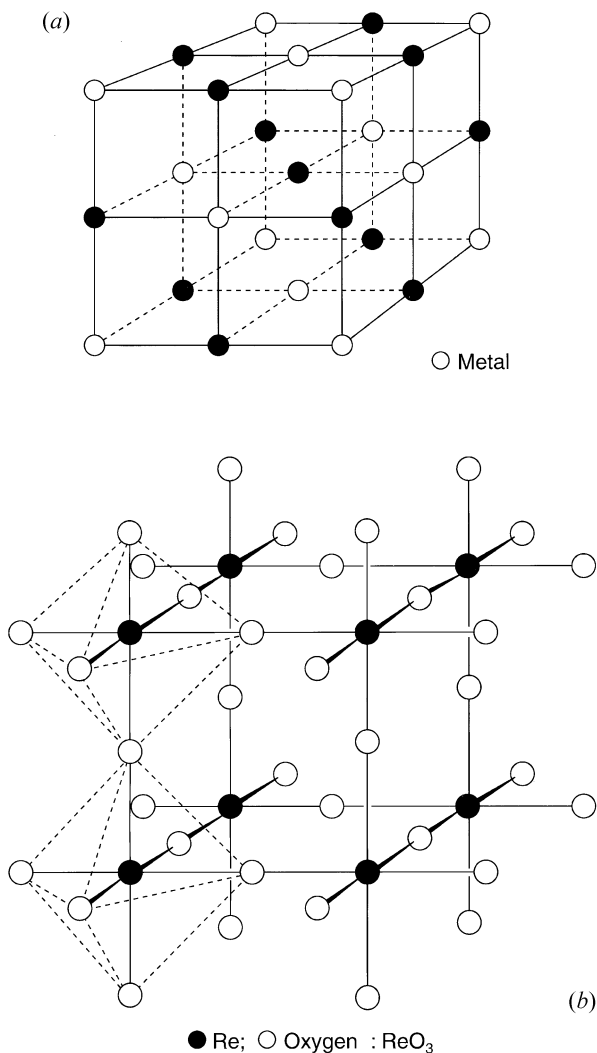


Figure 1.4. Schematic diagrams of the structure of (a) NaCl and (b) ReO_3 .

1.8.3 ReO_3

One of the simplest oxides is the rhenium trioxide (ReO_3) structure shown in figure 1.4(b). It consists of an incomplete fcc host lattice of O^{2-} with Re in one-quarter of the octahedral sites. (Crystallographic shear (CS) phases (discussed in 1.10.5) based on ReO_3 may be considered as consisting of the cubic MO_2 structure.) Many oxides and fluorides adopt the ReO_3 structure and are used in catalysis.

Another class of complex oxides are known as spinels. The structure is AB_2O_4 type where A and B are metal atoms, for example, $MgAl_2O_4$. In a normal spinel structure, both types of interstitial sites are partially filled: B^{3+} ions occupy half the octahedral sites and A^{2+} ions one-eighth of the tetrahedral sites in a close packed array. In another structural arrangement known as an 'inverse spinel', half of the B^{3+} ions are in the tetrahedral sites and the other half of B^{3+} together with the A^{2+} ions distributed in the octahedral sites. A simple structure of this type is Fe_3O_4 (magnetite) which can be written as $Fe^{3+}(Fe^{2+}Fe^{3+})O_4$, or $B(AB)O_4$. Calcite ($CaCO_3$) has a structure related to the sodium chloride ($NaCl$) structure but it is distorted by the planar oxygens. Several new catalysts reported in the literature as having calcite and rhodocrosite structures are described in chapter 3.

1.8.4 Jahn–Teller distortion

This effect is observed, for example, in inorganic complexes, where the metal ion is octahedral and the six ligands might be expected to occupy positions at equal distances at the corners of an octahedron, in an ideal structure. In the actual structure however, the octahedron may be distorted with four ligands in a square planar coordination and the remaining two ligands at opposite corners at longer distances. Many oxides exhibit Jahn–Teller distortions.

1.8.5 Titania (TiO_2) system

Rutile and anatase are used in photocatalysis and as catalyst supports and we describe some important structural features later. The titanium–oxygen system plays a key role in understanding stoichiometric variations. The highest oxide, TiO_2 , is polymorphic and the four known crystal structures are rutile, anatase, brookite and a high-pressure form similar to α - PbO_2 .

1.8.6 Rutile (TiO_2) structure

Rutile is an important and stable structure type for many binary oxides. It is tetragonal, with $a = 4.56 \text{ \AA}$ and $c = 2.93 \text{ \AA}$ (figure 1.5(a)). In this structure each Ti atom is surrounded by six oxygen neighbours at the corners of a slightly distorted octahedra. Each of the coordinating octahedra of oxygens shares its horizontal edges with adjacent octahedra which are thus linked in bands. Fluorides of many transition metals and of a number of other elements exhibit the rutile structure and it, therefore, is a very important structure type.

1.8.7 Anatase

Another polymorph of titania with a tetragonal structure: $a = 3.73 \text{ \AA}$ and $c = 9.37 \text{ \AA}$. Anatase has edge-sharing $[TiO_6]$ octahedra joined at the corners so that the oxygen atoms are in a slightly distorted cubic arrangement. At

La_2CuO_4 , Sr_2CuO_4 . As we show in chapter 6, when a perovskite forms a composite or intergrowth with other structures, new compounds of interest in catalysis can be formed (such as in high-temperature superconducting copper oxides) and EM is used to determine the structures and properties of these complex compounds. The merits of using perovskites in steam reforming, membrane catalysis and fuel cells are discussed in chapter 6.

1.8.9.2 *Pyrochlores*

The pyrochlore structure has the general formula $\text{A}_2\text{B}_2\text{O}_7$, where A and B are metals. Typically the A cation, with eight-fold coordination, is large and the unit cell contains eight formula units. The B cations lie in corner-sharing octahedra. The structure has been shown to be remarkable in its ability to tolerate vacancies at both the A and O sites. Defect pyrochlores can be formed by lowering the charge on the B cation and the seventh oxygen can be made partially or fully vacant, $\text{A}_2\text{B}_2\text{O}_{7-x}$ ($x = 0$ to 1). The structural flexibility of the pyrochlore provides a tremendous opportunity for EM studies in exploring substitutional chemistry and the catalytic properties of compounds of the pyrochlore family. $\text{Bi}_2\text{Ru}_2\text{O}_7$ is a member of this family.

1.8.9.3 *Alumina and silica structures*

Inorganic ceramic oxide supports for catalysts, such as alumina and silica, are used extensively in the catalysis industry because they are strong, they can have a range of shapes for different engineering needs and they are economical. They provide high surface areas for catalysis, ranging from 50 to 500 $\text{m}^2 \text{g}^{-1}$ and can have pore sizes ranging from 2 to 20 nm in diameter.

The oxides of alumina (Al_2O_3) are polymorphous; the α -form (corundum) may be denoted as a hexagonal close-packed array of oxygen atoms with metals in two-thirds of the octahedrally coordinated interstices (Anderson 1972). The structure of γ -alumina is complex: it has 32 oxygens per unit cell and these are arranged as in a spinel, with the corresponding 21.33 aluminum distributed randomly over 24 sites, leaving cation sites vacant. Fe_2O_3 exhibits similar behaviour. Alumina can also be made in amorphous form. These different forms can be used as catalyst supports and are discussed in chapter 4.

Silica is of particular importance because of its use as a stable catalyst support with low acidity and its relationship to zeolite catalysts, which will be discussed in chapter 4. Silicon is an abundant material in the earth's crust and occurs in various forms including silica. Silica is also polymorphous with the main forms being quartz, cristobalite and tridymite. The stable room temperature form is quartz (SiO_2). Recently, a new family of stable silica-based ceramics from chemically stabilized cristobalites has been described using electron microscopy (Gai *et al* 1993). We describe the synthesis and microstructures of these ceramic supports in chapters 3 and 5.

1.9 Carbons as supports in catalysis and new forms of carbons with atomic scale building blocks

1.9.1 Amorphous carbon, graphite, fullerene and carbon nanotubes (CNT)

The enormous importance of carbon in such diverse fields as inorganic and organic chemistry and biology is well known; however, only the aspects of carbon relevant to catalysis will be described here. The main topics we are concerned with are porous activated carbons, carbon black as catalyst supports and forms of coking. Carbon is also currently used as storage for natural gas and to clean up radioactive contamination. Carbon is available at low cost and a vast literature exists on its uses. Coal-derived carbon is made from biomass, wood or fossil plants and its microstructure differs from carbon made from industrial coke. Activated carbons are synthesized by thermal activation or by chemical activation to provide desirable properties like high surface area.

Carbon can exist in pure forms with graphite and diamond being well-known forms. It can also exist in disordered (amorphous) or metastable forms. The crystal structures of carbon at room temperature are graphite (figure 1.3(c)) below 1800 MPa and diamond at high pressures. A single crystal of graphite consists of parallel layers in which the carbon atoms are arranged in a hexagonal network of crystal planes called basal planes. The spacing of the carbon atoms within the planes (the carbon-carbon interplanar bond length) is 0.142 nanometres (nm) and between the planes 0.335 nm; (1 nm = 10 Å). Bonding between the atoms in the plane is covalent and strong sp^2 bonding whereas the planes are held together by weaker Van der Waal forces which enable carbon's easy incorporation into a composite structure. A schematic diagram of the parallel planes of carbon atoms in graphite stacked with a hexagonal geometry is shown in figure 1.6. Carbon and graphite fibres are often used in composite structures. They exhibit slightly different surface properties and these, including surface area, are crucial to any bonding between the fibre and matrix. Graphitization occurs by converting amorphous carbon into graphite and this has been reviewed by several workers (e.g. Thomas *et al* 1997 and Boudart 1981). The extent of graphitization depends on the origin of the amorphous carbons, for example, pyrolytic carbons or petroleum coke transform readily to graphite at $\sim 2700^\circ\text{C}$. Defects between planes can influence the disorder in carbons. Earlier work has shown that evaporated carbon films can have structures with both sp^2 and sp^3 bonding resulting in a network of both trigonal graphitic bonding and diamond-like tetragonal bonding. Recent progress includes the dramatic discovery of a new form of carbon known as fullerene or buckyball.

No other allotropic forms of carbon were known until ten years ago: then arising from studies of interstellar carbonaceous molecules, a new form of carbon, namely fullerene or 'buckyballs', was discovered (Kroto *et al* 1985), for which the authors received the 1996 Nobel Prize for Chemistry. Its structure is basically a ball or spherically shaped cage consisting of pure carbon. The most stable

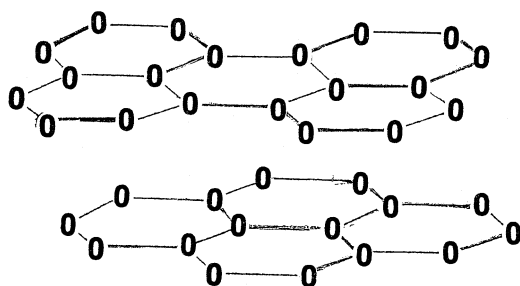


Figure 1.6. Schematic diagram of graphite layers with hexagonal symmetry.

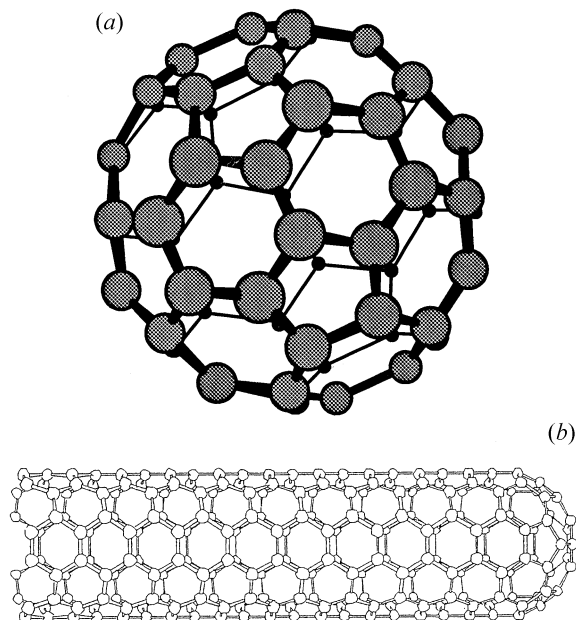


Figure 1.7. Schematic diagrams of the structure of (a) the C₆₀ molecule and (b) a single wall nanotube (SWNT).

molecule is C₆₀, or buckminsterfullerene (or buckyball), named after the architect of the geodesic dome roof, since the structures resemble each other! Its structure is shown in figure 1.7(a), with the atoms at the corners of polyhedra. Although the full potential uses of this new allotrope remain to be discovered, their hollow shape (or cages) has stimulated interest in the field of catalysis and medical sciences. In catalysis chemistry, cages are being used to encapsulate metal species, and in medical sciences they are being considered as an inert delivery system for drug molecules. These carbons were developed on a large scale

using ingenious methods of laboratory preparation involving the vaporization of graphite in a carbon arc in helium by Kratschmer *et al* (1990). This was followed by buckytubes and other complex forms of carbon. All the forms are based on a family of polyatomic molecules consisting of carbon atoms twisted into polygons and three-dimensional arrays. These represent a new allotropic form of carbon.

1.9.2 Nanotubes

Another form of ordered carbon called carbon nanotubes (CNT), based on fullerenes and produced under conditions similar to those used for fullerene synthesis, was reported by Iijima (1991). Catalytic reaction can also be used for their synthesis. The production of nanotubes via a catalytic process (instead of the arc-discharge technique) is thought to be better because of the lower reaction temperatures and greater control over experiments. In CNTs, carbon appears as long hollow tubes. The nanotubes can be thought of as 'rolled up' sheets of graphene, which is capped at each end with half a fullerene molecule. Single-wall nanotubes (SWNT) have single tubules with diameters down to 0.4 nm and multi-wall nanotubes (MWNT) have multiple concentric tubules with diameters up to several tens of nm and both have been observed by electron microscopy. Figure 1.7(b) shows a schematic diagram of SWNT. Both SWNTs and MWNTs can be micrometres long. Reports suggest that nanotubes may be commercially more useful for reinforcing composites: a nanotube has a better elastic modulus and greater strength than a carbon filament since shearing a nanotube along its axis means breaking strong covalent bonds, whereas in shearing a filament only weaker bonds between graphite layers need to be broken. Nanotubes are believed to be the most oxidation-resistant forms of carbon.

SWNTs have been synthesized in large quantities using laser vaporization of a carbon target with Ni-Co catalysts (Smalley *et al* 1996). Ordered arrays of SWNTs form ropes or bundles. Figure 1.8 illustrates a SWNT (e.g. at A) and ropes of SWNT (e.g. at B). CNTs, like buckyballs, can offer potential as catalyst supports and superconductors. Substitution of CNTs with metal catalysts have been reported (Tsang *et al* 1995). CNTs can also be used to make intercalation compounds by doping between the flat layers of carbon atoms in the graphite structure (Iijima 1993). Carbon materials in different forms thus exhibit a wide range of structural diversity and properties. The technological challenge is to design and control the structure of these new materials to meet the demands of new products and green processes in catalysis.

1.9.3 Carbons and catalytic reactions

Amorphous carbon is one of the most important and economical materials in catalysis and is generally used as a support for metallic catalysts. Normally, fine metallic particle catalysts are dispersed on such carbon supports. In the following section we briefly review such carbons, its uses and carbon deposits resulting

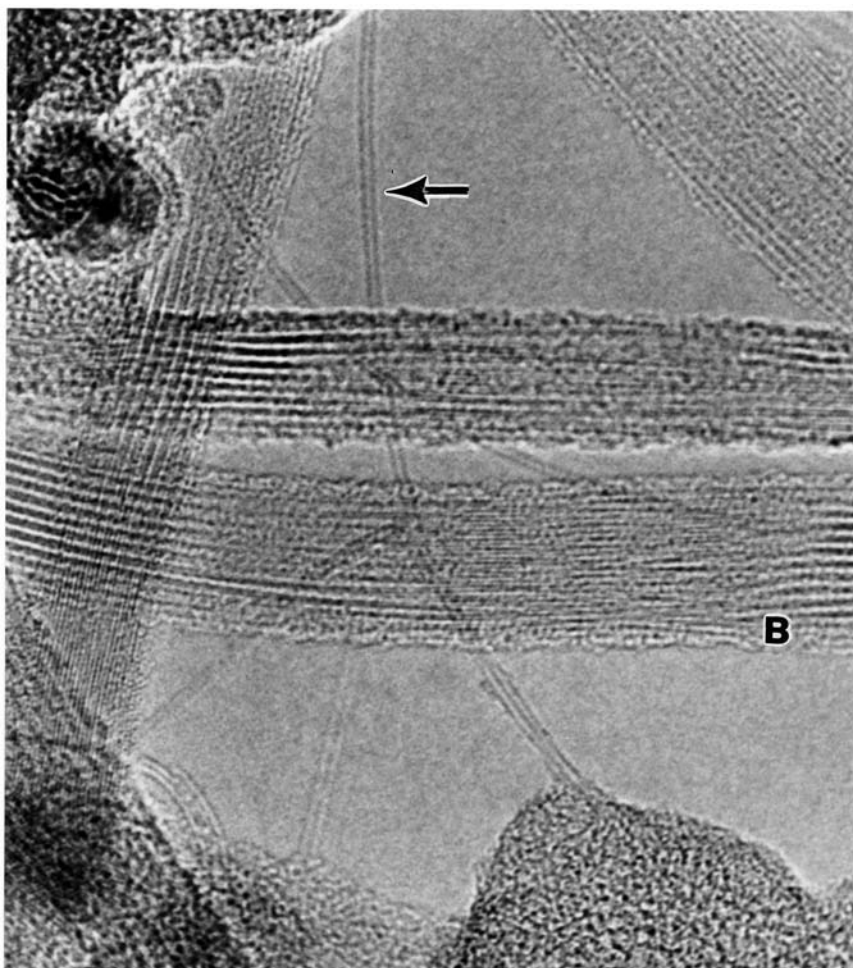


Figure 1.8. A single wall carbon nanotube (e.g. arrowed, with ~ 1.4 nm diameter) and ribbons or bundles of SWNTs (e.g. at B) after Gai 1999. (Sample courtesy of R E Smalley *et al* 1996.)

from catalytic reactions. EM has played a key role in elucidating structures of different forms and growth of ordered carbon filaments during the decomposition of hydrocarbons or carbon monoxide and in the studies of catalytic graphitization of disordered carbon in the presence of metals.

In earlier *ex situ* and vacuum heating studies of carbon using EM, it was suggested that the temperature for the onset of graphitization depended on the nature or origin of the carbon and, more importantly, the gas environment and that catalytic graphitization occurs at higher temperatures of ~ 800 °C (Boudart

1981). Recent *in situ* controlled environmental ETEM studies have shown that catalytic graphitization of carbon with Pd can occur at temperatures as low as $\sim 300^\circ\text{C}$ in H_2 atmospheres (Gai *et al* 1989–90). Reactions between Ni and amorphous carbon below 600°C have shown the formation of graphite (Itoh and Sinclair 1994). The catalytic graphitization of disordered carbon is explained by a solution–precipitation mechanism (Audier *et al* 1981). In this mechanism, carbon atoms are dissolved in the metal followed by precipitation of carbon as graphite, the driving force being the free-energy change between the initial and final forms of carbon. In some chemical reactions between metals and carbon, metal carbides may form at high temperatures (e.g. as intermediates): a graphite can result from the decomposition of the metal carbide by vaporization of the metal at high temperatures (Audier *et al* 1981). The solution–precipitation mechanism has also been proposed for the conversion of graphite to diamond, catalysed by a variety of transition metals and noble metals between $\sim 1230^\circ\text{C}$ and -2430°C at pressures of 5000–10000 kPa.

Small metal particles (e.g. of transition metals) decompose hydrocarbons or CO resulting in carbon filaments known as ‘filamental carbon’, with the catalytic particle at the leading edge at typical temperatures of $\sim 327\text{--}630^\circ\text{C}$ (figure 1.9(a)). The solution–precipitation mechanism is believed to operate with the decomposition of the gas on the front end of the metal particle, diffusion of the carbon through the metal and precipitation of the carbon on the other side of the particle. This mechanism has been confirmed by studies of such filamental carbon by *in situ* ETEM (Baker and Chludinsky 1981, Gai *et al* 1989). The rate-determining step is found to be the diffusion of carbon through the metal.

1.9.4 Choice and design of catalyst supports or carriers

The physical and chemical properties required by specific processes dictate the choice, design and manufacture of catalyst supports and carriers. Careful choice of materials, synthesis and calcination are necessary to obtain high catalytic performance. The general criteria for a good support are: it needs to be strong with high surface area; it should exhibit impact resistance, abrasion/attrition resistance; and it should not deactivate during catalytic cycles. In many applications the surface properties, e.g. acidity and chemical composition, are important. These materials exist in different forms: high surface area powders, honeycomb shapes, pellets etc. They are synthesized, for example, via coprecipitation, sol–gel methods and saturation. Various shapes are formed via extrusion, agglomeration and spray-drying. Drying or calcination procedures are also important in controlling their properties.

1.9.5 Carbon deposits

In the selective oxidation of hydrocarbons or in fuel technologies, catalysed carbon deposition from the gas phase can occur, which can lead to catalyst

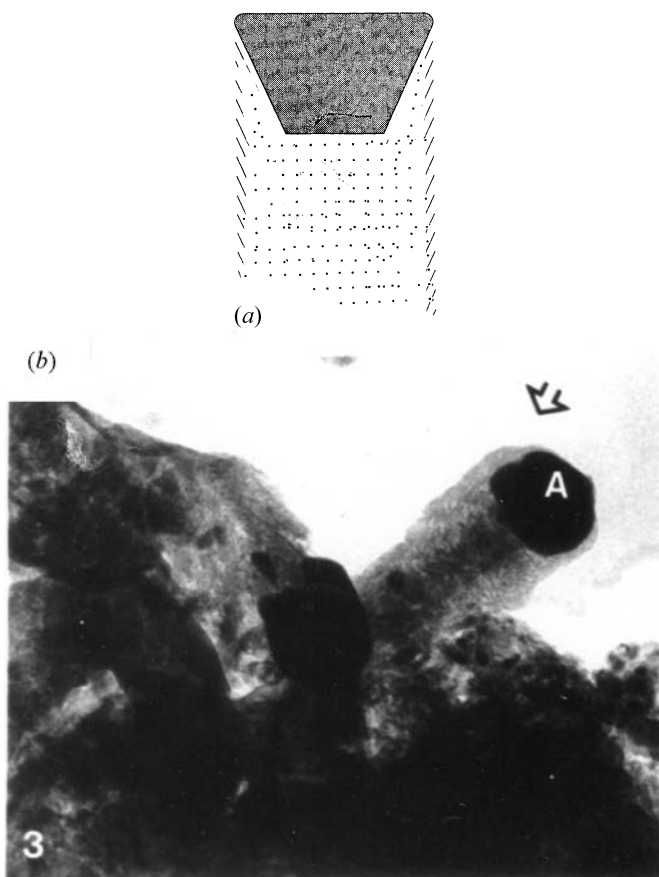


Figure 1.9. (a) Schematic diagram of filamental carbon with a catalytic particle at the leading edge; (b) a TEM image of filamental carbon with an Fe_5C_2 carbide particle (A), at the leading edge. Particle diam. ~ 20 nm.

deactivation. In addition, carbon deposits can build up on the reactor walls, decreasing reactor efficiency. The mechanisms for controlling carbon deposition and the forms of the deposit are not fully understood. The addition of a specific metal to metallic catalysts can diminish carbon deposition (chapter 5). Carbon filaments can be formed when a microcrystal fragments from the bulk metallic catalyst particle through the deposition of a graphitic carbon filament as described earlier. There have been numerous studies on catalytic particle shapes and the orientations of graphite in the filament and these are known to vary depending on the experimental conditions (e.g. Boudart 1981). For example, reaction temperatures, gas-feed composition, the chemical nature of the catalyst particles, reaction time and metal-support interactions are all thought to be important

factors affecting the carbon morphology. The studies have shown that carbon cones are stacked in the filaments and that graphitic basal planes do not lie along the filament axis, indicating that there are exposed lattice edges at the carbon outer-layers in the filament. Carbide formation depends on the carbon activity in the gas phase and the nature of the active metal (Rodríguez *et al* 2001). In some reactions carbide formation can lead to the fragmentation of the metallic particle and the formation of filaments. Audier *et al* (1981) have shown that another, perhaps less common, form of deposit consisting of multilayer shells encapsulating catalyst particles at higher reaction temperatures in the hydrogenation (with $\sim 0.2\%$ H_2) of CO at 500°C . However, hydrogen partial pressures are important in controlling the rate and type of the carbon deposit. EM (and, in particular, high-resolution transmission EM or HRTEM) has been pivotal in identifying carbon morphology directly. An HRTEM micrograph of a carbon filament formed in a CO/CO₂/steam environment with a Fe₅C₂ carbide particle at the leading edge is shown in figure 1.9(b).

1.9.6 Polymers

These are long chain molecules consisting of multiples of repeat units (monomers). These are linked by covalent bonds in a three-dimensional network which is characteristic of a polymer. The magnitude of the length of a polymeric molecule can extend up to several hundred nanometres. The dimensions of individual polymer molecules and their arrangement define the structure of polymers and their properties. Many catalytic processes are aimed at producing polymers as we describe in the following chapters. (Polymers can also be used as catalyst supports.)

1.10 Oxides and non-stoichiometry in catalysis and the unique role of electron microscopy

1.10.1 Methods of accommodating non-stoichiometry

In an ideal world, crystals would be perfect or stoichiometric with constant composition. But like people crystals are not exempt from imperfections or *defects*. Crystals with variable composition are termed non-stoichiometric crystals. The defect chemistry of oxides is enormously complex and is extremely vital to their properties. It has involved extensive research in many laboratories and is providing extraordinary insights into structural variations, the stability of structures and the formation of new structures. Here, we first define order-disorder phenomena that are commonly associated with oxides and describe our current understanding of them. The disorder or non-stoichiometry plays a crucial role in oxide applications including catalysis and it is therefore of paramount importance.

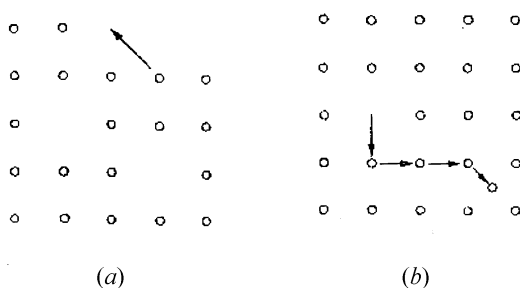


Figure 1.10. Point defects: (a) formation of a Schottky defect; (b) Frenkel defect. (Cottrell 1971; reproduced courtesy of Arnold Publishing.)

As is well established, in apparently stoichiometric crystals, point defects are present in low concentrations. The presence of impurity atoms disturbs the host lattice and affects the optical conduction together with other transport properties in essentially stoichiometric crystals (e.g. in semiconductors). Point defects can be classified as either vacancies or interstitials and they are inherently present in crystals by virtue of energy fluctuations above absolute zero (Adams 1974). Vacancies occur by the removal of atoms in crystals (i.e. holes left by missing atoms) and are called Schottky defects. Another type of point defect is an interstitial defect which occurs, for example, by the presence of an additional atom in a crystal. To produce a vacancy inside a perfect crystal, an interstitial also has to be created. This vacancy–interstitial pair is termed a Frenkel defect and a large amount of energy is necessary for it to form. From low-energy considerations, it is therefore easier for vacancies to form at the surfaces or grain boundaries of crystals, where an atom can be lost without forming an interstitial. We use this phenomenon later in understanding non-stoichiometry in oxide catalysts. The formation of a Schottky defect is shown in figure 1.10(a). The creation of a vacancy with the simultaneous formation of an interstitial is shown in figure 1.10(b). Frenkel and Schottky defects are the classical point defects (Cottrell 1971). Because they occur randomly, the statistical mechanical limitations of isolated point defect models are valid for very small deviations from stoichiometry. Ni_{1-x}O , with $0 < x < 0.001$ (or 1000 ppm), is such an example. Point defects are basic to the transport of matter in solids. In transition-metal oxides, stoichiometric oxides can be insulators, whereas non-stoichiometric oxides can be semiconductors (p-type, if there is an oxygen excess, or n-type if there is an oxygen deficiency).

However, structural chemistry in oxides with large departures from stoichiometry cannot be solely explained by point defects. Defects cannot remain isolated and interactions between them begin to occur. Our discussion therefore begins with a general description of the fundamental knowledge about non-stoichiometry in oxides. Understanding such disorder and the complex defect

structure is one of the most significant advances in solid state materials chemistry and catalysis and is due mainly to the unique role played by EM and electron diffraction methods. We first give some examples of non-stoichiometry in oxides and show the relevance of these to catalysis. For example, TiO_{1+x} with $-0.3 < x < 0.3$ and Fe_{1-x}O with $0.03 < x < 0.15$ are examples of larger deviations in stoichiometry. Non-stoichiometric oxides can exist over a chemically significant composition range.

There are many classes of non-stoichiometric oxides. Several workers have carried out pioneering work in non-stoichiometry, including primarily by EM methods, for example Magneli (1951, 1953, 1970), Wadsley (1964, 1967), Anderson (1970–1977), Thomas (1974–1986), Bursill and Hyde (1972), Tilley (1970, 1979), Bursill (1969, 1981) and Gai (1981–1997)) in oxidation catalysis. Some of the different classes of non-stoichiometric oxides are described here so that the various ways in which crystal non-stoichiometry can manifest itself will be apparent. Since oxides have the capacity to chemisorb oxygen at their surfaces or release (lattice) oxygen from their surfaces, they are the most useful in redox (reduction and oxidation) reactions. The broad field of non-stoichiometry ranges from isolated point defects, which are entropy-controlled systems, to larger deviations in non-stoichiometry resulting in sets of (discrete) intermediate phases which are enthalpy-controlled systems (Anderson 1970). Between these, non-stoichiometry can result in clusters of short-range order, shear structures, block structures, chemical twins, coherent intergrowths and infinitely adaptive structures. Because these are important in oxide catalysis, we will examine these criteria briefly.

1.10.2 Point defect models

In point defect models, vacancies and interstitial ions may be responsible for point defects. These defects may be independent of both the composition and external conditions.

1.10.3 Larger deviations from stoichiometry

Non-stoichiometric oxides with high levels of disorder may adopt two modes of stabilization: aggregation or elimination of point defects. Point defect aggregates forming clusters are examples of the former and extended defect structures like crystallographic shear-plane structures are examples of the latter.

1.10.3.1 Short-range clusters

In a non-stoichiometric oxide of the type M_{1-x}O (where M is a metal), the association of the vacancy and the positive hole, or M^{3+} ion, can form the simplest cluster complex for Fe_{1-x}O . X-ray and neutron diffraction measurements (Roth 1960) suggested that some Fe^{3+} ions are in tetrahedral sites (figure 1.11(a)). An

Fe^{3+} ion close to a vacancy can move to a tetrahedral site leaving a vacancy in an octahedral site. Refined diffraction data could only be obtained for defect models that included metal interstitials (with an interstitial concentration about half that of vacancies). This has led to an important result: that both interstitials and vacancies can exist in a cluster. This type of cluster is known as a Roth cluster (a forerunner to inverse spinel structures). Further diffraction refinements confirmed the earlier work that interstitials and vacancies can coexist in the Fe_{1-x}O phase: the data have suggested a vacancy:interstitial ratio higher than two in the cluster providing a detailed picture of the cluster in Fe_{1-x}O , called the Koch–Cohen structure (Koch and Cohen 1969) shown in figure 1.11(b). In this structure, there are 13 vacancies and four Fe^{3+} ions in tetrahedral sites and the rest are distributed in the regular lattice. Such clusters can exist in other non-stoichiometric transition-metal monoxides like MnO , NiO and CoO . Ordering of clusters can lead to a superstructure based on the host subcell.

The fluorite-type structure shows a high tolerance of disorder which may be introduced by dopants or catalytic processes. We discuss the latter in other sections. Clustering in fluorite-type structures (for example in urania UO_2 or lanthanide structures, figure 1.11(c)) can occur by oxygen excess (UO_{2+x}) (Willis 1964). Studies of $\text{UO}_{2.13}$ from neutron scattering studies have revealed that oxygen atoms are displaced along $\langle 110 \rangle$ from the high symmetry interstitial site. In addition, each interstitial displaces oxygen atoms along $\langle 111 \rangle$, creating vacant anion sites and interstitial oxygen with the basic defect aggregate structure known as the 2:2:2 cluster. Distorted interstitials are commonly present at higher disorder levels and defect clustering is therefore used to explain their formation. Interstitial clusters in other doped compounds have since been reported. Figure 1.11(d) shows the CaF_2 structure.

Anion-deficient fluorite oxides are also present, for example, UO_{2-x} , CeO_{2-x} . The presence of anion vacancies in reduced fluorites has been confirmed by diffraction studies. In reduced ceria for example, some well-ordered phases has been reported (Sharma *et al* 1999). The defective compounds show very high anion mobilities and are useful as conductors and as catalytic materials as will be described later. However, the structures of many anion-deficient fluorite oxides remain unknown because of the sheer complexity of the disordered phases. There are, therefore, many opportunities for EM studies to obtain a better understanding of the defect structures and properties of these complex materials which are used in catalysis.

1.10.4 Non-stoichiometry in metallic monoxides

1.10.4.1 Phases with the rock-salt structure

An interesting group of non-stoichiometric oxides are the transition-metal monoxides (MO, where $\text{M} \equiv \text{metal}$); for example, titanium monoxide (TiO) and vanadium monoxide (VO). These have a wide range of non-stoichiometric

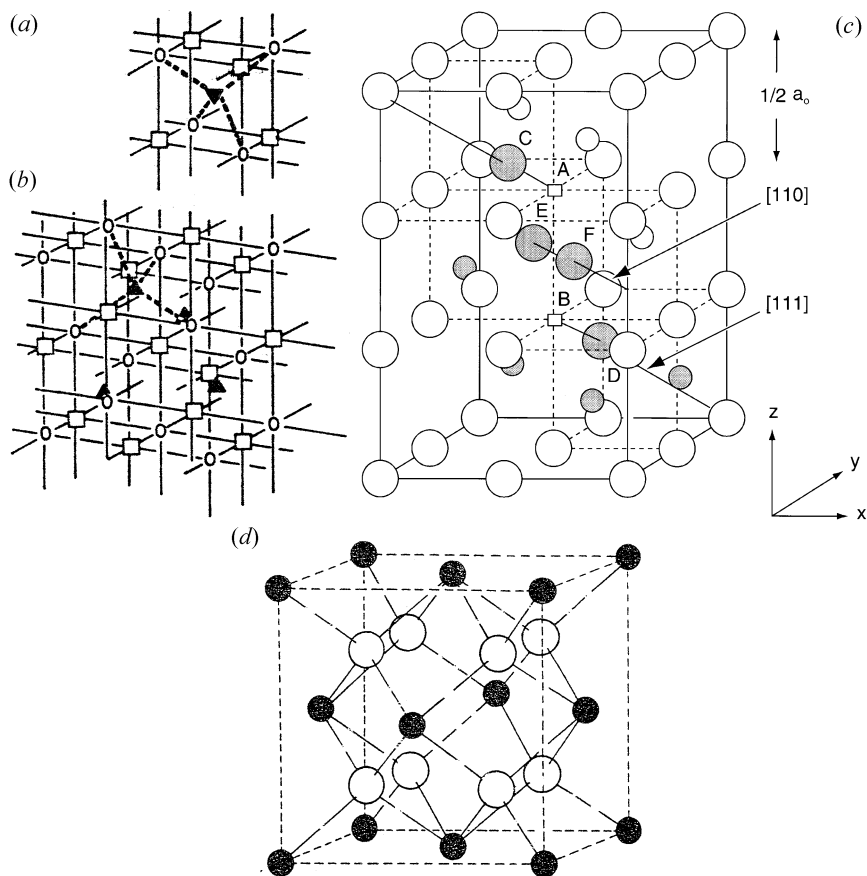


Figure 1.11. Schematic diagrams of (a) and (b) Fe_{1-x}O point defect clusters (after Koch and Cohen 1969); (c) clustering in fluorite-type structures; and (d) the CaF_2 structure.

compositions on either side of the stoichiometric composition $\text{MO}_{1.0}$ (Anderson 1971, Rao *et al* 1974, 1986). Their structures show a large number of both metal and oxygen vacancies: for example, at the ideal composition, up to 15% vacancies exist in each cationic and anionic sublattice in TiO . The vacancy concentration can be reduced under selected temperatures and pressures. Various ordered phases have been reported for $\text{TiO}_{0.70}$ – $\text{TiO}_{1.250}$. This wide range of non-stoichiometry arises from the electronic structure of the two oxides. The metal ions have overlapping d-orbitals leading to strong metallic bonding between the cations. This implies that the excess charge (negative or positive) involved in the defect formation (electrons or holes) is delocalized and not trapped on cations. Electron microscopy studies show a wide range of non-stoichiometry for VO_x (with $0.75 < x < 1.3$) (Rao *et al* 1976). The defect mechanism is primarily

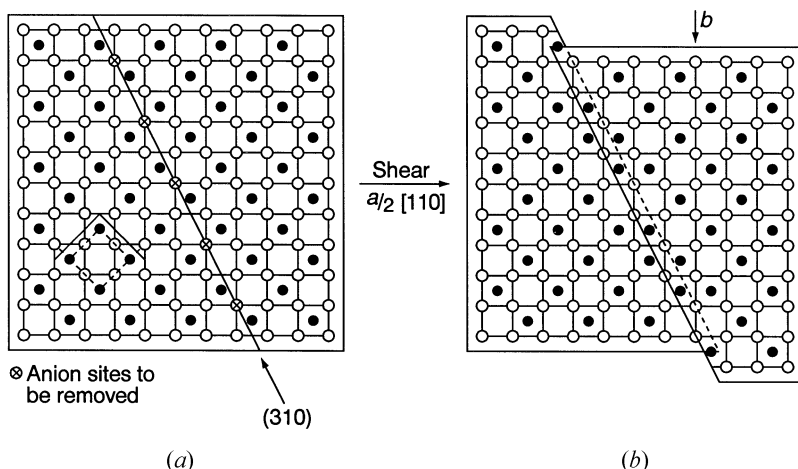


Figure 1.12. Principle of crystallographic shear (CS) in ReO_3 : (a) formation of anion vacancies; and (b) elimination of the vacancies by crystal shear and collapse, from corner-sharing octahedra to edge-sharing octahedra forming extended CS plane defects.

cation and anion vacancies as in TiO . Ordered phases exist in the composition range $\text{VO}_{1.2}\text{--VO}_{1.3}$.

1.10.4.2 Long-range order and elimination of point defects

Even at lower concentrations (10^{-4}), some interactions between point defects are possible. In forming new structures, the vacancies either order or they are eliminated. These vacancy accommodation processes are immensely important in heterogeneous oxidation catalysis using oxides and we examine these in the following sections.

1.10.5 Defect elimination: crystallographic shear (CS)

In some oxides, extensive disorder in non-stoichiometric crystals may be stabilized by the elimination of complete rows of anion point defects in specific crystallographic planes by simultaneous shear displacement and crystal structural collapse on the planes, by a mechanism called crystallographic shear (CS) (Magneli 1951, Wadsley 1964, Anderson and Hyde 1967). This leads to the formation of extended planar defects called crystallographic shear planes (CS planes). Pioneering x-ray diffraction (XRD) work of the structural principles of CS phases in oxides (e.g. in TiO_{2-x} as a function of the oxide reduction) have been described by Magneli (1951, 1970) and the phases are called the Magneli phases. The term ‘crystallographic shear’ was introduced by Wadsley (1964) to define both the elimination of anion vacancies and crystal structure collapse.

1.10.6 Background to earlier work

Following Magneli's work with XRD, work by Andersson *et al* (1968) showed further detailed non-stoichiometric phases in titania. A homologous series of compounds Ti_nO_{2n-1} were discovered with $1.75 < x < 1.9$ where $x \equiv O/Ti$. The structural determination of Ti_5O_9 indicated the boundaries of CS planes parallel to $\{121\}$ planes and across them and the displacement of adjacent slabs by the vector $\frac{1}{2}[011]$, necessitating the elimination of vacant anion sites in crystal planes for the process. This basic feature of the CS principle in understanding crystal structures in a number of transition-metal oxides was elucidated by Wadsley (1964). Anderson and Hyde (1967)¹ suggested a dislocation model for CS planes similar to that for forming intrinsic stacking faults in metals: that the loss of lattice oxygen creates anion vacancies which at low concentrations aggregate into discs; the discs collapse at a certain critical size (loop) to produce an element of a CS plane bounded by a partial dislocation. The elastic strain at such a dislocation creates a natural sink for vacancies, causing the loop to expand by climb of the bounding dislocation. This model was confirmed using electron-beam-heating studies MoO_3 in vacuum of MoO_3 (Bursill 1969) and by *in situ* ETEM studies of catalysts near the actual conditions of the dynamic catalytic reaction (Gai 1981).

The formation of a CS plane in an oxide involves two processes: the elimination of anion point defects followed by lattice collapse, leading from corner-sharing to, for example, edge-sharing octahedra. The process is therefore a heterogeneous one. The principle of the process is best explained in terms of coordination polyhedra of rhenium oxide or the ReO_3 structure, shown in figure 1.13. The ReO_3 structure consists of corner-shared octahedra. When a number of oxygen vacancy defects are generated in the structure (figure 1.13), the CS movement indicated by arrows removes the vacancies by edge-sharing octahedra. The figure illustrates how the CS process accommodates a change in the ratio of cation to anion sites, without changing the first neighbor coordination. The oxygen deficiency in the reduced oxide is incorporated by the formation of CS planes of edge-sharing octahedra in a specific crystallographic orientation. From this discussion, it may be seen that when an oxide is reduced, the driving force for the formation of CS planes is to lower the free energy of the system and for the preservation of the cation octahedral coordination.

The extraordinary feature of this process is that over a period of time, random CS planes can become ordered, with regularly spaced CS planes separated by slabs of an unperturbed parent matrix, leading to new phases. The overall stoichiometry of such a crystal depends on the spacing of the CS planes and the matrix slabs. At certain levels of anion deficiency this will produce the so-

¹ The Anderson-Hyde dislocation model differs from the earlier model based on the cooperative diffusion mechanism described by Andersson and Wadsley (1966), in which CS planes, e.g. in rutile, were thought to be produced by cation migration during reduction. The reduced oxygen potential at the surface means an enhanced Ti-potential and therefore the Ti ions diffuse cooperatively into the crystal down this Ti-potential gradient. However, there is no experimental evidence to support this hypothesis. This mechanism is also less likely since this would involve a large number of cations.

called homologous series of compounds, each with a definite composition and mixed valence cations as described earlier. For example, a homologous series of Ti_nO_{2n-1} has been reported as described earlier, with n the width or spacing of the CS planes (depending on the various interaction energies between parallel CS planes). Defects in titania are important. Case histories of CS planes in titania with various non-stoichiometries are described in detail in Bursill and Hyde (1972): during the reduction of TiO_x a gradual change in the orientation of CS planes is observed: they rotate (or 'swing' and hence the term 'swinging CS planes') from (132) to (121) via intermediate orientations. HRTEM micrographs of a pair of CS defects in $TiO_{1.9966}$ are shown in figures 1.13(a) and (b). A dynamic EM sequence of the annealing of (011) rutile microtwin at 380 °C and 700 °C is shown in figures 1.14(a)–(c) (Blanchin *et al* 1981). Figure 1.14(d) shows an HRTEM micrograph of the atomic structure of microtwin lamellae. Figure 1.15 shows a twinned region in rutile.

Some earlier thermodynamic studies on rutile reported expressions involving simple idealized quasi-chemical equilibrium constants for point defect equilibria (see, e.g., Kofstad 1972) by correlating the composition x in TiO_x with a function of $\Delta G_m(O_2)$, which is the partial molar free energy of oxygen. However, the structural effects were not accounted for in these considerations. Careful measurements of $\Delta G_m(O_2)$ in the TiO_x system (Bursill and Hyde 1971) have indicated that complete equilibrium is rarely achieved in non-stoichiometric rutile.

1.10.7 Reaction mechanism

The CS mechanism has been studied extensively by electron microscopy, in various binary systems, including rutile (TiO_2), molybdenum trioxide (MoO_3), V_2O_5 , WO_3 and other more complex structures (Bursill and Hyde 1972, Tilley 1970, Gai 1981–1993). Extensive tilting experiments (tilting the sample to required diffraction conditions) are essential in the electron microscope to understand the complete structure and geometry of a CS plane. A complete understanding of the CS structure requires full knowledge of the atomic mechanisms involved in the CS process. Calculations of oxides containing a finite number of CS planes (Catlow and James 1978 and Cormack *et al* 1982) show that a point defect concentration is present in equilibrium with CS planes. Early experiments relied on static samples (samples reacted elsewhere, cooled to room temperature and examined in the EM) and, based on these static studies, published reports suggested the complete elimination of anion vacancies to form the CS defect (Wadsley 1964, Andersson *et al* 1966, Anderson and Hyde 1967, Anderson 1970–1971 and Anderson *et al* 1973). However because of the difficulties in making direct *in situ* observations of the CS defect formation under controlled environments and at elevated temperatures, none of the CS mechanisms proposed (nucleation, growth etc) and the role of CS in catalysis were fully understood until the developments of *in situ* environmental TEM (ETEM) methods of studying the

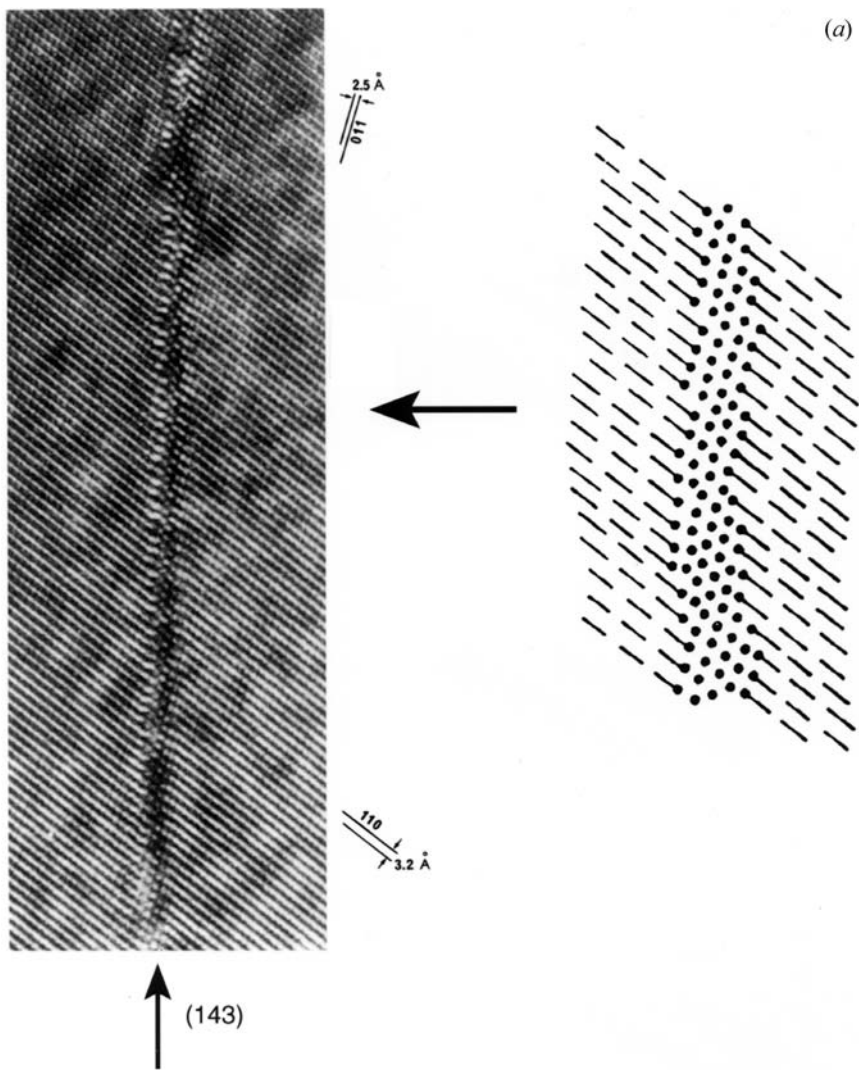


Figure 1.13. HRTEM images of CS planes in reduced $\text{TiO}_{1.9996}$: (a) (143) the CS plane and (b) the (132) CS plane (Blanchin *et al* 1981; reproduced by courtesy of EDP Sciences).

reaction under controlled conditions.

We describe the development of *in situ* (dynamic) ETEM for direct imaging of CS defects in dynamic catalytic oxides in chapter 3. These studies have recently led to better insights into the formation of CS planes (leading to further developments in the dislocation model) and their role in oxidation catalysis. By directly probing the formation of CS planes and their growth by *in situ* ETEM

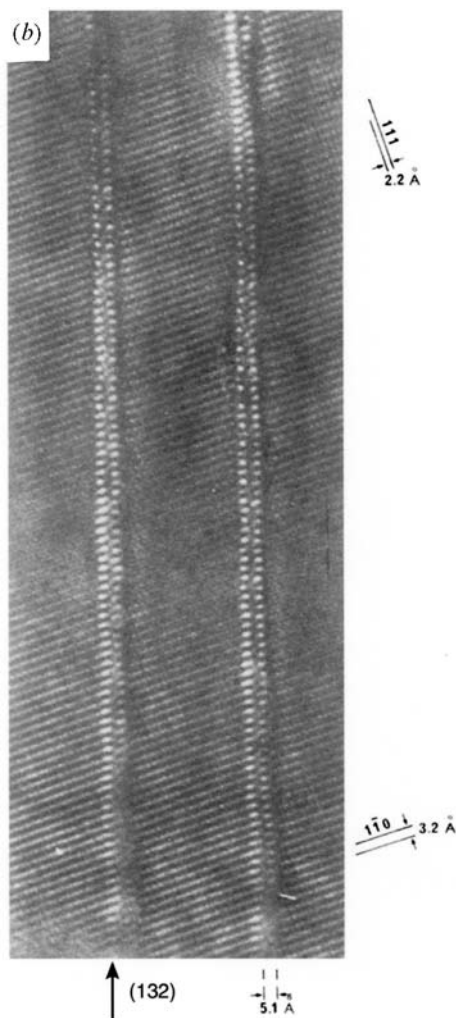


Figure 1.13. (Continued)

under reaction conditions, the formation of CS planes can be explained by the elimination of supersaturation of anion vacancies in oxides, supersaturation being defined in relation to the background equilibrium concentration of vacancies in the reacting crystal (Gai 1981–1982, 1983, 1992, 1997, Gai *et al* 1982). Thus, an important mechanism involving the supersaturation of anion vacancies in the formation of CS planes arose directly from *in situ* ETEM studies of catalytic oxides.

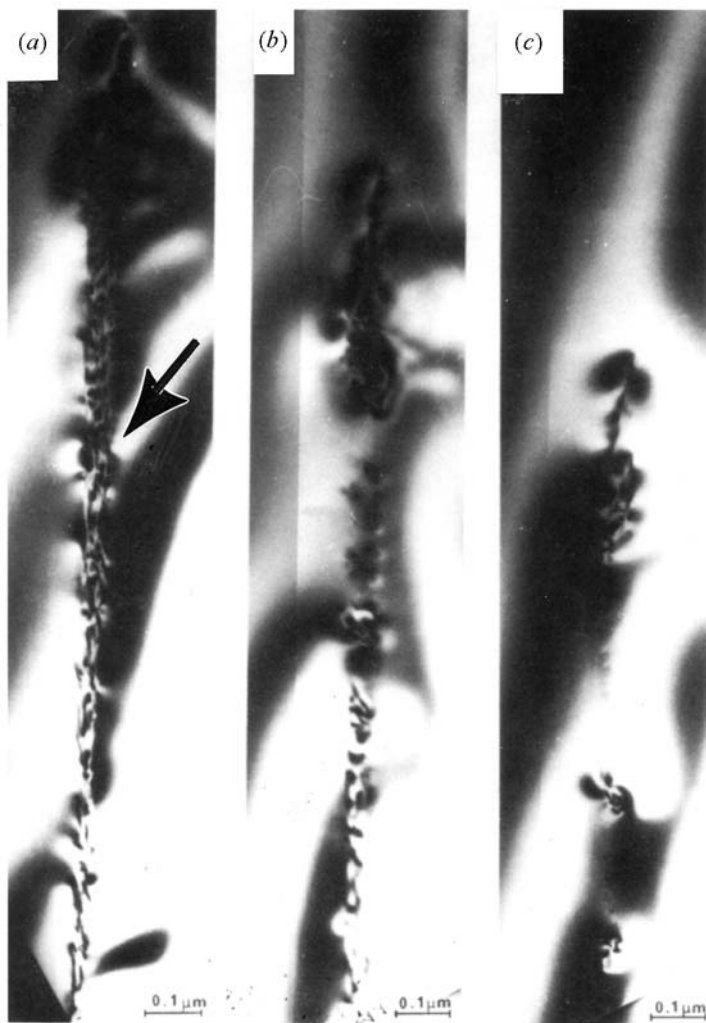


Figure 1.14. *In situ* time- and temperature-resolved annealing of twin lamellae in ECELL (arrowed): (a) room temperature, (b) 380 °C, (c) 700 °C (by 1000 °C, the annealing is complete and the lamellae disappear completely). (d) HRTEM image of the atomic structure of twins with the structural model. (Blanchin *et al* 1981; reproduced by courtesy of EDP Sciences.)

1.10.8 Block structures

Block structures are based on the ReO_3 lattice, niobium oxides (Nb_2O_5) being an example. Complex non-stoichiometry is present in the range of oxides $\text{NbO}_{2.4-}$

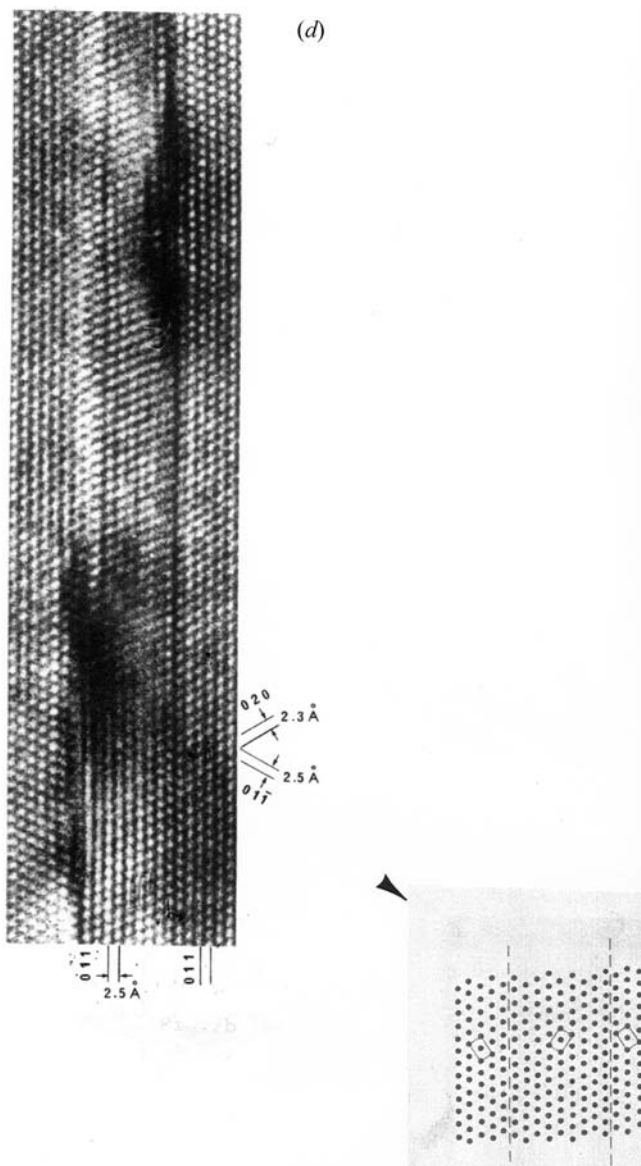


Figure 1.14. (Continued)

$\text{NbO}_{2.5}$ and this was described in detail in elegant papers by Anderson (1970, 1973). Ordered phases are based on shear structures, with parallel CS planes (double crystallographic shear) separating the blocks of the ReO_3 lattice. Ternary and intergrowth block structures have been discovered by extensive HRTEM

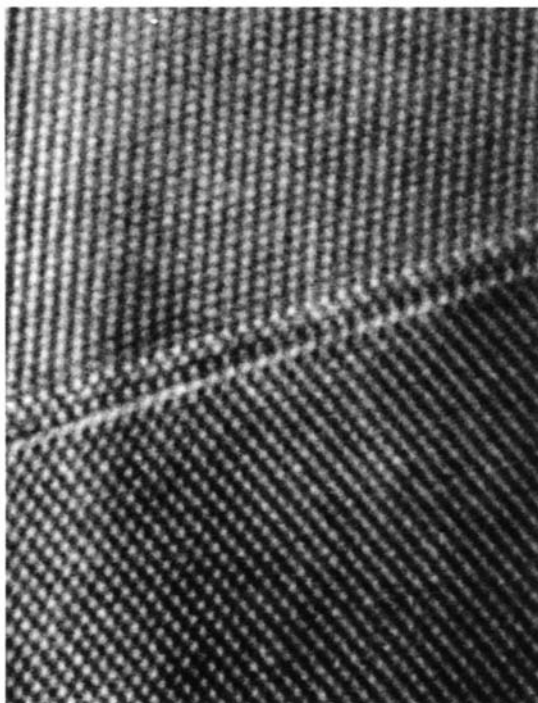


Figure 1.15. An HRTEM image of the twinned region in reduced rutile titania.

and XRD studies. Pioneering HRTEM work elucidating lattice images of block structures was carried out by Cowley and Iijima (1972), Allpress *et al* (1969, 1973), Anderson and co-workers (1973, 1977), Hutchison *et al* (1976) and Gai and Anderson (1976).

Generally, compounds of the type $\text{Nb}_{12}\text{O}_{29}$, $\text{Nb}_{18}\text{O}_{45}$ do not have filled tetrahedral sites and have a limited stoichiometry range, whereas block structures with tetrahedral atoms between blocks have a considerable stoichiometry range, e.g. $\text{Nb}_{25}\text{O}_{62}$, $\text{H-Nb}_2\text{O}_8$ and $\text{WNb}_{12}\text{O}_{39}$ (figure 1.16). These studies have been extended to a number of block structures which consist of blocks of more than one size (considered as intergrowths) of basic structures of one block size. An example is $\text{GaNb}_{11}\text{O}_{29}$ (a variation of $\text{Nb}_{12}\text{O}_{29}$), and is shown in figure 1.17(a) with twin orientations and intergrowth faults. Structural arrangements for these faults and dislocations are illustrated in figures 1.17(b)-(d).

1.10.9 Infinitely adaptive structures

In the shear structures discussed in the preceding sections, smaller compositional variations can be accommodated by changing the CS plane spacings. This, in

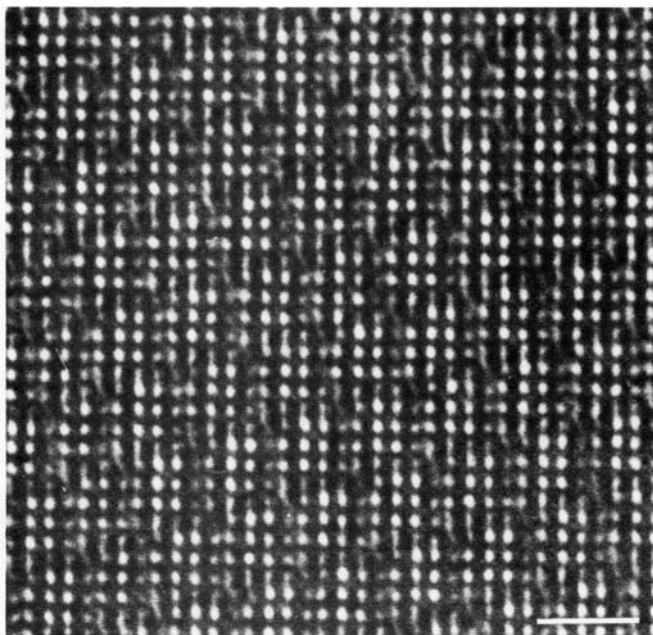


Figure 1.16. An HRTEM image of the block structure of $\text{WNb}_{12}\text{O}_{39}$.

turn, leads to a homologous series of compounds which are close in composition and are biphasic. In an equilibrium diagram these would constitute line phases, separated by the biphasic composition. In another important mechanism, discovered by Anderson (1973) for accommodating non-stoichiometry, the structure adapts to a prevailing stoichiometry. These compounds are known as infinitely adaptive structures. There is thus an ordered phase at every composition generating a network of closely spaced structures without the intervening biphasic regions. For example, in an adaptive structure, the structure with a long periodicity can be thought of as based on the regular stacking of two kinds of subcells. These differ in composition but may be inter-converted through small structural rearrangements when atoms are removed or inserted. The existence of such phases has been reported in the titania-chromia and $\text{Ta}_2\text{O}_5\text{-WO}_3$ series (Anderson 1973).

1.10.10 Vernier structures

In ‘vernier structures’ the modulation in the composition occurs on the basic structure thus combining variable composition with ordering (Anderson 1973). The essential feature of this structure is that the crystal unit can be resolved into two independent sublattices, one with a constant periodicity (based on that of the

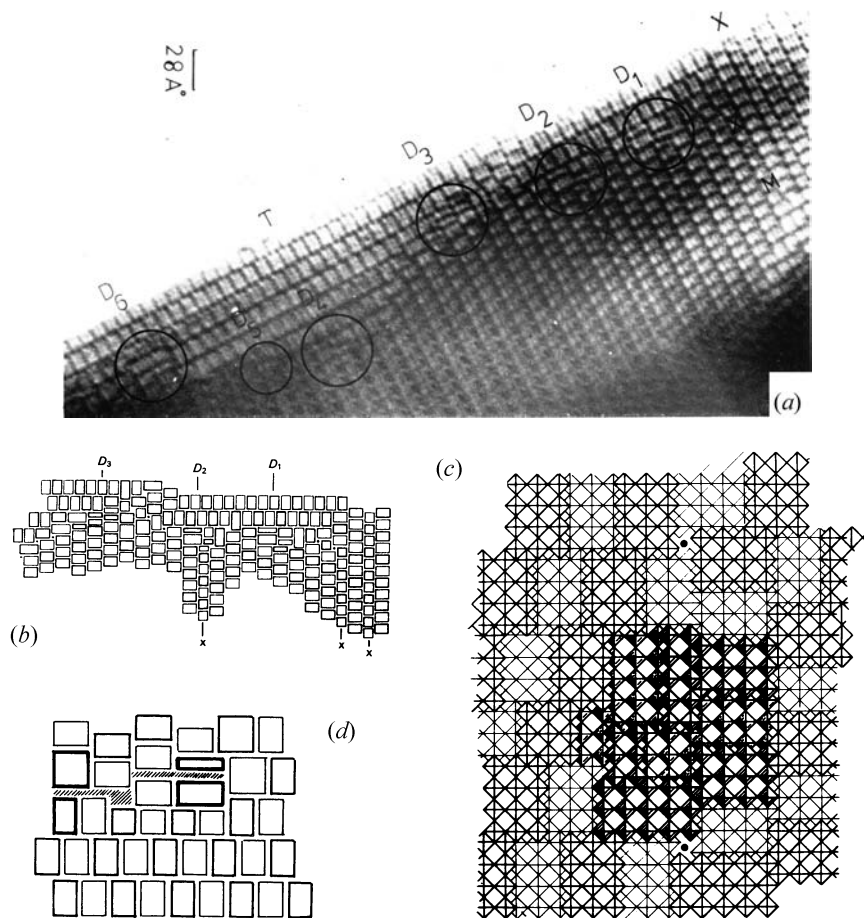


Figure 1.17. (a) An HRTEM image of the intergrowths and dislocations in a complex block structure using $\text{GaNb}_{11}\text{O}_{29}$ as an example; (b) a schematic diagram of the structure in the area shown in (a); (c) a structural model of the 'misfit fault' in D_2 ; and (d) the idealized structure of the dislocation D_6 . The Burgers (displacement) vector and mismatch of cation levels due to the dislocation are shown (after Gai P L and Anderson J S 1976 *Acta Cryst. A* **32** 157).

parent structure) independent of composition and one with a variable composition. This type of structure has been seen in transition-metal silicides and in fluorite-based systems (Thomas 1974, Collingues 1983). For example, in the MX_2 compounds (TiSi_2 , VSi_2 etc), the sublattices of M (metal) and X (non-metal) have the same periodicity at stoichiometry. In non-stoichiometric MX_{2-x} , changes occur in the non-metal periodicity generating a wide range of compositions for

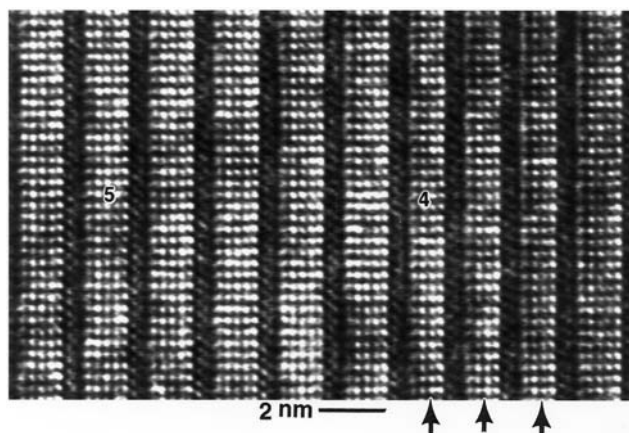


Figure 1.18. An HRTEM image of coherent intergrowths in $\text{TlBa}_2\text{Ca}_4\text{Cu}_5\text{O}_{13}$ (1245), a high-temperature superconductor (HTSC) with five Cu–O layers. Four Cu–O layers (arrowed) of the 1234 HTSC phase are intergrown in the five Cu–O layer compound. (After Gai 1992.)

x. Thus, in $\text{V}_{19}\text{Ge}_{31}$ (Anderson 1973, Collongues 1992), the two sublattices can come into coincidence every 19 and 31 subcells, respectively.

1.10.11 Coherent intergrowths

The concept of topologically compatible coherent intergrowths in non-stoichiometric solids is of great significance, both from the structural and thermodynamic points of view. Structural compatibility enables the elements of two distinct structures to coexist as coherently intergrown domains. An example of coherent (yet non-stoichiometric) intergrowths is shown in figure 1.18: $\text{TlBa}_2\text{Ca}_4\text{Cu}_5\text{O}_{13}$ cuprate superconducting oxide (a ‘1245’ compound with five Cu–O layers) shows four Cu–O intergrowth layers of the ‘1234’ compound. Coherence can be achieved by local ordering of defects, e.g. point defect ordering (vacancy or interstitial), substitutional ions within coherent crystal structures or by a polyhedral or compound shear mechanism. This would, in principle, also lead to models for defects. Intergrowths are only reliably revealed by HRTEM. If intergrowths are random, the material is non-stoichiometric and has a non-equilibrium phase. If they are ordered in a regular fashion, a new compound is produced. In the absence of other defects it should be possible to account for the stoichiometric variations from ideal stoichiometry in terms of coherent intergrowths. Dislocation structures facilitating layer insertion or removal are also present as we will see in subsequent sections.

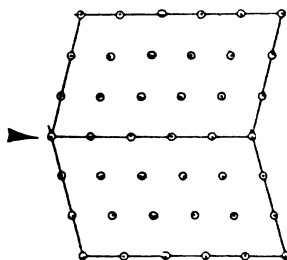


Figure 1.19. A schematic diagram of a twin in a crystal.

1.10.12 Chemical twinning

In a simple twinning mechanism, observed for example in metals, the crystal structure is reflected across some composition plane, with no change in composition, as shown in figure 1.19. In complex systems, e.g. in oxides or sulfides (e.g. in galena-bismuthinites), other possibilities for extended defects such as fine-scale mimetic twinning or chemical/unit cell twinning without the need for an anion-vacancy model have been described (Bakker and Hyde 1978, Bursill *et al* 1972). This type of chemical twinning is non-conservative and can lead to ordered structures. Chemical twinning is recognized as an important topological principle in solid state chemistry.

1.10.13 Novel glide shear mechanism in anion-deficient oxides

In situ ETEM studies of oxide catalyst–hydrocarbon interactions have led to the discovery of a novel crystal glide shear (GS) reaction mechanism which is key to efficient oxidation catalysis by oxides (Gai *et al* 1995, 1997). This important process, in which oxide surface layers undergo a structural transformation by glide shear to accommodate the surface misfit due to anion vacancies formed during catalytic reactions, essentially preserves anion vacancies associated with Lewis acid sites at the catalyst surface. This novel mechanism explains the release of structural oxygen and the preservation of Lewis acid sites at the surface without the structure of the catalyst collapsing. The sites are believed to be important in the activation of hydrocarbons and for oxygen exchange in catalyst regeneration. This mechanism has led to a new understanding of the solid state heterogeneous catalytic process as we discuss in the section on vanadyl pyrophosphate catalysts in chapter 3. This novel glide shear mechanism is relevant to the depletion and uptake of oxide systems generally, including high-temperature superconducting oxides (Gai *et al* 1990). The ordering of glide shear defects can give rise to new homologous series of phases or structures (Gai 1997).

1.11 Catalysis by oxides

1.11.1 Non-stoichiometry in oxidation catalysis

Complex oxide catalysts are widely exploited in many catalytic reactions because they provide lattice oxygen in the selective oxidation of hydrocarbons and can exchange with the gas phase oxygen used in the reaction stream as described in previous sections. Catalytic reactions using these redox systems are typically carried out at a few hundred degrees, typically 200–450 °C for hydrocarbons, confirmed by oxygen isotope studies. They are, however, often inhomogeneous resulting in extensive local microstructural and compositional variations. The loss of structural oxygen ions (O^{2-}), for example, results in non-stoichiometry through the formation of anion vacancies; the incorporation of gaseous oxygen (to replenish or regenerate the catalyst) can occur at these sites in the process.

Non-stoichiometry results in the generation of a variety of defects during the catalytic operation as will be shown in chapter 3. They can have a profound effect on the catalytic performance. One step is to systematically develop, experimentally and theoretically, our understanding of the nature of defect structures of simpler well-defined oxides; and extend this to the more complex commercially relevant mixed metal oxide systems. The nature of the active surface of catalysts under operating conditions is critical to the selective oxidation of hydrocarbons by metal oxide systems. EM studies are providing insights into defects, novel microstructural designs, synthesis and criteria for the selection of catalysts. These new methods arise directly from fundamental studies of the removal, transfer and re-incorporation of ions at the catalyst surface. These are described in the following sections.

Oxides (generally in the form of powders) can be used as catalysts without or with supports. The most widely used selective oxidation catalysts are molybdates and vanadates. Some highly selective catalysts for the oxidation of propylene hydrocarbon (C_3H_6) to acrolein (C_3H_4O), and ammoxidation of C_3H_6 with ammonia to acrylonitrile are based on bismuth molybdates and tellurium molybdates, whereas catalysts for the oxidation of methanol to formaldehyde are based on ferric molybdates and MoO_3 . For butane oxidation to maleic anhydride for use in polyurethane intermediates, agricultural chemicals and synthetic resins vanadium phosphate (compounds of V–P–O) catalysts are commonly used.

1.12 Extended defects and crystallographic shear

1.12.1 Relevance to oxidation catalysis

Extensive research on crystallographic shear (CS) planes has been reported in the literature as described earlier. Based on this research, including beam-heating studies in electron microscopy, it has been concluded that slight reduction of certain transition-metal oxides (e.g. simple model oxides, WO_3 , MoO_3 , V_2O_5 ,

VO₂ and TiO₂) leads to the formation of extended defects, i.e. CS planes, rather than to point defects. In the early literature reports, the definition of CS involved the removal of a complete sheet of anion sites to form an extended CS plane defect (Wadsley 1964, Anderson and Hyde 1967). Consequently, the role played by true point defects in non-stoichiometric oxides was not obvious from these earlier reports and answer to this was sought by Anderson (1970, 1971), Anderson *et al* (1973) (1.13.2). However, although this definition of CS is a convenient one, the situation is not so straightforward as we now demonstrate.

The properties of non-stoichiometric compounds raise a number of fundamental questions: the nature of stoichiometric variations, type of defects, e.g. whether they are point, line (dislocations) or planar defects, type of shear, methods of defect nucleation and, more importantly, the relationship between point and extended defects, the interactions between them and their role in heterogeneous catalysis (Gai 1981, 1992–1993). Ordered arrays of crystallographic shear (CS) planes can lead to homologous series (Magneli series) of compounds as described earlier. The orientations of these CS planes depends on the degree of reduction in these oxides. Many existing structural calculations about the formation and interaction energies of CS planes in WO_{3-x} use a continuum elasticity approach. Calculations have also been performed to identify the stability factors in point and extended defect equilibria (Catlow and James 1978). Tilley *et al* (1979) have reduced WO₃ *ex situ*, and have used EM revealing the formation of initially isolated and later quasi-ordered {120} CS planes, resulting in a homologous series W_nO_{3n-1}.

1.12.2 Distinction between shear mechanisms and defect structures

It is important to distinguish several types of shear mechanisms by quantitatively analysing defect structures so that models for the formation and the *nature* of extended defects and catalytic reaction mechanisms can be understood. This is essential to understanding the differences between defects, such as those between anti-phase boundaries (APB), stacking faults (e.g. CS planes) and other defects. Otherwise, the interpretation of defect structures becomes very confused indeed! In pure shear, for instance, the shear mechanism may involve no change in chemical composition. It is analogous to a screw dislocation mechanism (chapter 3). In pure mechanical shear, an APB is formed. It may also lead, with some lattice dilatation, to a martensitic type of transformation (Cottrell 1971). In crystallographic shear, however, a single CS plane eliminates a large number of point defects (e.g. anion vacancies) in oxides. As described in the preceding sections, the general view has been that, with slight reduction of oxides, anion vacancies would aggregate to form CS; a complete sheet of vacant oxygen atom sites on a particular crystallographic plane is eliminated as a result of shear followed by the collapse of the structure on that plane. The resulting extended defects, the CS planes as described earlier, accommodate a change in the ratio of cation to anion sites by switching from corner- to edge-sharing of some of

the oxygen octahedra in the structure. For a long period of time (more than two decades), it was believed that the formation of these extended CS planes and the resulting structural sites with the changed cation coordination were active centres for fast oxygen exchange (Stone 1975, Haber *et al* 1983).

1.12.3 Important issues in oxide catalysis and EM techniques

We thus address three major issues here:

- (1) Do CS plane defects occur under catalyst operating reaction conditions in oxides?
- (2) If so, what is the mechanism of their formation and their role in catalytic reactions?
- (3) Since CS planes cause the collapse of the catalyst structure, how can a catalyst have a long life? (If the catalyst structure is continually reduced by CS, after a period of time there might be no good catalyst left for the reaction.)
- (4) The question raised by Anderson (1970, 1971) and Anderson *et al* (1973) as to whether anion point defects are eliminated completely by the creation of extended CS plane defects, is a very important one. This is because anion point defects can be hardly eliminated totally because apart from statistical thermodynamics considerations they must be involved in diffusion process. Oxygen isotope exchange experiments indeed suggest that oxygen diffuses readily by vacancy mechanism. In many oxides it is difficult to compare small anion deficiency with the extent of extended defects and in doped complex oxides there is a very real discrepancy between the area of CS plane present which defines the number of oxygen sites eliminated and the oxygen deficit in the sample (Anderson 1970, Anderson *et al* 1973). We attempt to address these issues and elucidate the role of anion point defects in oxides in oxidation catalysis (chapter 3).

The complex and fine-scale chemical and local structural inhomogeneities (including surface defect layers and defects leading to new structures) in multicomponent oxides in heterogeneous catalysis are fully and unambiguously revealed only by direct electron microscopy. These data are very difficult to obtain from other methods, including the averaged molecular science information of x-ray and neutron diffraction studies, since the defect structures may be too small to differentiate in the scattering. The exploitation of the resulting diffuse scattering may require extensive computer modelling and chemical composition information is generally lacking. In favourable cases under careful experimental studies, EM techniques can provide crucial information on the local surface atomic defect structure and chemical composition of catalysts, the catalyst promotion and poisoning which often occur in the sub-nanometre range and the catalytic reaction mechanisms.

We now give a brief description of EM methods. We highlight the significance and the unique role of EM in providing fundamental understanding of the catalyst atomic structure and the nature of defects which control catalysis. In addition, we will critically examine some of the approximations about defect structures in the literature and compare these with data from electron microscopy studies. EM studies of heterogeneous catalysts lead to a new understanding of surface reactions which are applicable not only to catalysis but to the materials and chemical sciences in general.

Chapter 2

Electron microscopy and diffraction in heterogeneous catalysis

2.1 Background

Electron microscopy (EM) techniques are very powerful and versatile research tools with which to investigate directly the local structure and chemistry of complex heterogeneous catalysts from the macroscopic to the atomic scale. Catalysts are generally heterogeneous (consisting of more than one element) and are increasingly nanoscale materials. In traditional approaches to exploring catalysts based on indirect chemical and spectroscopic methods, results from large areas are averaged. Constructing models of the structure and mechanisms of the changing reactions over complex catalysts using such methods does not often provide satisfactory pictures of the process. Recent striking developments in EM methods have given the catalyst chemist methods for the direct visualization of the dynamic catalyst structure at the atomic level and the means for measuring its composition. EM of thin crystals pioneered by Hirsch *et al* (1977) and Cowley *et al* (1981) plays a pivotal role in materials science. There are detailed books on the principles of EM (Hirsch *et al* 1977, Cowley 1981, Eddington 1977, Williams and Carter 1996). In the following sections, we highlight some of the important principles in the study of heterogeneous catalysts. We describe some recent significant developments in EM methods including dynamical methods for studying catalysis. We outline the conditions necessary for obtaining the local atomic structure and chemistry of catalysts, their limitations and future trends.

EM provides local structural information about the samples in both real and reciprocal space, for example local structural information about the surface and the bulk of the sample at the atomic level, together with chemical, electronic and three-dimensional structural information are now routinely available. Some of these methods are described in this chapter. Electron-sample interactions and scattering are fundamental to EM. EM is a diffraction technique in which crystals diffract electrons in accordance with Bragg's law, $n\lambda = 2d_{hkl} \sin \theta$, where λ is the

wavelength of the electrons, d is the lattice planar spacing of the hkl reflection, and θ is the scattering angle. Discovery of the electron and the particle and wave duality of electrons (de Broglie 1925) has been well documented in the literature. E Ruska was awarded the Nobel Prize for EM. The electron has a low mass and is negatively charged. It can be easily deflected when close to electrons and the positive nucleus of the sample atom. These interactions are termed Coulombic or electrostatic interactions and lead to electron scattering. Electron microscopy deals with a complex electron wave with both its amplitude and phase modulated, as the electron interacts with matter. This interaction generates elastic scattering and a variety of other signals which can be used to obtain structural and chemical information about a sample as shown in figure 2.1(a). Elastic scattering occurs when incident electrons interact with the potential field formed by the nuclei of matter involved with essentially no energy loss in momentum transfer, whilst inelastic scattering occurs when interactions between incident electrons and the electrons of matter occur and scattered electrons lose energy (Hirsch *et al* 1977).

In a conventional transmission electron microscope (TEM), electrons are transmitted through the sample. Normally the incident and scattered electrons are referred to as electron beams. In TEM, the electron beam is transmitted through the sample and is transferred through the instrument's optics. The TEM has an electron gun and electromagnetic lenses which include condenser and objective lenses. The condenser lenses converge and control the electron beam and illuminate the sample, and the objective lens forms the image of the sample and diffraction. The images and diffractions are then magnified by other lenses in the system. A base reference line passing through the centre of all the lenses is called the optic axis of the electron microscope.

Figure 2.1(b) shows a 'ray diagram' for a finite object which scatters radiation and can be used to understand the image formation in an electron microscope. Rays scattered at an angle θ are gathered by the objective lens and converged to a point in the image plane. Parallel rays are focused in the back focal plane (bfp) of the lens. The intensity distribution in the bfp gives rise to diffraction. The diffraction pattern formed may be regarded as the Fourier Transform (FT) of the crystal. An apertured inverse Fourier transform (FT) in the objective lens forms the image. The objective lens takes the electrons emerging from the exit surface of the sample and disperses them to create an electron diffraction pattern (DP) in the bfp and recombines them to form an image in the image plane. In a TEM, accelerating electron voltages are normally between 100–400 keV and lower (a few hundred electron volts to ~ 30 keV) for scanning EM (SEM). Principles of EM imaging and diffraction (Hirsch *et al* 1977) are shown in figure 2.1(c). In EM, a two-dimensional planar projection of a three-dimensional object is observed. The principle is demonstrated in figure 2.2 where a thin-film TEM image of dislocations (imperfections or defects in a crystal lattice) is shown in (a) with the distribution of the dislocations in the lattice in (b). The imaging principles and methods in EM will now be discussed briefly.

For the EM of practical (real-life) catalysts as-synthesized powders are used.

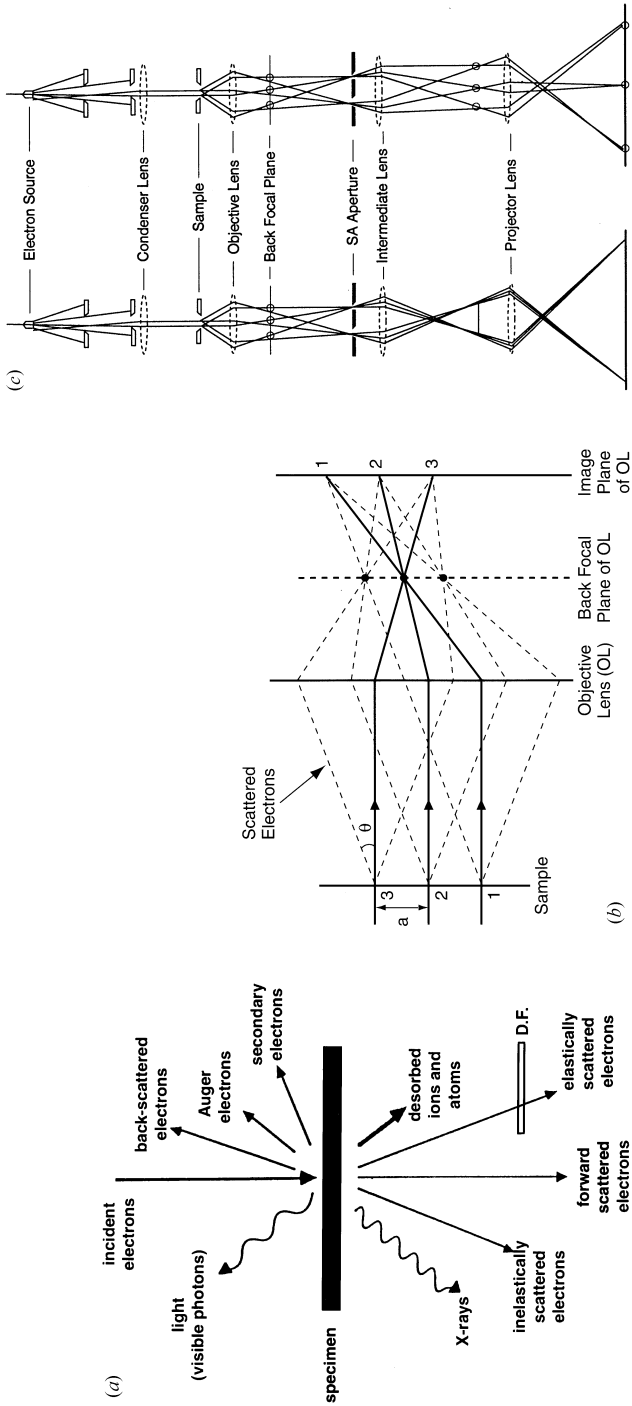


Figure 2.1. (a) Signals generated during electron beam-sample interactions; (b) a 'ray diagram' of image formation; and (c) a schematic diagram of the principles of electron microscopy: (A) imaging and (B) diffraction.

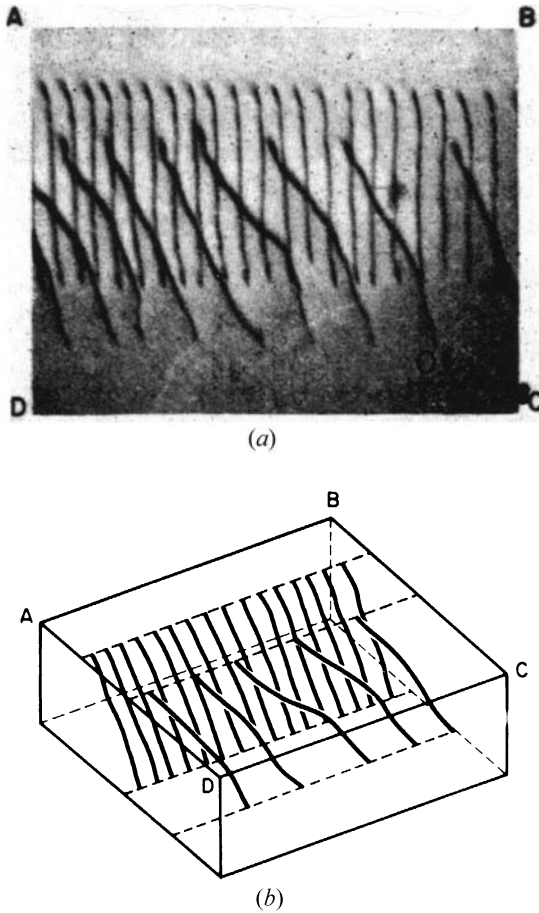


Figure 2.2. (a) A TEM image of two rows of parallel dislocations (dark lines) (a two-dimensional image); and (b) a line diagram illustrating the distribution of dislocations in the thin sample and demonstrates that (a) is a two-dimensional image of three-dimensional arrays of dislocations in (b). (Hull 1965; reproduced by courtesy of Butterworths.)

They are generally dispersed in alcohol and deposited on 3 mm carbon-filmed beryllium, copper or aluminum grids. If carbon or other support films are not desirable, finely meshed metal grids can be used. Ultra high purity grids are required for experiments. Conventional TEM (and HRTEM) operates at ambient temperature in high vacuum. To avoid electron-beam damage to sample, low beam currents should be used (Heinemann *et al* 1985). Catalyst powders are generally thin enough for penetration by the electron beam and no further sample

preparations are usually necessary. (For some specialized work, e.g. for access to grain boundaries, bulk pellets can be thinned by argon ion milling.) With adequate sampling, quantification of data is carried out. Various imaging mechanisms exist and we describe some of them in the following sections.

2.2 Imaging in the TEM

2.2.1 Classification of some important defect structures and diffraction contrast in catalysis

TEM diffraction contrast is the conventional TEM imaging technique where the Bragg condition is satisfied for a single diffracted beam (Hirsch *et al* 1977). If the objective aperture includes only the primary beam containing the directly transmitted electrons (and any low angle inelastic scattering), a bright-field (bf) image is obtained (figure 2.3). The bf image contrast is amplitude contrast since electrons scattered outside the aperture are not included in the image (which thus appears dark in the strongly scattering area of the sample). In thin crystals most of the amplitude contrast comes from Bragg reflection and the effect is known as 'diffraction contrast'. If only a scattered electron beam is included in the objective aperture by either displacing the aperture or by tilting the illumination to coincide with the optic axis, a dark-field image is formed. Figure 2.3 illustrates these imaging conditions.

Defects control the properties of materials including catalysts and understanding them is critical to controlling and optimizing catalytic properties. The diffraction contrast technique is particularly effective for characterizing defect structures or lattice imperfections in catalysts (generally without detailed calculations for defect models). The technique is powerful for analysing dislocations in catalyst materials by determining the components of their displacement vector (called the Burgers or shear vector \mathbf{b}) in the three crystallographic dimensions and defining the three-dimensional geometry of defects in imperfect crystals. In comparison, in an HRTEM image, which is a planar image, it is difficult to ascertain the component of the displacement vector normal to the plane of projection. For an unambiguous interpretation of the defect structures using HRTEM, modelling may be necessary, since the image contrast depends on such EM parameters as the defocus, astigmatism and lens aberrations.

Extended defects such as dislocations often create regions within crystals which are imperfect in register and thus involve characteristic displacements. The concepts of dislocations and stacking faults (which are faults in the stacking sequence of atomic planes, across which the atomic arrangement differs from the parent crystal) play an important role in the study of properties and structural modifications of catalysts. The two main types of point defects in a crystal were shown in the schematic diagrams in figures 1.10(a) and (b). In catalytic oxide crystals, which are generally operated at moderate temperatures, we are primarily concerned with anion vacancy defects. These defects control the fundamental

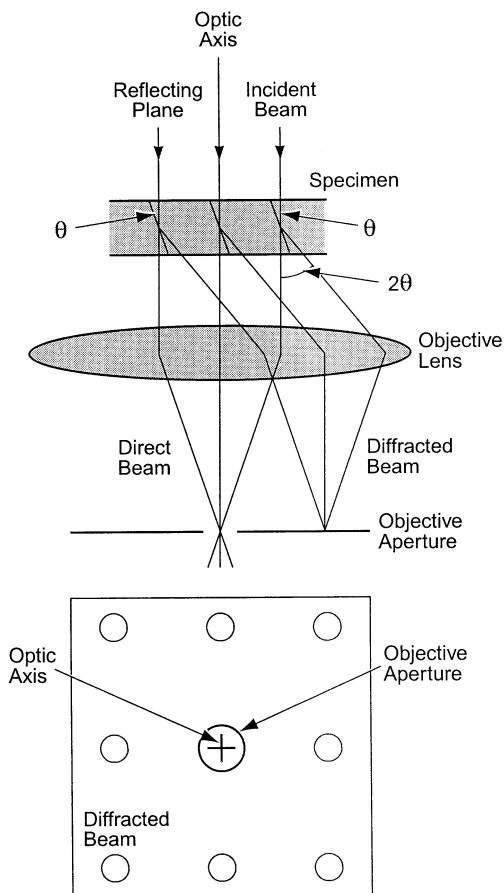


Figure 2.3. A schematic diagram of bright-field (bf) TEM imaging. A dark-field (df) image is formed using a diffracted electron beam.

processes in the diffusion of matter. Point defects in oxides behave differently to those in metals, alloys or semiconductors. They are ionic and consequently carry an effective charge. In the following sections, we discuss various types of defects and diffusion mechanisms and assess their role in the phenomenon of catalysis. This will elucidate the role of charged anion vacancies in the activation of hydrocarbons and in the regeneration of catalysts in heterogeneous catalysis.

In extended defects, the displacement vector \mathbf{b} (or \mathbf{R}) associated with them can be defined from the ‘Burgers Circuit’ shown in figure 2.4(a), for a simple cubic system (Frank 1951, Cottrell 1971, Amelinckx *et al* 1978). In the defective crystal (A), a sequence of lattice vectors forms a clockwise ring around the dislocation; precisely the same set of lattice vectors is then used to make a second

circuit in the perfect crystal (B). An extra vector (called the ‘Burgers vector’) is required to join the circuit to the starting point. There are established criteria for obtaining \mathbf{b} (Hirsch *et al* 1977). Briefly, the dislocation intensity (contrast) is mapped in several Bragg (hkl) reflections (\mathbf{g}) by tilting the crystal to different reflections (called the $\mathbf{g} \cdot \mathbf{b}$ product analysis). The reflections include a particular \mathbf{g} in which the dislocation is invisible (called the invisibility criterion), i.e. $\mathbf{g} \cdot \mathbf{b} = 0$ when \mathbf{b} is normal to the reflecting plane. With these criteria in diffraction contrast, one can determine the character of the defect, e.g. the screw, shown figure 2.4(b) (where \mathbf{b} is parallel to the screw dislocation line or axis), or edge, shown in figure 2.4(c) (with \mathbf{b} is normal to the line) or partial (incomplete) dislocations. The dislocations are termed screw, or edge, because in the former the displacement vector forms a helix and in the latter the circuit round the dislocation immediately shows its most characteristic feature, the half-plane edge (figures 2.4(b) and (c)). Dislocations can move in two ways; they can glide or climb: in the former, a dislocation moves in the surface defined by its line; and in the latter, it moves out of the glide surface. By definition, a partial dislocation has a stacking fault on one side of it and the fault is terminated by the dislocation.

The nature of dislocations (e.g. screw, edge or mixed) is very important in understanding how planar defects form and grow in catalysts, especially in complex oxide catalysts, under reaction conditions. Planar defects such as CS planes are stacking faults bounded by partial edge dislocations which form a pair of parallel lines. Figure 2.4(d) shows a schematic diagram of a stacking fault in a simple fcc system. In general, the conditions for imaging the partial dislocations bounding the stacking fault differ from those needed to image the fault itself (Hirsch *et al* 1977, Gai *et al* 1990). Contrast or intensity calculations can be performed for different crystal and depths of defects in crystals to check experiments with theory. Here we briefly review some theoretical aspects of transmission electron diffraction using high-energy electrons based on electron wave mechanical formulation of the dynamical theory of contrast (Hirsch *et al* 1977).

2.2.1.1 Theoretical procedures

The scattering of electrons from atoms is described by the Schrödinger equation: $\nabla^2 \Psi(r) + 8\pi^2 m e (E + V(r)) \Psi(r) = 0$ for stationary states (where the wavefunction $\Psi(r)$ describes electrons with energy E moving in a crystal potential $V(r)$, m and e are the electronic mass and charge and r is the space coordinate) (Hirsch *et al* 1977). Translational properties called Bloch waves are necessary for solving this equation. In order to interpret electron micrographs and diffraction patterns it is essential to understand the electron scattering mechanisms occurring through the crystal. In the kinematical theory of diffraction contrast, the amplitude of the scattered wave (ϕ_g) is a small fraction of the amplitude of the incident wave (ϕ_0) and the theory is really only valid for thin crystals. In thicker crystals, kinematical theory breaks down due to multiple electron-scattering

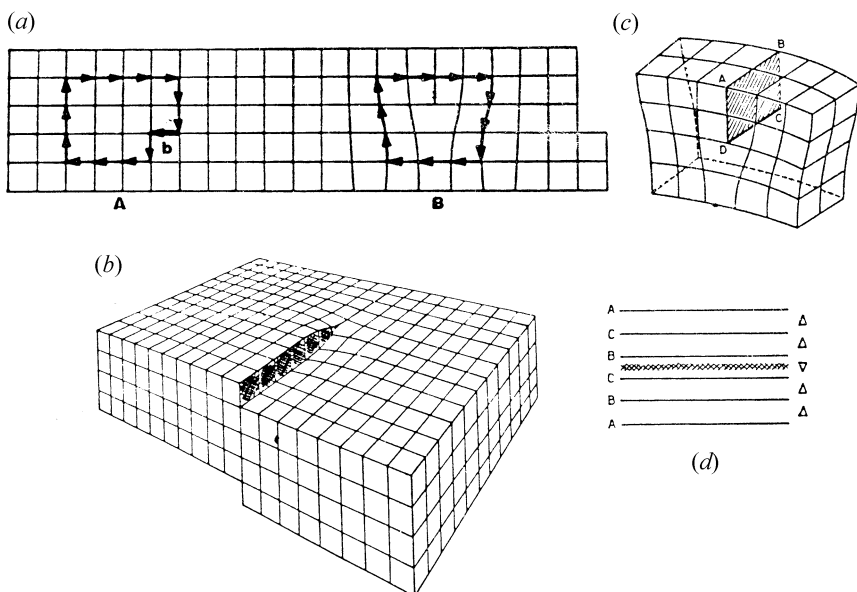


Figure 2.4. Definition of a displacement (Burgers or shear) vector b : (a) a Burgers vector around a dislocation (defect); A: in a perfect crystal there is a closure failure unless completed by b ; (b) a schematic diagram of a screw dislocation—segments of crystals displace or shear relative to each other; (c) a three-dimensional view of edge dislocation DC formed by inserting an extra half-plane of atoms in ABCD; (d) a schematic diagram of a stacking fault. (Cottrell 1971; reproduced by the courtesy of Arnold Publishers.)

effects and the dynamical theory which incorporates Bloch wavefunctions should be used. (Schrödinger's equation is solved in dynamical theory using Bloch waves which consist of a combination of plane waves (transmitted and diffracted) in the crystal.) Intensity (contrast) calculations for defects located at a certain depth in a crystal of thickness t can be performed using the dynamical theory of electron diffraction (Howie and Whelan 1962). Many-beam dynamical theory which includes absorption effects is employed for thicker crystals. In the case of dark-field weak-beam images of defects, the perturbation theory of electron diffraction (Gai and Howie 1974) can be used to simplify defect intensity calculations, where the scattering by the crystal is treated dynamically and that by the defect, kinematically.

2.2.2 High-resolution transmission electron microscopy (HRTEM)

One of the most powerful methods of direct atomic structural analysis of solids is high-resolution TEM (HRTEM), where two or more Bragg reflections are used for imaging. Although Menter's first images of crystal lattice periodicity were

taken in 1956 (Menter 1956), the experimental technique began to be used in earnest in the 1970s (Cowley *et al* 1957) with studies of mixed complex oxides of niobium and tungsten. Following the early theoretical work (Cowley *et al* 1972), the viability and power of HRTEM in exploring, in real-space, the structures of complex inorganic solids that were beyond the reach of conventional structural techniques (e.g. x-ray, neutron crystallography) were demonstrated by Anderson (1970) and Thomas (1974). Unlike conventional diffraction techniques (XRD, neutron), HRTEM provides localized real-space information, now routinely at the atomic level, about the bulk and surface properties of solids together with the corresponding chemical information as well as electron diffraction information in reciprocal space. Conventional HRTEM requires thin samples. Lattice images and molecular images of organic materials have also been possible (Kobayashi *et al* 1984, Fryer *et al* 1986).

In HRTEM, very thin samples can be treated as weak-phase objects where the image intensity can be correlated to the projected electrostatic potential of crystals, leading to atomic structural information. In addition, the detection of electron-stimulated x-ray emission in the electron microscope (energy dispersive x-ray spectroscopy or EDX, discussed later) permits the simultaneous determination of the chemical compositions of the catalysts to the subnanometre level. Both the surface and bulk structures can be investigated. One of the deficiencies of HRTEM at present is its inability to probe directly the oxygen point defect (vacancy) concentration when the oxygen atoms are scattered in an isolated fashion. Under favourable conditions, imaging of cation point defect clusters is possible as described later. Bursill *et al* (1983) have established the conditions for imaging point defect clusters in titania samples.

The micrograph or the image obtained on the EM screen or photographic film is the result of two processes: the interaction between the incident electron wavefunction and the crystal potential followed by the interaction of this resulting wavefunction with the EM parameters which incorporate lens aberrations. In the wave theory of electrons, during the propagation of electrons through the sample, the incident wavefunction is modulated by its interaction with the sample and structural information about the sample is transferred to the wavefunction, which is then further modified by the transfer function of the EM.

2.2.2.1 Conditions for HRTEM

The HRTEM requires samples that are electron transparent (normally, a few tens of nms in thickness). HRTEM image interpretation can be quantified by matching experimental images with computations using the *n*-beam dynamical theory of electron diffraction (Cowley and Moodie 1957, Spence 1981). Variations in image detail can be computed as a function of sample thickness, electron wavelength and lens characteristics (spherical and chromatic aberrations and focusing conditions) as first considered by Scherzer (1949). These are described briefly here. On-line digital image-processing can be used to quantify images.

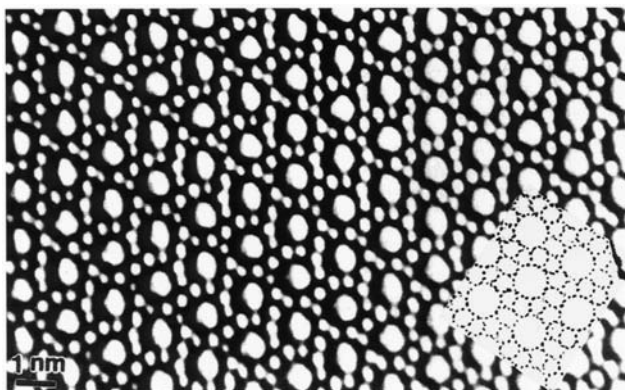


Figure 2.5. An HRTEM image of the atomic structure of germanium-silicalite (GeSiO_4), (which is a zeolitic form of silica with Ge dopants) along the [010] direction. Larger channels are 0.55 nm in diameter, by Gai and Thomas (after Gai 1999(b)).

As described in the preceding section, electrons are scattered by interactions with the inner potential of a crystal (specimen or sample). These interactions result in phase and amplitude changes in the electron wave. For a thin sample and high-energy electrons, the transmitted wavefunction at the exit face of the sample contains structural information. However, this is modified by the size, aberration (spherical and chromatic) and defocus effects of the objective lens. The objective lens of a microscope thus serves as a kind of Fourier transformer. The diffraction pattern formed at the bfp of the objective lens is further Fourier transformed to yield the image of the specimen. The contrast of images at the atomic level is due to phase contrast (amplitude changes are small in thin crystals), caused by a small phase-shift in the diffracted beams caused by the scattering and by objective lens aberrations. For a thin enough crystal, the ‘weak phase object (WPO) approximation’, which assumes that the electron wave is only phase-modulated (phase contrast) and not amplitude-modulated, is used. The image intensity is then linearly related to the thickness-projected potential distribution of the sample (similar to the charge density) and can be expressed in terms of the crystal structure. Figure 2.5 shows an atomic-structure image of a Ge-silicalite (GeSiO_4) which is a zeolite-based catalyst. The channels have an aperture diameter of 0.55 nm and they are along the [010] crystallographic direction. The structural model is shown in the inset and shows five- and six-membered rings. Zeolite catalysts are discussed in chapter 4.

The phase contrast is produced by the phase modulation of the incident electron wave when it is transmitted through the sample crystal potential $V(x, y)$. The propagation of a plane electron wave traversing through a thin sample is thus treated as a weak (scattering) phase object. The wavefunction $\Psi(x, y)$ at the exit

face of a thin sample can be written as follows:

$$\Psi(x, y) = \exp(i\sigma V(x, y))$$

where $V(x, y)$ is the thickness-projected crystal potential and σ is the interaction constant which is a function of the electron wavelength and energy, $\sigma = \pi/\lambda E$ (Cowley 1981). For very thin crystals this can be approximated to

$$\Psi(x, y) = 1 + i\sigma V(x, y).$$

The image intensity $I(x, y)$ at the image plane of the objective lens results from two-dimensional Fourier synthesis of the diffracted beams (the square of the FT of the waves at the exit face of the crystal), modified by a phase-contrast transfer function factor (CTF, $\sin \chi$), given by Scherzer (1949), as

$$I(x, y) \sim 1 - 2\sigma V(x, y) * FT \sin \chi$$

(Cowley 1981) (* is a convolution integral and FT is the Fourier transform). The phase-contrast imaging performance of an HRTEM is controlled by $\sin \chi$, which contains the basic phase-contrast sinusoidal terms modified by an attenuating envelope function, $F(\theta)$, which is essentially due to the partial coherence of the electron beam:

$$\sin \chi = F(\theta) \sin((2\pi/\lambda)(\Delta f \theta^2/2 - C_s \theta^4/4))$$

where θ is the radial scattering angle, Δf is the objective lens defocus value and F depends on the coherence conditions of the incident beam. CTF is a quantitative measure of the trustworthiness of the lens in recording a reliable image. Directly interpretable structure images are recorded near the Scherzer defocus, defined as $\Delta f(S) = -C_s^{\frac{1}{2}} \lambda^{\frac{1}{2}}$ down to the point resolution corresponding to the first zero in the CTF (figure 2.6). (In some studies, an optimum defocus value of $\sim 1.2 \times \Delta f(S)$ is used.) Thus under the WPO approximation, near $\Delta f(S)$, the image can be directly related to the two-dimensional projected potential of the specimen (sample) and with dark regions corresponding to columns of heavier atoms.

Beyond the point resolution, calculations to match experiments are required. In the following section we discuss the progress in HRTEM instrumentation applicable to catalysis.

2.2.3 Development of HRTEM

In order to improve the point resolution, a number of important 'custom or home-built' instruments at higher voltages (~ 500 – 600 keV) were developed during the 1970s (including at the Universities of Cambridge (UK) and Kyoto (Japan)). Some of these impressive and highly specialized instruments were,

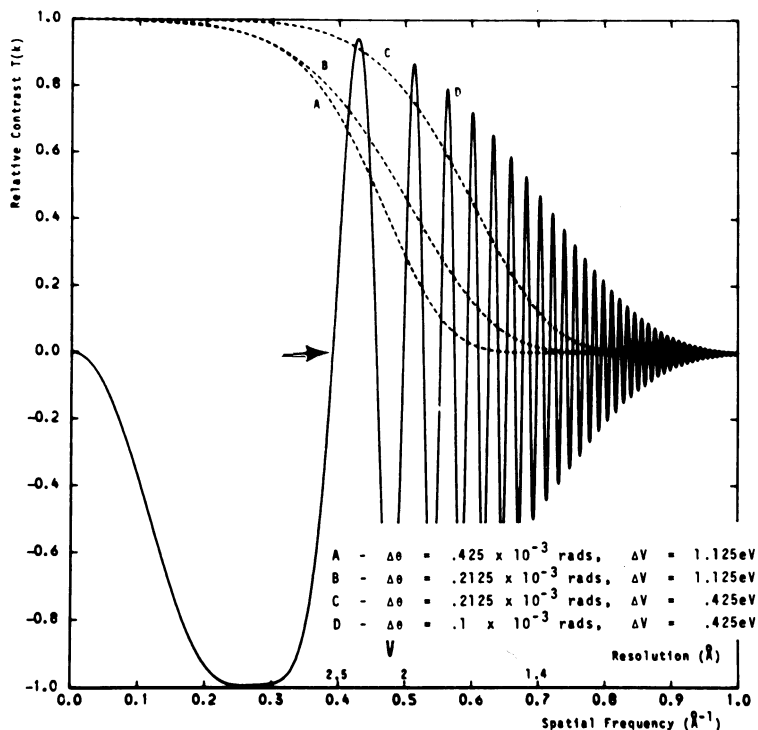


Figure 2.6. An example of a contrast transfer function (CTF). The calculated CTF of a 200CX HRTEM at Scherzer defocus and $C_s = 1.2$ mm. The first zero is arrowed (corresponding to 0.23 nm resolution) and the resolution in ångströms is shown on the horizontal axis. A–D are envelope functions plotted as a function of convergence angle (θ) of the beam and beam energy spread (ΔV). Parallel illumination is necessary for high resolution (after Boyes *et al* 1980).

however, associated with increased costs and resolution issues (some had difficulty in meeting theoretical resolution specifications) and some lacked a proper goniometer stage for tilting the samples.

The breakthrough in broadening the applications of HRTEM came with the development of the first state-of-the-art medium voltage of 200 kV HRTEM by Boyes *et al* (1979) at the University of Oxford, UK (with Jeol Co.). The key points of this significant development were that the instrument had a resolution similar to that of the best ‘home-built’ HRTEMs (~ 2 Å) at lower cost; and it came in a user-friendly package, routinely achieving the full theoretical performance. The instrument required no special building and fitted into a standard laboratory (a CTF graph of the instrument is shown in figure 2.6). Incremental improvement in resolution (~ 1.3 – 1.6 Å) was achieved later with the development of a 400 kV

HRTEM (Boyes *et al* 1985).

Thus, this state-of-the-art HRTEM has achieved very high resolutions of $\sim 1.7\text{--}2.3 \text{ \AA}$ (0.17–0.23 nm) and $\sim 1.3\text{--}1.6 \text{ \AA}$ (0.13–0.16 nm) at operating voltages of 200 and 400 keV respectively, providing information at the atomic level. On-line digital image-processing techniques are also available to quantify the images. Recently, a high-voltage (1250 kV) commercial instrument (installed in Germany and Japan), approaching a point resolution of $\sim 1 \text{ \AA}$ (0.1 nm) has been reported (Ruhle *et al* 1994). However, the cost of such instruments can be very high and careful image simulation is routinely required for interpreting images.

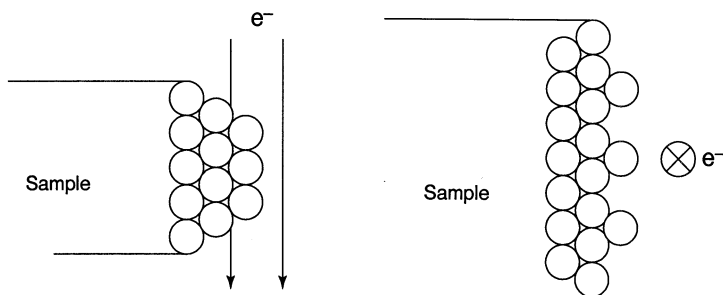
In HRTEM studies of complex catalyst structures, complementary multi-slice image simulations using the dynamical theory of electron diffraction (Cowley 1981) may be necessary for the nanostructural analysis and to match experimental images with theory.

2.2.4 Multi-slice HRTEM image simulations

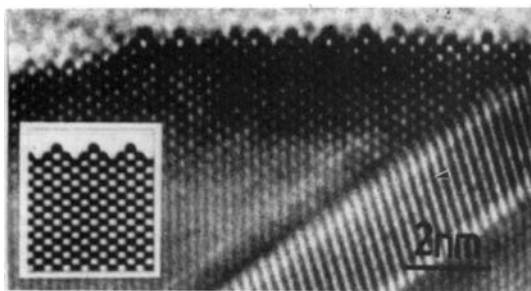
A major consideration in HRTEM studies is whether recorded images can be simply related to the crystal structure. For simple structures HRTEM images taken at conventional Scherzer or optimum defocus from thin enough samples should be easily interpreted. However, for complex structures and thicker samples quantitative HRTEM structural information can only be obtained with computer simulations, normally using the ‘*n*-beam multi-slice’ method (Anstis *et al* 1973, Cowley 1981). The basis of the method is to divide the sample into a number (*n*) of thin slices normal to the incident electron beam. The dynamic scattering of electrons through the sample and the transfer function theory are calculated using the HRTEM principles outlined earlier. These calculations can provide accurate information about electron scattering by thin crystals. Computer programs based on the multi-slice methods (e.g. the SHRLI suite of programs developed by O’Keefe *et al* (1973)) are well proven at 100 keV and are readily available.

2.2.5 Surface-profile imaging in HRTEM

In catalytic reactions, surface atomic structures differ from the bulk structure and understanding them is important for catalyst design. HRTEM also offers information about the surfaces of solids. The special imaging technique used here is called surface-profile imaging (Marks and Smith 1981). In this imaging mode, the instrument is operated using a large objective aperture (Smith and Marks 1981). The sample is aligned with the low-index crystallographic zone axis parallel to the electron beam (figures 2.7(a)–(b)). Studies of surface structures with different characteristics from those of the bulk structure (and known as reconstructed surfaces) include the reconstructed surfaces in gold and semiconductors using the imaging capability (Smith *et al* 1981, Iijima *et al* 1984). Surface-profile images in zinc chromium oxide catalysts have also been reported



(a)



(b)

Figure 2.7. (a) A schematic diagram of HRTEM surface-profile imaging with sample in: side view surface (left) and plan view (right). In HRTEM the profile image can be directly interpreted in terms of atomic columns along the sample surface. Because profile-imaging is a planar projection, relative height information is not available. (b) Surface-profile image of gold (Datye and Smith 1992; reproduced by the courtesy of Marcell-Dekker).

(Briscoe *et al* 1984). Figure 2.7(b) shows a surface profile image (Datye *et al* 1992).

2.3 Chemical composition analysis of catalysts in the EM

Analytical EM using electron-stimulated characteristic x-rays is a well-known chemical composition characterization technique for analysing materials. High spatial resolution chemical analyses (from areas of a few nm or less) using electron nanoprobe are now possible in a modern EM and can provide information of the catalyst composition at the subnanometre level. Details of EDX in the EM are described by Goldstein *et al* (1984) and some important definitions are highlighted in the following sections.

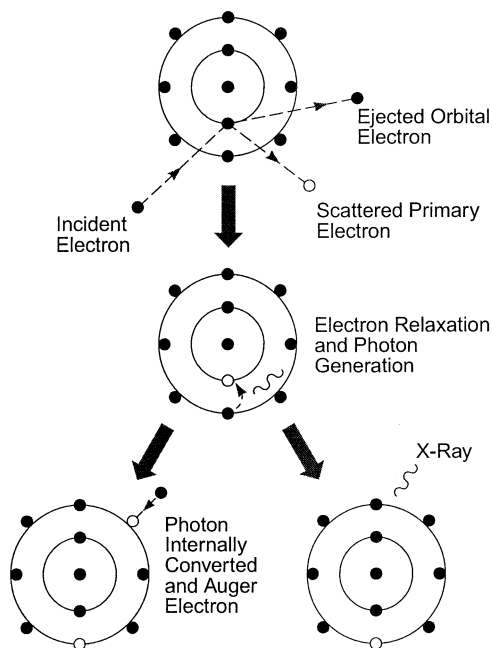


Figure 2.8. The process of electron-stimulated x-ray emission in the electron microscope.

2.3.1 X-ray spectroscopy in the electron microscope

In electron-sample interactions, x-rays can be formed during inelastic scattering of electrons. The following principles describe the generation and character of the x-rays.

Characteristic: Interaction between a high-energy electron from the beam and an inner-shell electron from the sample atom results in the ejection of a bound inner-shell electron from the attractive field of the nucleus in the sample atom, leaving the atom in an excited state with an electron-shell vacancy. De-excitation by transition from the outer shell involves a change in the energy state of the atom between sharply defined levels, producing *x-rays* (or Auger electrons). The process is elucidated in figure 2.8. These x-rays are characteristic of the elements in the sample and are used for composition analysis. EDX, in which x-ray intensities are measured as a function of the x-ray energy, is the most convenient and common method for chemical composition analysis in the electron microscope.

Continuum: Deceleration of beam electrons (e.g. those which do not participate in removing sample electrons) leads to the production of a continuous range of x-rays. They contribute to the background of a spectrum and are termed Bremsstrahlung x-rays.

Chemical composition analysis complementing the microstructural information obtained from EM is known as analytical EM (AEM). Important compositional variations or non-stoichiometry in a material which is seemingly 'phase pure or stoichiometric' by the criterion of bulk diffraction techniques and compositions of surface layers can be revealed using AEM. For quantitative microanalysis a ratio method for thin crystals (Cliff and Lorimer 1975) is used, given by the equation:

$$C_A/C_B = K_{AB}I_A/I_B$$

where C_A and C_B are the concentrations of elements A and B and I_A and I_B are the background subtracted peak intensities for A and B; and typically a few dozen crystals are analysed. The sensitivity factor K_{AB} is determined using appropriate standards. For bulk materials, more complex correction procedures are required for atomic number (Z), absorption (A) and x-ray fluorescence (F). Thus, AEM provides real-space imaging together with crystallographic and microcompositional information about the sample on a very fine scale. Furthermore, AEM can be used to obtain partial occupancies within cation sites, (and under special conditions, in anion sites) which will be discussed in chapter 6. When elemental peaks overlap, wavelength dispersive x-ray spectroscopy (WDS—where x-ray intensities are measured as a function of wavelength) may be advantageous for composition analysis. Detection sensitivity in WDS can be very high (<100 ppm), due to the much higher x-ray count rates.

In addition to composition analysis from a particular point in a sample, in many cases it may be advantageous to probe chemical variations of entire crystals in a catalyst sample by analysing x-ray intensities from elements in a crystal area, e.g. across a line or over an area under view of the sample. This latter two-dimensional scanning technique is known as x-ray mapping. Quantification of the intensities in x-ray maps can provide details of the relative amounts of the elements in the chemical composition (note: caution is required when peaks overlap). Further details can be found in Goldstein *et al* (1984). Conventional simple x-ray mapping (where intensities can become distorted) is now largely replaced by digital mapping in modern EM instruments. This method provides better quantification via the dead-time corrected acquisition of x-rays at each spot of a digital grid. Digital mapping after processing can yield a better spatial distribution of the elements in a sample.

2.4 Electron energy loss spectroscopy

In electron energy loss spectroscopy (EELS), energy losses produced by the interaction between incident electrons and the sample are measured. The energy losses result from inelastic scattering effects. EELS has normally been used to detect light elements in a material. Measurements via EELS spectra can provide quantitative information about chemical or oxidation states, elemental or chemical compositions and can be particularly effective in catalyst studies. EELS

in a scanning-TEM (STEM, described later) or TEM can provide high spatial resolution for analysis. Normally EELS spectra are divided into various regions: a low-loss region which characterizes the losses in the range 0 (containing the zero-loss peak) to ~ 50 eV (losses due to the excitation of valence electrons). The next is the core-loss region (>50 eV) characterizing the excitation of core electrons. In the early days, spectra were recorded using a serial detection spectrometer (e.g. Issacson *et al* 1975) using slow acquisition rates. The development of parallel detectors (starting with Shuman *et al* (1981), Egerton (1981), Krivanek and Swann (1981) and others) enabled faster acquisition rates and better digital storage facilities. Recently much progress has been made in the quantification of EEL spectral analysis (McComb and Howie 1990). Compositional maps in a TEM fitted with an energy filter (Energy Filter TEM or EFTEM) have been used to give the local elemental distribution in catalysts (Crozier *et al* 1996). EFTEM imaging has progressed with the availability of post-column filters as add-ons to TEM or an in-column (omega) filter.

2.5 Convergent (or focused) beam electron diffraction

Convergent (or focused) beam electron diffraction (CBED) is particularly attractive for determining local crystal structures and space groups in three dimensions (Steeds *et al* 1979, Tanaka *et al* 1985). In a modern TEM, CBED is now routinely available. In this technique, two principles of TEM electron diffraction are employed: departure from Friedel's law and the formation of extinction bands within reflections that are forbidden by space groups.

In CBED, zone-axis patterns (ZAP) can be recorded near the relevant zone axis and the pattern may also include a higher-order Laue zone (referred to as a HOLZ). The radius of the first HOLZ ring G is related to the periodicity along the zone axis [c] and the electron wavelength, by $G^2 = 2/\lambda c$. CBED can thus provide reciprocal space data in all three (x, y, z) dimensions, typically with a lateral resolution of a few nanometres. As in any application, corroborative evidence from other methods such as HRTEM and single-crystal x-ray diffraction, where possible, can be productive in an unambiguous structural determination of complex and defective materials such as catalysts. We illustrate some examples in later sections.

2.6 The development of *in situ* environmental-TEM (ETEM) under controlled reaction environments to probe catalysis at the atomic level

Heterogeneous catalysis is a dynamic process and gas-catalyst reactions occur at the atomic level. In gas-catalyst reactions, the dynamic atomic structure of catalysts under operating conditions therefore plays a pivotal role in catalytic properties. Direct observations of the microstructural evolution and active sites of

catalysts under dynamic reaction conditions is a very powerful method. Therefore there is a strong need for *in situ* environmental EM (ETEM) for direct, real time probing of the dynamic catalyst–gas molecule reactions at operating temperatures. The recent pioneering development of *in situ* atomic-resolution ETEM by Gai and Boyes (reported in Gai and Boyes 1997, Boyes and Gai 1997, Gai *et al* 1995, Gai 1997, 1998) for probing working catalysts directly at the atomic level is now described.

In ETEM, a gas reaction cell (or environmental cell (ECELL) or microreactor) is fitted inside an electron microscope column, which is differentially pumped. *In situ* ETEM under controlled-reaction conditions provides direct real-time dynamic information on processes which cannot be readily obtained by other methods. It permits direct observations of atomic motion and chemical modification of the catalyst surface while it is immersed in gas (or liquid) environments. *In situ* ETEM studies under carefully simulated conditions close to those in a practical reactor yield insights into active sites, transient states, reaction mechanisms and kinetics which can be directly related to structure–property relationships in technological processes. Thus *in situ* ETEM can be used as a nanolaboratory to probe dynamic catalysis. In heterogeneous catalysis, the properties of catalysts employed in or proposed for commercial reactions, which may include environmental control as well as products, and the structure–property relationships associated with them, are particularly important (Gai 1992). Dynamic studies of catalysts are important because post reaction examinations of a static catalyst (reacted *ex situ* and cooled to room temperature) carried out in high vacuum do not often accurately represent its dynamic state in the reaction environments. There may also be atmospheric contamination. This is illustrated in the example shown in figure 2.9. Figures 2.9(a) and (b) show metal-particle coarsening and atomic migration between particles in Cu supported on carbon at $\sim 200^\circ\text{C}$, reacting in H_2 /balanced by He; (c) shows the same area after the sample has been cooled to room temperature and the H_2 /He gas removed. It may be noted that the morphology and the surface structure of the particles upon cooling (i.e. the static sample) differ from those under dynamic conditions. In *in situ* studies, care should be taken to ensure that contamination effects (due to poor EM column vacuum or stale samples) are eliminated. *In situ* studies can also offer scope for modifying catalyst surfaces on the atomic scale.

2.6.1 Background to *in situ* ETEM

Before discussing novel *in situ* ETEM developments for heterogeneous catalysis, we present some background information about various *in situ* developments in the materials sciences. A number of notable *in situ* experiments have relied upon modifications to the standard TEM operations. The main electron optical functions of the TEM, especially the electron gun, depend on a high vacuum environment. The typical 10^{-6} – 10^{-7} mbar TEM environment is mildly reducing. With an ECELL, controlled chemically reducing atmospheres, such as

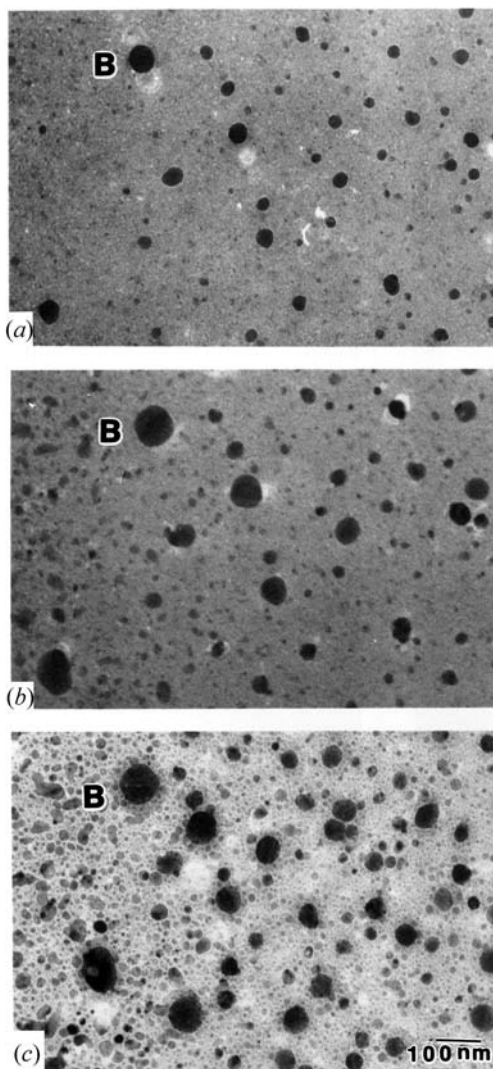


Figure 2.9. The importance of dynamic (*in situ*) ETEM studies: (a) Cu/C catalyst (particles are, e.g., at B) reacting at $\sim 200^\circ\text{C}$ in 10% He/He gas after 30 min; (b) time-resolved studies of the growth of catalyst particles (e.g. at B) indicative of Ostwald ripening, after 45 min; (c) static studies of the same sample (the sample is cooled to room temperature and the gas is turned off): the image is not the same as in the dynamic studies in (b)—particles (e.g. at B) have moved (have faint contrast around them) and more features are present.

H₂, hydrocarbons, CO and oxidizing atmospheres (such as O₂) or solvent-rich (He/water vapour) are used. A wide range of gases and vapours can be used.

Some of the earlier *in situ* experiments on semiconductors carried out in high vacuum in the TEM produced important results (Hashimoto *et al* 1968). The value of using a hot stage to study *in situ* crystallization with lattice imaging in a high vacuum environment of a TEM has already been demonstrated (Sinclair *et al* 1981, Saka *et al* 1997). A genuine ultra high vacuum (UHV) range suitable for surface science studies was first incorporated by Pashley *et al* (1964) and this has since been developed into an important scientific tool by Yagi and his coworkers (1985). Elegant experiments have been performed and the results of these studies are relevant to the wider surface science community. Venables *et al* (1985) have performed surface science investigations on semiconductors with a series of specialized SEM instruments. In the TEM, the use of UHV methods has been combined with the highest resolution of which the instrument is capable.

However, there are important applications in the chemical sciences, such as catalysis, in which the role of the environment on a sample is critical. Some of the earlier applications, summarized in Butler and Hale (1981), were to provide a water-saturated environment to prevent degradation of a solvated sample. Some workers made use of the high penetrating power and relatively large space of the high voltage electron microscopes (HVEM) operating at 1 MeV introduced around 1970 (Agar *et al* 1982, Westmacott *et al* 1984), but rarely available today.

Low-resolution electron-transparent window cells have been used to contain gases, solvent vapours (Parsons 1974, Double *et al* 1978, Daulton *et al* 2001), but window cells do not generally have a heating or tilting capability. In addition, there are problems in reliably sustaining a large pressure difference across a window which is thin enough to permit electron penetration. The additional diffuse scattering in the windows may further obscure the already limited image contrast. Superimposition of an additional diffraction pattern can be a problem. Where the controlled atmosphere comprises a gas or vapour, it is important to limit the pathlength for additional electron scattering in the gas and, hence, the length of the ECELL controlled-environment zone, to a length of a few millimetres. This is also the configuration typically used for (non-vacuum generators whole column) UHV systems.

The complications and potential for catastrophic failure of windows can be avoided by substituting small apertures above and below the sample to restrict the diffusion of gas molecules, but to allow the penetration of the electron beam. Unlike windows, aperture systems are robust and they can easily be made compatible with sample heating or cooling; sometimes even regular specimen holders can be used for this purpose. However, there are two problems to consider. First, the pressure differential which can be sustained across a single aperture (of a useful size and sealed around the perimeter) is limited to a factor of $<100\times$ (Butler and Hale 1981). In practice, a series of apertures, with differential pumping systems connected between them, are needed above and below the sample (shown in figure 2.10) to get from a minimum useful vapour pressure of,

e.g., 0.001–1 mbar around the sample, back to a maximum of 10^{-6} mbar in the electron gun. Typically, pairs of apertures are added above and below the sample with pumping lines attached between them (i.e. the region between the apertures is differentially pumped). Most ECELL ETEM systems have used either older HVEM (Swann and Tighe 1971) or medium (400 kV) electron microscopes. If the inherent performance limitations and alignment problems of the basic instruments were retained, these were exacerbated by the design of ECELL systems and the attachment of the attendant pumping lines. Furthermore, many of these systems were made interchangeable, which meant rebuilding the microscope every time there was a change in function. To maintain reliability, minimally invasive ECELL systems were designed which could ‘simply’ be inserted between the polepieces of the objective lens. Such systems have been a major step forward in scientific capability and excellent work has been carried out with them (Swann and Tighe 1971, Gai 1981–1992, Butler and Hale 1981, Baker *et al* 1981 [at low (a few torr) pressures], Doole *et al* 1991, Lee *et al* 1998, Crozier *et al* 1998, Sharma *et al* 1999, Goringe *et al* 1996).

2.6.2 *In situ* studies of dynamic oxidation catalysis in action under high gas pressures and at operating temperatures

In situ dynamic ETEM studies of oxide catalysts in selective hydrocarbon conversions under controlled realistic gas pressure environments and at operating temperatures was pioneered at the University of Oxford by Gai (1981, 1992) in Prof. Sir P B Hirsch’s department. She probed the critical role of point and extended defects in model and commercial catalyst systems under reaction conditions. To address the role, a multi-dimensional approach of correlated studies of *in situ* EM, compositional analyses and parallel reaction chemistry was developed. These early *in situ* ETEM developments to study dynamic oxidation catalysis included an AEI-EM7 HVEM at 1 MeV and fitted with a Swann-type environmental cell. In the HVEM ECELL, gas pressures up to 1 atm (or more for lighter gases), and a sample stage with a furnace capable of temperatures up to ~ 1000 °C were used. At these high pressures, a resolution of ~ 1 nm (improved to ~ 0.5 nm at lower gas pressures) was obtained. The furnace sample stage equipped with a limited tilting capability allows the crystals to be set to the desired Bragg reflections (g). In dynamic studies, very low electron-beam currents are used to prevent beam damage and a low light level TV camera is fitted to enhance the image contrast and to record video images of dynamic sequences. *In situ* studies are performed at various pressures and temperatures. They are confirmed by blank experiments (without the electron beam), with the beam switched on for a few seconds only to record the final state of the material and checked with *in situ* data. Under these careful conditions, no invasive beam damage is observed. Parallel chemical reaction experiments were performed on larger amounts of the sample in a microreactor (gas reaction cell) under conditions similar to those used in *in situ* studies to correlate microstructural studies with catalytic reactivity. This

in situ development (Gai, 1981) laid the basis for the *in situ* atomic-resolution ETEM by Gai and Boyes (1995–1998) which is described below.

2.6.3 Recent advances in *in situ* atomic-resolution ETEM for probing gas–catalyst reactions at the atomic level

Recently *in situ* atomic-resolution ETEM for direct probing of chemical reactions at the atomic level has been developed by Gai and Boyes and reported in Gai (1997), Boyes and Gai (1997), Gai and Boyes (1997), Gai *et al* (1995) and Gai (1998). This development demonstrated for the first time that atomic resolution is possible under reaction conditions with gas pressures of a few mbar and elevated temperatures. In this development, a new approach has been taken to organize and design instruments which are dedicated to ECELL operations and the ECELL is integral to the HRTEM. This atomic-resolution ETEM (also referred to as environmental-HRTEM or EHRTEM) development has been highlighted by the American Chemical Society in C&E News (Haggin 1995, Jacoby 2002). The ECELL design developed by the authors Gai and Boyes (Boyes and Gai 1997, Gai and Boyes 1997) has now been adopted by commercial TEM manufacturers and the authors' *in situ* atomic resolution data demonstrated under controlled gas and temperatures have been reproduced by other researchers using commercial instruments (Hansen *et al* 2000, 2001).

In this novel approach, a high-resolution Philips 300 kV CM30T HR (S)TEM has been extensively modified (figure 2.10(a) and (b)). The whole EM column, and not just the region around the sample, has been redesigned for the ECELL function. A custom set of objective polepieces with radial holes, for the first set of differential pumping is designed for the instrument (figure 2.10(c)). The ECELL is fully integrated and permanently mounted inside the atomic-resolution ETEM operating at 200 kV. The design and development enable studies of gas–catalyst reactions at the atomic level in controlled gas atmospheres and at temperatures up to ~ 1000 °C. The full 0.23/0.2 nm 'atomic' lattice resolution of the original instrument is retained in TEM images at elevated temperatures. With the apertures in place for differentially pumping the cell and column, the STEM (BF and ADF) mode has ~ 2.5 nm resolution and medium-to-high-angle electron diffraction, including microdiffraction and CBDP have been recorded. Chemical microanalysis is provided with in-cell EDX and a PEELS spectrometer and Gatan image filter (GIF) for local chemical state analysis and mapping. Some important features of this development follow.

The basic ECELL geometry consists of small apertures above and below the sample and the apertures are mounted inside the bores of the objective lens polepieces (figure 2.10(d)). The controlled environment ECELL volume is the normal sample chamber of the microscope. It is separated from the rest of the column by the apertures in each polepiece and by the addition of a gate valve, which is normally kept closed, in the line to the usual ion-getter pump (IGP) at the rear of the column. Differential pumping systems are connected between the

apertures using molecular drag pumps (MDP) or turbomolecular pumps (TMP). This permits high gas pressures in the sample region, while maintaining high vacuum conditions in the rest of the ETEM. Dynamic atomic-resolution imaging and electron diffraction are complemented by chemical analysis capability by incorporating a GIF-PEELS and scanning transmission EM (STEM) attachment in the atomic-resolution ETEM. A conventional reactor-type gas manifold system enables inlet of flowing gases into the EHRTEM, and a sample stage with a furnace (hot stage) allows samples to be heated. For dynamic atomic resolution, a few mbar of gas pressures are routinely used in the ECELL. Higher gas pressures (up to 1 atm) are possible with some loss of resolution due to multiple scattering of electrons through thicker gas layers. A mass spectrometer is added for gas analysis. A video system connected to the ETEM facilitates digitally processed recording of dynamic events in real-time, with a time resolution of $\sim 1/30$ s. Figure 2.10(a) shows the atomic-resolution ETEM instrument. Figures 2.10(b)–(d) show schematic diagrams of various components of ETEM and ECELL in the electron microscope column, respectively. Figure 2.10(e) shows a schematic diagram of the combination of ECELL for chemical reaction and HRTEM imaging.

2.7 Novel wet-ETEM development for nanoscale studies of liquid–catalyst reactions at operating temperatures

Recent developments include wet-environmental transmission EM (hereafter referred to as wet-ETEM) for probing controlled liquid–catalyst reactions directly at operating temperatures at the molecular level (Gai 2001, 2002). The method opens up new opportunities for high-resolution EM studies of a wide range of solution–solid and solution–gas–solid reactions in the chemical (especially polymer) and biological sciences.

For *in situ* wet-ETEM, a specimen holder has been developed to inject nanolitres to microlitres of liquids in a controlled manner and to have heating capabilities. This holder is referred to as a liquid injection goniometer hot stage (or LIGHTS). A nano/microlitre of liquid is injected via a stainless steel tube (liquid line) onto the sample immersed in liquid under flowing conditions, located in the furnace of the holder (figure 2.11). This development permits the catalyst sample to be heated in liquid environments to reaction temperatures. It also allows liquid–gas–catalyst studies at operating temperatures, utilizing the gas-manifold system for insertion of gases. We describe examples of wet-ETEM studies of polymerization reactions in chapter 5.

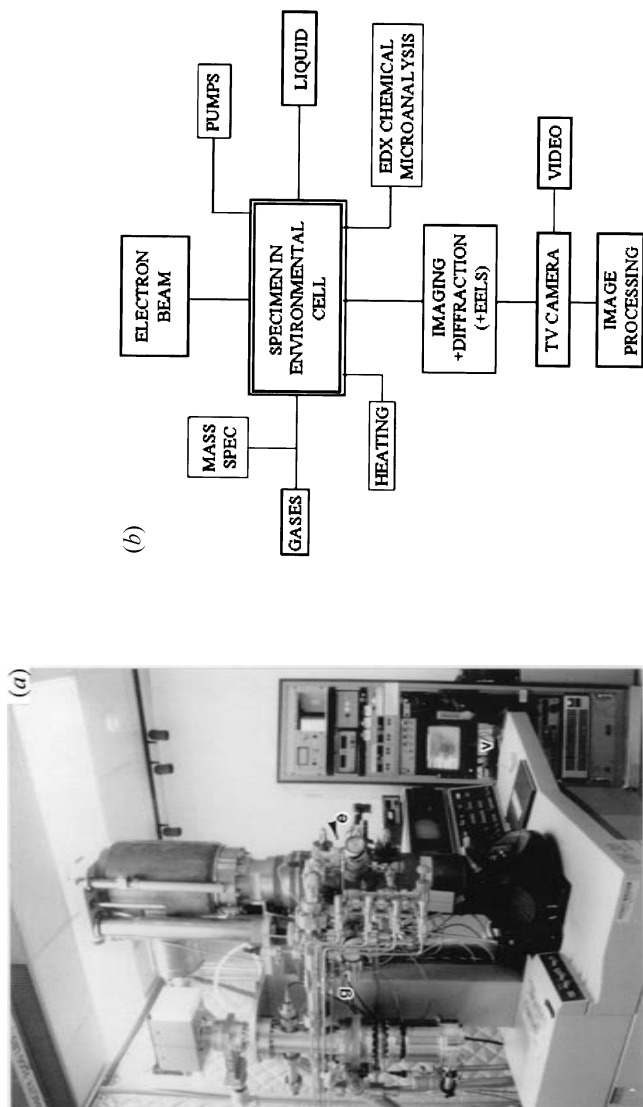


Figure 2.10. Development of novel *in situ* atomic-resolution ETEM instrument developed by Gai and Boyes (Gai and Boyes 1997, Boyes and Gai 1997) (e = environmental cell, g = gas manifold); (b) a schematic diagram of the various accessories for *in situ* studies in gas or liquids; (c) a schematic diagram of the basic geometry of the aperture design in the ETEM, with gas lines through objective polepieces for differential pumping; (d) column zones and apertures (in micrometres) (TMP, turbomolecular pump; MDP, molecular drag pump; IGP, ion-getter pump); (e) a schematic diagram of the combination of ECELL and HRTEM in the atomic-resolution ETEM.

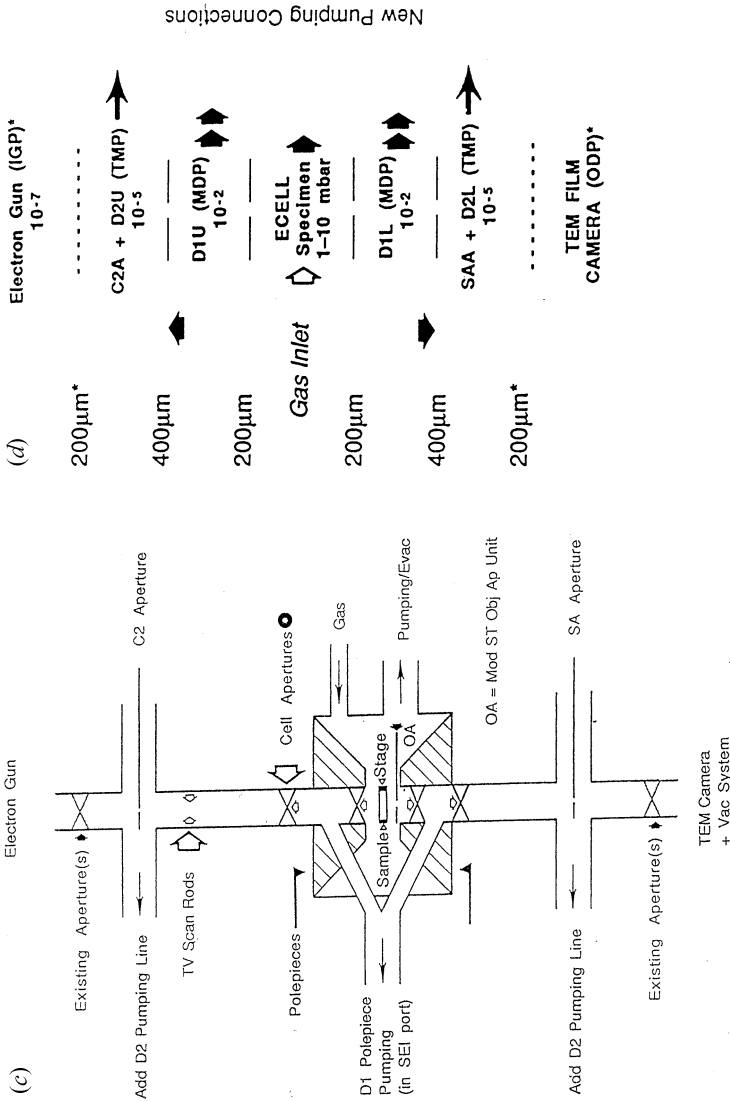


Figure 2.10. (Continued)

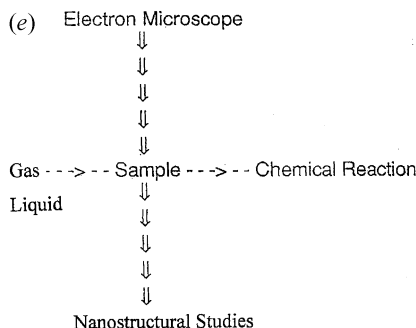


Figure 2.10. (Continued)

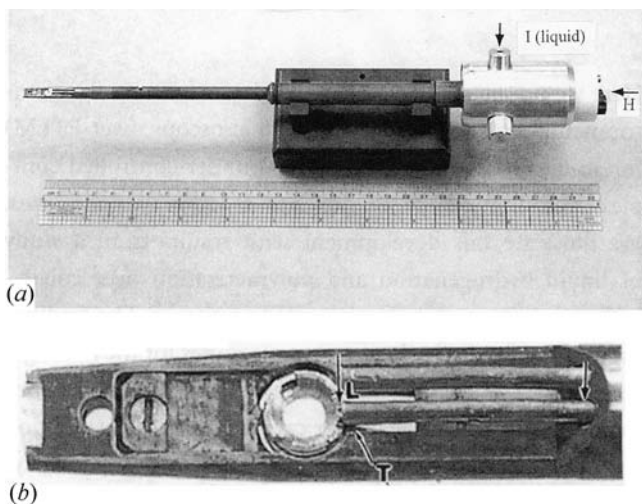


Figure 2.11. (a) Novel wet-ETEM sample-holder for studies of catalyst–liquid reactions at the molecular level at operating temperatures. Ports for liquid injection (I) and heating (H) are shown. (b) Enlarged tip of the holder. L and T denote the tube for injecting the liquid on to the sample and the thermocouple, respectively (after Gai 2002).

2.8 Scanning EM (SEM), cathodoluminescence in catalysis and environmental SEM (ESEM)

SEM utilizes a focused electron beam that systematically scans across the surface of a sample. It can be used to characterize the surface topography of bulk powders or pellets. Early SEM developments have been described by Von Ardenne (1938) and by Smith *et al* (1977). The principal high-resolution SEM imaging method is surface sensitive with an escape depth ~ 10 nm and sensitive to or

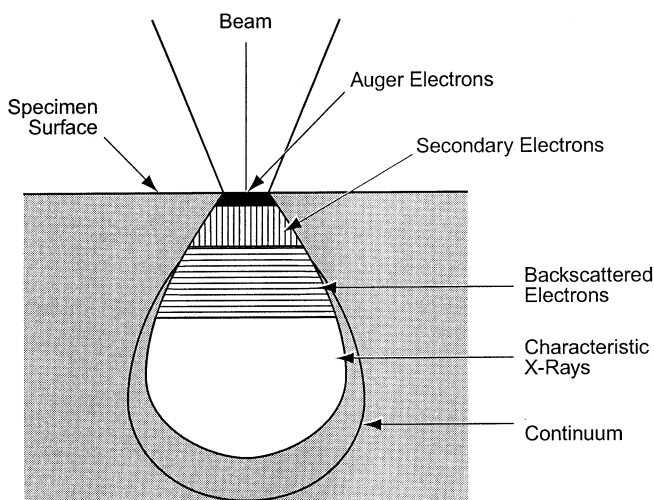


Figure 2.12. Primary excitation volume within the sample due to electron beam–sample interactions.

distorted by surface changes (Wells 1979, Goldstein *et al* 1984 and Postek *et al* 1980). In conventional SEM, samples (specimens) should either be conducting electrically or be coated with metal or carbon. However, recent pioneering developments in new ultra high-resolution low-voltage field emission gun (FE) SEM with chemical analysis (Boyes 1994) described later are revolutionizing surface science applications, especially in catalysis and ceramic sciences where uncoated samples can be examined at high resolution. Interactions between the electron beam and a sample creates a volume of primary excitation within the sample (figure 2.12) in which the electrons are scattered. Some SEM signals produced as a result of the interactions are: backscattered electrons (BSE), which are essentially elastically scattered electrons; and secondary electrons (SE), which may result from inelastic scattering with the loss of some electron energy and have low energy (<50 eV).

2.8.1 Recent advances in ultra high-resolution low-voltage FE SEM (HR-LVSEM) and extreme FESEM in catalysis

A new ultra high-resolution low-voltage FE SEM instrument with a 0.5 nm probe at 30 kV, and 2.5 nm at 1 kV, integrated with high-sensitivity EDX has been designed by Boyes (1993, 1994) to explore high-resolution imaging and chemical microanalysis in reflection from bulk samples. The instrument is equipped with an optimized high-brightness cold-field emission gun, combined with a very low aberration condenser objective final lens. The low voltages allow studies of uncoated, non-conducting samples (e.g. ceramics in catalyst

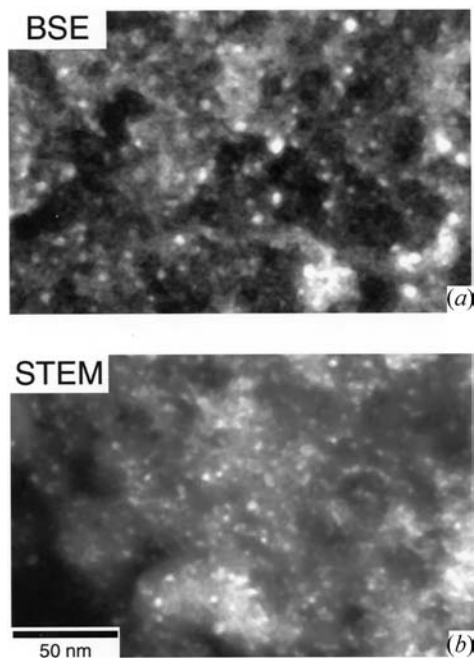


Figure 2.13. Pd/C nanocatalyst in (a) BSE and (b) HAADF STEM in the same LVSEM instrument. For real-life catalysts on uneven (irregular) supports, BSE appears to be an effective method.

supports). Low-voltage electron probes (<5 kV) generally yield inherently better secondary electron (SE) images, making HRLVSEM a powerful tool in the catalytic sciences. This advance is particularly important because it has made high-resolution surface analysis from bulk catalyst samples possible, which was long thought to be very difficult to achieve in an SEM. With this development, the resolution gap that previously existed between the SE microscope and many of the STEM applications (described later) has also been bridged.

A practical application of the BSE technique in the study of a commercially important Pd/C nanocatalyst is shown in figure 2.13(a) and the STEM image recorded in the same HRLVSEM in figure 2.13(b). BSE are scattered to high angles and so yield sharp images of nanoparticles and obey Rutherford's scattering law (described later). BSE scattering may be thought of as 'reverse Rutherford scattering' although the exact form of the experimental BSE scattering is modified by the high scattering angle and by the bulk specimen environment (Gai *et al* 2000). A low-voltage high-resolution image of uncoated sample of alumina with surface Pt catalyst particle (figure 2.14(a)) recorded with TV integration $\times 1024$ at 4 keV and EDX fast scan analysis from the catalyst particle is seen in figure 2.14(b). The contrast mechanisms and visibility of finely

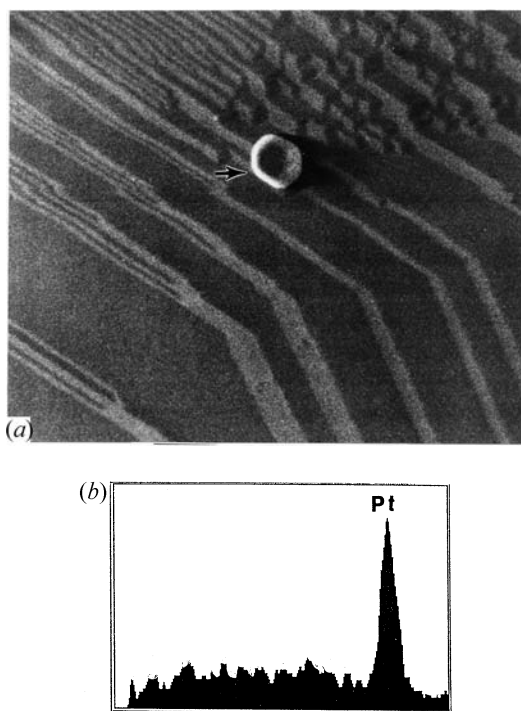


Figure 2.14. (a) LVSEM of Pt catalyst particle (arrowed); (b) EDX in LVSEM showing the Pt. (The particle site is ~ 0.1 micron, after Boyes 1994.)

dispersed supported nanocatalysts and their dependence on the catalyst size, location and incident electron voltage have been described using a FESEM and Monte Carlo simulations (Liu 2000).

2.8.2 Extreme FESEM

A novel approach to FESEM design by Boyes (2002) integrates new levels ($> \times 2$) of low-voltage image resolution (~ 1 nm at 1 keV and subnanometre at a few kV) with greatly improved ($0.3 \text{ sr}/\times 15$) sensitivity for EDX elemental microanalysis, chemical imaging at new levels of spatial resolution down to < 100 nm, and in favourable cases with sensitivity limits of 1–10 nm while retaining the advances of robust and representative bulk (mm) samples. Figure 2.15 shows a FESEM image of gold nanoparticles at a beam energy of 1 kV and figure 2.16(b) shows high-resolution x-ray mapping of a bulk $\text{SiO}_2/\text{ZrO}_2$ of interest as catalyst supports at 5 kV. These powerful capabilities are improving our understanding of catalysts.

ESEM (Danilotos 1990, 1997) is being used for *in situ* studies of polymers to understand a variety of surface effects in the presence of water such as swelling

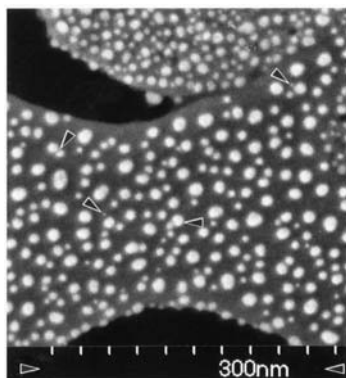


Figure 2.15. High-resolution extreme FESEM of gold nanoparticles (after Boyes 2001).

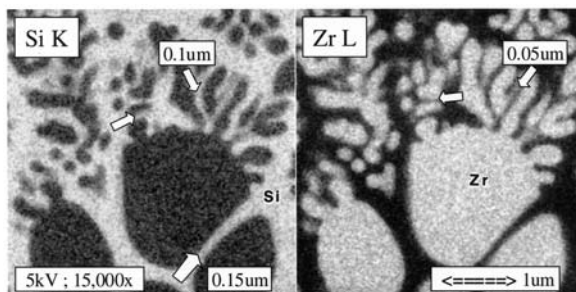


Figure 2.16. X-ray map of silica/zirconia in the Extreme FESEM (after Boyes 2001).

and drying. Uncoated, non-conductive polymer samples are also being studied (Donald 1996).

2.8.3 Cathodoluminescence in catalysis

When an energetic electron scatters inelastically, an electron from the (filled) valence band can be promoted to the (empty) conduction band creating an electron/hole pair. On recombination, the excess energy is released as a photon, the wavelength of which is well defined by the band-gap transition. The technique is powerful in catalysis: it is diagnostic of the electronic/chemical state and is sensitive to point defects. It can be used to probe the distribution of dopants in catalytic oxides.

In the cathodoluminescence (CL) technique in the EM, the wavelength of light emitted by selective electron stimulation can be directly related to the local band-gap energy of the catalyst material, and the intensity of the signal to the

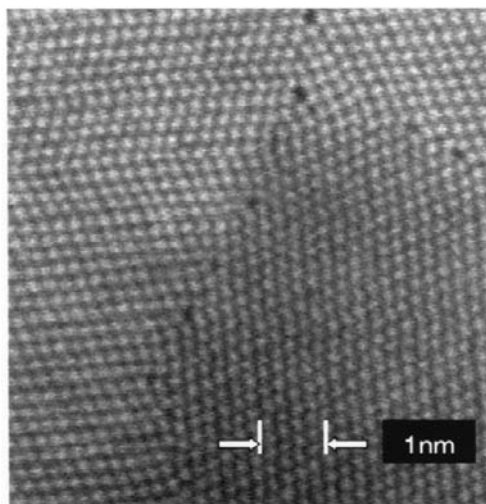


Figure 2.17. 2–2–2 FSTEM: Directly interpretable incoherent (HAADF) atomic-resolution image of grain boundaries in gold (after Boyes *et al* 2001).

point defect level, providing information on electronic properties of catalysts and promoter distributions as elucidated by Boyes, Gai and Warwick (1985). We describe CL studies in probing dopant distributions in chapter 3.

2.9 Scanning transmission EM (STEM)—recent advances

Scanning transmission EM (STEM) as a structural and analytical tool was pioneered by Crewe and co-workers (1970, 1971). STEM offers high-resolution microanalytical capabilities of EDX and EELS together with bright-field, dark-field and high-angle annular dark field (HAADF) imaging. HAADF imaging (known also as Z-contrast imaging) uses high-angle Rutherford-scattered electrons and is described later. STEM is essentially a combination of scanning EM and TEM (Batson (1979)). STEM imaging uses a finely focused probe of (<1 nm) over a thin sample. (In dedicated STEM instruments, the electron optics is reversed compared to a TEM and this aspect is called reciprocity.) Modern EMs now have both STEM and TEM functions and in the former, electrons are focused to a spot on the sample.

A new development in powerful FE STEM/TEM by Boyes *et al* (2001), called 2–2–2 200 kV field emission STEM/TEM, is now becoming available which combines atomic-resolution imaging with atomic level chemical and crystallographic analyses with 2 \AA (0.2 nm) resolution in each of the TEM, STEM and chemical analysis modes (hence 2–2–2), providing new opportunities in catalysis. In the 2–2–2 FSTEM, the incoherent HAADF-STEM provides

directly interpretable atomic-resolution images (figure 2.17), opening up new opportunities for imaging at the sub-0.2 nm level in catalysis.

Microanalysis in STEM: There are modern dedicated STEMs with field emission electron guns (FEG-STEM). Because of the high electron currents in a small probe, compositional and structural analysis with high lateral spatial resolution (from atomic scale to a few nanometres) is possible. Modern TEM/STEM instruments are also capable of high-precision analysis. For elemental identification, using EDX, the detection sensitivity in a dedicated FEG-STEM can be up to 0.5% cations. C_s -corrected STEMs are being developed to obtain sub-ångström probe sizes. However, the instrumental stability is expected to play a key role in accomplishing this goal.

2.9.1 Z contrast and three-dimensional electron tomography

An important method in high-resolution STEM (HRSTEM) is Z -contrast (or atomic number) imaging. It utilizes the fact that high angle scattering (with scattering angles >30 mrad) obey Rutherford's law, i.e. the scattering cross section is proportional to Z^2 . The use of a HAADF-STEM signal removes the complexity of conventional bright-field scattering in HRTEM and the associated diffraction complications and the incoherent images are directly interpretable. Single-atom HAADF sensitivity has been demonstrated by Crewe *et al* (1970) and the method is very useful in detecting catalytically active metallic clusters. Since this pioneering work, there have been significant advances in atomic number (Z) contrast imaging of nanoparticles led by Howie (1979). For example, Treacy *et al* (1978, 1980) and Pennycook *et al* (1980, 2000) have successfully imaged very small metal-particle catalysts using the Z -contrast. Using the HAADF technique, low concentrations of dopants (~ 1 atm%) in semiconductors with high resolution chemically sensitive images have been demonstrated (Treacy *et al* 1988) and in zeolite catalysts (Ozkaya *et al* 1997). Other spectroscopies are also possible in the STEM.

The novel use of the HAADF-STEM to determine the three-dimensional structure of supported metal nanocatalysts at very high spatial resolution of <1 nm has been elegantly demonstrated for Pd-Ru nanocatalysts supported on mesoporous silica (Midgley *et al* 2002). It is achieved by tilting the sample to a series of different and finely spaced angles of the two-dimensional projection. The novel use of an HAADF-STEM signal removes the complexity of conventional bright-field scattering in HRTEM and the associated diffraction complications and the images are directly interpretable. In addition, this powerful signal has the added benefit in maximizing the signal contrast between the high atomic number (Z) metal particles and the relatively low Z -support. The method uses an STEM electron beam with a tip diameter of 0.8 nm or less to scan the supported catalyst sample and a detector is used to collect transmitted electrons that are scattered at high angles. The sample is tilted through a series of angles. In the same way as in established x-ray tomography methods, the information from

the tilt series of two-dimensional projections are analysed to yield a detailed three-dimensional construction of the structure, with the full resolution of the process (in this case ~ 0.8 nm). The method is thus important in three-dimensional catalyst nanostructural analysis.

The three-dimensional electron tomographical construction of silica-supported metallocene catalysts using conventional TEM (Steinmetz *et al* 2000), and a novel method for the automated acquisition of tilt series for electron tomography of nanoparticles using STEM have been reported (Zeisse *et al* 2000). The HAADF-STEM is shown to be capable of determining the compositions of individual nanoparticle catalysts of a few atoms supported on porous substrates (Vaughan *et al* 1999).

2.10 Image processing

Digital-image-processing techniques are increasingly being used to enhance and, in some cases, replacing the existing photographic recordings in EM and are described later. With image processing it is possible to quantify an otherwise qualitative image and to obtain more detailed information from a single image. It is a very useful analytical technique.

In digital imaging, the image is converted to a digital form and stored in a framestore attached to a computer, which can be used for contrast enhancement and noise reduction (Boyes *et al* 1982 and Boyes 1983). Signal-to-noise ratios can be improved by averaging successive frames from a TV camera with a controlled output or by summing the data from adjacent pixels.

2.10.1 Charge-coupled devices

With recent advances in sophisticated solid state electronics, a new type of image-recording system known as a charge-coupled device (CCD) has become commercially available for EM (Janisek *et al* 1987), to record HRTEM images and diffraction under low electron dose conditions. The superior properties of the CCD including slow-scan (low noise) mode, high dynamic range and the ability to record digital images are making the CCD an attractive and strong candidate to replace conventional photographic recordings. The low noise level in CCDs is helpful in recording HRTEM images with very low incident electron beam intensities. Therefore it is finding applications in the studies of beam-sensitive catalysts like zeolites, where HREM structure information can be retrieved from their digital diffractograms (Pan *et al* 1992). The digital storage of CCDs allows one to carry out Fourier transforms and lattice diffraction measurements on-line. Commercial products (e.g. Gatan slow-scan CCD cameras) are available with, for example, 1024×1024 pixels.

2.11 Other developments

2.11.1 Reflection EM

Atomic imaging of surfaces with the TEM has also been carried out using reflection EM or REM (Yagi *et al* 1979, Minoda and Yagi 1997). In the REM mode, the incident electron beam is tilted through an angle of approximately a couple of degrees to strike the sample at a glancing angle. The final REM image is formed from one of the diffracted beams using an appropriate objective aperture configuration. Using this technique, the monolayer details of surface steps and defects in semiconductors have been revealed. Applications of this technique are possible in catalysis.

2.11.2 Electron holography

Electron holography is an imaging process which uses both electrons and light. It was pioneered by Gabor (1948) and followed by Mollenstedt *et al* (1956), Lichte *et al* (1991) and Tonomura (1997). As described earlier, the complex electron wave is modulated in amplitude and phase upon interaction with the object. The aberrations of the objective lens obscure the available information. However, back-propagation of this corrupted image back to the object is possible in an approach called holography by employing the registration of the image wave amplitude and phase and lens aberrations. In an FE-HRTEM equipped with an electron biprism, the electron beam transmitted through a sample and a reference plane wave beam produce an interference pattern which is recorded as a hologram. Since the hologram interference pattern can act as carrier wave for the amplitude and phase, the electron image wave can be extracted (reconstructed) from the hologram (Lichte 1991). The aberration-corrected amplitude and phase of the electron object wave is reconstructed to provide complete information about the amplitude and phase of the complex electron image wave. This approach in high-resolution holography can lead to further improvement of the point resolution in an HRTEM. Electron holography has been used recently to examine the shapes of catalyst particles (Datye *et al* 1997). However, there is scope for much work in catalysis using this method and in the interpretation of complex catalyst images.

2.11.3 Other surface techniques

Other techniques such as low-energy electron diffraction (LEED) are also used for surface analysis, primarily for large single crystals. Single crystal metal surfaces have been used to study hydrocarbon catalysis on platinum (Anderson 1975). Techniques such as x-ray photoelectron spectroscopy (XPS) are also used for surface analysis but normally the reports describe mostly idealized single-crystal surfaces in high vacuum as opposed to using real-life (practical) catalyst systems under reaction environments.

Scanning probe methods such as scanning tunnelling microscopy (STM) and atomic force microscopy (AFM) are applied to study surface phenomena. In scanning probe methods, information about the surface relationship to the bulk underneath and diffraction (structure), defect contrast modes and chemical information are currently not well defined. Although scanning probe methods are, strictly speaking, variants of microscopy, their theoretical basis, mode of operation and scope of applicability are so different from those of EM-based methods that they will not be considered further here. Extended x-ray absorption fine structure (EXAFS) in x-ray diffraction using a synchrotron is an attractive tool in catalysis for studying local atomic environments, e.g. interatomic distances, coordination numbers and the chemical nature of neighbouring atoms. It may be noted that with PEELS in the electron microscope, such fine structure information is also possible at perhaps much lower costs.

2.12 Parallel chemical studies and correlations with the catalyst microstructure

The catalyst microstructures are correlated with reactivity measurements under conditions identical to those used in dynamic EM experiments, using a microreactor (gas reaction chamber), with a gas chromatography mass spectrometry (GC-MS) system. Figure 2.18 is a schematic diagram of a GC-MS and a catalytic microreactor. The microreactor has a furnace (to heat samples), and contains larger amounts (~1–2 g) of catalyst samples similar to those used in the EM. Both flow and pulse reactions can be studied. In pulse studies, pulses of gases can be passed over the catalyst at regular intervals (many minutes). The reaction gas flows through the reactor and to the GC-MS. Conversion and selectivity of hydrocarbons to desired products and mass signals as a function of temperature are obtained using standard procedures, described in chapter 1.

Complementary techniques in catalytic chemistry involve temperature programmed (TP) methods where a reaction is investigated by subjecting the catalyst immersed in a reactant, to a temperature ramp. Rates of both reduction and oxidation can be studied. The extent of the catalytic reaction is then plotted as a function of temperature. In TP-desorption (TPD), the desorbed material is detected and plotted against temperature.

2.12.1 Analysis and characterization of catalyst dispersion and surface areas

Gas adsorption is the most commonly used method for characterizing the surface area of catalysts. Both physical adsorption and chemisorption may be used. Furthermore, EM can provide supplementary information. A large surface area is desirable since activity is defined as the rate per unit active surface area ((per metre)²), and this necessitates porous catalysts. For an idealized porous system,

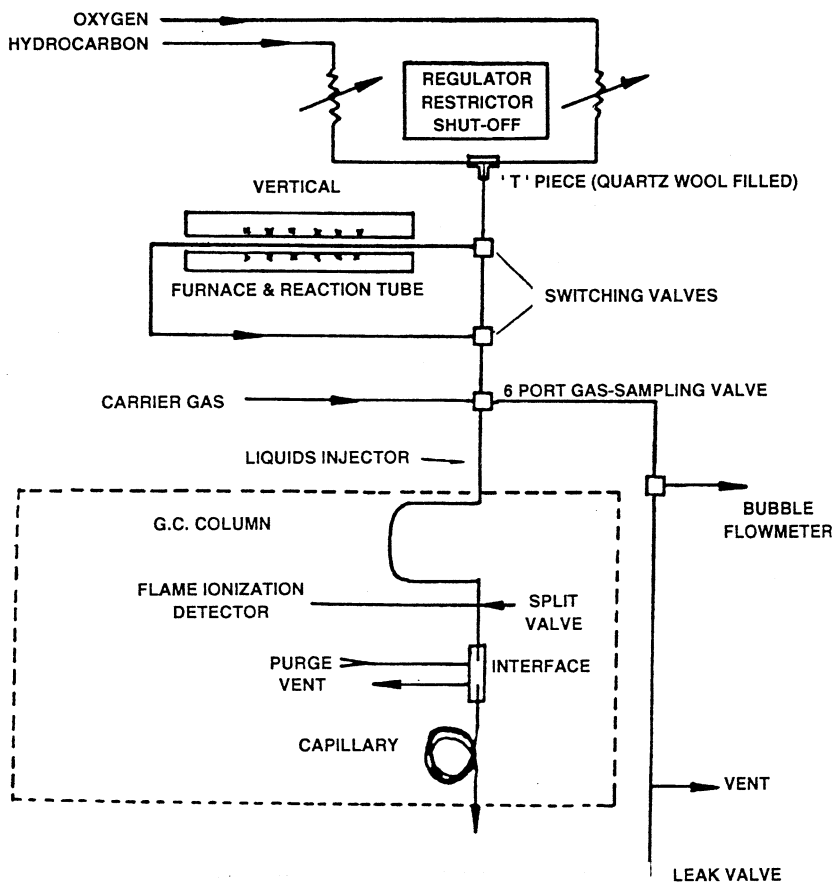


Figure 2.18. A schematic diagram of a gas chromatography-mass spectrometry (GC-MS) system for measuring the reactivity of a catalyst.

the pore volume is given by $S_A r/2$), where S_A is the surface area and r is the pore radius. Pores less than 2 nm in size are called micropores, 2–50 nm are mesopores and above 50 nm, macropores. Pore-size distribution in a catalyst system is usually carried out by mercury porosimetry where the mercury is pressurized through different pore sizes at different pressures and the change in volume of the catalyst is measured.

2.12.2 Physical adsorption

In a simple solid, a 'Langmuir adsorption isotherm' (Moore 1950) can be used to obtain the surface area assuming monolayer coverage (where the adsorption of gas molecules is measured at a temperature above its condensation into a liquid

so that only a monolayer is covered) so that $S_A = \text{number of molecules} \times \text{area per molecule}$. However, generally using temperatures near to the condensation of the gas, determination of the surface area of a catalyst is obtained using a standard Brunauer, Emmett and Teller (BET) method (Brunauer *et al* 1938).

2.12.3 Chemisorption

When the catalyst contains more than one component, selective gas chemisorption methods are normally used for analysing the surface area associated with a particular component. In this procedure, a gas (H_2 or CO for Group VIII metals) is adsorbed on only the component of interest. The method is also particularly useful for studying the dispersion state and surface areas in highly dispersed metallic systems.

2.12.4 Comparison of surface areas with electron microscopy

EM techniques provide important information in the characterization of the dispersion of metallic catalysts. Surface areas of catalysts are measured by the standard BET method described previously. An isotherm is produced using nitrogen as the adsorbate; chemisorption of certain gases (e.g. H_2 or CO) is also used, including for particle size distributions. We give some examples in chapter 5.

Chapter 3

Electron microscopy studies of catalysis by oxides

3.1 Single and mixed metal oxide systems: redox pathways and anion deficiency

Oxides are widely exploited as catalysts for the selective oxidation of hydrocarbons. They provide lattice oxygen in selective oxidation reactions and exchange it with oxygen gas (e.g. from air in the reactant stream). The periodic lattice oxygen loss for the hydrocarbon oxidation occurs because of reducing gases, despite the presence of gas phase oxygen in the reactant stream. This results in the formation of anion vacancies, local non-stoichiometry and defect structures as discussed in chapter 1.

We first consider simple metal oxide systems. The experiments and discussions presented here are, in general, applicable to other reacting simple oxide catalysts belonging to the ReO_3 , and the related rutile, V_2O_5 and MoO_3 groups. It is important to perform studies on single oxide systems first, because if we understand the catalytic behaviour of single oxide systems, a better understanding of the more complex, multicomponent, mixed-metal catalytic systems might be possible. Practical (real-life) catalysts employed in a number of commercial reactions are generally multicomponent, mixed-metal systems in the form of powders (prepared, for example, from coprecipitating solutions and calcination). The following sections demonstrate that oxides generally have orthorhombic or tetragonal structures compared to the simple cubic or fcc structures of many transition and noble metals. Thus, defect and structural analyses in oxides are much more complex. Defects are immensely important since in many catalytic reactions, only a small fraction of defects (<1%) can govern the processes.

We first discuss EM studies of MoO_3 and V_2O_5 catalysts. MoO_3 is used along with other catalysts in the selective catalyzation of hydrocarbons. The wealth of novel information revealed by EM studies is key to understanding the

performance of catalysts. Defects or structural modifications due to catalysis and the nature of the defects play a critical role in determining the catalytic properties of oxides and therefore understanding them is immensely important. We describe the imaging and interpretation of defects in oxide catalysts in the following sections.

3.2 Single metal oxide catalysts: MoO₃

MoO₃ represents a group of metal oxides which readily exchange lattice oxygen with oxygen gas and provide lattice oxygen for the catalytic oxidation of hydrocarbons. We will show that direct EM studies, especially under controlled gas reaction environments and temperatures, reveal a series of changes in the surface's structure during the different stages of the reduction leading to the formation of different crystallographic defects. We systematically examine the nucleation and growth of these defects, their diffusion into the bulk as a function of the reaction time, their role in catalytic reactions and the thermodynamics of defect structures in reacting oxides. Constant changes between the different stages of the reduction suggest that vacancy diffusion is active.

The structure of MoO₃ is orthorhombic, with $a = 3.965 \text{ \AA}$, $b = 13.855 \text{ \AA}$ and $c = 3.695 \text{ \AA}$ (Kihlberg *et al* 1963, Bursill 1969) and is shown in figures 3.1(a), (b) and (c) in (001), (010) and (100) projections, respectively. It consists of double layers of linked distorted MoO₆ octahedra parallel to (010), as shown in figure 3.1(a). Each double layer consists of chains along [001], of octahedra sharing edges with neighbouring chains linked by corner-sharing to form the layers. Successive layers are held together by weak Van der Waals forces only, with easy cleavage along (010). Thus there are no dangling bonds on the (010) surface. Oxygen appears to be very mobile as indicated by facile oxygen isotope experiments and diffusion of oxygen vacancies is thought to be the rate-determining step in hydrogen reduction (Jiru and Novakova 1963, Kennedy and Bevan 1974). Electron beam heating studies in EM vacuum under uncontrolled conditions (i.e. unknown temperatures) have shown changes which are attributed directly to the early stages of reduction of the oxide (Bursill 1969). The reaction temperatures in vacuum are considerably higher than those in reducing gas environments.

In situ dynamic ETEM studies in controlled environments of oxide catalysts permit direct observations of redox pathways under catalytic reaction conditions and provide a better fundamental understanding of the nucleation, growth and the nature of defects at the catalyst surface and their role in catalysis (Gai 1981–1982: 92). The following paragraphs describe the methods of observation and quantitative analyses of the surface and microstructural changes of the catalyst, and correlation of microstructural data with measurements of catalytic reactivity. We examine examples of pure shear and crystallographic (CS) shear defects that occur under catalytic conditions.

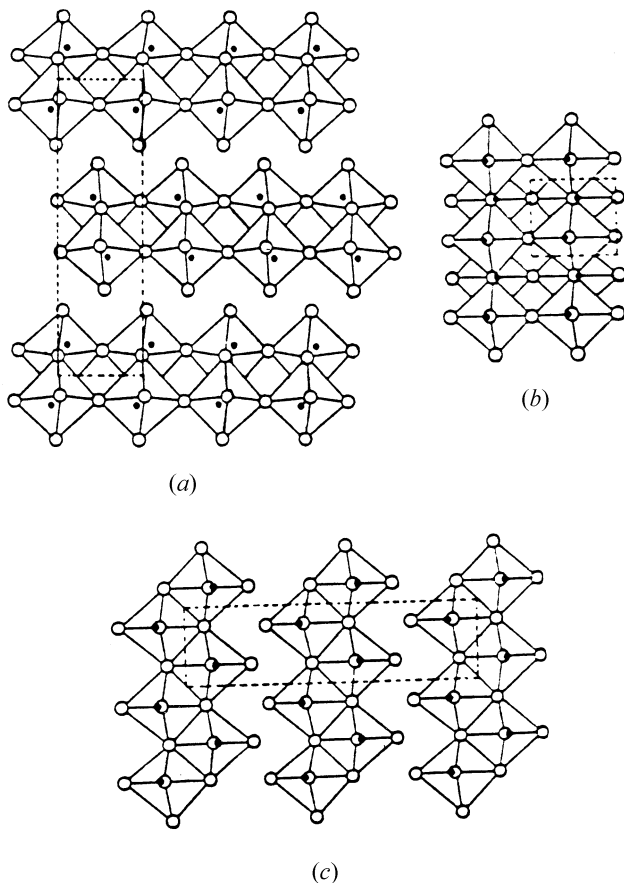


Figure 3.1. Structural projection of MoO₃ in (a) (001), (b) (010) and (c) (100).

3.3 *In situ* direct observations of surface defect structures in catalysts under controlled reducing environments and methods for defect analysis

In MoO₃ catalysts, on increasing the temperature from room temperature to $\sim 100^\circ\text{C}$, in reducing environments such as H₂ (or CO or propylene), a new type of straight defect is observed (arrowed) at the catalyst surface, in an otherwise clean matrix in the (010) crystal projection, as shown in the *in situ* ETEM dynamic diffraction contrast image in figure 3.2. The two sets of defects are approximately parallel to the [101] directions, but deviating from it by a few degrees. In the MoO₃ structure, the displacement vector analysis (described in chapter 2) shows that they are formed by pure shear in (101) planes. Figures 3.2(b) and (c) show

schematic diagrams of the structure of the defects. The defects exhibit a strong black–white contrast (evident in the initial stages of nucleation as shown in the inset), characteristic of defects nucleated close to the crystal surface. (This can be confirmed by calculations of the defect contrast as described in chapter 2.) The defects (or dislocations) are formed due to the loss of lattice oxygen under reduction conditions and are thus of vacancy type. The corresponding dynamic electron diffraction patterns exhibit two sets of diffuse streaks confirming the disorder.

The formation of the surface structural changes can be understood as follows: under the reducing gaseous conditions, there is a large driving force for the generation of vacancies following the gas–solid reaction at the surface. Since the surface defects are generated by reducing MoO_3 in H_2 (or in CO or C_3H_6 or methanol), it is believed that they arise as a result of the loss of anions from the catalyst's surface. A general description of the reaction would be chemisorption of H_2 at the catalyst's surface (followed by desorption of water), resulting in the creation of anion vacancies and the nucleation of defects. At low temperatures, this leads to the formation of partial screw dislocations at the surface to accommodate the misfit between the reduced surface layer, thought to contain a high concentration of anion vacancies, and the underlying crystal. The creation of misfit dislocations at the interface is to minimize the overall free energy. (The importance of this type of defect is described in the sections on multicomponent catalysts for alkane oxidation technology [3.9].) The displacements at the idealized faults do not lead to a change in the metal to oxygen ratio (figure 3.2(b)), although the octahedra across the faults now share edges. Each oxygen ion in the fault plane is shared by only two octahedra as in the equivalent positions in the perfect crystal. From figure 3.2(a) and its inset, we see that the screw (glide) dislocations grow. These defects may be nucleated as surface shear loops in the presence of large stress or they may be nucleated as small collapsed discs (see later) normal to the shear vector \mathbf{b} , part of the loop then expanding by glide on (101) planes containing the defects, under stress, to form a line defect (figure 3.2(c)) (Thoni *et al* 1977).

3.4 Shear domains and crystallographic shear (CS) planes in catalytic reduction

On increasing the temperature in the reduction of MoO_3 to $\sim 120^\circ\text{C}$, the misfit defects are replaced by two sets of twin-related platelets at the surface (also referred to as precipitates or surface domains), shown in figure 3.3(a). The traces of their habit planes can vary and the reasons for this are yet to be understood. The angles between the domains vary between $70\text{--}76^\circ$ and, in particular, larger domains tend to be along the $\langle 304 \rangle$ directions. They are formed by a near pure shear mechanism analogous to a martensitic transformation and are normally associated with $\{304\}$ planes. The bridging oxygens are involved in the formation

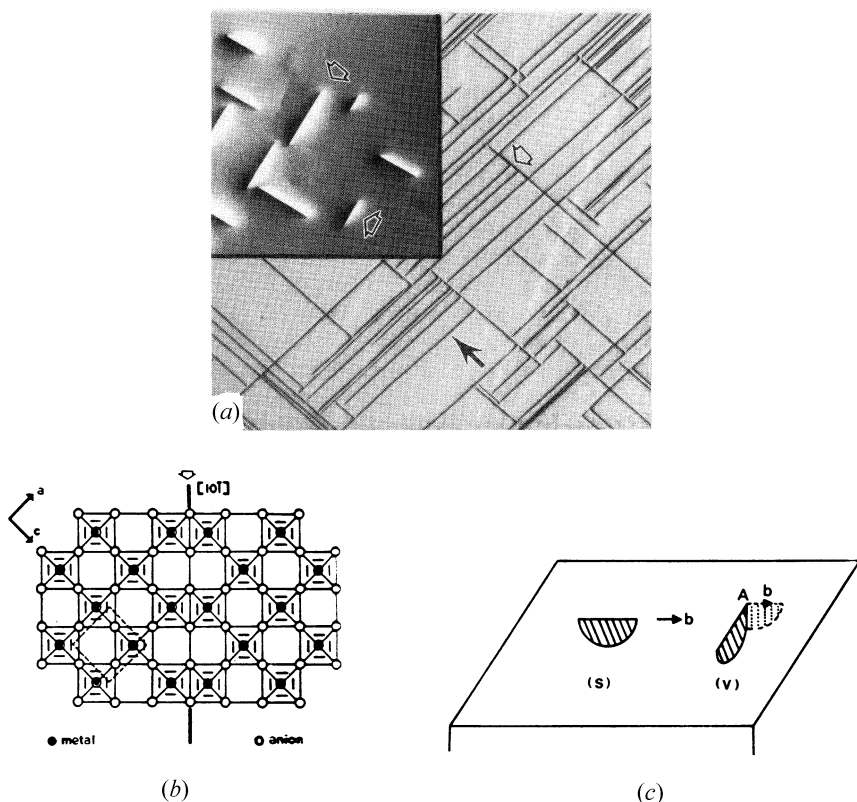


Figure 3.2. (a) *In situ* ETEM image of changes in the surface structure leading to a variety of extended defects (arrowed) in a dynamic catalytic reaction in MoO_3 in (010) projection (H_2/He gas environment with pressure ~ 100 torr): (a) Line defects (two sets are arrowed) at $\sim 100^\circ\text{C}$. Their strong black–white contrast in the inset shows they are close to the surface and are parallel to the $\langle 101 \rangle$ directions (after Thoni *et al* 1977). (b) Model for interpreting defects in (a) in which one layer of idealized MoO_3 is projected onto (010), showing a stacking fault formed by pure shear. The $[101]$ shear direction is shown by the arrow. (c) A small shear loop nucleated at the catalyst surface (S); a small collapsed vacancy disc loop at the surface (V): part of the loop at A expands under stress to form a line defect.

of the misfit defects and surface domains. Increasing the temperature to $\sim 300^\circ\text{C}$, the surface domains grow and extend throughout the bulk (figure 3.3(b)), giving an oxygen-deficient ordered ($7a \times 7c$) superlattice. Vacancies precipitate and order in the bulk domains. They are similar to the bulk domains obtained by heating the material under the electron beam. Anion-deficient domain formation is confirmed by reducing MoO_3 in CO , N_2 and vacuum, ruling out the formation

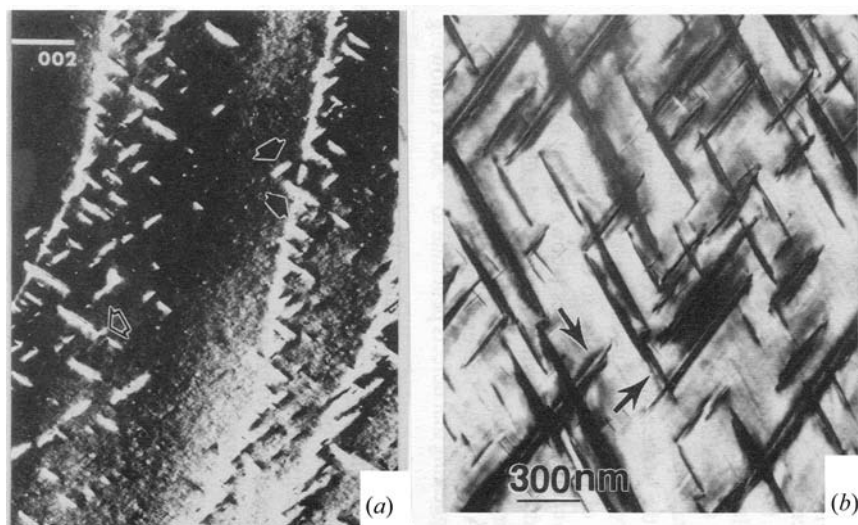


Figure 3.3. (a) Surface domains observed at $\sim 120^\circ\text{C}$ parallel to $\langle 304 \rangle$; (b) growth of domains (bulk domains) at $\sim 300^\circ\text{C}$, in the reduction of MoO_3 .

of molybdenum hydroxide bronzes (Gai and Goringe 1979, 1981). Further annealing of the domains leads to $\text{Mo}_{18}\text{O}_{52}$ -type structure.

Crystallographic shear is an elegant structural transformation mechanism in oxides. We now address one of the most fundamental issues in heterogeneous catalysis by oxides: the formation and the role of CS planes in oxidation catalysis.

3.4.1 Do CS planes form at catalyst operating temperatures and how quickly do they form?

Answers to these questions have been possible only by *in situ* ETEM studies under controlled catalytic reaction conditions. In MoO_3 , *in situ* ETEM provides the first direct evidence for the nucleation and growth of CS planes under reducing environments of H_2 near the catalytic operating temperature of $\sim 400^\circ\text{C}$. They are formed close to the surface after only ~ 35 s, as shown in the diffraction contrast images in figure 3.4(a) in (010), and are parallel to [001] directions. (Similar results are obtained in CO, C_3H_6 and methanol environments.) The associated electron diffraction (ED) image shows streaking along [001] indicating disorder (figure 3.4(b)). EHRTEM images of CS planes in the (010) orientation are shown in figures 3.5(a) and (b) respectively. As described before, for a long time it was thought that the mechanism by which oxygen could be released and absorbed by the oxide was associated with CS planes and that CS planes were the origin of activity (Stone 1975, Haber *et al* 1975, 1983). Here we describe analyses of CS

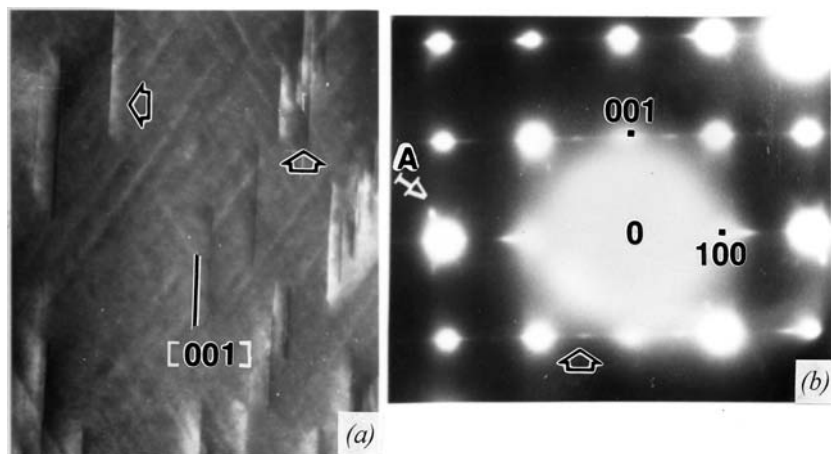


Figure 3.4. (a) *In situ* nucleation of CS planes at the operating temperature of $\sim 400^\circ\text{C}$ along [001] in MoO_3 . (b) The corresponding electron diffraction (ED) image with streaking along [100] due to the CS planes. (A shows superlattice reflections from domains.)

planes and their role in catalysis. In general, the procedures described here can be applied to probe other catalytic oxide systems.

3.4.2 Collapse in the catalyst's structure leading to the formation of CS planes

In dynamic ETEM studies, to determine the nature of the high temperature CS defects formed due to the anion loss of catalysts at the operating temperature, the important $\mathbf{g} \cdot \mathbf{b}$ criteria for analysing dislocation displacement vectors are used as outlined in chapter 2. (HRTEM lattice images under careful conditions may also be used.) They show that the defects are invisible in the $g = 002$ reflection suggesting that \mathbf{b} is normal to the dislocation line. Further sample tilting in the ETEM to analyse their habit plane suggests the displacement vector $\mathbf{b} = \pm(a/2, b/7, 0)$ and the defects are in the (120) planes (as determined in vacuum studies by Bursill (1969) and in dynamic catalysis studies by Gai (1981)). In simulations of CS defect contrast, surface relaxation effects and isotropic elasticity theory of dislocations (Friedel 1964) are incorporated (Gai 1981).

A comparison between experiment and theory suggests that they nucleate and penetrate from the surface to a depth of $\sim 300 \text{ \AA}$ in $\sim 35 \text{ s}$. Based on careful analyses of \mathbf{b} as previously described, a model for a collapsed disc of vacancies leading to a collapsed structure on (120) plane emerges for the formation CS plane defects and this is shown in figure 3.6(a). Figure 3.6(b) shows the projection of the structure on to (001) (Bursill 1969). A pair of weakly bound oxygen-vacancies

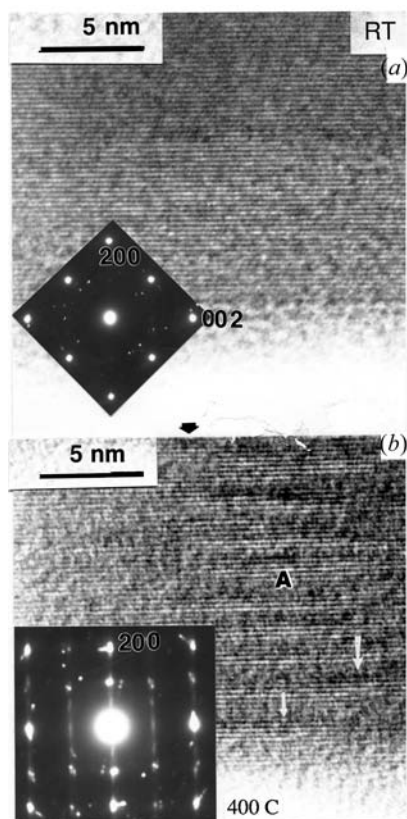


Figure 3.5. *In situ* EHRTEM image of CS at (a) room temperature and (b) 400 °C.

are eliminated by shearing by $\pm\frac{1}{2}a + \frac{1}{7}b$ along an octahedron edge as shown in figure 3.6(b). This model gives rise to lattice collapse which is consistent with CS. The defects are partial dislocations bounding the stacking fault created by the CS mechanism and the catalyst lattice collapse, leading to (120) CS planes. As shown in figure 3.6, terminal oxygen atoms of the catalyst are involved in this process. (It may be noted that for other models of b many bonds would have to be broken in the dislocation slip process, which are not supported by the experimental observations under the reaction conditions.)

3.4.3 Growth of surface defects: CS planes in catalytic reduction and climb of dislocations

Dynamic ETEM studies of the nucleation and growth of CS planes in reducing environments provide direct experimental proof of the motion of CS planes. They are consistent with the model of anion vacancies aggregating into discs

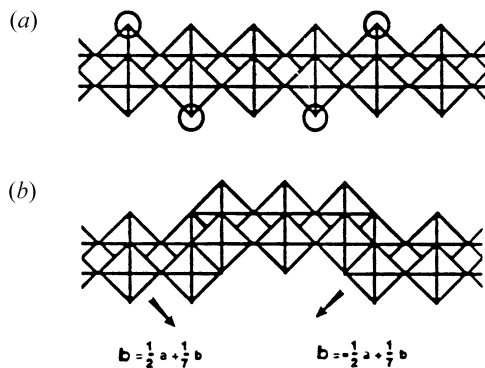


Figure 3.6. Model to interpret CS planes in figure 3.4, (001) projection: (a) weakly bound anion vacancies; (b) elimination of pairs of the vacancies by shearing by, e.g., $\pm\frac{1}{2}a + \frac{1}{7}b$ along an octahedral edge.

on a crystallographic plane, which collapse into a more stable dislocation loop, and of the collapsed vacancy discs climbing by their bounding dislocation loop, following Anderson and Hyde's (1967) model. The most common collapsed form is a planar dislocation loop which is energetically preferred (Frank 1950, 1951, Cottrell 1971). In the present case, partial edge dislocation loops bounding a collapsed disc of vacancies are nucleated at the surface, which expand by climbing on to the $\{120\}$ planes. Nucleation of partial dislocations is energetically more favourable compared to perfect dislocations. The dislocation loops are regions of high elastic strain energy and can therefore act as sinks for additional anion vacancies and growth. This is observed directly by ETEM as shown in figures 3.7(a) and (b). The figures show that CS defects grow along their length (e.g. 1–7) and the growth process and the nucleation of new CS planes (e.g. at N) occur simultaneously as reduction proceeds (Gai 1981).

We thus ask: What causes CS planes to nucleate (i.e. what are the reasons for anion vacancy aggregation and collapse in an oxide catalyst) and grow. We examine the response of defects in oxidizing atmospheres and, in particular, the role of anion vacancy concentrations in catalytic oxides. The EM results have led to novel concepts in oxidation catalysis (Gai 1981, 1992–1993, Gai *et al* 1982).

From the preceding discussion, the distinction between misfit defects shear domains formed by pure shear and CS planes formed by the elimination of anion vacancies in a specific crystallographic plane by shear and the collapse of the oxide lattice on that plane can be understood. This distinction between defects is central to catalytic reaction mechanisms in oxides. However, it is often not made in the literature on oxide catalysis and solid state oxide chemistry. This can result in an incorrect interpretation of observed data and of the role played by lattice oxygen atoms in catalytic reactions. The former are regions containing

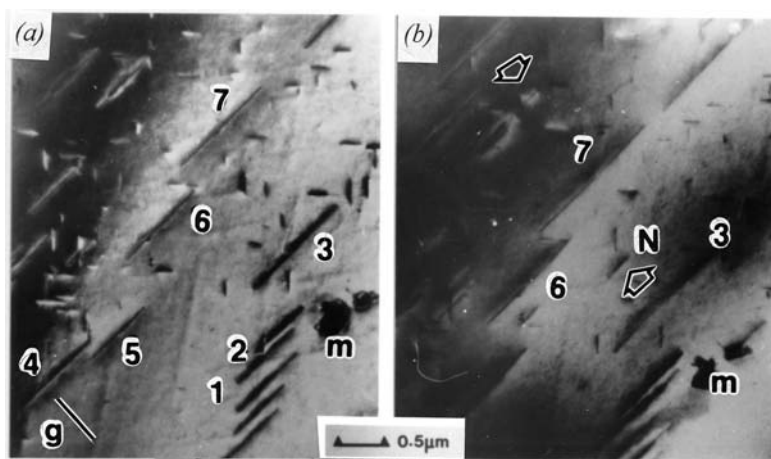


Figure 3.7. *In situ* growth of CS planes in dynamic reduction of MoO_3 in the same area of sample, marked 'm': (a) $\sim 400^\circ\text{C}$; and (b) $\sim 460^\circ\text{C}$. Growth of CS defects, e.g. 1–7, along their length and nucleation of new surface loops (e.g. at N) are shown. (After Gai 1981).

anion vacancies (which can be ordered), whereas CS planes nucleate and grow by eliminating anion vacancies and collapsing the structure.

3.4.4 Direct observation of dynamic redox processes in $\text{C}_3\text{H}_6:\text{O}_2$ (or air) mixtures: behaviour of surface defect structures

To investigate directly the formation and response of defects in reducing-oxidizing gas mixtures, *in situ* ETEM studies are performed on MoO_3 in $\text{C}_3\text{H}_6:\text{O}_2$ environments (figure 3.8). It is important to note from figure 3.8 that even in the presence of an oxidizing gas, domains which are characteristic of oxide reduction (as described earlier) are observed up to 275°C and bulk domains up to 370°C . At 370°C , some CS planes are also observed at the surface, some of them reoxidizing over time in the presence of gas-phase oxygen. These ETEM studies of redox have thus provided direct evidence that catalyst surface reduction occurs in a gas mixture containing a reducing gas, even in the presence of an oxidizing component (Gai 1981).

3.4.5 Methanol oxidation over MoO_3

On MoO_3 , methanol (CH_3OH or MeOH) chemisorbs at a low temperature of $\sim 100^\circ\text{C}$, which suggests that some defects (or dangling bonds) are necessary for chemisorption. *In situ* ETEM experiments in methanol show the formation of misfit defects at $\sim 100^\circ\text{C}$ (and surface domains) accommodating the shape

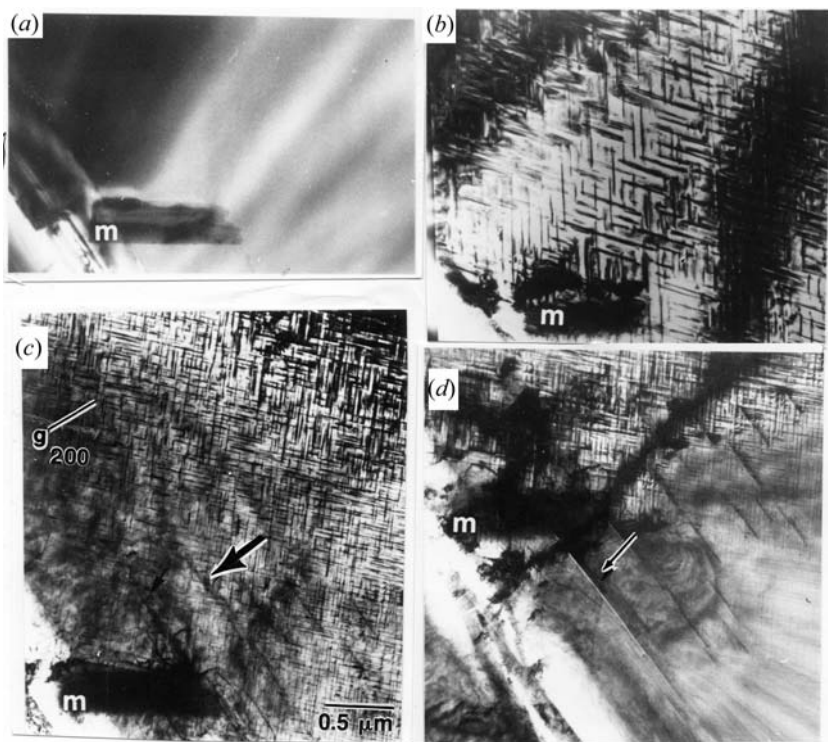
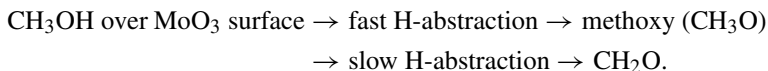


Figure 3.8. Dynamic redox experiments in propylene:oxygen mixtures around the same sample area m: (a) fresh catalyst; (b) domains; (c) bulk domains with CS nucleation (arrowed); and (d) CS planes. The domains and CS planes are formed even in the presence of oxygen gas (after Gai 1981).

misfit between regions of surface layers with anion vacancies and the bulk catalyst (Gai and Labun 1985). The studies indicate that these vacant anion sites are related to the observed chemisorption. The ETEM studies have been confirmed by subsequent chemical reactivity studies of methanol oxidation over MoO_3 (Chung *et al* 1988) showing chemisorption at $\sim 100^\circ\text{C}$. The following mechanism for the reaction leading to formaldehyde can be written:



3.4.6 V_2O_5 catalysts

V_2O_5 with promoters is used in a variety of industrial processes, for example the oxidation of ethylene. Recently, catalysts, such as supported MoO_3 and 1 wt%

V_2O_5 supported on silica, have found use in the direct conversion of natural gas. Various studies on the partial oxidation of methane to oxygenates have reported these to be highly active and selective catalysts, with V_2O_5 slightly outperforming MoO_3 (Spencer 1988). It is proposed that MoO_3 is capable of inserting an oxygen into a C–H bond while V_2O_5 is capable of abstracting H from and inserting O into the CH_4 molecule.

A schematic diagram of the V_2O_5 structure with square pyramids is shown in figure 3.9(a). An idealized octahedral model in the (001) projection is shown in figures 3.9(b) and (c), respectively. V_2O_5 is orthorhombic with $a = 11.51 \text{ \AA}$, $b = 3.563 \text{ \AA}$ and $c = 4.369 \text{ \AA}$, space group $Pmmn$ (Bachmann *et al* 1961). In this oxide, dynamic ETEM studies of the H_2 gas show that misfit dislocations (of the type observed in MoO_3) are not observed in the reduction. Instead, two sets of surface domains (figure 3.10(a)) are nucleated at $\sim 100^\circ\text{C}$. Defect analysis with the $\mathbf{g} \cdot \mathbf{b}$ criteria shows that they are formed by pure shear. The domains grow and extend into the bulk at higher temperatures (figure 3.10(b)), forming regions of ordered anion vacancies. The growth of bulk domains leads to a composition similar to V_4O_9 structure. At higher temperatures of $\sim 460^\circ\text{C}$, CS planes are observed (figure 3.11), with $b = \pm \langle a/6 \ 0 \ c/2 \rangle$. CS planes exist only in a narrow temperature regime in this system as found by *in situ* ETEM. The structural changes can lead to the V_6O_{13} structure at higher temperatures (Gai 1983(a)).

3.5 Electron microscopy and defect thermodynamics: a new understanding of oxidation catalysis

3.5.1 Development of thermodynamics of reacting catalysts based on EM

Thermodynamic studies greatly complement structural studies of a catalyst in a catalytic reaction and facilitate a complete analysis of the reaction. The thermodynamic behaviour of solids, including the formation of defects, is determined by the change in free energy in response to changes in their composition. In apparently stoichiometric oxides, the defect structures contain equal amounts of positively and negatively charged point defects, e.g. Schottky disorder, or, in some cases, Frenkel disorder. In the non-stoichiometric (oxygen-deficient) oxides considered here, there is a deficit of oxygen due to the loss of structural oxygen for catalysis and doubly and positively charged anion vacancies are expected to predominate (Kofstad 1972). The collapse of vacancy discs leads to extended CS planes at an operating temperature of $\sim 400^\circ\text{C}$ in MoO_3 .

Earlier work in the literature on the defect thermodynamics of oxides containing CS planes is based on conventional TEM studies of CS planes on static oxide systems. However, much of the earlier work contains the implicit assumption that all point defects due to the oxide anion loss are eliminated to produce CS planes. Several workers have made important contributions to understanding defect thermodynamics in oxides containing a finite number of

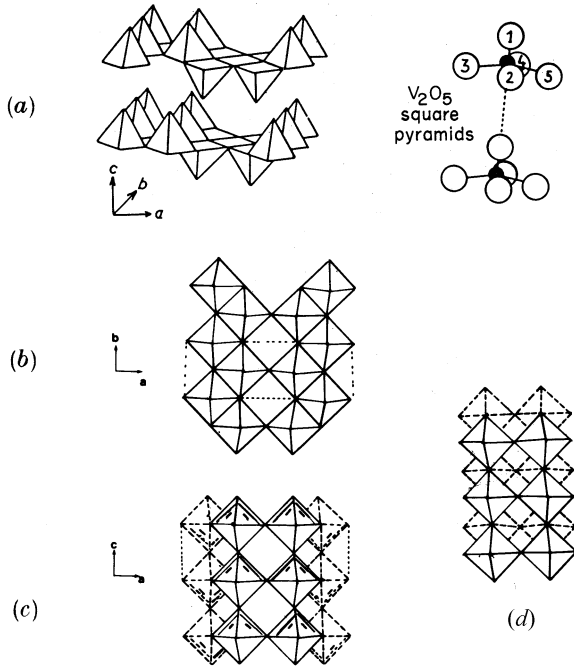


Figure 3.9. A structural model of the V_2O_5 catalyst: (a) square pyramids; and the idealized octahedral model in the (001) (b); (010) (c) and (100) (d) projections.

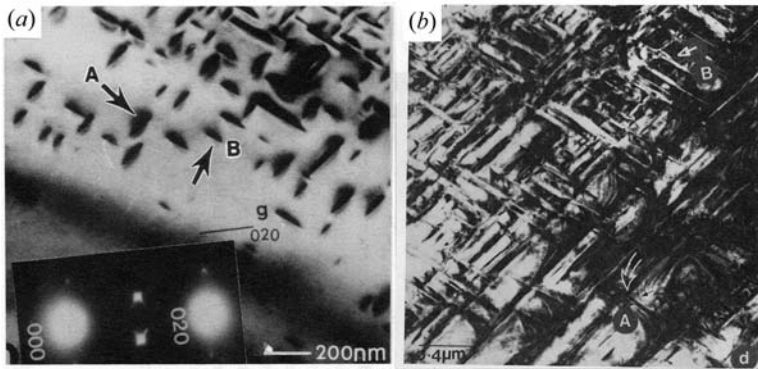


Figure 3.10. Reduction of the catalyst (001) in H_2/He : (a) surface domains at $\sim 100^\circ\text{C}$ with ED showing disorder; (b) bulk domains with varying trace boundaries (leading to the V_4O_9 structure).

CS planes using conventional TEM methods (e.g. Merritt and Hyde 1973) and by calculations using lattice potential models (Catlow *et al* 1978, Cormack *et al*

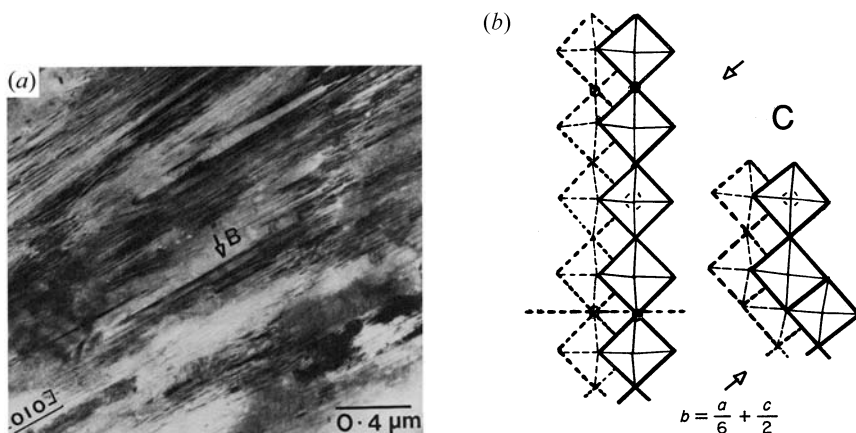


Figure 3.11. V_2O_5 reduction in H_2/He : (a) CS planes parallel to [010] at $\sim 460^\circ C$ (leading to V_6O_{13}); and (b) a model for CS in (010) V_2O_5 .

1982). The key role of electron microscopy is illustrated by Merritt and Hyde (1973) in studies of rutile. In the studies, the coexistence of (121) and (132) CS planes revealed only by TEM, is shown to lead to more correct thermodynamical interpretations. However, thermodynamic treatments in the literature tend to be incomplete as they have not included the reaction mechanism or the nature of the CS defect formation.

EM plays a crucial role in the development of thermodynamic data, especially for defective solids, multi-phase solids and solids with coexisting intergrowth structures. These microstructural details, which are essential to catalytic properties, cannot be revealed readily by other diffraction methods which tend to average structural information. The formation of anion vacancies in catalytic reactions and the resulting extended defects are described here, from which an improved understanding of the formation of CS planes and their role in catalysis can be obtained. These general results are applicable to other CS structures.

3.5.2 New understanding of defect mechanisms in oxidation catalysis from dynamic electron microscopy

Here we present thermodynamic discussions and developments based on recent *in situ* ETEM studies. These are important in predicting the enthalpy of formation of vacancies in oxide catalysts, the probability for CS planes to form and catalyst performance. They are also important in the design of new or improved oxide catalysts.

From the *in situ* reduction studies described in previous sections, it is clear that non-stoichiometry in an oxide catalyst results from the loss of the catalyst's

structural oxygen. This non-stoichiometry can be accommodated by isolated anion vacancies or, as in the present case, by a collapsed disc of vacancies at the operating temperature (in the case of MoO_3 at $\sim 400^\circ\text{C}$). There have been some reports in the literature as described earlier (3.5.1), on the concentration of isolated vacancies in the presence of crystallographic shear planes. They suggest that an equilibrium concentration of point defects exists in systems containing a finite number of CS planes. It may be seen that the concentration of isolated vacancies is governed by the difference between the free energy of an isolated vacancy and that of the one absorbed in a collapsed CS fault plane. The thermodynamic parameters for many of these complex non-stoichiometric oxides are not known but estimates can be made from empirical approaches to predict defect concentrations (Gai 1981, 1992). The background equilibrium concentration of vacancies c_0 in an oxide crystal can be deduced using a relation between the free energy ΔG_v of an isolated vacancy, the surface free energy (γ) of the fault plane of the collapsed disc due to CS and the area per vacancy on the fault plane (ds/dn).

If the isolated vacancies and collapsed disc are in equilibrium:

$$c_0 = \exp\{-(\Delta G_v - \gamma ds/dn)/kT\}. \quad (3.1)$$

More generally, c_0 is independent of the external gas pressure; k is the Boltzmann constant (1.38×10^{-16} erg deg $^{-1}$) and T is the temperature in Kelvin. Furthermore, the equilibrium between c_0 and a collapsed CS plane fault is maintained by exchange at dislocations bounding the CS planes. Clearly, this equilibrium cannot be maintained except by the nucleation of a dislocation loop and such a process requires a *supersaturation* of vacancies and CS planes eliminate supersaturation of anion vacancies (Gai 1981, Gai *et al* 1982). Thus we introduce the concept of supersaturation of oxygen point defects in the reacting catalytic oxides, which contributes to the driving force for the nucleation of CS planes. From thermodynamics,

$$\Delta G_v = \Delta H_v - T \Delta S$$

where ΔH_v and ΔS are the enthalpy and entropy of formation of doubly and positively charged anion vacancies. It should be noted that the entropy term contains only the vibrational entropy due to the change in the vibrational modes in the neighbouring atoms of a vacancy and not the small configurational entropy term associated with the formation of defects. ΔH_v can be estimated as follows. From an empirical relation (Kofstad 1972):

$$\Delta H_v = 2(E_{\text{atm}}/y - 167) \text{ kcal mole}^{-1} \quad (3.2)$$

where E_{atm} is the energy of atomization of an oxide with the general formula M_xO_y ; and is the energy required to dissociate the oxide into gaseous atoms of its components. Using the relation between E_{atm} , the heat of formation of the oxide

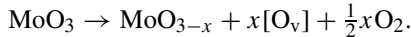
($-\Delta H_f$), the heat of its sublimation (L_s), at 298 K and the dissociation energy of the oxygen molecule, ΔD_0 (~ 120 kcal/mole):

$$E_{\text{atm}} = -\Delta H_f + xL_s + y\Delta D_0. \quad (3.3)$$

Using the values for $-\Delta H_f$ and L_s (Kubashevski and Evans 1962), we can estimate that for MoO_3 , $\Delta H_v \sim 0.4 \text{ eV} \pm 0.1 \text{ eV}$. ΔH_v is low for MoO_3 , which means that it is easy to remove anions from its lattice to form vacancies.

Qualitatively, in expression (3.2), ΔH_v is the energy needed to remove one mole of oxygen atoms from anion sites in the oxide and E_{atom}/y is the average bond strength of the oxide per gram-atom oxygen. Using these principles, for V_2O_5 , ΔH_v is $\sim 1.3 \text{ eV}$. Similarly, in WO_3 , ΔH_v is $\sim 3 \text{ eV}$, which is quite large. This means that vacancy formation is difficult in this oxide system at low or moderate temperatures. It is possible to calculate the activation energies for vacancy migration in these oxides from *in situ* ETEM.

Under reducing conditions, there is a large driving force for the removal of lattice oxygen and the formation of doubly and positively charged anion vacancies [O_v]:



Assuming that the anion vacancies drift to the CS defect as a result of the point defect–extended defect interaction, an estimate can be made of the activation energy for the migration of anion vacancies.

3.5.3 Supersaturation leading to a modified mechanism for the formation of CS planes in oxides

Following the reaction between H_2 and the oxide catalyst (producing H_2O), the actual average anion vacancy concentration c can be written:

$$c \sim \{(k_v k_{\text{H}_2\text{O}})/4\}^{1/3} \{p_{\text{H}_2}/p_{\text{H}_2\text{O}}\}^{1/3} \exp\{-\frac{1}{3}[(\Delta H_v + \Delta_{\text{H}_2\text{O}})/kT]\}$$

where k_v and $k_{\text{H}_2\text{O}}$ are the rate constants for the formation of anion vacancies and water and the p s are the partial pressures. The actual average anion vacancy concentration c in a defective catalyst can also be obtained from estimating the defect depth (d) (which is the diffusion front of anion vacancies) in time t of the reaction. From the diffusion problem in solids (Shewmon 1963), $d \sim 2\sqrt{Dt}$, where D (the diffusion coefficient) follows the rate equation:

$$D = D_0 \exp(-E/RT)$$

where R is the universal gas constant and equals $1.986 \text{ cal deg}^{-1} \text{ mole}^{-1}$.

In EM studies of CS plane defects, the actual concentration of anion vacancies (c) in the collapsed discs in the region covered from the surface to the depth of the defects can be estimated from the density of the defects observed and the area covered by their depth (at temperature T), assuming that a large

number of vacancies are absorbed by CS defects into collapsed discs. For a defect extending to a depth of $\sim 300 \text{ \AA}$, in 35 s (figure 3.4), c is then $\sim 3 \times 10^{-2}$, and from equation (3.1), c_0 is $\sim 5 \times 10^{-4}$, giving a supersaturation of c/c_0 .

The results indicate that a supersaturation of vacancies, $c/c_0 \simeq 10^2$, at the catalyst's surface is required to nucleate CS planes in MoO_3 catalysts. CS planes are formed by the elimination of anion vacancies in supersaturation (where the supersaturation is defined relative to the background concentration of anion vacancies in equilibrium with CS planes, as described earlier) (Gai 1981, Gai *et al* 1982). The driving force for the nucleation of the CS fault is the difference between the chemical stress due to the supersaturation of anion vacancies of the faulted (defective) structure and the force required to create the fault. The estimate of c_0 is consistent with the equilibrium concentration of anion vacancies found in electron beam heating studies of MoO_3 in vacuum (Bursill 1969).

As shown in the previous sections, from *in situ* ETEM, the depth d of a defect in time t can be determined using the diffusion phenomenon in solids. The activation energy for migration normal to the MoO_3 layers (E_n) is estimated as ~ 0.9 eV. This is generally consistent with the value obtained in the diffusion-controlled hydrogen reduction of MoO_3 to MoO_2 and interpreted as arising from reactions occurring at the edges of the layers (Batist *et al* 1967). The lower activation energies for anion vacancy migration means that the diffusion of anion vacancies is quite fast at the operating temperatures discussed here.

In situ ETEM studies of catalytic reactions at the different temperatures described earlier provide critical data showing that the extraction of oxygen from the MoO_3 surface results in anion vacancies which assemble into a variety of extended planar defects. The extended defects which accommodate non-stoichiometry lead to the lowering of the free energy of the oxide catalyst system and this lowering of the free energy is the driving force. Higher temperatures are required for nucleation of defects since the diffusion of anion vacancies is slow at room temperature. In catalysts reduced for longer periods, defects can order to form reduced oxides with a composition close to that of MoO_3 (e.g. $\text{Mo}_{18}\text{O}_{52}$, Mo_8O_{23} , $\text{Mo}_{17}\text{O}_{47}$, Mo_4O_{11}). Some of these phases have been synthesized (Kihlborg 1963). The transformation of MoO_3 to MoO_2 at high temperatures has been described using RHEED and Auger spectroscopy (DuFour 1984, Firmont *et al* 1983, Haber *et al* 1973, 1997, Volte *et al* 1985). As we describe later, catalytic operations without CS planes has been established in some commercial systems (Gai *et al* 1982, Gai 1983, 1995).

3.6 The role of defects in catalytic reactions

3.6.1 Correlations of the catalyst microstructure with catalytic activity and selectivity

The role of defects in heterogeneous catalysis, including the role of CS planes which form near the catalyst operating temperature in single metal oxides such

as MoO_3 , is of fundamental importance. The role of defects in oxidation catalysis has been examined in C_3H_6 and methanol oxidation reactions by correlating the catalyst microstructure to catalytic reactivity studies performed under conditions similar to those employed in ETEM (Gai 1981, Gai *et al* 1980, 1982), and subsequently in methanol chemical reactions (Miranda *et al* 1987). The investigations of MoO_3 and other model oxides in C_3H_6 suggest that selectivity to acrolein decreases with increasing CS plane formation at the operating temperatures (figure 3.12). In MoO_3 , dynamic EM studies of CS planes (Gai 1981 and Gai *et al* 1982) described in 3.4.2 and 3.5.2, have shown that CS planes are present at the operating temperature of $\sim 400^\circ\text{C}$, but they appear to be only secondary defects, accommodating supersaturation of anion vacancies in the reacting oxide. These studies therefore attempt to answer the questions raised by Anderson (1970, 1971) and Anderson *et al* (1973) whether anion point defects are eliminated completely: the studies show that anion point defects are not eliminated completely, but only the supersaturation of the point defects is eliminated to form CS planes. Significantly, studies on commercially important tellurium molybdate (Gai *et al* 1982), Bi-molybdate (Gai 1983) and vanadyl pyrophosphate systems (Gai *et al* 1995, discussed later) have not shown CS plane formation at catalyst operating temperatures in either hydrocarbon oxidation or ammoxidation. Figure 3.12 shows conversion (activity) and selectivity of propylene and ammonia over MoO_3 , TeO_2 and mixed Te–Mo–O catalysts at $\sim 400^\circ\text{C}$. MoO_3 exhibits very little selectivity to acrolein. (As in Te–Mo–O catalysts, mixed Bi–Mo phases show higher selectivities compared to single component oxides.)

Dynamic ETEM experiments on CS defects have shown that they consume anion vacancies and grow (figure 3.7). These correlation studies indicate that CS planes are secondary or detrimental to catalytic reactivity. They eliminate anion vacancies by accommodating the supersaturation of the vacancies in the reacting oxide catalyst and the catalyst reactivity (selectivity) begins to decrease with the onset of CS formation, i.e. CS planes are the consequence of catalyst reduction reactions rather than the origins of catalytic reactivity (Gai 1981, 1992, 1993, Gai *et al* 1982).

The results that CS planes (which eliminate anion vacancies in supersaturation by shearing and collapsing the lattice) are detrimental to catalysis are also consistent with the fact that if the catalyst structure continues to collapse to form CS planes, after a period of time the catalyst is no longer an efficient oxidation catalyst. An efficient catalyst is essential for prolonged catalytic activity. This has led to the discovery of a novel glide shear mechanism (Gai *et al* 1995, Gai 1997). The role of this mechanism in mixed-metal practical (commercial) catalysts will be examined when we discuss butane oxidation technology.

These studies have led to a new understanding of the fundamental defect processes that occur at the oxide catalyst's surface and of the role of extended CS plane defects in oxide catalysts. Furthermore, the studies suggest that anion point

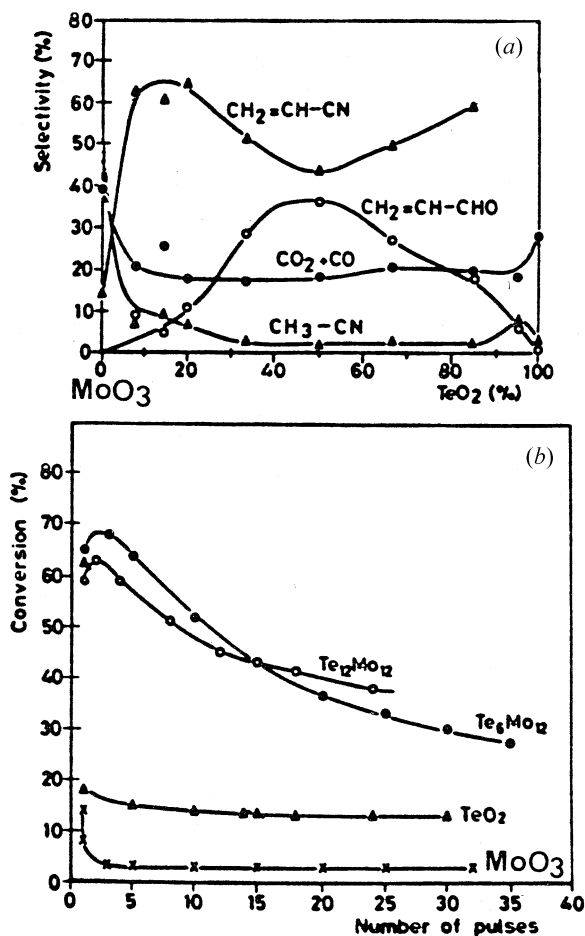


Figure 3.12. (a) Conversion and (b) selectivity of C₃H₆ (with NH₃) over MoO₃, TeO₂ and Te-Mo-O catalysts. (After Gai *et al* 1980, 1982, Gai 1993.)

defects (which may include point defect clusters) are active sites, which facilitate fast diffusion of oxygen (Gai 1981, 1992, Gai *et al* 1980, 1982). Subsequent chemical studies carried out on methanol oxidation over MoO₃ confirm these conclusions (Chung *et al* 1988). These studies show that in the oxidation of methanol involving methoxy as a reaction intermediate, a significant decrease in the formation of products occurs as the concentration of terminal oxygen vacancy sites decreases by the formation of CS planes. The increase in bridged anion vacancy concentration observed in the studies above ~100 °C correlates well with the formation of misfit defects and surface domains (with regions of random or ordered anion vacancies) and a decrease above ~380 °C correlates well with the

formation of surface CS planes, as elucidated in section 3.3.

Chemical reaction studies have been carried out using allyl iodide on a previously reduced $\text{WO}_{2.95}$ system containing CS planes and also on MoO_3 (Haber *et al* 1983). In these, acrolein activity was found between operating temperatures of 300°C and $<400^\circ\text{C}$, but a drop in selectivity to $\sim 4\%$ was observed above 380°C ; whereas, $\text{W}_{18}\text{O}_{49}$ and WO_3 , WO_2 were found to be inactive. ($\text{WO}_{2.95}$ containing CS planes is obtained by high temperature reduction of WO_3 .) Although it is known that CS planes cannot be nucleated above moderate catalyst operating temperatures ($300\text{--}400^\circ\text{C}$) in WO_3 and $\text{WO}_{2.95}$ (the energy cost of creating them is quite high as shown earlier in the discussion on defect thermodynamics), the activity in this work is attributed to the ability of $\text{WO}_{2.95}$ (and Mo oxides) to rearrange their coordination polyhedra by the formation of CS planes and these CS planes are thought to be responsible for the catalytic insertion of oxygen into hydrocarbons. In these studies and of others (e.g. Stone 1975), the chemical data are not accompanied by the corresponding microstructural results and therefore direct correlations between them are not possible. The background equilibrium concentration of anion vacancies is also not considered. The thermodynamic discussions presented (section 3.5) show that oxide systems with a finite number of CS planes also contain a certain concentration of anion point defects in equilibrium with the CS planes. The role of the background vacancies and domain platelets which contain regions of anion vacancies (and precede the formation of CS planes) are important in the interpretation and attribution of activity as already explained. In MoO_3 , above $\sim 380^\circ\text{C}$ (where a drop in selectivity is observed), anion vacancies in supersaturation are annihilated by the formation of CS planes. They are in equilibrium with the background anion vacancy concentration. Other suggestions that oxidative catalysis over MoO_3 shows structural sensitivity depending on the type of crystallographic plane exist in the literature (Volta *et al* 1985). For example, oxidation of propene with (100) planes is thought to be relatively more active. This is attributed to coordinatively unsaturated sites for the selective oxidation to acrolein. However, in these studies, the nature and role of the defects remain to be probed by electron microscopy.

3.7 Multi-component (practical) oxide catalysts

3.7.1 Bismuth molybdate catalysts

Light hydrocarbons consisting of oxygen or other heteroatoms are important intermediates in the chemical industry. Selective hydrocarbon oxidation of alkenes progressed dramatically with the discovery of bismuth molybdate mixed-metal-oxide catalysts because of their high selectivity and activity ($>90\%$). These now form the basis of very important commercial multicomponent catalysts (which may contain mixed metal oxides) for the oxidation of propylene to acrolein and ammoxidation with ammonia to acrylonitrile and to propylene oxide.

Fundamental kinetic studies of butene and propylene oxidation reported in the literature show zero-order dependence on the oxygen partial pressure, indicating the participation of lattice oxygen in the oxidation reactions (McCain *et al* 1963). The history of Bi-molybdates dates from 1931. Work on them continued until 1961 (Ponec 1977), with subsequent large-scale developments of catalysts (Burrington *et al* 1981). Because of the commercial importance of these products, the mechanisms of their formation from propylene have become the subject of considerable chemical research, initially on the mixed metal (Bi–Mo) oxide system (Snyder and Hill 1989) and figure 3.13(a). However, our understanding of the complex microstructure of mixed-metal-oxide catalysts and the nature of active surface structures during the reactions remains limited.

The important work by McCain, Gough and Godin (1963) on isotopically labelled propene showed that both ends of the propene molecule would react to form the carbonyl group of the product acrolein molecule with equal probability. This has led to the now widely accepted mechanism over Bi-molybdates in which hydrogen abstraction from the alkene (by a basic surface oxygen), forming ‘allylic’ (i.e. unsaturated) species (C_3H_5) is one of the first steps in the reaction. Second, hydrogen abstraction followed by incorporation of oxygen occurs and desorption of water (H_2O) and the acrolein molecule $CH_2=CH-CHO$ (i.e. C_3H_4O) takes place (figure 3.13(b)). Elucidation of further steps in the mechanics of oxidation is difficult since the allylic intermediates quickly react and chemisorption experiments with the hydrocarbon to determine the active sites for its activation have not been possible.

3.7.2 Review of crystal structures

Detailed solid state chemical and structural work on the BiMo system reported in the literature has revealed three major phases in the active region of the phase diagram: $Bi_2Mo_3O_{12}$ (α -phase), $Bi_2Mo_2O_9$ (β -phase) and Bi_2MoO_6 (γ -phase). The activity and selectivity of the catalysts are known to depend on their microstructures. However, despite extensive chemical studies, the structural changes in Bi–Mo–O catalysts under operating conditions are not fully understood. As previously described, it is likely that conventional bulk diffraction techniques are not always useful in detecting the presence of active structures or defect layers at the catalyst surface and post reaction examination of a static catalyst is often not representative of the dynamic catalyst. *In situ* ETEM and HRTEM methods are playing a key role in increasing our understanding of complex catalytic reactions (Gai 1983). α - $Bi_2Mo_3O_{12}$ has a monoclinic unit cell, space group $P2_1/C$; with $a = 7.68 \text{ \AA}$, $b = 11.491 \text{ \AA}$, $c = 11.929 \text{ \AA}$ and $\beta = 115.4^\circ$ (Van den Elzen and Rieck 1973) and is related to the scheelite (AMo_4 ($A \equiv Bi$) or $CaWO_4$) structure. The α -phase contains one cation vacancy for every two Bi^{3+} ions and can be written as $Bi_{2/3}j_{1/3}MoO_{4-x}$ where the j are vacancies. This indicates that the respective oxygen sites should also be vacant to achieve a charge balance. The presence of anion vacancies may lead to higher oxygen mobility.

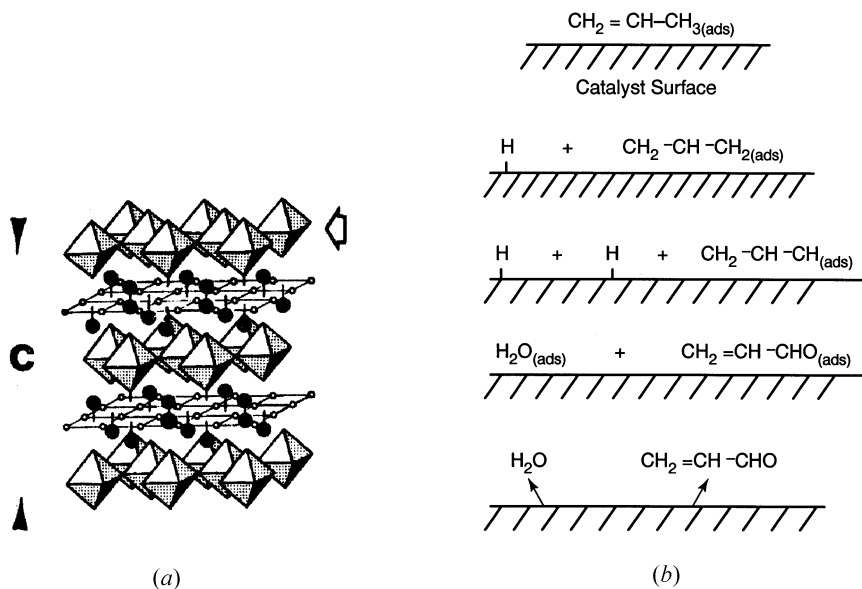


Figure 3.13. (a) Structural model for a Bi_2MoO_6 catalyst (γ -phase) with MoO_6 octahedra (arrowed) between Bi_2O_2 units: Bi, full circles; O, open circles. (b) Schematic diagram of the reaction steps in C_3H_6 oxidation.

The structure of $\gamma\text{-Bi}_2\text{MoO}_6$ is orthorhombic (space group $Pca2_1$) and is similar to that of the natural mineral koechlinite, with $a = 5.487 \text{ \AA}$, $b = 16.22 \text{ \AA}$ and $c = 5.506 \text{ \AA}$ (van den Elzen and Rieck 1973). It consists of layers of $(\text{MoO}_2)^{2+}$ and $(\text{Bi}_2\text{O}_2)^{2+}$ units interconnected by intermediate layers of O^{2-} ions (figure 3.13(a)). The O^{2-} ions and the $(\text{MoO}_2)^{2+}$ units form slightly distorted $(\text{MoO}_4)^{2-}$ octahedra. The intermediate oxygen layers can facilitate rapid transport for O^{2-} ions.

The structure of $\text{Bi}_2\text{Mo}_2\text{O}_9$ is complex, consisting of a large unit cell with $a = 11.946 \text{ \AA}$, $b = 10.759 \text{ \AA}$, $c = 11.876 \text{ \AA}$ and $\beta = 90.15^\circ$, space group $P2_1C$ and eight formula units; attempts have been made to solve the structure (Van den Elzen *et al* 1975): in one model, all the MoO_4 units are considered equivalent, whereas the other considers two types of MoO_4 . Furthermore, the latter work illustrates various surface enrichments depending on whether the compounds are Bi-rich or Mo-rich. We now examine these in a series of *in situ* electron microscopy, HRTEM and chemical experiments.

3.7.3 Experimental procedures

3.7.3.1 Catalyst surface structures and redox reactions

Bismuth molybdates are prepared either by solid state reactions of Bi_2O_3 and MoO_3 in stoichiometric proportions or by co-precipitating aqueous bismuth nitrate and molybdic acid or ammonium paramolybdate solutions. Co-precipitated catalysts are normally used in catalysis. The powders have surface areas ranging from 5–30 $\text{m}^2 \text{g}^{-1}$. The preparations normally contain small amounts of unreacted MoO_3 (up to a few %) and other oxides. The existence of excess MoO_3 in industrial bismuth molybdate catalysts is well known. EDX/WDS analyses of the nominal compositions show significant concentrations of cation vacancies (and presumably anion vacancies) in the compounds.

Structural investigations by HREM of the γ -phase reveals the presence of the majority γ -phase and small amounts (~ 1 –2%) of the tetragonal phase γ' , with $a = 3.95 \text{ \AA}$, $c = 17.21 \text{ \AA}$ and space group D_{2d}^{11} (Blasse 1966) and MoO_3 . An HRTEM lattice image of the γ -phase indicating a layered structure in (100) projection is shown in figure 3.14 with the electron diffraction pattern in the inset. An SEM image of the co-precipitated powder illustrating the fine grain structure of the catalyst is given in inset (c). The fine grains are all crystalline. The HRTEM image, a computed model and the structure of the tetragonal γ' phase are shown in figure 3.15.

3.7.4 Dynamic electron microscopy in controlled environments

An isotherm of C_3H_6 conversion on γ is shown in figure 3.16, where the products are monitored at $\sim 450^\circ\text{C}$. The figure shows various stages of activity and the activity begins to decrease after ~ 1 hr. A drop in the selectivity to acrolein is also observed above $\sim 450^\circ\text{C}$. Sample C, for example, shows the presence of γ , and a structure with dimensions $8.4 \text{ \AA} \times 10.8 \text{ \AA}$. Sample D has more metallic Bi and reduced Mo-oxides.

The corresponding *in situ* ETEM studies in C_3H_6 on $\gamma\text{-Bi}_2\text{MoO}_6$ catalyst powder samples containing excess MoO_3 reveal a precipitate (or domain) superstructure at an operating temperature of $\sim 400^\circ\text{C}$, with spacings of $8.4 \text{ \AA} \times 10.8 \text{ \AA}$ in (001) grains. No extended CS plane defects are observed. The reaction sequence for propylene is shown in figure 3.17: (a) the sample at room temperature; (b) the corresponding diffraction pattern; (c) the sample in propylene at $\sim 400^\circ\text{C}$, with precipitate defects or domain-like features nucleated at the surface (arrowed with strong black–white contrast), in the reaction environment; and (d) the corresponding diffraction pattern, showing the superlattice. The surface domains can be stabilized by annealing and detailed EDX/WDS indicates the presence of a Bi:Mo ratio of $\sim 1:1$ (e) and the presence of Bi vacancies in the domains. The superlattice spacings observed in ETEM are consistent with the lattice dimensions of a $\text{Bi}_2\text{Mo}_2\text{O}_9$ phase prepared separately, shown in an HRTEM image (figure 3.18(a)), with a (101) diffraction pattern (figure 3.18(b)).

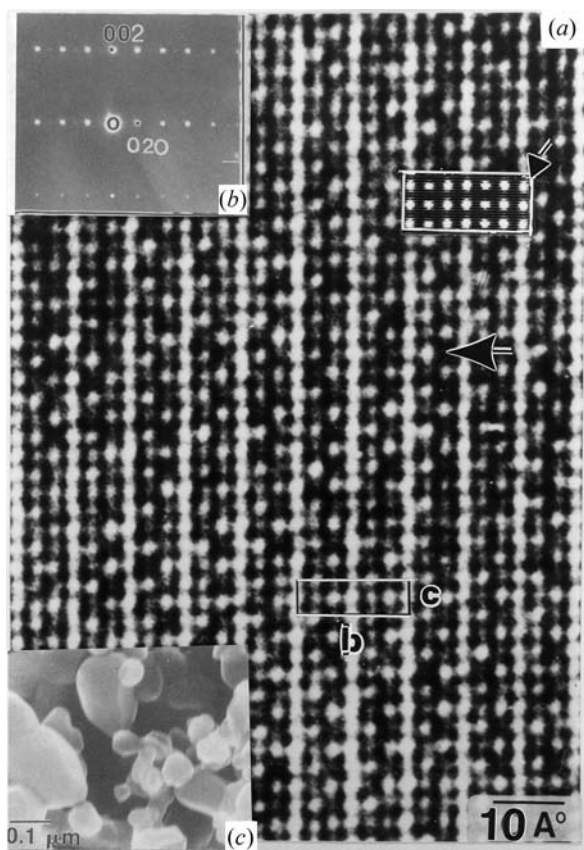


Figure 3.14. An HRTEM lattice image of the γ -phase in (100) showing a layered structure, with an ED image and the computed structure shown in the insets. Inset (c) shows an SEM image of the catalytic crystals (after Gai 1983).

The superlattice can be indexed as the (101) β -phase. The HRTEM in figure 3.18(a) shows a contrast (circled and arrowed) indicative of cation point defect clusters.

These results suggest that the (101) superstructure observed on the (001) β -phase at the catalyst's operating temperature is closely related to $\text{Bi}_2\text{Mo}_2\text{O}_9$. A quantification of the microanalysis of the β -preparation shows a Bi-deficiency. Similar results are observed in the reaction of the α -phase in propylene. In a $\text{C}_3\text{H}_6\text{-O}_2$ mixture under working conditions both phases show the presence of this superstructure similar to the β -structure. The ETEM results are consistent with XPS and Raman data which show that the surface structure of the active bismuth molybdate is close to the β -phase and that the β -phase is more active (Matsurra *et al* 1980, Burrington *et al* 1983). In these studies dramatic increases in the activity

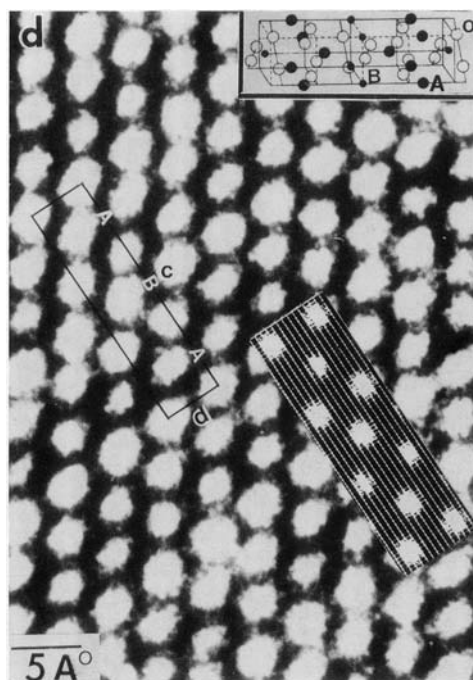


Figure 3.15. An HRTEM image of the tetragonal γ' -phase with a simulated image and structure inset.

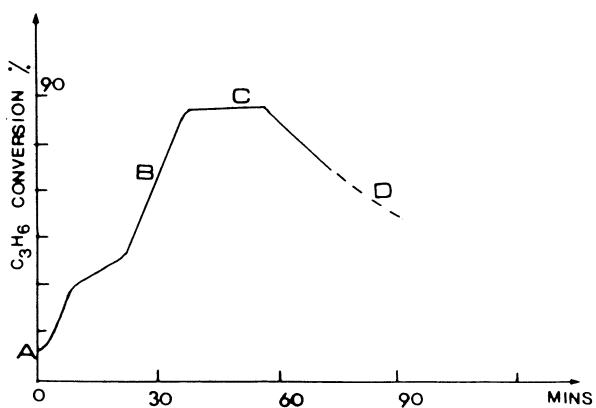


Figure 3.16. Isotherm of the conversion on a γ -phase catalyst. Sample C showed the presence of the $Bi_2Mo_2O_9$ phase.

have been observed on the addition of $\sim 4\%$ MoO_3 (atom%, with respect to Mo) to the co-precipitated sample. *In situ* ETEM results thus reveal active phase

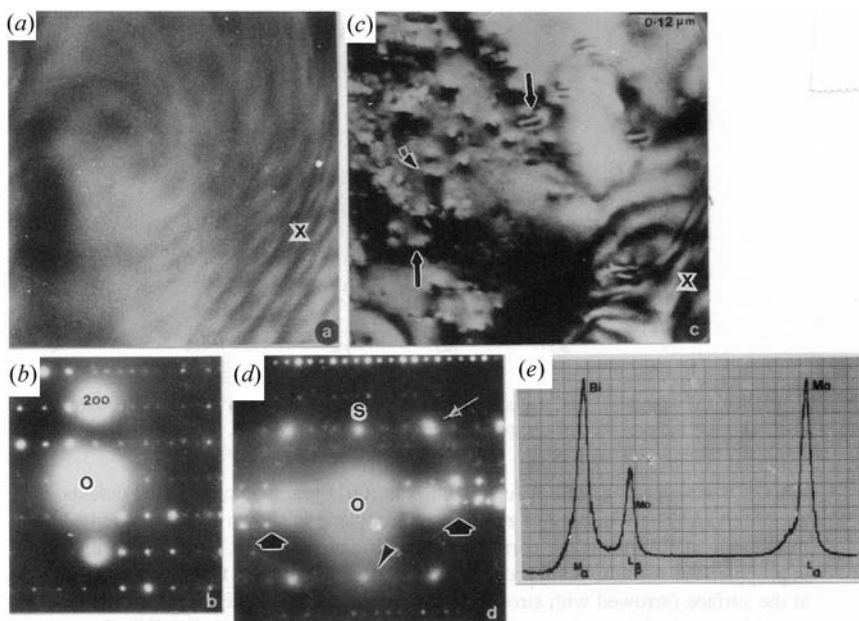


Figure 3.17. Dynamic catalytic reduction sequence of a (001) γ -phase catalyst with excess MoO_3 in C_3H_6 : (a) the fresh catalyst; (b) the ED pattern; (c) the sample at $\sim 400^\circ\text{C}$ showing a 'domain' structure at the surface (arrowed); and (d) the corresponding ED pattern showing a superlattice close to the (101) $\text{Bi}_2\text{Mo}_2\text{O}_9$ β -phase; (e) WDS of 'domains'. The quantification indicates a Bi:Mo ratio of 1:1 and Bi vacancies (after Gai 1983, 1985, 1992).

formation under operating conditions. Catalysts richer in Bi or fully oxidized (stoichiometric) catalysts show lower activity and selectivity. Initial activation of the catalysts by a slight reduction in hydrogen enhances the activity and selectivity of the catalyst, presumably by creating anion point defects and maintaining the oxidation state. The pertinent question is why do complex catalysts exhibit specific surface enrichments under working conditions. This may be related to the energetically favourable low energy configuration discussed earlier.

There has been some discussion in the literature described below about the nature of the active sites. From chemical studies, lattice oxygen is removed for the hydrocarbon oxidation, creating anion vacancies. From tracer studies using labelled γ -bismuth molybdates, it is suggested that lattice oxygen participates in the reaction. It is believed that the hydrocarbon and oxidation adsorption sites may be different on the molybdates, i.e. catalyst reduction and reoxidation occur at different sites. Differences of opinions exist, however, as to the nature of the sites for hydrocarbon chemisorption and oxygen insertion (Burlington *et al* 1983, Sleight 1977, Haber *et al* 1973): it is suggested that hydrocarbon chemisorption

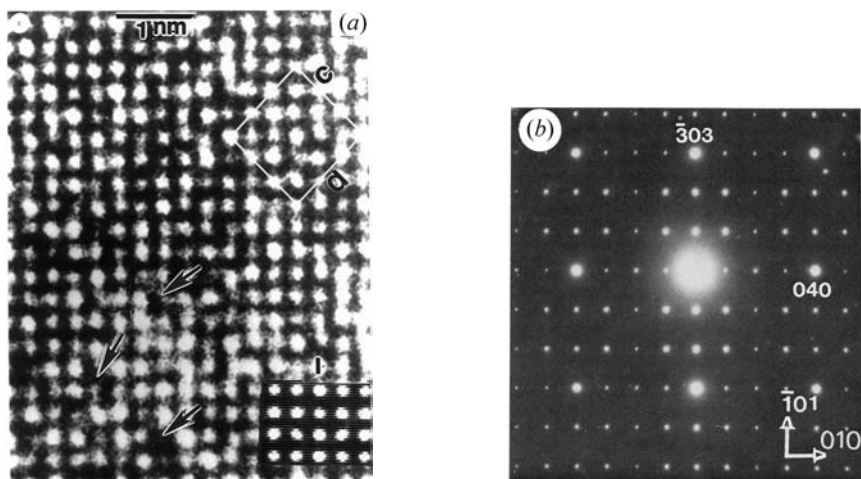


Figure 3.18. (a) An HRTEM image of $\text{Bi}_2\text{Mo}_2\text{O}_9$ (β -phase) catalyst with an image contrast indicative of cation point defect clusters (arrowed). (b) (101) ED image with dimensions consistent with those in the superstructure in figure 3.17(d). The data suggest that the superstructure in the *in situ* studies in figure 3.17(d) is similar to the β -structure.

occurs via Mo units, with oxygen insertion at Bi sites, whereas it involves Bi units, with Mo units participating in the insertion of gaseous oxygen in another model. In addition, it is suggested that H-abstraction occurs at the Bi sites and Mo units participate in the hydrocarbon chemisorption and oxygen insertion. *In situ* ETEM observation of an ordered surface phase with a composition close to β , at operating temperatures is consistent with the enhanced catalytic activity in the presence of β found in chemical studies. From this discussion, it can be seen that the β -phase has a favourable balance of chemisorption sites (Mo) and hydrogen abstraction sites (Bi and vacancies). Vacancies may be important in the catalysis of hydrocarbons. Indeed, scheelite phases (α and also Pb-doped α) are found to be the most active when they contain vacancies and Bi on A-sites; hydrocarbon activity and the number of active sites correlate well with the number of point defects (Sleight 1977).

From HRTEM studies, it is proposed that the majority of the bismuth molybdate phases can be derived from the fluorite structure, in which both the cation and anion vacancies can be accommodated within the fluorite framework (Buttrey *et al* 1987). Several industrial processes containing multicomponent bismuth molybdates may suffer loss of Mo oxides by volatilization under operating conditions, resulting in the loss of catalytic activity. Monitoring the catalyst microstructure using EM is therefore crucial to ensuring the continuity of these catalytic processes.

3.8 Iron molybdates in methanol oxidation reactions

Methanol is a feedstock for a variety of important organic products. It is converted by catalytic processes into formaldehyde. Formaldehyde (HCHO) is one of the most important heavy chemicals with uses in cross-linking agents for thermosetting resins and urea-formaldehyde resins. One of the commercial processes for the selective oxidation of methanol (CH_3OH) to formaldehyde uses a catalyst system which is a mixture of ferric molybdate and molybdenum trioxide (Triffiro *et al* 1979) (the other being silver metallic catalysts). Ferric molybdate ($\text{Fe}_2\text{Mo}_3\text{O}_{12}$) is the active phase in the system for the oxidation catalysis. The MoO_3 in the system acts as a reservoir giving an adequate surface Mo concentration to maintain the selectivity and to provide an increased surface area. Ferric molybdate is more active than MoO_3 since unlike MoO_3 , all its crystallographic faces are active. Methanol oxidation over $\text{Fe}_2\text{Mo}_3\text{O}_{12}$ is of the redox type, proceeding via the release of lattice oxygen. This results in a partially reduced catalyst surface. Differences of opinions exist regarding the rate-determining step in the methanol oxidation reaction, e.g. reoxidation of the surface, desorption of products (Pernicone 1974); and breaking of the C–H bond (Sleight *et al* 1982) have all been mentioned. Detailed work on the complex chemical and microstructural composition of the system has been reported using dynamic ETEM under controlled methanol environments (Gai and Labun 1985, Taylor *et al* 1986).

Iron molybdates are prepared by precipitating ammonium molybdate and ferric chloride solutions. The precipitate is calcined at $\sim 400^\circ\text{C}$ and dried in air for longer periods to obtain the pure ferric molybdate phase. Kinetic studies of the selective oxidation of methanol reported in the literature confirm that the initial chemisorption of methanol is dissociative (involving the breaking of O–H bonds), forming surface methoxy (the organic CH_3O) groups. These studies also show that the rate-limiting step is the breaking of a C–H bond of the methyl group to form adsorbed formaldehyde and that Fe acts as a stabilizer in the reactions.

$\text{Fe}_2\text{Mo}_3\text{O}_{12}$ is monoclinic: $a = 15.7 \text{ \AA}$, $b = 9.23 \text{ \AA}$, $c = 18.2 \text{ \AA}$ and $\beta = 125.1^\circ$ (Chen 1979). An HRTEM image and the atomic projection are shown in figure 3.19. In dynamic ETEM studies of a ferric molybdate catalyst powder in methanol environments, the molybdate is observed to decompose into aggregates with ordered phases of (a) $\beta\text{-FeMoO}_4$, (b) $\alpha\text{-Fe}_2\text{O}_3$, (c) a spinel composition of the type Fe_2MoO_4 or, sometimes, into mixtures of these. Prolonged reaction reveals small amounts of $\alpha\text{-Fe}$. Some of the redox reactions are shown in figure 3.20. The formation of a new phase during the methanol reaction with additional rings in the ED pattern are shown in figure 3.20(a). The lattice spacing measurements, image computations (inset) and EDX composition analysis indicate the formation of $\beta\text{-FeMoO}_4$, which is monoclinic, $a = 10.29 \text{ \AA}$, $b = 9.39 \text{ \AA}$, $c = 7.07 \text{ \AA}$ and $\beta = 106.1^\circ$. The $\alpha\text{-Fe}$ ED pattern superimposed on the diffraction of $\beta\text{-FeMoO}_4$ crystals after prolonged reduction is shown in figure 3.20(b). The ED patterns from several regions of the sample also show the

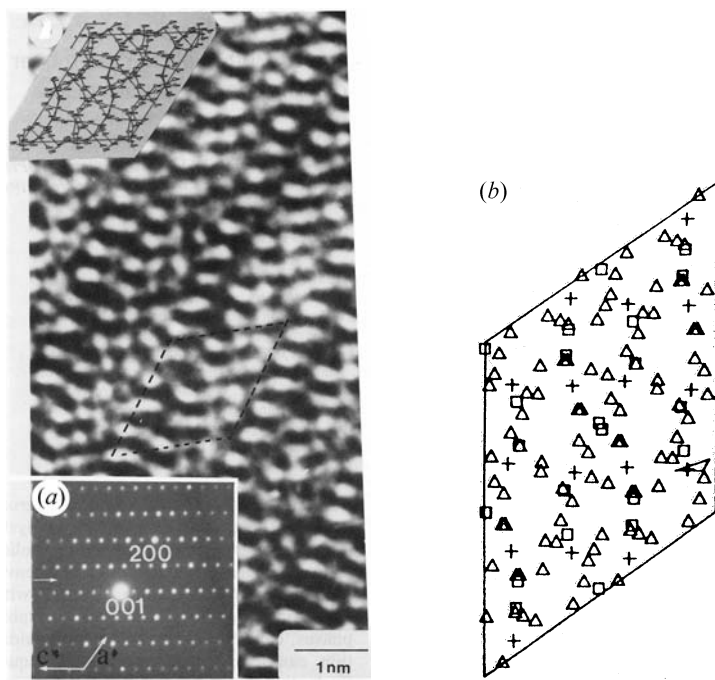


Figure 3.19. (a) An HRTEM image of a (010) $\text{Fe}_2\text{Mo}_3\text{O}_{12}$ catalyst, with ED pattern; (b) the projection of atoms in (010): +, Fe; \square , Mo; Δ , O).

presence of $\alpha\text{-Fe}_2\text{O}_3$. The microstructural data show that two or more possible reduction mechanisms occur simultaneously. The presence of extended defect structures (described in section 3.3) are observed in MoO_3 under these operating conditions. In addition, the formation of the $\text{Mo}_{17}\text{O}_{47}$ type phase is observed in the catalyst mixture.

3.9 Vanadium phosphate (V–P–O) catalysts for butane oxidation technology: the elucidation of active sites by *in situ* electron microscopy

Complex vanadium–phosphorus–oxide catalysts are the most successful industrial catalysts for the selective oxidation of *n*-butane to maleic anhydride (MA) with uses in tetrahydrofurans (THF) and polyurethane intermediates. A schematic diagram of the reaction is shown in figure 3.21(a). These catalysts have been studied extensively (e.g. Centi *et al* 1993, Bordes 1987). In the selective catalysation of *n*-butane to MA, the ‘best active phase’ in the V–P–O system is identified as the vanadyl pyrophosphate, $(\text{VO})_2\text{P}_2\text{O}_7$ (hereafter

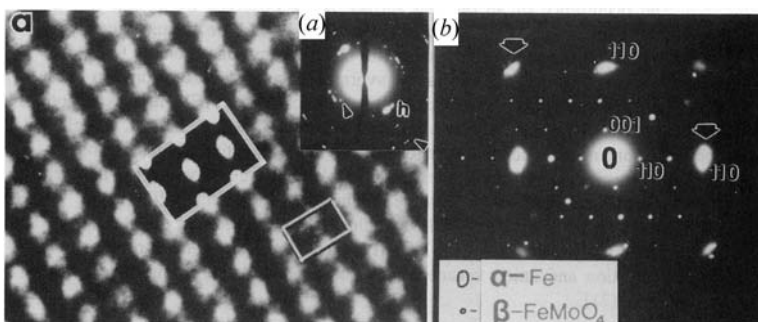


Figure 3.20. (a) β -FeMoO₄ formed in methanol oxidation reaction over Fe₂Mo₃O₁₂ with the larger insets showing the simulated image and an outline of the unit cell and ED are inset. (b) α -Fe (large reflections) formed in prolonged reduction of (a), superimposed on the β -FeMoO₄ ED pattern, with the orientation relationship [110] β -FeMoO₄ parallel to [001] α -Fe.

referred to as VPO), with active centres located at the exposed (010) planes, described later. There are also some claims that the active phase is a combination of VPO and VOPO₄ or a P-rich phase. VPO catalysts have been examined extensively by international groups (Centi 1993) using chemical studies and bulk diffraction techniques (e.g. XRD). Most of the studies, however, are post-reaction examinations of static samples which are not the same as dynamically reacting samples under operating conditions as described earlier. Therefore considerable uncertainty can exist as to the nature of the active sites in the butane oxidation reaction. Recently, the selective catalysation of butane over VPO catalysts under operating conditions has been directly probed for the first time using atomic-resolution ETEM. The dynamic ETEM studies reveal a novel glide shear mechanism which explains the release of catalyst structural oxygen and the preservation of active Lewis acid sites without the collapse of the catalyst structure (Gai *et al* 1995, Gai 1997). This mechanism is important for the continuing operation of catalysts in oxidation catalysis.

The active VPO phase is usually prepared by the calcination of the precursor phase, vanadium hydrogen phosphate hemihydrate (VO)HPO₄·0.5H₂O (hereafter referred to as VHPO). Transforming the precursors to active catalysts is of fundamental importance. The structural relationship between the two phases, VHPO and VPO, is shown in figures 3.21(b) and (c), respectively. Figure 3.21(d) shows the three-dimensional structure of VPO. The (201) oxygen plane is indicated. The structure of VHPO consists of vanadyl hydrogen phosphate layers stacked along the *b*-axis which are held together by interlayer hydrogen bonding (Torardi and Calabrese 1984). It is orthorhombic, with *a* = 7.416 Å, *b* = 5.689 Å and *c* = 9.592 Å. The layers contain face-sharing VO₆ octahedra. One of the face-sharing oxygens comes from the water molecule (H₂O) bridging the two

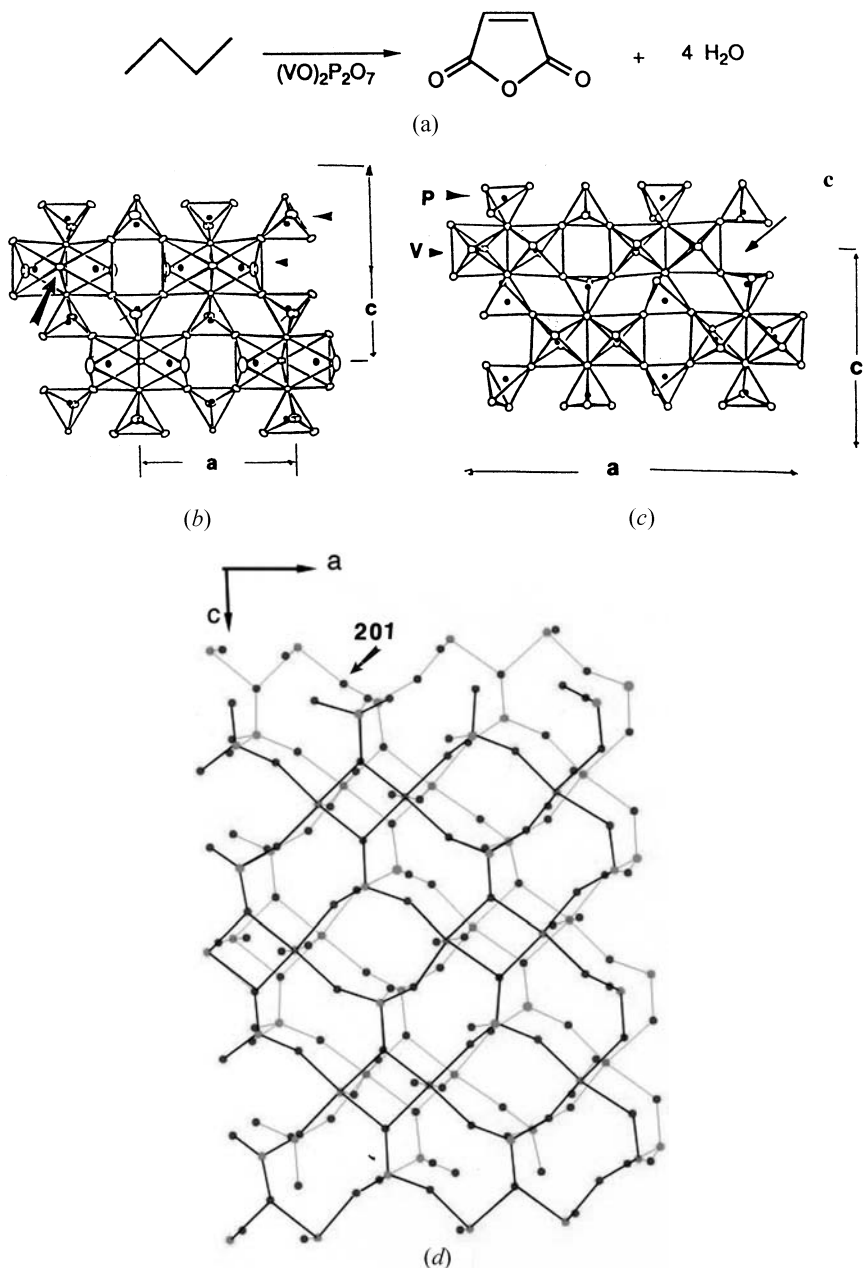


Figure 3.21. (a) Butane selective oxidation over VPO to maleic anhydride ($C_4H_2O_3$). Structures of (b) $VOHPO_4 \cdot 0.5H_2O$ (VHPO) and (c) $(VO)_2P_2O_7$ (VPO). The $[201]$ direction is arrowed. V-octahedra and P-tetrahedra are indicated at V and P, respectively. (d) A three-dimensional network of (010) VPO. $[201]$ is arrowed.

vanadium atoms and is located *trans* to the vanadyl (V=O) oxygen atoms.

It is generally accepted that the structure of VPO is orthorhombic, with $a = 16.694 \text{ \AA}$, $b = 7.735 \text{ \AA}$ and $c = 9.588 \text{ \AA}$ (Gorbunova and Linde 1979). Unlike VHPO which has a layered structure, VPO is covalently bonded in the three crystallographic dimensions. Pairs of edge-sharing VO_6 octahedra are connected along the b -axis to form double chains of VO_6 octahedra sharing opposite oxygen corners. Along the chains, the V-O bonds alternate with short-long distances, namely, 1.6 and 2.3 \AA . Within the edge-shared octahedral pairs, the vanadyl bonds are oriented in an up-down arrangement along the b -direction. Pyrophosphate groups link the double chains into a three-dimensional network (figure 3.21(d)).

3.9.1 Synthesis and characterization of VPO catalysts

The procedures for synthesizing the catalysts have a marked effect on their activity. The active VPO catalyst phases are produced as follows.

- (1) In organic media, the process involves the reduction of V_2O_5 with isobutyl alcohol, benzyl alcohol and addition of orthophosphoric acid.
- (2) In an aqueous media the process involves the reduction of V_2O_5 and HCl, with orthophosphoric acid and water.
- (3) VOPO_4 is reduced through the formation of crystallographic shear planes.

For high performance industrial catalysts capable of activating butane, organic media are used for the synthesis of VPO, which results in a large area of active (010) orientations. VPO catalysts synthesized in organic media are therefore used in the present chapter to elucidate dynamic butane catalysis by *in situ* ETEM. The other methods of preparation can be multi-phasic, which can result in the modification of the reactivity of the catalyst (Centi 1993, Kiely *et al* 1996).

3.9.1.1 Precursor to active catalyst transformation: VHPO to active VPO catalysts and dynamic electron diffraction

In the dynamic precursor transformation experiments using ETEM described in figure 3.22, single crystals of VHPO grown from an aqueous medium are used for simplicity. The crystals, a few millimetres (mm) in size, are grown hydrothermally in a sealed gold tube, under 3 kbar pressure by heating a mixture of 1.05 g VO_2 , 0.28 g of V_2O_3 and 8 ml of 3 M H_3PO_4 at 500 °C for 12 hr and slowly cooling the reaction (Gai and Torardi 1996).

Dynamic atomic-resolution ETEM and diffraction studies provide fundamental insights into the catalyst precursor transformation mechanism. The studies reveal that the temperature regimes are critical to the formation of active catalysts. They show that the nature of the VHPO \rightarrow VPO transformation is topotactic. Topotaxy is defined as the conversion of a single crystal to a pseudomorph

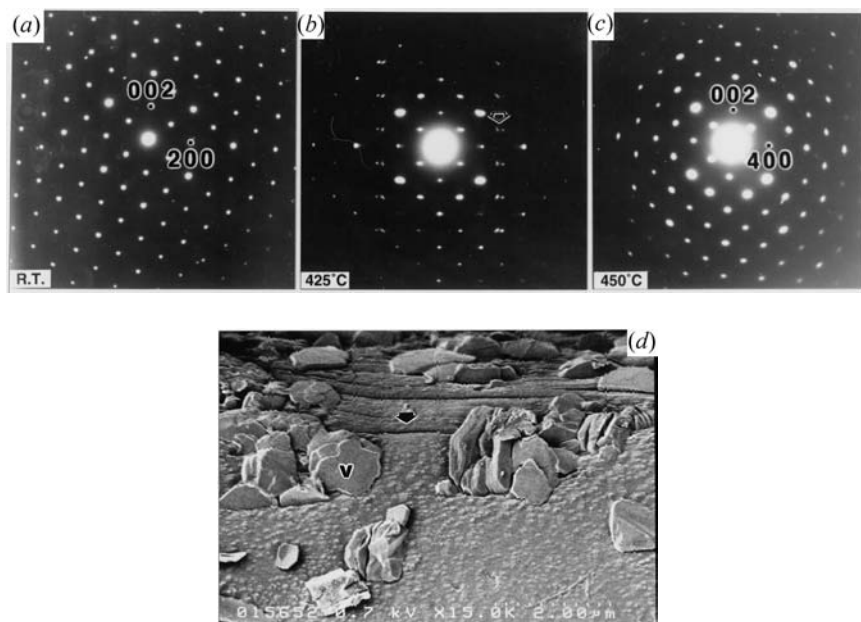


Figure 3.22. Dynamic electron diffraction (ED) image of the topotactic transformation of the VHPO precursor to active VPO catalyst in N_2 : (a) (010) VHPO at room temperature; (b) physical mixture of VHPO and VPO at 425 °C; (c) final VPO in the (010) active plane; and (d) VPO microcrystals (V) and cracks (arrowed) on the precursor surface.

containing one or more product and that these products have a definite crystallographic relationship with the parent structure (Dent *et al* 1962).

In situ atomic-resolution ETEM studies of VHPO precursors performed initially in nitrogen environments show that the precursor structural transformation begins at ~ 400 °C, and a mixture of the precursor and the pyrophosphate exists at ~ 425 °C. At 450 °C, most of the conversion to VPO takes place. Atomic-scale studies reveal no amorphous phases during the transformation and the atomic periodicity is maintained throughout. Figures 3.22(a)–(c) show dynamic electron diffraction patterns taken during the transformation of the precursor to the active VPO. No other phases are identified in the nitrogen or in butane environments. *In situ* data from the (001) faces show microcracks separating VPO microcrystals (figure 3.22(d)).

The diffraction and ETEM images indicate that significant changes in the unit-cell dimensions accompany the phase transformation. As VHPO loses water and OH groups, the layers condense into the three-dimensional VPO structure, shown in the schematic diagram in figure 3.23. The resulting microstructure appears to be due to the disintegration of the parent crystal topotactically. Accommodation of the unit-cell changes occur via slightly misoriented VPO

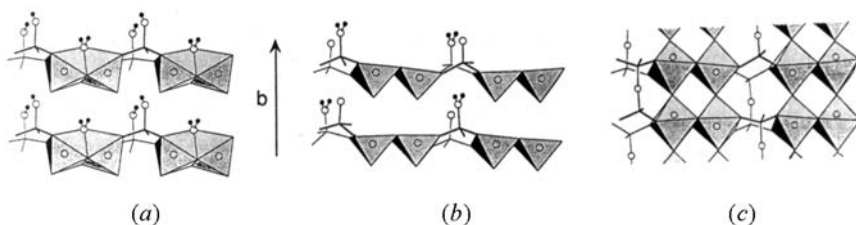


Figure 3.23. Model for topotactic transformation of the precursor to the active catalyst: (a) face-sharing VO₆ octahedra and H-phosphate tetrahedra (H atoms are shaded); (b) removal of bonded water (resulting in VO₅ which rotate, and transfer of H-atoms from H-phosphates); and (c) final reconnected VPO after removal of water.

microcrystals in the *ac*-plane and via cracks due to the reduction along the *b*-axis. Some of the cracks may result from the escape of steam when the crystals lose water. The formation of the microcrystals and the porosity are manifest in an increased surface area for the active VPO. The transformation is consistent with the topotactic phosphorus inversion mechanism shown in figure 3.23. Figure 3.23(a) shows two adjacent layers in the precursor with pairs of face-sharing VO₆ octahedra. One of the face-sharing oxygens belongs to an H₂O molecule. Vanadium forms its short vanadyl bond with O trans to oxygen atom of this H₂O. The loss of bonded water molecules from the vanadyl pairs results in edge-shared VO₅ groups, and a decrease in the interlayer spacing. These groups pivot or turn about the shared edge to form a configuration with approximately parallel V=O bonds (figure 3.23(b)). This motion expands the layers along the unit-cell direction resulting in an increase of ~12% relative to the starting VHPO. Condensation of the hydrogen phosphate groups, via proton transfer, H₂O removal and inversion of P atoms to form pyrophosphate bonds on either side of a layer allows the sheets to fully condense into a three-dimensional VPO network structure. This causes contraction of ~32% along the *b*-direction. Figure 3.23(c) shows the final interconnected structure of VPO.

During the activation of VHPO, very small concentrations of minor VOPO₄ phases are occasionally present and these minor amounts may be below the XRD detection limit. This has implications in understanding the redox couple active in the butane oxidation reaction. These aspects are discussed later.

3.9.1.2 *The nature of active sites elucidated by in situ atomic-resolution electron microscopy*

An SEM image of a rosette-shaped, well-calcined and activated VPO catalyst is shown in figure 3.24(a). VPO catalyst structure at room temperature and the corresponding ED patterns are shown in figures 3.24(b) and (c), respectively.

The catalysts reacted in *n*-butane and other reducing environments have

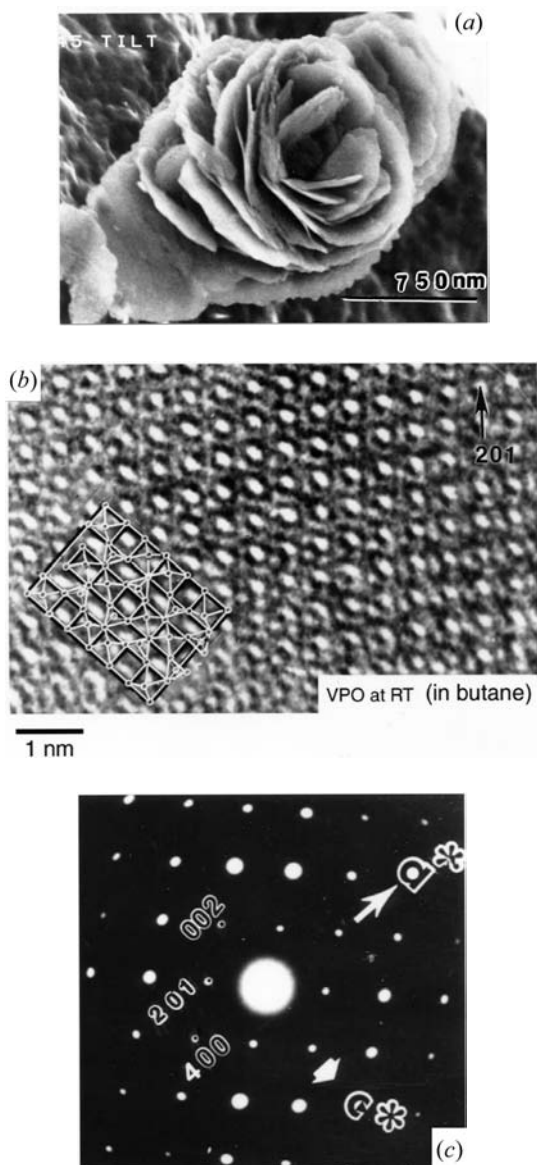


Figure 3.24. (a) An SEM image of rose-shaped VPO catalysts; (b) *in situ* atomic-resolution ETEM of well-ordered (010) VPO in butane at room temperature (inset: model of the structure); (c) ED pattern of (b): 002, 400 reflections are shown and 201 are arrowed (after Gai *et al*, *Science*, 1995).

shown evidence for surface structure modifications accompanied by two sets of symmetry-related extended defects along the $\langle 201 \rangle$ directions. *In situ* ETEM data of the dynamic reaction of VPO (010) in *n*-butane at room temperature and at the operating temperature ($\sim 390^\circ\text{C}$) after ~ 2 min are shown at the atomic level in figures 3.25(a) and (b) respectively. Figure 3.25(c) shows an enlarged image of the reacted sample. It reveals dislocated lattice with terminating lattice planes and the presence of partial dislocations (defects) in the (201) lattice planes.

The two partial dislocations, P1 and P2 (arrowed), are close to the catalyst surface (at S shown in profile, with the projection of the structure along the beam direction), bounding a stacking fault associated with them. The two symmetry-related (201) planes are indicated on the dynamic atomic image. The corresponding dynamic electron diffraction of the reacting VPO is shown in figure 3.25(d). It reveals diffuse streaks along $\langle 201 \rangle$ which are indicative of the structural disorder associated with the defects in the (201) planes. They provide further important evidence of the disorder in the (201) planes. This means that anions in (201), between vanadyl octahedra and phosphate tetrahedra, are involved in the alkane oxidation reaction. Furthermore, the disorder due to the anion loss is revealed only in the (201) lattice planes, thus excluding all other planes in the crystal structure. ETEM studies show that the defect density increases with time. The two sets of symmetry-related extended defects along the $\langle 201 \rangle$ directions in the ETEM diffraction contrast are shown in figure 3.25(d) and one set is shown in high resolution in figure 3.25(e) after a few hours of reduction.

To determine the character of the dislocations and the displacement vector \mathbf{b} under dynamic reaction conditions, the $\mathbf{g} \cdot \mathbf{b}$ criteria are used. The dislocation contrast is mapped in several reflections (\mathbf{g}) by tilting the crystal, including the reflection in which the dislocation is invisible, i.e. $= 0$ when \mathbf{b} is normal to the reflecting planes. Careful analysis (figure 3.25(f) and (g) of defects from the same crystal area (c)) shows that the displacement vector lies in the plane of shear (i.e. parallel to the shear plane), consistent with glide shear, with no lattice collapse. These criteria show the displacement vector to be $\mathbf{b} = \pm \langle a/7, 0, c/4 \rangle$.

The dynamic observations of the extended defects along (201) can be understood as follows. During the dynamic reduction of VPO in *n*-butane at the operating temperature ($\sim 390^\circ\text{C}$), anion vacancies are created along the $\langle 201 \rangle$ directions at the catalyst surface by the loss of lattice oxygens between vanadyl octahedra and phosphate tetrahedra (figure 3.26(a)). Similar structural changes are observed in VPO reduction with CO, N₂ ruling out hydroxyl groups. (The same defects are also observed at different gas pressures.) The reduction of the catalyst surface introduces misfit strains at the interface between the reduced surface and the underlying unreduced bulk. To accommodate the misfit strains at the interface, the crystal simply glides along $\langle 201 \rangle$ generating extended defects by this novel glide shear mechanism. These defects form close to the surface and their nature is thus such that they accommodate the shape misfit between the reduced surface layers and the remainder of the crystal. These are shown schematically for one layer of VPO in figure 3.26. Figure 3.21(c) shows the

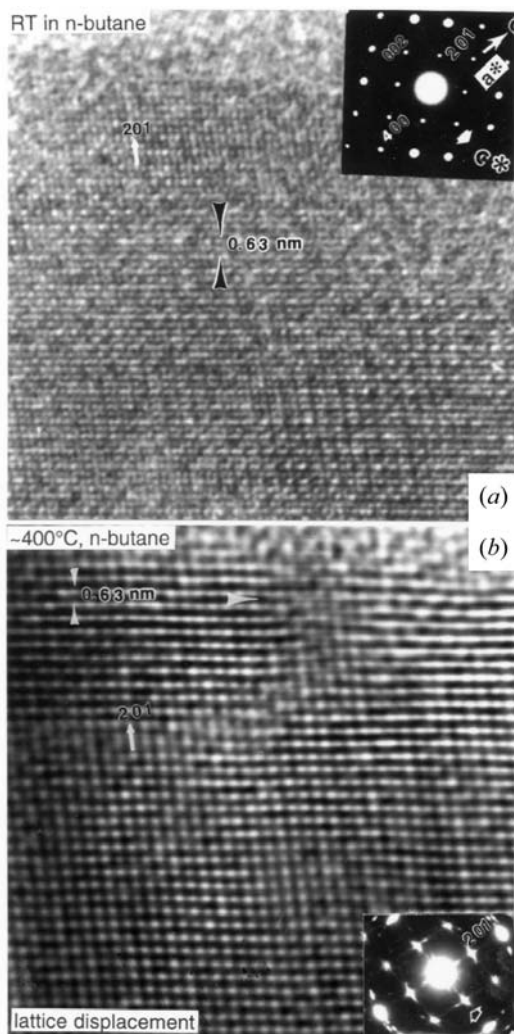


Figure 3.25. *In situ* catalysis: (a) fresh VPO catalyst; (b) dynamic real-time formation of atomic scale catalyst restructuring in butane after ~ 2 min at $\sim 400^\circ\text{C}$; (c) enlarged image of (b) showing two sets of partial dislocations; and (d) dynamic image of two sets of extended defects along symmetry-related $\langle 201 \rangle$ in (010) VPO after reduction in butane for several hours (diffraction contrast). The inset shows the defect nucleation near the surface. Careful defect analysis shows them to be formed by novel glide shear. (e) One set of the defects in high resolution (f) and (g) show diffraction contrast images of defects in 201 and $20\bar{1}$. (After Gai *et al*, *Science*, 1995 and 1997 *Acta Cryst. B* **53** 346.)

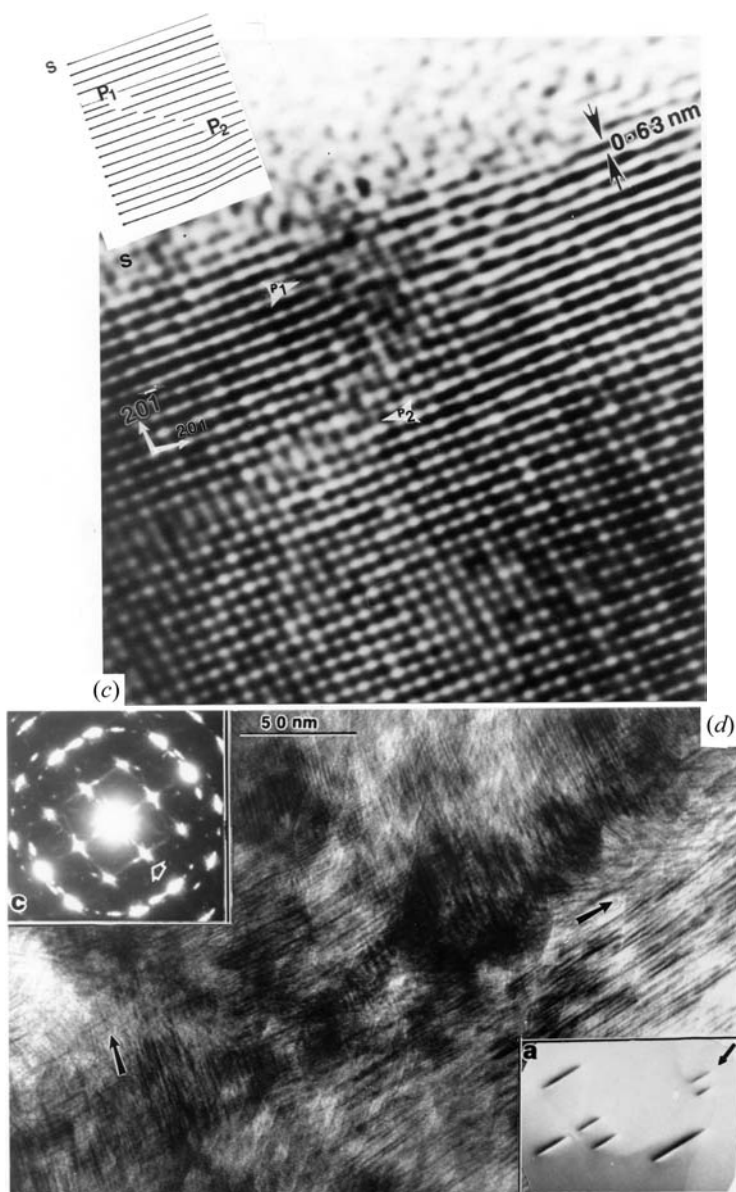


Figure 3.25. (Continued)

projection of the (010) VPO structure; figure 3.26(b) shows the accommodation of non-stoichiometry by glide-shear (idealized model). The resulting structure with extended glide plane defects is a disordered structure of VPO differing only in its

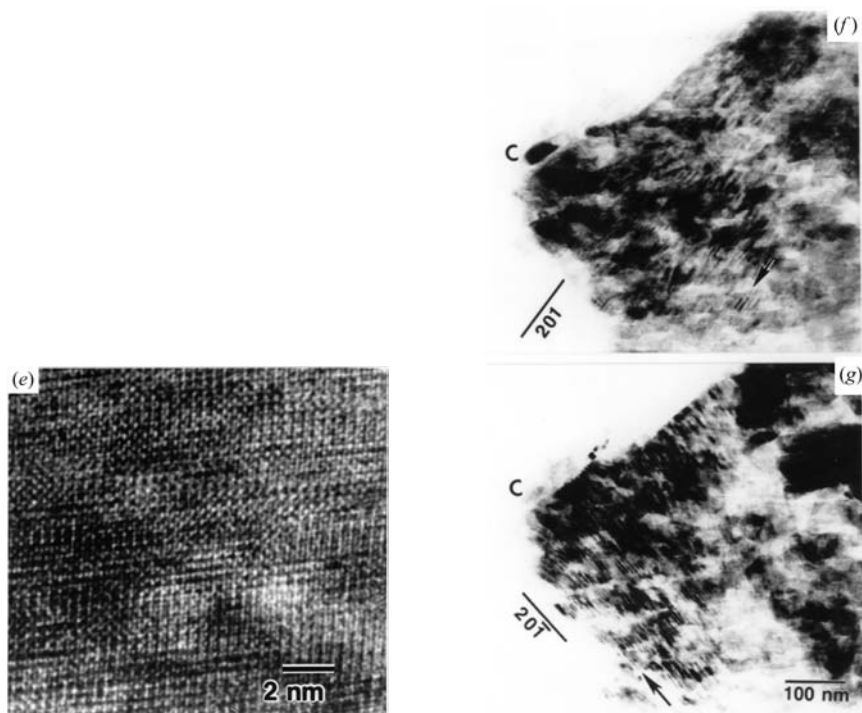


Figure 3.25. (Continued)

local symmetry and thus it does not affect the bulk crystalline structure of VPO, i.e. the VPO lattice does *not* collapse. Figure 3.26(c) shows a three-dimensional model of the glide shear plane defect. Figures 3.26(d) and (e) show schematic diagrams of the surface anion vacancies and of crystal glide, respectively. In the latter, two parts of the crystal simply glide creating glide defect regions with glide direction (g) and glide plane (g -plane). Similar glide shear defects are observed in N_2 and steam. Figure 3.26(f) shows the model used to interpret the glide shear defects close to the surface.

On exposure to the reducing gases, VPO loses oxygens, leaving vacancies along (201) between the V and P columns which are positively charged and they increase the strength of the surface Lewis acid sites. They are readily available for hydrocarbon activation (they can accept electrons from the alkane molecule) and for catalyst regeneration in the air of the gas stream. In partial oxidation with 1.5% butane/air, the selectivity to MA was measured to be high and nearly uniform: $\sim 80\%$ selectivity at 20–60% butane conversion (figure 3.27). This indicates that because these anion vacant sites are readily available as active sites for gas oxygen exchange, the oxidation and regeneration of the catalyst can proceed quickly. The faster regeneration can prolong the operational life of the catalyst. The energy

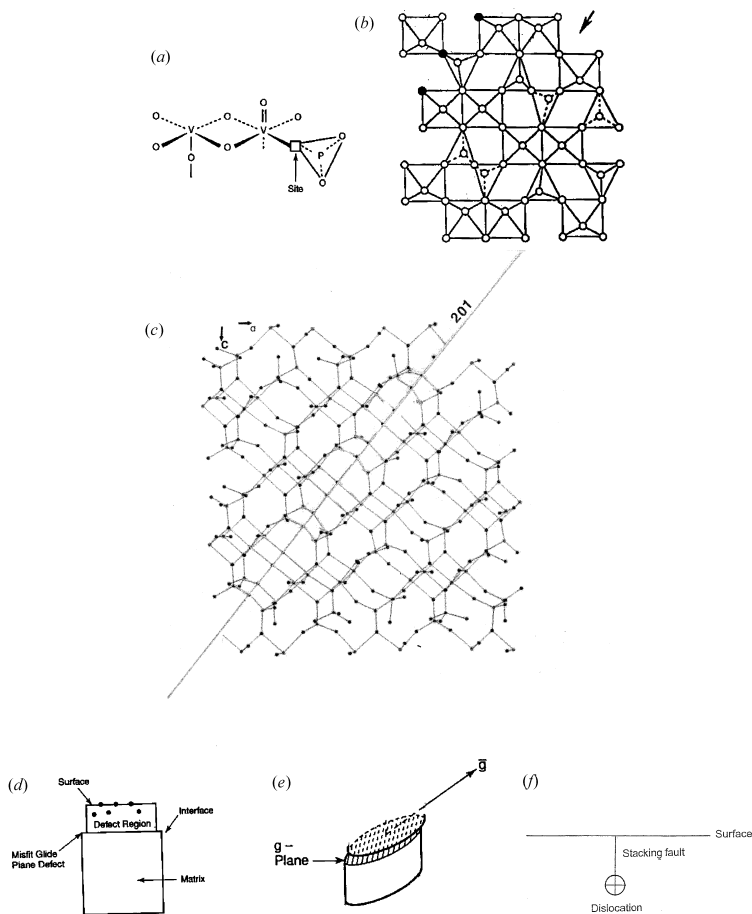


Figure 3.26. Active sites and novel glide shear mechanism in oxidation catalysis by *in situ* ETEM studies: (a) The studies reveal modifications to the catalyst's structure and disorder along $\langle 201 \rangle$, indicating in-plane anion vacancies between V-octahedra and P-tetrahedra (arrowed). These are associated with Lewis acid sites at the surface and may be important active sites in the alkane activation and the catalyst regeneration. (b) A model of the structure for extended glide shear plane defects giving the projection of one layer of idealized (010) VPO showing the novel glide shear process. The defects accommodate the misfit between the reduced surface with anion vacancies (filled circles) and the underlying bulk. (c) A three-dimensional projection of the glide shear plane fault. (d) and (e) show schematic diagrams of glide shear. (d) Model of glide shear accommodating misfit between surface layers containing anion vacancies and the underlying bulk. In (e) two crystals simply glide creating transformed glide defect regions with glide direction, g , and the glide-plane (g -plane). (f) Model to interpret the glide plane defects close to the surface: a partial screw dislocation bounds a stacking fault extending to the surface.

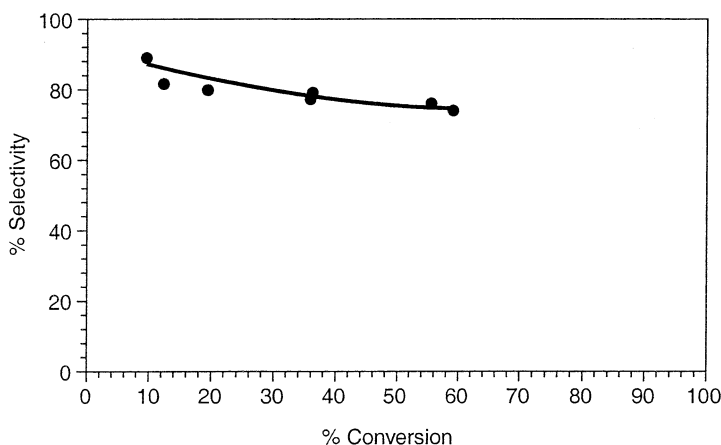


Figure 3.27. Reactivity data for VPO in a butane/air mixture.

requirement for the glide shear defect mechanism is much less than that for a CS plane which eliminates lattice sites and causes lattice collapse. The glide defect structure does not affect the bulk crystalline structure of VPO. Hence, the disordered regions of VPO reacted in N_2 , steam or butane have the same XRD of diffraction lines as VPO (with some variations in intensity). An example is shown in figure 3.28. The defect regions are, therefore, very difficult to unravel by x-ray diffraction alone. *In situ* ETEM studies under reaction conditions have been crucial for these studies.

The EM studies show that the novel glide shear mechanism in the solid state heterogeneous catalytic process preserves active acid sites, accommodates non-stoichiometry without collapsing the catalyst bulk structure and allows oxide catalysts to continue to operate in selective oxidation reactions (Gai 1997, Gai *et al* 1995). This understanding of which defects make catalysts function may lead to the development of novel catalysts. Thus electron microscopy of VPO catalysts has provided new insights into the reaction mechanism of the butane oxidation catalysis, catalyst aging and regeneration.

3.9.1.3 Reactivity of VPO catalysts and design of promoted catalyst systems

VPO catalyst selectivity is tested by both fixed-bed microreactor measurements and by pulsed microreactor measurements. In the former, the rate constants are measured in a microreactor on about 1 g of catalyst at temperature between 360 and 390 °C in a 1.5% butane/air environment. The pulsed microreactor evaluations are carried out by injecting 0.05 ml pulses of butane using a gas-sampling valve over about 0.5 g of catalyst in a microreactor heated to about 380 °C. *n*-butane conversion and selectivity to maleic anhydride (MA)

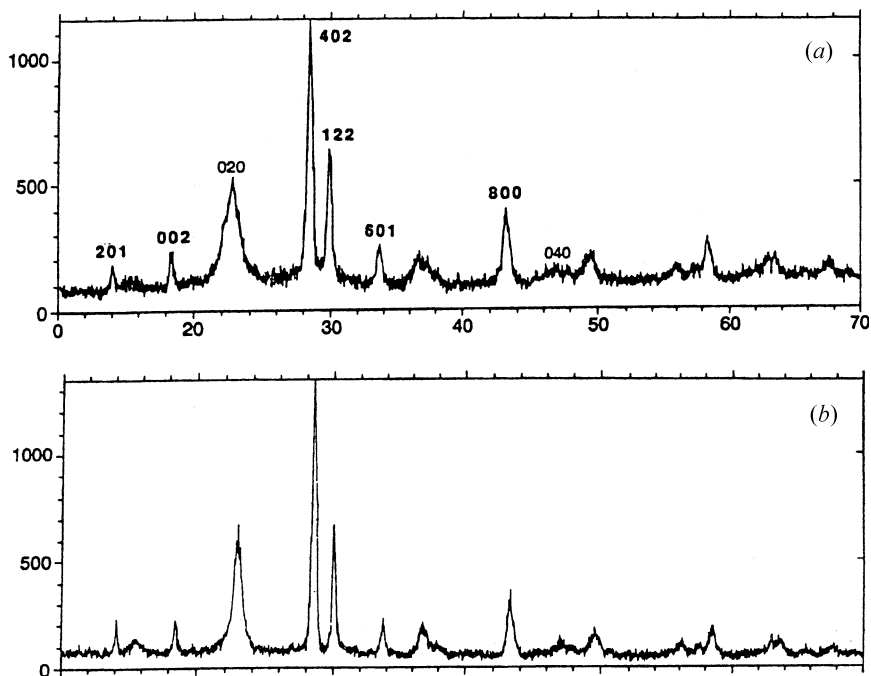


Figure 3.28. XRD data do not reveal defect structural changes due to peak overlap: (a) in N₂ or (b) in steam and are similar to the XRD in butane. EM studies are therefore crucial for obtaining insights into alkane catalysis (after Gai *et al* 1997).

decrease with successive butane pulses in the anaerobic case. Figures 3.29(a) and (b) show micromoles of oxygen reacted per gram of catalyst plotted against *n*-butane conversion and selectivity to MA. It is clear that important differences are obtained in the presence and absence of air and in different environments. Conversion and selectivity data show that in the butane–air mixture high selectivity is maintained for longer periods at 20–60% conversion (figure 3.27). The glide shear defects facilitate the continuity of the selective catalytic reaction. In a prolonged reduction of VPO ordering of the glide defects can result leading to homologous series of phases as a function of the reduction (Gai 1997). To increase the catalyst's performance, the anion (oxo)capacity can be controlled by doping in the V-site to induce selective glide shear transformations. A cation-promoted VPO catalyst with a nominal composition $(\text{Fe}_{0.05}\text{Sb}_{0.05}\text{V}_{0.9})_2\text{P}_2\text{O}_7$ indicates higher lattice oxygen diffusion capacities in the promoted catalyst (Gai *et al* 1997). Microstructural studies indicate that Fe and Sb maintain optimal anion point defect concentrations in the reacting catalyst.

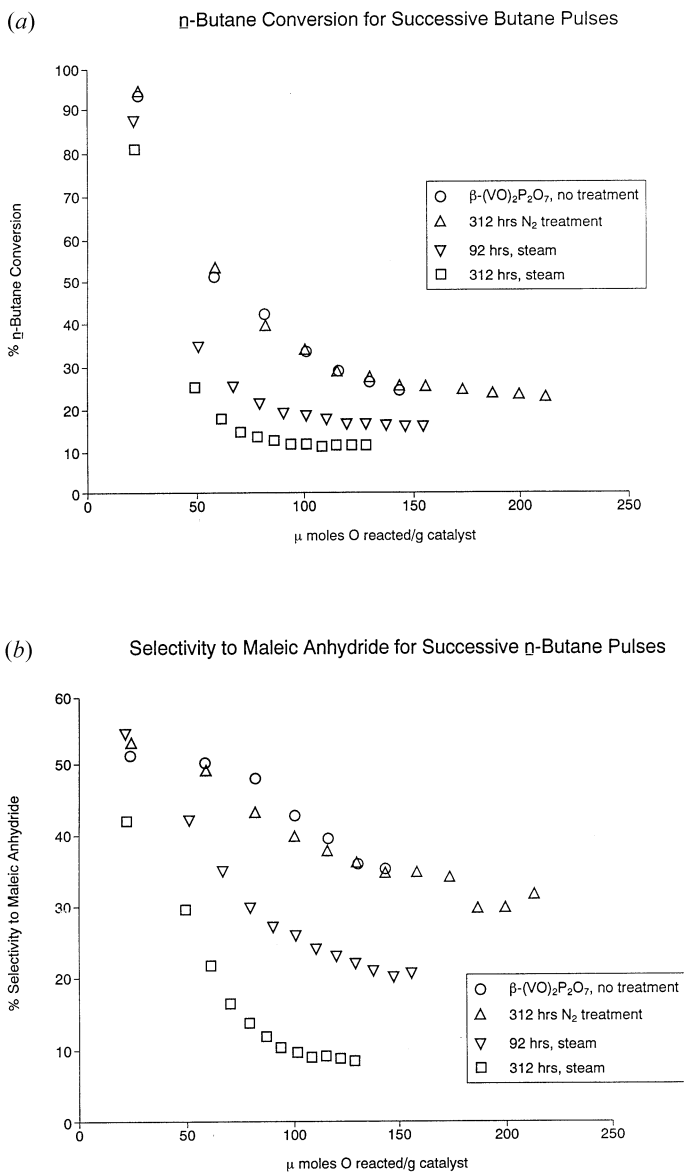


Figure 3.29. Conversion against selectivity to maleic anhydride for successive butane pulses (after Gai *et al* 1997).

3.10 Examples of other mixed metal oxide systems

3.10.1 Heteropolyacids

Efforts to use heteropolyacids and their salts as highly acidic catalysts started in the 1960s and the research on them has progressed rapidly in the last couple of decades. They are also called superacids because of their high acidic strength. The structure of a heteropolyacid (HPA) (first discovered by Berzelius (Moeller 1952)) was determined by Keggin (1934). These oxygenated compounds carry a central atom (e.g. P or Si) and Mo (or V, W) and a large number of protons (Misono *et al* 1997). Important industrial processes using HPA include catalytic oxidation of acrolein and methacrolein to their corresponding acids (acrylic/methacrylic acid with end uses in polymers), the gas phase ester synthesis to ethyl acetate and hydration on *n*-butane.

Literature reports suggest that the catalytic agent for the reaction is a heteropolyanion with the Keggin structure which is principally the 12-molybdophosphates anion $(\text{PMo}_{12}\text{O}_{40})^{3-}$ (shown in figure 3.30(a)). So far, microstructural details of these complex compounds under working conditions are very limited indeed and there is much scope for EM to achieve progress in this field. Compounds containing Keggin anions are suitable candidates for understanding the multi-functional characteristics of the 12-molybdophosphoric acid and its salts, ranging from, for example, the Bronsted acidity to the oxidizing power of individual anions in catalytic reactions. Catalytic particles with surface Keggin units can be prepared to provide a microsurface of known composition and structure on which the selective catalytic reaction can take place. The catalysts are therefore ideal for mechanistic studies. A combination of electron microscopy and reactivity can provide insights into the reaction processes, as we demonstrate in the following examples.

Various compositions x in the catalyst system $\text{K}_x\text{H}_{3-x}\text{PMo}_{12}\text{O}_{40} \cdot n\text{H}_2\text{O}$ can be prepared by mixing stoichiometric $\text{H}_3\text{PMo}_{12}\text{O}_{40} \cdot 24\text{H}_2\text{O}$ and K_2CO_3 . They are mixed in water and calcined at $\sim 400^\circ\text{C}$. The catalysts are highly unstable in the electron beam and low beam currents/CCD should be used for imaging. The catalyst microstructures and reaction mechanisms have been elucidated using HRTEM and ETEM (Black *et al* 1987). Contrary to presupposition, no significant solid solution range is detected in the compounds. The $x = 3$ phase is stable up to 650°C . Samples with the $x = 0$ phase (i.e. K_0 or H_3 phase) lose their n -water of crystallization at $\sim 180^\circ\text{C}$ and their constitutional water between 230 and 430°C . Decomposition of the Keggin anion $(\text{PMo}_{12}\text{O}_{40})^{3-}$ of the $\text{H}_3\text{PMo}_{12}\text{O}_{40} \cdot n\text{H}_2\text{O}$ is accompanied by the loss of water and the formation of the product, MoO_3 . K_3 contains clean surfaces containing Keggin anions. The end member K_0 is a water-soluble Bronsted acid, with a variable n -water concentration similar to that in as-prepared samples.

The potassium heteropoly molybdates exhibit high selectivities as shown in figure 3.30(b) in the oxidation of acrolein to acrylic acid for the various

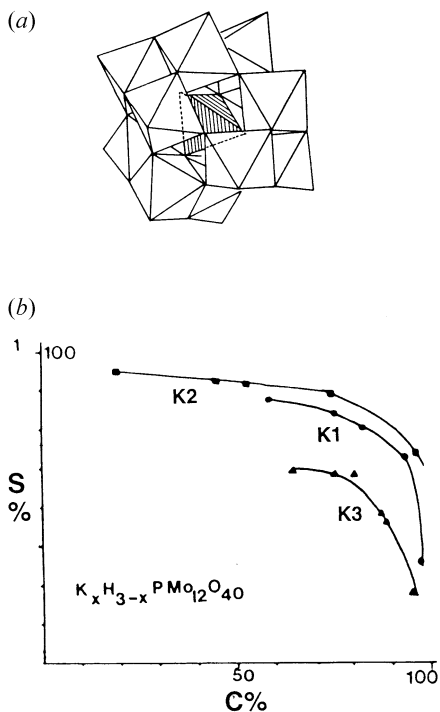


Figure 3.30. Heteropoly molybdate catalysts: (a) Keggin anion $(\text{PMo}_{12}\text{O}_{40})^{3-}$ (the central PO_4 tetrahedron is shaded and the MoO_6 octahedra are unshaded); and (b) selectivity (S) against conversion (C) data for acrolein to acrylic acid over $\text{K}_x\text{H}_{3-x}\text{PMo}_{12}\text{O}_{40}$ (with $x = 1-3$) at $\sim 350^\circ\text{C}$ show high selectivities. (After Black *et al* 1987, Gai *et al* 1983.)

multiphasic $\text{K}_x\text{H}_{3-x}\text{PMo}_{12}\text{O}_{40}$ salts ($x = 0-3$). An SEM image of the potassium salts ($\text{K}_{2.5}$), the cubic (111) ED pattern of cubic K_3 (with 110 reflections, arrowed) and an HRTEM image of K_1 (with a simulated image) are shown in figure 3.31. A particularly important result from EM studies of K_0 show its isostructural relationship with K_3 . *In situ* ETEM coupled with high precision AEM and chemical reactivity measurements of catalysts of the K_x series have revealed an epitaxial, isostructural ordered surface defect layer derived from the $\text{H}_3\text{PMo}_{12}\text{O}_{40}$ phase (referred to as the H_3 phase) which is stabilized on the water-insoluble K_3 particles in the mixed salts. The EM results further show that the enhanced selectivity of the catalysts is due to the monolayer coverage of H_3 . The isostructural relationship between the two phases could facilitate proton transfer across the interface, thus enhancing the stability of the formed surface layer. Similarly, other compounds can be designed with important catalytic properties and electron microscopy offers a wealth of opportunities to explore these further.

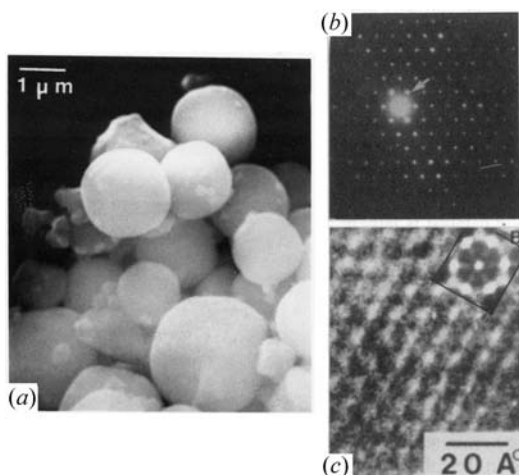


Figure 3.31. (a) An SEM image of heteropoly $K_{2.5}$ with (b) predominant (111) ED and (c) (111) HRTEM lattice image (with simulations inset).

3.10.2 Mixed metal amorphous and spinel phase oxidation catalysts derived from carbonates

3.10.2.1 EM studies of carbonates and spinels containing Cu, Co and Mn

It has long been known that amorphous manganese oxides promoted by transition metals catalyse the oxidation of CO and hydrocarbons even at ambient temperature (Jones *et al* 1923). Amorphous Mn-oxide promoted by Cu (known as hopcalite) has been investigated to understand the Cu–Mn redox couple, the Cu oxidation state and the extent of crystallinity (Schwab 1977). Spinel of similar compositions are also found to be active catalysts. Mixed metal oxides of cobalt, copper and manganese are prepared by calcining the co-precipitated hydroxides. Reactivity studies on the compounds have suggested that their high activity is due to the presence of active copper and cobalt ion species on the catalyst surface and that the ions are in their higher oxidation states (Yang *et al* 1991). Manganese-rich carbonates of the ‘rhodocrosite’ structure ($MnCO_3$ or calcite-type structure), which contain Cu and Co in solid solution, can be prepared by co-precipitation methods to yield active catalysts with high surface areas.

EM studies of mixed metal carbonates of the type $CuMn_2(CO_3)_3$, $CuMn(CO_3)_2$, $CoMn_2(CO_3)_3$ and $CuCoMn(CO_3)_3$ compounds and amorphous and spinel phase catalysts resulting from the decomposition of the carbonates provide insights into the relationship between nanostructures and the reactivity of these fascinating catalysts (Wright *et al* 1992). EXAFS and AEM have shown that Co substitutes without distortion into the rhodocrosite structure in $CoMn_2(CO_3)_3$, whereas Cu substitution occurs in a distorted environment in $CuMn_2(CO_3)_3$.

Heating the carbonates in air at 500 °C produces spinel structures consisting of cubic Cu-containing spinels and tetragonal Co-containing spinels (CoMn_2O_4 , with Jahn–Teller distortion). The Cu is mainly tetrahedral in the spinels whereas the Mn occupies mainly octahedral sites. Co is octahedral in CuCoMnO_4 and occupies both sites in CoMn_2O_4 . Mn has mixed oxidation states of 3+ and 4+ in CuMn_2O_4 and CuCoMnO_4 (with Co^{3+}), and 3+ in CoMn_2O_4 (Co has a mixture of 2+ and 3+). These oxides are shown to catalyse the complete reaction of an undiluted 2:1 CO/O_2 gas mixture at room temperature and are active at higher temperatures with diluted gas.

High-precision EDX analyses have provided the fundamental insight that these complex preparations have uniform chemical homogeneity throughout the temperature regimes ranging from room temperature to 500 °C. HRTEM and ED reveal that carbonates of the Cu–Mn and Co–Mn systems and their spinels have excellent crystallinity. EM data are shown in the following sections. Most of the microcrystals in the catalysts heated to 500 °C, are single crystals. Samples heated in the region 300–400 °C show a mixture of amorphous and crystalline regions. Figures 3.32(a)–(c) illustrate the microstructural evolution in CuMn_2 carbonate catalysts. There is generally no evidence of twins or strains at the boundaries where the randomly growing microcrystals happen to meet, suggesting that they relax structurally as they grow. Normally these crystals expose planes in the (100), (110) and (111) orientations. The lack of shapes for the microcrystals may mean that their shape is dictated by the atomic arrangement in the neighbouring grains. The selected-area diffraction (figure 3.32(c)) and EDX analyses (figure 3.33) are consistent with the spinel structure and composition. In contrast, in the CoMn_2 system, the catalysts exhibits a plate-like morphology (figure 3.32(d)). The different shapes in the two carbonates can be attributed to the two different surface energies associated with the systems. Conversion rates of CO to CO_2 indicate that among the spinels, the CuMnCo spinel oxide possesses a higher specific activity than the others, probably due to the presence of Co^{3+} . In other spinels, e.g. in CoMn_2O_4 , Co is mainly in the 2+ state.

3.10.3 Ca–Mn–O perovskites

Ordering of vacancies also plays a key role in selective oxidation catalysis over perovskite-based catalysts such as CaMnO_3 oxides. CaMnO_3 has a CaTiO_3 (AMO_3) perovskite structure which is made up of A^{2+} cations coordinated to 12 O^{2-} anions. They, in turn, are connected to corner-sharing MO_6 octahedra. CaMnO_3 was used as a model catalyst on a laboratory scale by Thomas *et al* (1982) in propene oxidation to benzene and 2-methyl propene to paraxylene. In such reactions the compounds are found to undergo reduction to form anion-deficient metastable phases of the type CaMnO_{3-x} where $0 < x < 0.5$, forming several distinct phases.

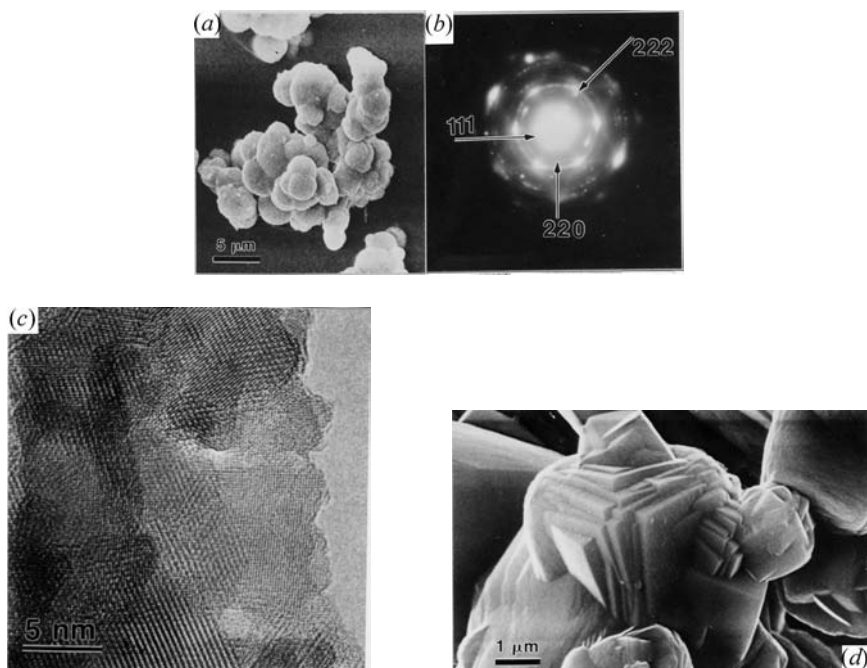


Figure 3.32. Evolution of the microstructure of CuMn_2 carbonate catalysts: (a) an SEM image showing spherical catalyst morphology; (b) an ED pattern with, e.g., (111) and (110) crystal orientations; (c) an HRTEM image of the catalytic crystals (~ 10 nm); (d) SEM of plate-like morphology of CoMn_2 carbonate. (After Wright *et al* 1992.)

3.11 Electronic structure of crystallites and dopant distributions by cathodoluminescence electron microscopy

3.11.1 Sb–Sn oxide catalysts and Fe–Sb–O catalysts

Tin-oxide (SnO_2) has a rutile-type tetragonal structure, with $a = 4.74$ Å and $c = 3.18$ Å. SnO_2 doped with antimony oxide ($\text{SnO}_2\text{--Sb}_2\text{O}_4$) is of interest as a catalyst for hydrocarbon oxidation reactions. Cathodoluminescence (CL) has been useful in the interpretation of the catalytic behaviour of complex Sb–Sn–O systems used in the oxidation of C_3H_6 and isobutene to acrolein/methacrolein reactions. Figure 3.34 shows CL spectra from reacted and unreacted catalysts showing a shift in peak. This suggests variations in composition and band gaps and correlated SEM and AEM studies confirm the segregation of Sb to the surface (Boyes *et al* 1985). The development of CL in the electron microscope for catalysis has become an important method for understanding the electronic structure and promoter distributions of catalysts. From these studies, an electronic

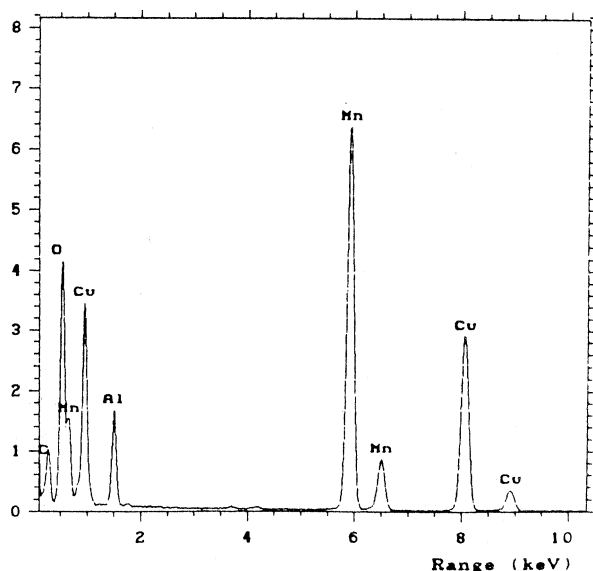


Figure 3.33. An EDX image showing the composition of a well-ordered CuMn_2 spinel catalyst. (Sample on AL support grid.)

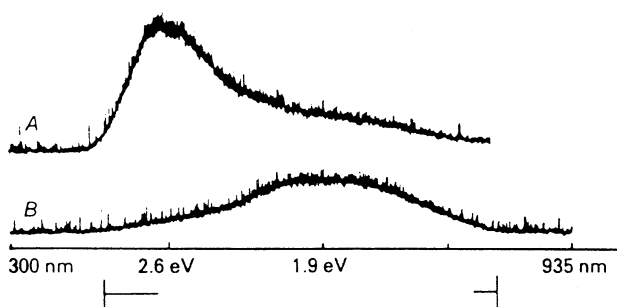


Figure 3.34. Electronic structure and dopant distributions in catalysts revealed by cathodoluminescence in electron microscopy: unreacted Sb/Sn oxide catalyst with a band-gap of ~ 1.9 eV is shown by the spectrum B. The reacted catalyst at A shows a band-gap of ~ 2.6 eV, demonstrating a peak shift indicative of surface segregation of Sb. (After Boyes *et al* 1985.)

contribution to the promoter mechanism is suggested.

$\text{Fe}_2\text{O}_3\text{-Sb}_2\text{O}_4$ has been shown to be an excellent catalyst for the allylic oxidation of olefins. The surface oxygen content and the ratio of Fe/Sb are believed to be important for catalysis (Aso *et al* 1980). The active surface is shown to be an Sb-enriched surface layer, as found in the Sb-Sn oxide systems.

An HRTEM study of Zn–Cr Fe oxides using surface-profiling methods in the EM has been reported by Briscoe *et al* (1984, 1985). Chemical kinetic studies of the oxidation of benzene to maleic anhydride over V–Mo–O catalysts (prepared using $\sim 3 V_2O_5:MoO_3$), have been described using GC–MS techniques (Lucas *et al* 1983). However, microstructural information is limited and there are opportunities for EM studies of these catalyst systems.

3.12 Zirconia (ZrO_2)-based solid-acid catalysts and ceria (CeO_2) systems

Recently, there has been much effort in understanding the catalytic properties of zirconia-based systems. The interest in heterogeneous catalysis stems from the fact that the system can exhibit both acid-base and redox properties. Figure 3.35 shows an HRTEM image of zirconia. Several preparative procedures have been reported in the literature (Tanabe *et al* 1994). Notable among the catalysts are sulfated zirconia (SZ) systems where zirconia treated with sulfuric acid exhibits strong acidity and can selectively catalyse *n*-butane to isobutane at room temperature. Chemical studies of Pt/SZ as catalysts in the oxidation of NO to NO_2 and in the oxidation of soot to CO_2 have been reported but microstructural data are lacking. Pt/SZ systems are found to be more active than unsulfated Pt/zirconia ones. Transition-metal-promoted SZ catalysts are also being prepared for light paraffin isomerization reactions at low temperatures.

Ceria is important in hydrocarbon oxidation reactions. It is also used as a catalyst support (increasingly with zirconia) in environmental catalysis (described in chapter 6). It has a CaF_2 structure (described in chapter 1) with lattice parameter $a = 5.411 \text{ \AA}$, space-group $Fm\bar{3}m$ and four ceria groups per unit cell. In reducing atmospheres such as hydrogen and butane, anion-deficient defect structures due to the loss of (111) anions are observed, as shown in the *in situ* atomic-resolution ETEM of the same area in figure 3.35(b) and (c).

3.13 The key role of electron microscopy in the discovery of novel reaction mechanisms in selective oxidation catalysis

As described in the preceding sections, fundamental studies of heterogeneous catalysis at the surface of catalysts are important for understanding reaction pathways and for the development of new or improved catalysts and processes. There have been earlier hypotheses proposed for selective oxidation catalysis: for example, the ‘multiplet’ theory which suggests that the activity depends upon correctly spaced groups (multiplets) of atoms to accommodate the reactant molecule (Balandin, 1969); and ‘electronic theory’ based on the nature of adsorption on semiconductors and empirical correlations between activity, work function and electrical conductivity (Wolkenstein 1960). The importance

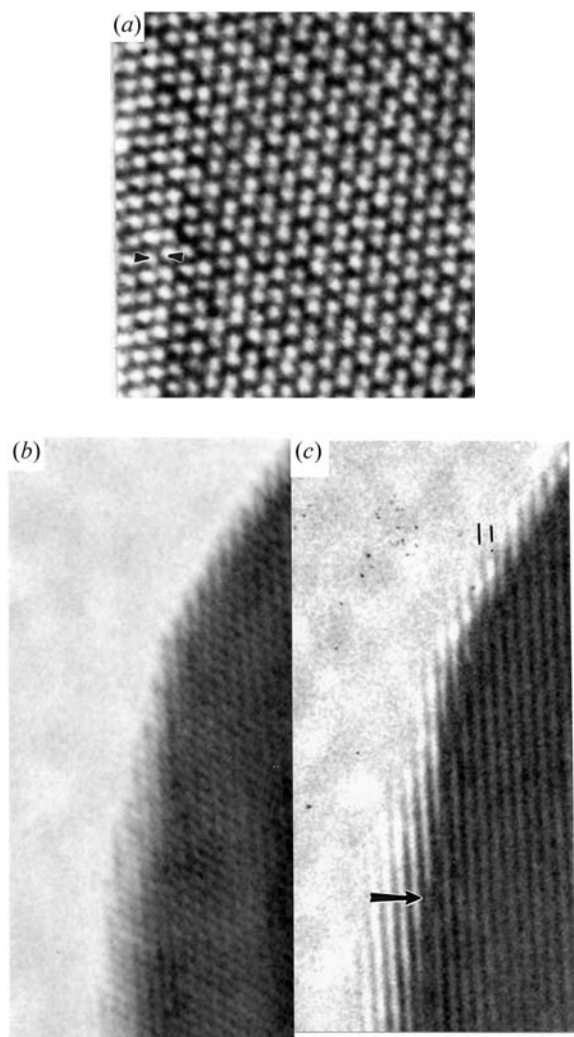


Figure 3.35. (a) Zirconia; (b) *in situ* atomic-scale ETEM image of ceria at room temperature; (c) *in situ* reduction at $\sim 400^\circ\text{C}$ in butane. The (111) anions are lost with the formation of defects (arrowed). (The layer spacings are 0.31 nm.)

of lattice imperfections in stereo-regular polymerization (e.g. in ethylene polymerization) and in the subsequent development of Ziegler–Natta catalysts, is also mentioned (Natta *et al* 1959). As described earlier, based on the work on molybdates, a two-component active site has been suggested: an active hydrogen-abstracting component and a selective oxygen-inserting one (Burrington *et al* 1983, McCain *et al* 1963, Snyder and Hill 1989). However, the correlation

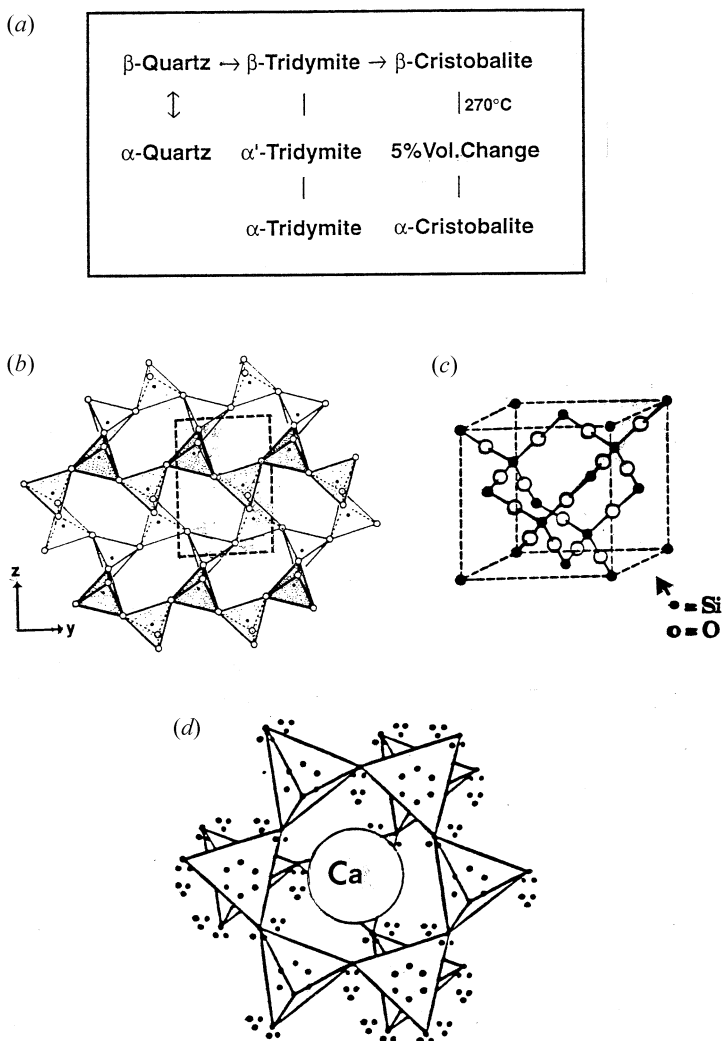


Figure 3.36. (a) Polymorphs of silica, (b) structure of α -cristobalite, (b) structure of β -cristobalite; and (d) Ca in the interstices of α -cristobalite.

between the local surface structure modification of the reacting solid catalyst and the selective oxidation reaction process (which is central to every heterogeneous catalytic process) is essentially absent in many of these hypotheses. This is precisely the area where EM is playing a pivotal role.

As we have seen, EM-based techniques are the most effective and direct methods for obtaining the surface microstructure, reaction pathways and

compositional issues in heterogeneous catalysts. They play a unique role in elucidating the nature of defects. The dynamic observations of the evolution of surface structures in working oxide catalysts presented here have illustrated that a variety of disordered structures or defects result from a change in the atomic arrangement of the surface at different temperatures. Generally, it seems likely that for chemisorption, high-energy surfaces where coordinations are unsatisfied are necessary.

The selected EM studies described here illustrate this point and the fact that point and extended defects are inextricably linked to the process of catalysis, affecting both chemisorption and reaction mechanisms. The EM studies have resulted in an improved mechanism for the formation of CS planes and their role in heterogeneous catalysis (Gai 1981, 1982). They have led to a new understanding of defects and their role in solid state heterogeneous catalytic progress.

Two different phenomena compete: the removal of the catalyst's structural oxygen from the surface of the oxide catalyst leads to the formation of anion vacancies and the restructuring of the surface to accommodate this loss. EM shows that a variety of extended crystal defects are introduced into the catalyst to accommodate the non-stoichiometry at different temperatures. *In situ* ETEM studies of model systems such as MoO_3 , have shown the formation of crystallographic shear (CS) planes at the catalyst operating temperature of $\sim 400^\circ\text{C}$. Based on ETEM studies of the nucleation and growth of CS plane defects in the reacting catalysts, the concept of the supersaturation of anion vacancy concentrations emerges (Gai 1981, 1993; Gai *et al* 1982). Supersaturation is defined relative to the background concentration of isolated vacancies in equilibrium with collapsed discs of CS planes. The driving force for the nucleation and growth of CS planes is the difference between the chemical stress due to the supersaturation of anion vacancies and the force required to create the CS planar fault. The ETEM studies have shown that only anion vacancies in supersaturation are eliminated by the formation of extended CS planes by simultaneous shear and collapse of the catalyst structure, leading to the lowering of the free energy of the system. (Earlier reports suggested that complete sheets of anion vacant sites were eliminated in the formation of CS planes (Wadley 1964, Magneli 1970, Anderson 1970–71 and Anderson *et al* 1967, 1973).) A better fundamental understanding of the formation of CS planes and their role in heterogeneous catalysis has thus emerged from these dynamic EM studies, which has modified earlier proposals.

As described in section 3.3, correlation studies between CS plane defects observed by ETEM and parallel reaction chemistry (under conditions similar to those used in ETEM) indicate that the CS planes which eliminate supersaturation of anion vacancies are a consequence of catalytic activity and not active oxygen exchange sites for catalysis as was originally believed. They are secondary or detrimental to catalysis. The correlation results strongly suggest that anion point defects are active centres in the rapid diffusion of oxygen in

selective oxidation reactions (Gai 1981, 1992). A simple thermodynamic equation connects the equilibrium concentration of anion vacancies in an oxide catalyst containing a finite number of CS planes, and the difference in the free energy of the vacancy occurring in an isolated fashion, or incorporated in the CS fault plane. In reducing catalysts, this equilibrium is maintained by the exchange of anion vacancies at the dislocations bounding the CS planar fault. The thermodynamic relation is also useful in estimating the enthalpies for the formation of vacancies and to predict whether nucleation of CS planes or any other type of defect is feasible in a given oxide. A method for measuring the activation energy for migration is also described by ETEM observations of defect formation and kinetics, by identifying the position of CS plane defects with the diffusion front of anion vacancies. This is central to the rate of anion vacancy diffusion into the bulk and the extent of their subsequent ordering to a new phase, which impact on the lifetime of the catalyst. Operation without CS defects has been established by *in situ* ETEM studies in commercially important mixed metal oxides, including phosphates and molybdates under working conditions.

In the selective oxidation of *n*-butane over the highly successful commercial vanadyl pyrophosphates, a novel glide shear mechanism has been discovered by ETEM for the release of oxide structural oxygen and accommodation of anion non-stoichiometry without collapse of the bulk oxide crystal lattice. Although the CS mechanism (which eliminates anion vacancies) resulting in shear and lattice collapse (Magneli 1970) is structurally elegant, in important applications such as catalysis EM studies indicate that the novel and simple glide shear mechanism is the most effective structural transformation mechanism for efficient oxidation catalysis (Gai *et al* 1995, Gai 1997). The glide mechanism effectively preserves anion vacant sites associated with Lewis acid strength at the surface without collapsing the catalyst structure. These sites are important active centres for alkane activation and in catalyst regeneration. Furthermore, the EM results can be used to tailor specific catalyst surfaces by suitable substitutions to induce selective glide shear.

3.14 Stable silica-based ceramic oxide supports for catalysts: some recent developments

As previously described silica, which is an important catalyst support, is polymorphous (figure 3.36). Forms of silica other than quartz (SiO_2), can be stabilized chemically for use as catalyst support materials. Here we describe EM studies of the chemical stabilization of the cristobalite form of silica. It can be used as a stable catalyst support.

Structures based on networks of corner-shared tetrahedra of oxygen ions round a central cation are some of the most important in crystal chemistry. Silica-based ceramics belong to such a class of compounds. The cristobalite form of silica has two modifications, α (low) and β (high), which are separated

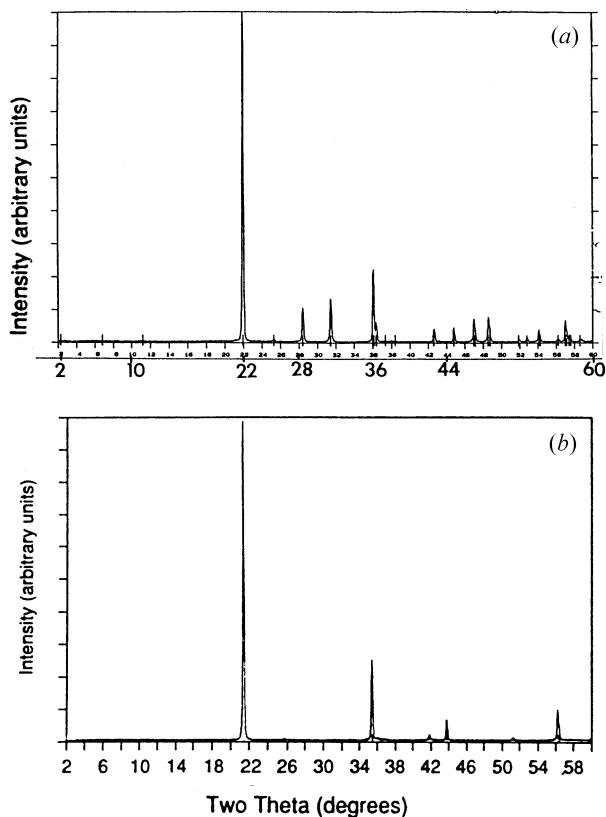


Figure 3.37. XRD spectra of (a) tetragonal α -cristobalite and (b) chemically stabilized cristobalite (CSC, $\text{CaO}:2\text{Al}_2\text{O}_3:40\text{SiO}_2$ or 1:2:40 composition) at room temperature with Ca and Al dopants, which exhibits the structure of the high-temperature β -phase.

by a sudden displacive transition at $\sim 270^\circ\text{C}$. The transition is reversible. Synthesis of ' β -cristobalite-like phases' by solid state or sol-gel routes have been reported (e.g. Perrotta *et al* 1989), but such preparations yield poorly crystallized, multi-phasic ceramic materials. Microstructural studies of novel chemically stabilized cristobalite (CSC), a silica-based ceramic containing small amounts of dopants have been described recently (Gai *et al* 1993). CSC displays many of the structural characteristics of the high-temperature β -cristobalite at room temperature and does not undergo phase inversion to α -cristobalite upon cooling.

3.14.1 Structural principles

The structure of both cristobalite and tridymite are composed of layers of six-membered rings of Si-O tetrahedra. The stacking sequence of these layers

in cristobalite is 'cubic'—ABCABC. Figures 3.36(b) and (c) show schematic diagrams of the structure of the α - and β -phases, respectively (O'Keefe *et al* 1976, Wright *et al* 1975). The structure of α is tetragonal, space group $P41212$, with $a = 4.98 \text{ \AA}$ and $c = 6.95 \text{ \AA}$. The structure of β is not yet completely understood. The general consensus is that the structure is cubic, its space group $Fd3m$ and $a = 7.17 \text{ \AA}$. According to Wright *et al*'s (1975) hypothesis, the oxygen atoms occupy the six (96h) sites in $Fd3m$. The presence of diffuse scattering in the β -phase has been reported in the literature and will be discussed briefly later.

In earlier literature reports, x-ray data of α -based ceramics, the β -like phase observed in certain silica minerals was explained by a structural model based on disordered α -tridymite. However, others have suggested that the structure of the stabilized ' β -cristobalite-like' ceramics is closer to that of α -cristobalite than that of α -tridymite, based on the ^{29}Si nuclear magnetic resonance (NMR) chemical shifts (Perrota *et al* 1989). Therefore, in the absence of ED data it is impossible to determine the microstructure of the stabilized ' β -cristobalite-like' phase. ED and HRTEM have provided details of the ceramic microstructure and NMR has provided information about the environments of silicon atoms in the structure. Infrared spectroscopy views the structure on a molecular level.

Novel stabilized α -cristobalites are synthesized by the wet chemical route and are referred to as chemically stabilized ceramics (or CSC, Saltzberg *et al* 1992, Gai *et al* 1993) since the true structure of these materials is not fully understood. A clear sol can be prepared from colloidal silica, aluminium nitrate nonahydrate and calcium nitrate hexahydrate in proportions to form a final composition 2.3 mole % CaO 4.7 Al_2O_3 93% SiO_2 , i.e. a 1:2:40 composition. This sol is spray-dried yielding an amorphous powder. This precursor is calcined at 1100°C for 24 hr to form CSC. Well-ordered α -cristobalite is prepared by crystallizing aerosol, a very pure form of amorphous silica at 1400°C for 24 hr. CSC does not undergo a phase transformation and is thus chemically stabilized. XRD patterns of α -cristobalite and CSC are shown in figures 3.37(a) and (b), respectively. The tetragonal supercell reflections of α are absent in the CSC pattern just as in the β -phase. The reflections of the CSC are sharp, indicating a well-crystallized structure, in contrast to the relatively broad reflections observed in synthetic cristobalites and in natural cristobalitic opals reported in the literature. Other compositions with varying Ca/Al can be synthesized leading to additional new ceramic materials. CSC compositions using a transition metal (Cu) and an alkali metal (K) have also been prepared in the systems $\text{CuO}:\text{Al}_2\text{O}_3:\text{SiO}_2$ and $\text{K}_2\text{O}:\text{Al}_2\text{O}_3:\text{SiO}_2$. Experimental procedures thus lead to new ceramic materials of interest as support materials in catalysis.

HRTEM, LVSEM, dynamic ED and EDX microanalysis play a key role in solving the structure and compositions of the catalytically interesting new CSC materials. (Samples are studied at room temperature and *in situ*, under dynamic conditions at elevated temperatures using a hot sample stage and at liquid nitrogen temperatures using a cold stage, to understand local structural changes (disorder), diffuse scattering and compositional changes.) The NMR magic angle spinning

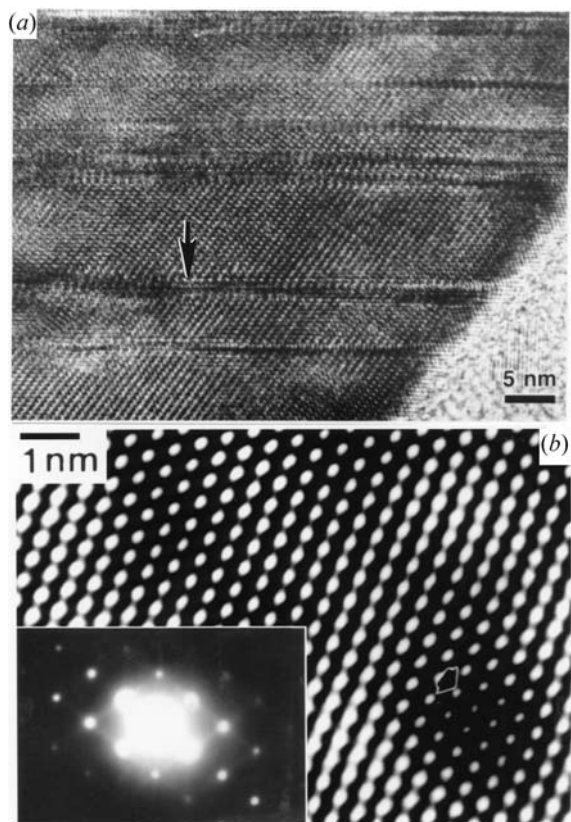


Figure 3.38. (a) High concentration of twins and faults in α -cristobalite in (010); (b) CSC with no faults (inset: ED pattern with streaks).

(MAS) method (to record ^{29}Si signals) provides complementary information on the chemical bonding (Si–O–Si bond angles), aluminum distribution in the silica framework and secondary phases.

3.14.2 Nanostructure and microchemistry

ED examinations reveal remarkable differences between CSC and the undoped α -cristobalite. As shown in figure 3.38(a), the local structure of undoped α -cristobalite in the (010) projection reveals a high concentration of (twins) faults along the $\langle 101 \rangle$ directions. These defects are probably introduced when the ‘cubic’ β -cristobalite structure inverts to a tetragonal α -cristobalite upon cooling below 270°C (discussed in the next paragraph). The CSC microstructure is shown in figure 3.38(b) showing the absence of defects and a composition $\text{CaO}:2\text{Al}_2\text{O}_3:40\text{SiO}_2$ (1:2:40 structure). The composition is confirmed by

quantification of the EDX.

The chemical stabilization of the structure is thus characterized by the absence of faults or discernible defect structures, confirmed by sample tilting experiments in diffraction contrast and by HRTEM. The corresponding electron diffraction in the (101) orientation, however, shows diffuse streaks (figure 3.38(b)). The streaks are mainly along the $\langle 111 \rangle$ and $\langle 010 \rangle$ directions. Some weak diffuse streaking along (101) is also observed. The streaks are indicative of considerable disorder in the structure. These results are consistent with the NMR data.

This α - β phase transition is accompanied by a 5% volume change and is thus expected to disrupt the crystal structure. CSC, which does not undergo any detectable phase transformation upon cooling, is essentially free of stacking fault defects and is found to be stable up to 1000 °C. The images in figure 3.38(b) also confirm that the long-range order of the CSC structure is maintained over distances greater than 100 nm. The stabilization of CSC structures is consistent with the 'stuffing concept' described by (Perrota *et al* 1989). It explains the stabilization of the ' β -cristobalite-like phase' as being due to the 'stuffing' concept, where the incorporation of the foreign ions into the interstices of silicate structures is charge-compensated by the substitution of Al^{3+} for Si^{4+} in the framework (figure 3.36(c)). The presence of foreign ions in the interstices presumably inhibits the contraction of the structure normally occurring as $\beta \rightarrow \alpha$ thus stabilizing the β -cristobalite-like structure. NMR spectra for several $\text{CaO}:\text{Al}_2\text{O}_3:\text{SiO}_2$ compositions and analyses of silica framework geometry show short-range lattice deformations in CSC. These may include local distortions caused by the incorporation of Ca and Al atoms in the crystal.

3.14.3 Stabilization mechanisms

The causes of diffuse streaking indicative of disorder and stabilization mechanisms in CSC are of considerable importance, since novel stabilized ceramics can be engineered by suitable dopants. HRTEM imaging (figure 3.38(b)) and dark-field imaging using the diffuse streaks have not revealed any discernible extended defect structures. Dynamic heating to 300 °C and cooling to -171 °C show no significant difference in the streak intensities within experimental errors.

Thermal diffuse scattering (TDS) is ascribed to low-frequency lattice vibrations. The atoms in a perfect crystal are not fixed to their sites and oscillate about their positions. The Bragg intensities are reduced by the Debye-Waller factor, proportional to

$$\exp\left(-\frac{1}{2}(8\pi^2v^2 \sin^2 \theta_B/\lambda^2)\right)$$

where θ_B is the Bragg angle and λ is the wavelength of the electrons. The TDS is reduced with reduced temperatures. *In situ* heating and cooling studies of CSC in ETEM suggest that the TDS may not be significant. The studies described here have shown that the structure of the CSC is complex, combining

a relatively long-range order (high crystallinity), with local disorder. EM data suggest that this local disorder is related to the substitution of Al^{3+} ions for Si^{4+} in the structure, which is accompanied by the incorporation of the Ca^{2+} ions in interstitial sites. These substitutions can be expected to cause local distortions, and could lead to the type of disorder observed. However, this may not account for the streaks observed in the undoped β -form which needs further study. Monte Carlo calculations performed to understand the cause of streaking in β -cristobalite (Wright *et al* 1975) do not provide satisfactory agreement with experimental data.

The nature of the disorder, i.e. whether it is static (individual atoms frozen in one of a range of possible sites) or dynamic (each atom vibrating through a range of possible sites), requires some discussion. *In situ* hot and cold stage experiments indicate that the intensity distribution is constant, i.e. that the disorder is static. It is fascinating that even in the presence of local disorder, the long-range order of the CSC structure is maintained. The structure of the undoped high β -cristobalite (stable only above 270 °C) is not fully understood, but it is possible that room temperature CSC and the high-temperature β -cristobalite have very similar structures, as indicated by x-ray and electron diffraction data. EM results for CSC strongly suggest a model where interstitial Ca^{2+} ions enter the relatively open β -structure and stabilize it by inhibiting the β - α cristobalite transition. The Si-O-Si bond angles in CSC observed by NMR are relatively large consistent with an open structure and the ED data show a cubic structure with a lattice parameter similar to that of the β -phase.

Chapter 4

Catalysis by zeolites and molecular sieves

Zeolites are porous aluminosilicate structures and are derived from silica and alumina ceramic oxides. They are of great importance in catalytic cracking of hydrocarbons as will be described later. In zeolites with a framework consisting of large holes or cages, gas molecules can move in and out of them with ease and the structures also have large ions and water molecules with a considerable degree of movement. Zeolites are capable of accommodating gas molecules (or promoter ions) in the size range 0.3–1 nm. Recently larger sizes have been reported. The large surface areas associated with zeolites and active sites that can be distributed throughout the sample make zeolites excellent catalysts. Because they are not toxic materials, they are increasingly able to meet the rigid demands of environmentally safe standards of modern industrial processes.

4.1 Structures, acidity and uses of zeolites

The structures and catalytic activity of zeolites have been reported extensively in the literature (Thomas and Thomas 1997, Breck 1974, Bond 1987, Thomas *et al* 2001, Treacy *et al* 1996). Their open structures give rise to crystalline porosity (figure 4.1(c)). Single oxides like alumina or silica do not normally exhibit enough acidity for acid-catalysed reactions and zeolites fulfil this requirement. In silica which may be thought of as consisting of SiO_4^{4-} tetrahedra (as described in chapter 3), with each oxygen sharing two tetrahedra, substitution of Al for Si over AlO_4^{5-} creates an excess of negative charge. To satisfy electroneutrality, it is suggested that either a proton (e.g. from ionizable hydroxyl groups) can be used, which renders the material acidic or Al with a 3-coordination, which is equivalent to being a Lewis acid site (with SiO_4^{4-} carrying excess negative charge that may be balanced by a proton (Bond 1987)). Its interaction with a silanol group may lead to a Bronsted site. Many naturally occurring minerals have zeolite structures, e.g. faujacite (figure 4.1(b)) and mordenite. Hexagonal faces of the units can join to give x, y zeolites (figure 4.1(c)). The effective pore diameter can be determined by the type of cation compensating for the negative charge of the structure (Bond

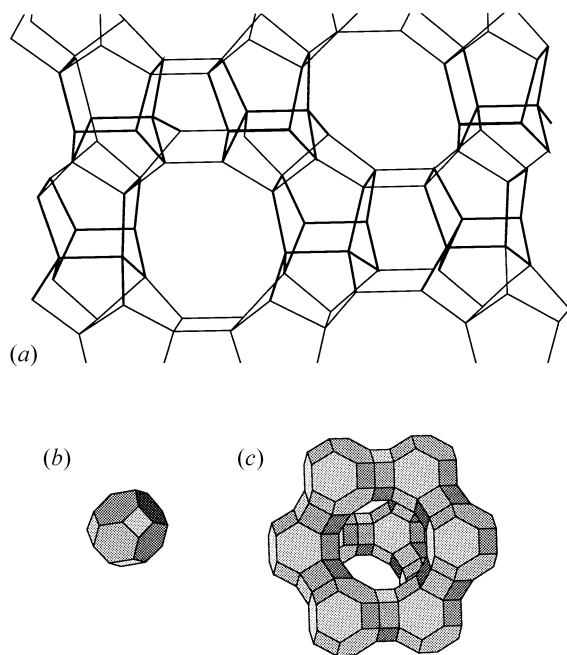


Figure 4.1. Schematic diagrams of (a) zeolite catalyst structures, (b) cuboctahedral unit of faujacite and (c) X, Y zeolites (by courtesy of Oxford University Press: *Het catalysis* By Bond (1987)).

1987). Synthetic zeolites are also produced by varying the cation and the cage diameter.

Zeolites are now used in a majority of catalytic cracking reactions in which heavier hydrocarbons are broken into smaller volatile components for use as fuels. For example, $n(C_{12}H_{18})$ is broken into ethylene, butene and benzene species, reforming petroleum to produce high octane fuel and to produce gasoline from methanol (e.g. using zeolite-structure-mobil-5 or ZSM-5 by Mobil (now ExxonMobil)). The mechanisms for catalytic cracking reactions over zeolites are well documented (Thomas and Thomas 1997). Zeolites are also used as ion exchangers and molecular sieves since they have the ability to absorb and retain molecules at certain sites. They are also used as catalyst supports. Recently, zeolites have gained importance in the cosmetic and food industries! Fragrances for perfumes as well as food technology form an important part of the chemical industry. The use of zeolites should enable the manufacture of selective products with less environmental pollution than conventional acid or base catalysts, because of lower energy consumption and the lack of toxic byproducts and separation problems.

Transition (Co, Mo) or noble metals (Pt, Pd) on zeolites like mordenite are used for hydrocracking where these 'dual function' zeolites combine the acidity of the host zeolites with the hydrogenation/dehydrogenation activity of the exchanged metal. Transition-metal ions can also be exchanged with the sodium ion in zeolites: catalysts with cerium (IV) exchange with zeolite NaY for the oxidative cleavage of pinacol with oxygen have been reported in the literature (Bond 1987). Transition-metal-exchanged Y-zeolites have been used for olefin epoxidation and for many other uses. Synthesis and characterizations of silicalites modified with Cr, Ge and other elements have been reported. Bifunctional acidic zeolite catalysts modified with the addition of a metallic component have been found to be very effective in catalytic reforming and especially in converting naphtha from crude oil into desired hydrocarbons. Metal-ion-exchanged zeolites and metal-substituted aluminophosphates (ALPOs) have led to the synthesis of a new family of compounds (Wilson *et al* 1982). ALPOs contain corner-sharing tetrahedral AlO_4 and PO_4 units.

The use of HRTEM in deciphering the structure and composition of zeolites was pioneered by Thomas *et al* (1997, 2001). Some important complex zeolite systems and the unique role played by HRTEM and ED in our understanding of their structures and catalytic properties are described later. Information about framework substitution, structural changes as a function of doping and their effect on catalysis has only become available through electron microscopy and microanalysis (Thomas *et al* 2001, Brydson *et al* 1984). ALPOs and silicon-aluminophosphates (SAPOs) are special classes of solid acid catalysts. Solid acids are able to provide protons (H^+) which are released either from ionizable hydroxyl groups, leading to O^- and H^+ , or from hydrated ions H_3O^+ . When a reaction occurs over a solid acid catalyst, a positively charged intermediate is formed incorporating the proton, which greatly impacts on the shape and configuration of the final product. We describe the impact of EM in deciphering the complex structures of ALPO catalysts in the following sections.

4.1.1 Shape-selective catalyst

Zeolites are well known for shape-selective catalysis. Here the shape of the zeolite pores or cavities can control the shape of product. When catalytic reactions take place in channels of zeolites only those products that can be accommodated in the channels advance and emerge. Mobil's ZSM-5 is an example of a shape-selective catalyst. Many more zeolites with different pore sizes or large surface areas are being synthesized, extending the principle of shape-selective catalysis. Such developments are helpful for both existing industrial processes and environmental protection.

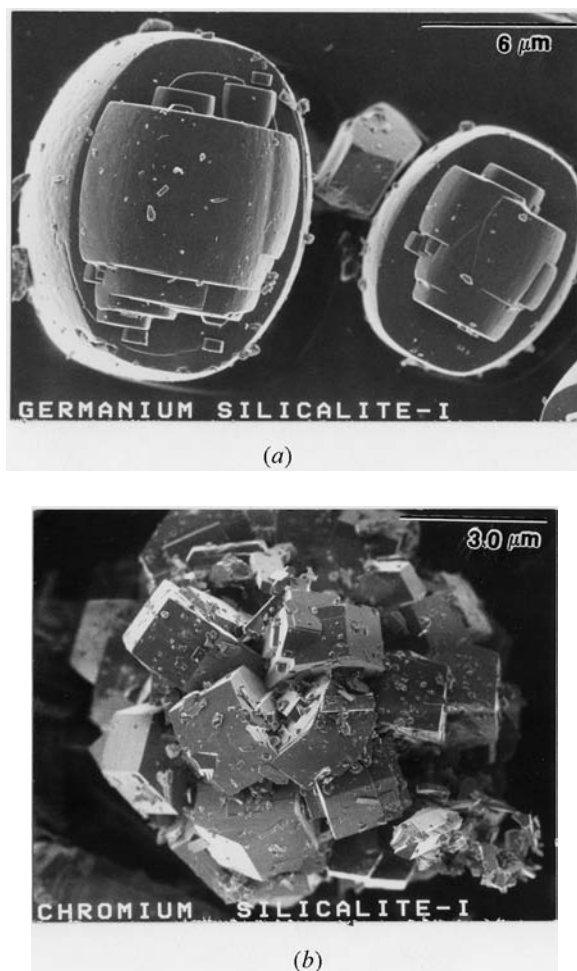


Figure 4.2. Effect of doping on catalyst morphology using SEM: (a) Ge-doped silicalite and (b) Cr-silicalite.

4.2 Silicalites and aluminophosphates

Silicalites, ALPOs and their metal-substituted analogues are becoming increasingly important as catalysts in selective oxidation of hydrocarbons. Silicalites can be synthesized with dopants such as Ge or Cr. The effect of doping on the silicalite morphology is shown in the scanning electron micrographs in figure 4.2.

Since the synthesis of aluminophosphate (AlPO_4) molecular sieves (Wilson *et al* 1982), other novel catalyst materials have been developed by the

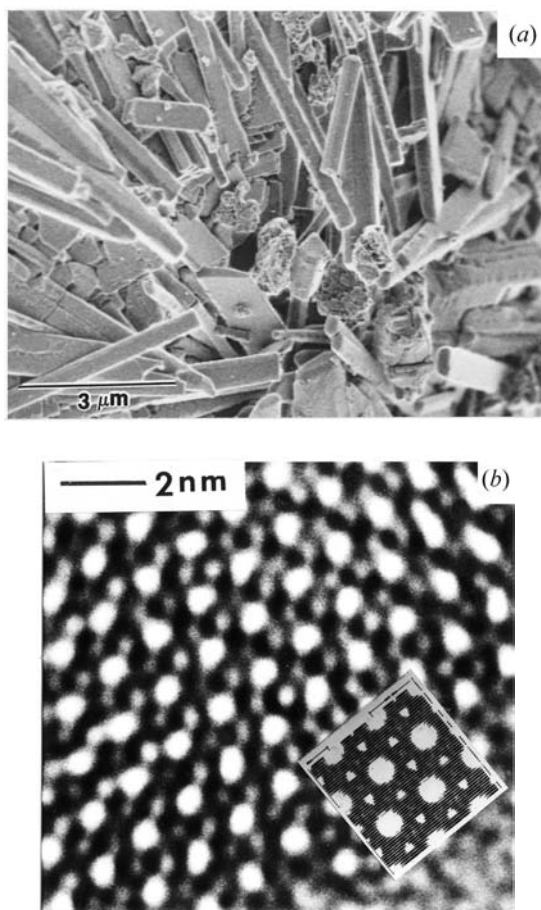
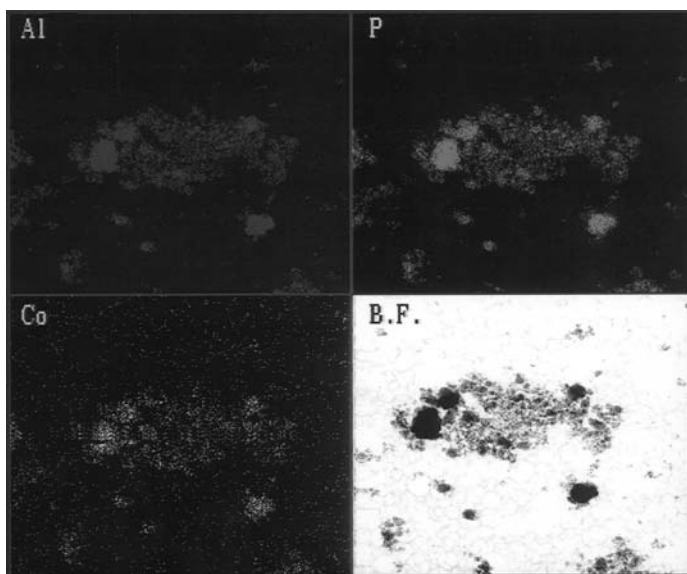


Figure 4.3. Co-ALPO₅ catalyst (with $(\text{Co}/\text{Co} + \text{Al}) = 0.036$): (a) an SEM image; (b) an HRTEM image (inset—: simulated structure); and (c) x-ray elemental map of Co-ALPO indicating uniform distribution of the elements Al, P and Co. The bright-field image is also shown.

isomorphous substitution of various elements for either Al or P in the aluminophosphate (ALPO) framework. These ‘uniform heterogeneous catalysts’ are used for the oxidation of hydrocarbons and methanol (Thomas *et al* 1997, 2001). The electron micrographs in figures 4.3(a) and (b) produced by SEM and HRTEM show the morphology and structure of Co-ALPO (CoALPO-5 ($\text{Co}/\text{Co} + \text{Al} = 0.036$), respectively. Figure 4.3(c) shows an x-ray elemental map of uniform Co-ALPO catalysts.

The incorporation of silicon leads to a new class of compounds termed SAPOs. These exhibit catalytic properties intermediately between those of zeolite



(c)

Figure 4.3. (Continued)

aluminosilicates and ALPOs. Silicon is believed to substitute for phosphorus in ALPO, giving the catalyst cation-exchanging properties. Similarly, the substitution of titanium (IV) in the framework leads to TAPOs. Pentavalent cations like vanadium substitution are useful in the epoxidation catalysis of allylic alcohols.

Substituting divalent or trivalent elements for the Al in the framework has been successfully carried out by several groups yielding novel heterogeneous catalysts (metal-substituted ALPOS, MALPOs; Thomas *et al* 2001) for hydrocarbon oxidation and liquid phase oxidation. MALPO catalysts can be complementary to metal-doped silicalite catalysts. Particularly interesting compounds are MALPOs in which a divalent metal (Me) substitutes for the framework Al^{3+} , for example MALPO-36 (where $\text{M} \equiv \text{Mg, Mn, Zn, Co}$) and MALPO-34 ($\text{M} \equiv \text{Mg, Mn, Co}$ etc).

Although many new compounds have been reported, the crystal structure of many of these has not been determined mainly because of the difficulty in obtaining good-quality single crystals for x-ray diffraction studies and this has hindered our understanding of catalytic mechanisms. Peak overlap also poses a problem in structural analyses. In the following sections we show that a combination of HRTEM real-space images, ED and energy minimization procedures have led to a new method for determining the three-dimensional structure of ALPO and MALPO catalysts (Gai *et al* 1992). These general

principles for determining structures using HRTEM and ED are applicable to other complex catalyst systems.

4.3 Determining three-dimensional structures by ED and HRTEM: MALPO solid acid catalysts

HRTEM has been a crucial tool in determining the structures of complex zeolites. Our understanding of new structures in the aluminosilicate and ALPO zeolitic family of compounds and their catalytic activity has greatly improved as a consequence. Direct proof of the existence of defect structures, the intergrowth of different zeolitic structures and other reacted phases have been established solely because of HRTEM and new insights into novel structures are being gained. The question which often arises in the context of silico-aluminophosphate microcrystalline catalysts is whether three-dimensional structures of new microporous catalysts can be determined by electron diffraction and HRTEM, since single-crystal x-ray analyses are not possible for many of these materials. The application of HRTEM, least-squares distance and energy minimization calculations, and selected-area ED has led to the determination of the three-dimensional structures of a new family of compounds in the MeALPO series.

The application of HRTEM and ED can be difficult, however, because of the tendency of the catalysts to become amorphous under the beam. Use of higher accelerating voltages (to minimize the production of inelastic collisions which are primarily responsible for the structural disintegration of the sample), better vacuum in the sample chamber and, when possible, dealumination of the aluminosilicate (by replacing Al^{3+} with Si^{4+} in the framework) without losing structural integrity avoids these problems. These studies have indicated that Al–O bonds are more susceptible to rupture under electron-beam irradiation than Si–O bonds.

MALPOs, ALPOs and SAPOs are even more extraordinarily beam-sensitive (amorphization can take only a few seconds) compared to aluminosilicates, hampering detailed HRTEM and diffraction studies. In HRTEM, suitable reduced-gun-bias setting, smaller condenser apertures (30–50 μm), and defocused illumination are used to minimize beam damage. Attempts are made in some cases to subtract the noise (non-periodic Fourier coefficients) to improve the image quality. Multi-slice image simulations are performed to interpret the images. High-precision nanochemical analysis is carried out simultaneously with integrated EDX to determine the composition. HRTEM work encourages us to believe that soon progress in structural elucidation comparable to that achieved for aluminosilicates will also be achieved for the ALPO family of compounds.

Monophasic samples of, for example, MgALPO-36, ZnALPO-36 (MALPO-36) are synthesized from gels with tripropylamine as a base by heating the gels at 110 °C. The organic template is removed by calcining in oxygen at 550 °C

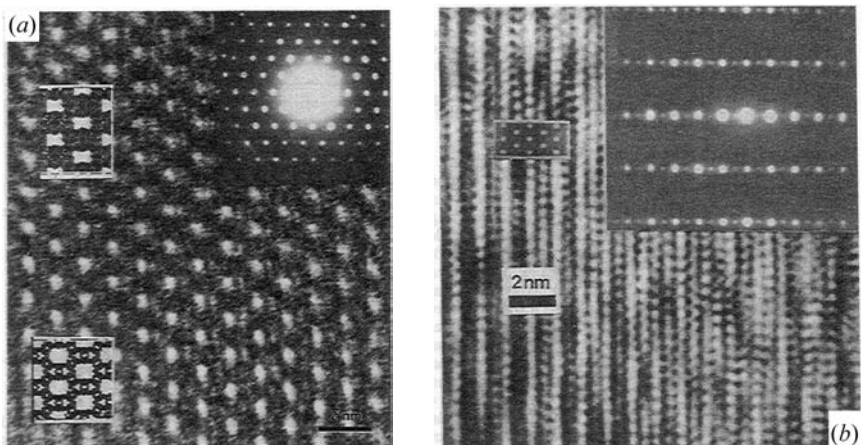


Figure 4.4. (a) (001) ED pattern and the corresponding experimental HRTEM image of MeALPO ($\text{Me} \equiv \text{Zn}$, $\text{Zn}/(\text{Zn} + \text{Al}) = 0.04$) showing 12-ring channels parallel to [100]. Simulated images with and without the electron beam damage are inlaid at the top and bottom, respectively. (b) ED and HRTEM images in (010) with simulated image inset. (After Gai *et al* 1992, Thomas *et al* 2001.)

for 12 hr. Thin sections of MAPO-36 are examined using HRTEM and ED. Figure 4.4(a) shows a [001] ED pattern and the experimental image of MeALPO-36 (with $\text{Me} \equiv \text{Zn}$; $\text{Zn}/\text{Zn} + \text{Al} = 0.4$), simulated images with and without electron beam damage are shown at the top and bottom, respectively of the inset. Figure 4.4(b) shows the HRTEM [100] projection. Determining the short ($\sim 5 \text{ \AA}$) axis by ED is important, because it limits the possible structures to those built up from chains of tetrahedra parallel to the short axis. Examples of such structures are cancrinite, ZSM-23 and ALPO-31. Once the outlines of the structure have been obtained, the atomic coordinates can be refined by distance least-square (DLS) procedures. Further refinements of the crystal structure come from energy minimization computations (Thomas *et al* 2001, Wright *et al* 1992).

The spatial arrangement of the channels is revealed by HRTEM taken parallel and normal to the crystal needle axis. Combining this information with a unit cell derived from ED suggests a tentative structure. Subsequent energy minimization produces atomic coordinates from which an x-ray intensity pattern can be computed (Wright *et al* 1992). It is seen from figure 4.5 that the simulated pattern shows excellent agreement with the observed experimental pattern. Using these methods the framework of MeALPO-36 is determined to be built from four- and six-membered rings and contains large-pore channels bounded by 12-membered rings, half at $z = 0$ and half at $z = 0.5$ (figure 4.6). The structure of MeALPO-36 is similar to that of ALPO-5 where the large apertures are circular. The refined structure is a slightly triclinic (or pseudomonoclinic) unit cell with

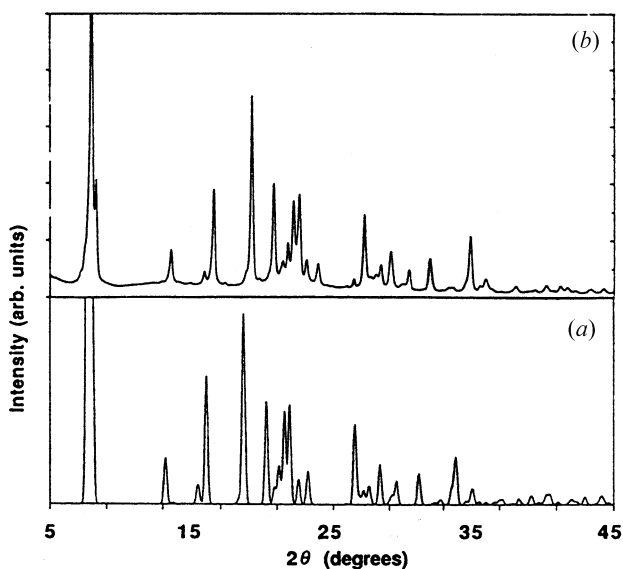


Figure 4.5. (a) XRD of ALPO equivalent of MeALPO-36 simulated based on the lattice constants from figure 4.4 and atomic coordinates by energy minimization; and (b) experimental XRD image (after Gai *et al* 1992, Wright *et al* 1992).

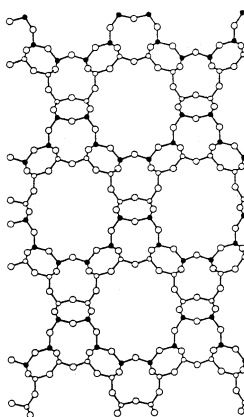


Figure 4.6. Structure derived from figures 4.4 and 4.5. (After Wright *et al* 1992.)

$a = 13.46 \text{ \AA}$, $b = 22.17 \text{ \AA}$ and $c = 5.2 \text{ \AA}$, with $\alpha = 90.16^\circ$, $\beta = 92.01^\circ$ and $\gamma = 89.95^\circ$. Knowledge of the three-dimensional structure of uniform heterogeneous catalysts provides greater insights into their catalytic properties.

Viable solid acid SAPO catalysts can be synthesized and developed to meet

the needs of cleaner and efficient process technologies. As discussed in the previous sections, HRTEM and ED are playing a unique role in determining the structure of complex SAPO structures which are important for understanding their catalytic properties and guiding their development as catalysts.

Chapter 5

Catalysis by supported small metal particles

5.1 Recent developments

A variety of industrial catalytic processes employ small metal-particle catalysts on porous inorganic supports. The particle sizes are increasingly in the nanometre size range which gives rise to nanocatalysts. As described in chapter 1, commonly used supports are ceramic oxides, like alumina and silica, or carbon. Metal (or metallic) catalysts in catalytic technologies contain a high dispersion of nanoscopic metal particles on ceramic oxide or carbon supports. This is to maximize the surface area with a minimum amount of metal for catalytic reactions. It is desirable to have all of the metal exposed to reactants.

The function of the support is also to minimize sintering or coalescence. Higher catalytic conversions are possible with higher metallic dispersion, especially where the turnover frequency (TOF) is small. Other species (e.g. metals or alkaline elements) can be added to change the catalyst surface to yield higher selectivity and activity and such species are called promoters. Some additives give rise to a superior overall activity and this phenomenon is called synergy. The complex compositional and structural heterogeneity of supported metal-particle systems and their nanosizes present great challenges in the identification of the active species and reaction mechanisms that control the catalytic performance. EM-based methods are proving crucial to understanding and developing novel and optimum catalysts. In the following sections we describe how EM methods can be successfully employed to identify local changes in the metal catalyst in catalytic reactions and to design novel systems for rapidly growing technologies in fine chemicals, environmental pollution control and fuel cells.

This chapter aims to present some recent results on the characterization and properties of small metallic and intermetallic particles (a few nanometres (nm) in diameter) supported on ceramic oxide substrates or on carbon. Due to the rapidly expanding development in materials sciences and technology and,

in particular, in the fields of heterogeneous (nano)catalysis, electronics and the related advanced ceramic sciences, all of which incorporate metal–ceramic bonding, the structural properties of metal–ceramic interfaces are of fundamental importance. This is particularly critical in metal–particle catalysis for determining the extent of the catalytic reaction and catalyst regeneration. They are the topics of fundamental research. Furthermore, metal surfaces can be modified by molecular self-assembled (chemisorbed) layers on metal surfaces introducing changes in the wetting of metal particles on the substrate and adhesion. The selectivity and activity of metal catalysts on ceramic substrates are often influenced by specific interfacial chemical interactions, which can also influence catalyst regeneration mechanisms. For a high activity catalyst, retaining both the activity and stability of such fine metals free from agglomeration or sintering yet accessible to reactants becomes a primary consideration. Fundamental research on the characterization of these fine metal–particle systems including bimetallic and intermetallic ones is therefore necessary.

With finely dispersed metal particles (with nm sizes) on ceramic substrates, catalysis is generally facilitated by active sites on the exterior surfaces of the metallic systems following gas adsorption and chemisorption. During the reaction processes, these small particles may sinter and agglomerate resulting in the loss of surface area. The diffusion phenomena governing the dynamics of these small metal-particles and metal–substrate interfacial interactions are increasingly important in determining the catalytic properties of supported metal catalysts, the catalyst deactivation, regeneration and for the stability of these composite materials during operational cycling. In addition, active sites may well be on certain equilibrated metal crystal surfaces, which may be labile during reactions. These issues are addressed in the following sections. Recently, many techniques, including HRTEM, EELS and EXAFS have been pushed to their limits in the analysis of small supported particles, surfaces and clusters, since very small particles are thought to be the active species. The relationship between the state of dispersion of metals and catalytic properties is important (Anderson 1975, Boudart 1981).

5.2 Facile versus structure-sensitive reactions

Reactions which may occur on sites consisting of one or two atoms only on the surface of the catalyst are generally known as facile reactions. Reactions involving hydrogenation on metals are an example. For such reactions, the state of dispersion or preparation methods do not greatly affect the specific activity of a catalyst. In contrast, reactions in which some crystal faces are much more active than others are called structure sensitive. An example is ammonia synthesis (discovered by Fritz Haber in 1909 (Moeller 1952)) over Fe catalysts where (111) Fe surface is found to be more active than others (Boudart 1981). Structure-sensitive reactions thus require sites with special crystal structure features, which

in turn depend greatly on the catalyst's particle size and synthesis. Normally only a fraction of the surface is active in structure-sensitive reactions. Since the speed of the catalysed reaction may depend on the crystal face exposed by the metal-particle catalyst, the shape and crystallographic orientation of the particles are of great importance.

Based on TEM studies of supported metal catalysts, several workers have concluded that their catalysts were made of two-dimensional discs or 'rafts', where virtually all atoms are at the particle surface. However, sample tilting experiments in TEM have shown that great care should be exercised in the interpretation of TEM images of small particles (<2 nm in size), since phase contrast effects may dominate and variations in the particle contrast with specimen orientation can occur as a result of amplitude contrast effects (Treacy and Howie 1980). Sample tilting is therefore necessary to ensure correct interpretations of TEM images of metal-particle catalysts. This will be discussed further in the following sections.

We first review the factors affecting catalyst structures, sintering of small metal particles and ceramic substrates and describe the unique contributions of electron microscopy.

5.3 Preparation and characterization of model and practical metallic catalysts

In supported metallic catalysts, the metals are usually from Groups VIII and VB of the Periodic Table. For highly dispersed metallic catalysts, the support or the carrier is usually a ceramic oxide (silica or alumina) or carbon with a high surface area, as described in chapter 2. Supported metallic catalysts can be prepared in a number of ways as described by Anderson (1975). A description of some of the methods used to prepare representative model (thin film) and practical (technological) powder systems follows.

5.3.1 Monometallics: single metals on amorphous alumina

Model metal catalysts can be prepared by vacuum evaporation of the metal on supports and this method offers a simple and convenient way of investigating surface reactions between metals and gases. Some selected examples of support preparations are as follows.

Non-porous amorphous alumina films (several hundred ångströms thick) can be prepared by the anodic oxidation of clean, high-purity Al. The oxide film is separated by dissolving any unoxidized metal in a mercury chloride solution. The oxide films are then washed in distilled water and collected on suitable electron microscopy grids. They are dried and heated to $\sim 800^\circ\text{C}$ to obtain amorphous Al_2O_3 . High-purity wires of the desired metals can then be vacuum evaporated on to the films in an evaporator. These films can also be prepared using Al-nitrate,

tartaric acid and an organic reducing agent and heating the mixture at moderate (~ 200 – 400 °C) temperatures.

As described in chapter 1, alumina constitutes a family of materials which are highly significant in heterogeneous catalysis and ceramic science. The solid state chemistry and the materials science of aluminas are quite complex. Several metastable phases form under different preparative procedures. Varying hydroxyl (OH) population on the surface gives rise to different structural characteristics. At high temperatures, the most stable form is α -alumina or corundum. 'Transition aluminas', namely γ - Al_2O_3 and η - Al_2O_3 , have cubic structures and may be prepared with reasonably good surface areas. γ - Al_2O_3 is a defect spinel. The surface areas of α -alumina are typically $50 \text{ m}^2 \text{ g}^{-1}$.

Silica substrates can be prepared by chemical etching and ion milling (using argon ions) single-crystal Si discs which are then oxidized in air at ~ 1200 °C. A thin uniform layer of amorphous silica is obtained. Model silica supports can be prepared by thermal oxidation of Si. Metallic films can then be deposited as previously described. Co-precipitation or impregnation techniques use silica suspended in solution (Anderson 1975). Small silica spheres have been employed for HRTEM studies (Datye *et al* 1992). α - and β -cristobalites forms of silica have also been used as catalyst supports (Berneau *et al* 1990). Novel chemically stabilized forms of cristobalite-silica can be synthesized as described in chapter 3 (Gai *et al* 1993) for use as stable catalyst supports. Chemical vapour deposition (CVD) method can also be used to prepare model catalysts. In this method, organometallic catalytic precursors with high vapour pressure are applied to a support by heating in vacuum or in gas environments. Methods such as chemical impregnation of the support by the metal catalyst are also common. The presence of hydroxyl groups on an oxide support facilitates the chemical process.

5.3.2 Model and practical (real-life) bimetallic systems

For model evaporated binary alloy or bimetallic systems, normally a double crucible containing ingots of the two components of the alloy are used in an evaporator and the electron beam is switched between the two metallic sources. The dwell time is varied so as to obtain a uniform distribution of each metal in the required amounts on the support.

For practical (real) catalyst systems, precipitation, ion exchange, impregnation and sol-gel processing procedures are used. In precipitation methods, a hydroxide or a carbonate of a metal may be precipitated from a solution of a metal salt onto the support material held in the solution. Thus, a copper-silica catalyst may be prepared using a Cu-nitrate solution in which silica is suspended. Additives of any alkali cause the precipitation of copper hydroxide onto the silica support. This is then dried and normally reduced in hydrogen at moderate temperatures (~ 400 – 500 °C) to form the catalyst. In 'co-precipitation techniques', the support is precipitated simultaneously with the active catalyst. In the ion-exchange method, for example, highly dispersed Pt on

silica can consist of the exchange of Pt-tetrammine ions from the solution with protons on the silica. In a sol-gel process, in the preparation of the gel from a solution, finely dispersed colloidal particles are generated which are normally held together by Van der Waal forces. Highly concentrated solutions with a good supersaturation are required for the formation of small crystallites. We describe EM examples of a commercial Pt/alumina catalyst prepared by the sol-gel process and of nanocatalysts (clusters) in the following sections.

5.4 Catalytic mechanisms on supported metals

5.4.1 Single metal particles

In processes employing supported metal particles, catalyst deactivation may occur either by the growth or sintering of small metal particles during the reaction resulting in a decrease in the surface area of the active phase; by foreign species acting as poisons; by carbon or coking or (hydro) carbon residues during reactions; or by metal-support interactions. We examine microstructural modifications in each case later.

5.4.2 Ceramic surfaces

Scientific understanding of ceramic surfaces and, in particular, of catalytic supports is important and there has been much progress in recent years. Here we describe some of the important developments in understanding ceramic surfaces and applications in catalysis.

The most important characteristics of a ceramic surface are its composition, geometry and thermodynamic properties such as the surface energy, surface tension and surface entropy. The surface energy determines crystal habit, modes of crystal fracture, growth directions and cleavage planes. Surface energy and the related surface tension profoundly influence pore geometry and wetting (e.g. with metal), the latter is of great importance in supported metal-particle catalysis. Of course, these properties are greatly influenced by the presence of surface defects and impurities. The surface energy (s_A) of a surface area A and the surface tension (γ) of a solid are related by the formula:

$$\gamma = d(s_A)/dA.$$

Atoms in the free surface of solids (with no neighbors) have a higher free energy than those in the interior and surface energy can be estimated from the number of surface bonds (Cottrell 1971). We have discussed non-stoichiometric ceramic oxides like titania, FeO and UO₂ earlier where matter is transported by the vacancy mechanism. Segregation of impurities at surfaces or interfaces is also important, with equilibrium and non-equilibrium conditions deciding the type of defect complexes that can occur. Simple oxides like MgO can have simple anion or cation vacancies when surface O²⁻ and Mg²⁺ are removed from the surface,

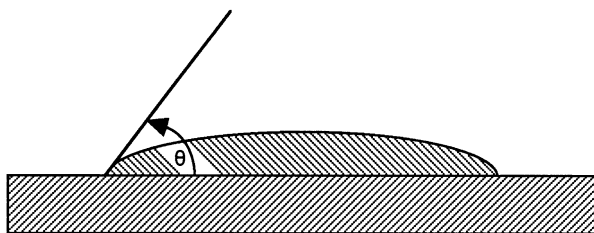


Figure 5.1. Schematic diagram of a crystallite (or droplet) on a support with wetting or contact angle θ .

respectively. The physics of interionic potentials is used in the calculations of surface energies and tensions. Calculations for formation energies of such atomistic defects exist for simple oxides like MgO, NiO (Stoneham 1981).

5.4.3 Metal–ceramic interface interactions: wetting and interfacial energies

The phenomena which occur in metal–ceramic interface interactions are of great importance in catalysis. There are two types of interactions: those which depend on the epitaxy between the metal and the support and those which are independent of it. Strong metal–support interactions are described by the term SMSI.

In practice, the characteristics of the metal–ceramic interface are the metal-particle wetting angle and adhesion. These can be related to several components of the interfacial energy. In addressing the metal–ceramic interfaces, the surface energy term becomes very important. For a droplet or a crystallite on a ceramic support (figure 5.1), the two important quantities are the wetting angle (or contact angle with the support) θ , and work of adhesion w . Another term influencing catalytic reactions is the interfacial energy between the metal and the support. The calculation of these energies is complicated by surface roughness, any chemical reactions which are dependent on gas atmospheres and impurity effects and it becomes even more complex under dynamic reaction conditions. Various phenomena such as spreading, contraction, shape change, etc can be explained by the concept of wetting of metal-particle crystallites on ceramic substrates using Young's well-known equation (Stoneham 1981):

$$\gamma_{sg} - \gamma_{cs} = \gamma_{cg} \cos \theta$$

and

$$w = \gamma_{cg} + \gamma_{sg} - \gamma_{cs}$$

where γ are the surface energies between pairs of crystallite (c), support (s) and gas (g) and θ is the wetting angle.

In the equation, generally if the magnitude of the right-hand side exceeds one, the wetting angle would be complex with crystallite (or particle) spreading

occurring for positive values. For negative values, metal–support contact is maintained by applied forces. The interfacial free energy between the crystallite and the substrate is given by

$$\begin{aligned}\gamma_{cs} &= \gamma_{cg} + \gamma_{sg} - (U_{\text{int}} - U_{\text{str}}) \\ &= \gamma_{cg} + \gamma_{sg} - U_{cs}\end{aligned}$$

where U_{int} is the interaction energy per unit area between the catalytic crystallite and the substrate and U_{str} the strain energy per unit area to the mismatch of the two lattices (Ruckenstein *et al* 1981). When there is a chemical interaction, U_{cs} becomes very large and γ_{sg} decreases. This favours the extension of the crystallite over the substrate. This can happen in H_2 because of the interaction between TiO_2 and metal particles, as well as in O_2 .

5.4.4 Particle nucleation and sintering in supported metal catalysts

Metal-particle sintering (or growth) plays a key role in the deactivation (i.e. loss of activity) of supported metallic catalysts, resulting in the loss of the entire surface area in some cases. This has now been well established in a number of studies using a variety of methods, namely, TEM, x-ray diffraction and selective chemisorption following early studies of Pt on titania supports by Tauster *et al* (1978). Platinum supported on alumina is the most widely studied system and EM techniques are providing direct observations of the sintering phenomena. There have been various studies to elucidate sintering mechanisms using ‘model’ catalysts which, as described earlier, are normally thin films of metals evaporated onto ceramic substrates. The situation becomes more complex in practical (commercial or technological) systems which are normally powders, where the preparation methods as well as the micro structure and morphologies of the metal and support are different.

As the concepts and conclusions derived from platinum/alumina and related systems have sufficiently general applications in other related systems, we address these issues in the following paragraphs. In supported metal particles, the small particles may sinter during the reaction to form a smaller number of larger particles. This can result in a loss of active surface area (e.g. of the active metal, of the support or both). The sintering process can occur by several mechanisms involving surface or volume diffusion of the species, migration of the species and coalescence and evaporation. However, these mechanisms are not fully understood. We first review earlier models and then describe recent developments.

5.4.4.1 Mathematical models of sintering processes

Two mathematical models for sintering mechanisms for supported metals have been put forward: (1) a particle migration model where particles migrate over the surface of the support, collide and fuse, causing loss in dispersion (e.g. Ruckenstein *et al* 1984); and (2) an atomic migration model involving the

migration of atomic or molecular species from small metal particles to large metal particles is considered (Flynn and Wanke 1974, Wynblatt and Gjostein 1975). The species migrate over the support surface and are incorporated into larger metal particles. These two proposals are, however, not new and are based on Brownian motion similar to that associated with the coagulation of a colloidal suspension in the case of model (1), and the Ostwald ripening mechanism in the case of model (2). It is important to know which mechanism dominates in a reaction and this, in turn, is influenced by the reaction conditions and metal–support interactions. These postulations and quantitative theoretical models have been described in the review by Wynblatt and Gjostein (1975) and this is now summarized.

EM techniques are powerful structural methods for exploring these sintering phenomena directly. The most important parameters affecting catalyst sintering include: gas atmospheres, temperature of the reaction, nature of the support and metal loading. *In situ* dynamic ETEM and microanalysis are proving to be very powerful tools with which to observe these effects directly. Here, we review both the theoretical and experimental approaches to understanding metal-particle sintering. A better fundamental understanding of catalytic sintering is necessary to improve the stability and design of metal catalysts.

5.4.4.2 Early empirical correlations of sintering data

The earlier investigations, previously referred to, used empirical models to understand sintering. Here, the dispersion (D') of a sintered catalyst (e.g. Pt/alumina) is correlated with the dispersion of the fresh catalyst (D'_0), using a power law:

$$-dD'/dt = kD'^n$$

where k is given by a rate function obeying Arrhenius' law

$$k = A \exp(-E/RT)$$

in which E is the activation energy for the process, and n the order of the power law and D' is the dispersion after time t (and is used as a function of time at constant temperature). However, care should be taken when applying these somewhat idealized mathematical models to understand often complex dynamic catalytic reactions. The best method at present appears to be direct probing of dynamic catalytic reactions by *in situ* ETEM to understand specific sintering processes during the reaction.

5.4.5 Particle size distributions (PSD): measurement of dispersion of metal particles on supports

Catalytic treatment of supported metals can lead to a change in the metal surface area. Therefore it is necessary to obtain the metal dispersion (size) as a function of the reaction conditions. EM methods including HRTEM, ETEM,

diffraction contrast, STEM annular dark-field imaging are very powerful direct techniques for observing particles down to the sub-nanometre level but skill and knowledge of these methods are necessary to use them successfully. For very small particles (<1 nm in size), support effects (e.g. phase contrast effects of the image generation) may obscure the visibility of the metal particles in HRTEM and particle dispersion may be non-uniform. Representative samplings are therefore important. These aspects and the visibility of metal particles are discussed later. Researchers should be aware of these effects for accurate analysis. If necessary, complementing the EM information with other techniques such as chemisorption is also recommended. These are outlined along with their limitations. In practice, EM methods remain the most powerful ones for direct analyses of particle-size distributions and for the characterization of particles.

Some of the earlier investigations have used XRD to obtain particle sizes utilizing x-ray line broadening, and small angle x-ray scattering (SAXS). However, both of these methods have limitations in the size analysis in that small particle sizes may escape x-ray detection by being averaged out in a highly dispersed metallic system and scattering from porous supports in SAXS may be overwhelmed by strong metallic scattering.

5.4.6 Selective gas adsorption or chemisorption

As discussed in chapter 3 on oxide catalysis, the surface areas of powders or solids are determined using the N₂ adsorption at its boiling point by the BET method. An adsorption apparatus is used to monitor the amount of N₂ adsorbed. The BET formula then gives the amount of N₂ corresponding to a monolayer for a given sample. Selective gas adsorption or chemisorption is the most common method for measuring particle dispersion. The amount of gas uptake by the metal particles is measured at a standard temperature and pressure, and converted to dispersion by assuming adsorption stoichiometry (i.e. it equals the ratio of the number of adsorbate atoms adsorbed/surface metal atoms), and is reported as the number of square metres of surface per gram of metal (m² g⁻¹). Selective adsorption (chemisorption) thus allows an estimate of the amounts of metal surface available for catalysis.

Measurements can be made either statically or dynamically and selective gases like CO (or H₂) can be used. In the static experiment, a known amount of gas is added to a known amount of metal catalyst. Each gas molecule takes up a specific area on the metal surface (typically the gas is not adsorbed on the inert support surface). In the dynamic experiment, gas is pulsed over a catalyst. The amount of gas remaining in the pulse after contact with the metal is measured and, as before, the gas on the metal surface is calculated by difference to estimate the surface area available for catalysis.

Selective adsorption results before and after a reaction can indicate the loss in surface area due either (1) to poisoning of the metal surface or (2) to reaction of the metal to form non-catalytic surface layers (e.g. the formation of support oxide

layers on metal surfaces), (3) coke (carbon) formation on particle surfaces and (4) sintering of the metal particles leading to a loss of active area or a combination of some or all of these phenomena. We illustrate correlations between electron microscopy and adsorption data using the example of Pt/alumina catalysts and SMSI in Pt/titania catalysts. Pt-based catalysts are of interest in automotive emission control catalysis and steam reforming of methane ($\text{CH}_4 + \text{H}_2\text{O} \rightarrow \text{CO} + 3\text{H}_2$) to produce H_2 .

5.4.7 Particle migration model and its limitations

Earlier studies (Wynblatt and Gjostein 1975) on particle migration were limited to particles less than 5 nm in diameter. The rate-limiting steps are believed to be (1) surface diffusion controlled (where the rate of migration is the controlling process) and (2) coarsening controlled (where the fusion of two particles becomes the rate controlling process). Wynblatt and Gjostein suggest that the fusion of metal particles may not be the rate-controlling process above 500 °C. During the initial stages, metal sintering may occur by particle migration but this may not be relevant to the agglomeration of larger metal particles. In the case of Pt/alumina, agglomeration is observed to continue even when the size of the metal particles exceeds the size of the support particles. This suggests the presence of other sintering mechanisms such as Ostwald ripening. In very small crystallites (with sizes of ~ 1 nm), a partial migration model has been proposed whereby the interactions between metal atoms are thought to be stronger than those between the metal and the support. Under catalytic conditions at or above the Tamman temperature (defined as 0.5 melting point (MP)), the crystallites are in a quasi-liquid state and the entire atomic species can migrate across the support, collide and coalesce. However, in the 'atomic migration' model, migration of atoms is involved. This incorporates transport of atoms from a metal crystallite to the support, migration across the support and capture of these atoms by other particles. In evaporation, vapour transport of an atomic species from a convex surface with higher vapour pressure to concave areas takes place, usually at high temperatures. Diffusion via grain boundaries can also occur.

Catalyst particle nucleation in the initial stages and their subsequent growth play an important role in catalytic mechanisms. In a model Pt/alumina catalyst, the general view is that the formation of particles is a stepwise process incorporating the following steps (Wynblatt and Gjostein 1975, Cottrell 1971): individual metal atoms (called monomers) transform to two-dimensional islands, which subsequently transform to three-dimensional clusters. These clusters eventually transform into finite-sized particles.

5.4.7.1 Particle migration, collision and coalescence

A binary collision model has been developed for particles migrating over planar supports. The rate-controlling steps in these mechanisms are either particle

migration or coalescence. Growth by interparticle transport can occur by diffusion either by vapour phase transport or over the support surface.

In particle growth by interparticle transport, larger particles with a lower chemical potential will grow at the expense of smaller particles with a higher chemical potential. Particle growth expressions are then derived from the classical Ostwald ripening mechanism described in the next section. Particle growths on irregular supports (a situation normally encountered in practical commercial catalysts), the support curvature (or irregularity) and contact or wetting angles greatly influence particle migration and sintering.

5.4.7.2 Ostwald ripening mechanism

Precipitation of particles from supersaturation of a solute in a crystal matrix was investigated by Frank (1950). Models for such a process were developed by Greenwood, Lifshitz and Wagner *et al* and Zener, and these have been reviewed by Christian (1975). For shorter nucleation times, the particle size distribution (PSD) is narrow during the precipitation of particles from a high supersaturation. When most of the excess solute is precipitated, greatly reducing the supersaturation, the smaller particles begin to dissolve and the larger particles grow by consuming the smaller particles, which is a process known as Ostwald ripening. The driving force for ripening is the concentration gradient, the concentration of the solute at the smaller particles is greater than the average supersaturation and is less at the larger particles. There is therefore a flow of solute atoms from smaller to larger particles through the crystal matrix.

Extensive experimental work and modelling exist on the precipitation process in metallic alloys (e.g. Cottrell 1971, Jain and Hughes 1978). Considering the ripening process by volume diffusion of solute atoms through the crystal matrix, these studies suggested a growth law for the precipitates, where the particle radius R seems to follow the $t^{1/3}$ law. However, in general, the diffusion of a solute is much more complex, especially in the presence of grain boundaries and dislocations which affect the process. For simplicity, we can consider three types of processes that determine the kinetics of particle ripening:

- (1) evaporation or condensation of solute atoms across the surface of crystal matrix (i.e. regardless of diffusion through the bulk) at the precipitate particles;
- (2) bulk or volume diffusion; and
- (3) diffusion of a solute through the crystal matrix dominated by dislocation pipe or grain boundary diffusion.

In the case of supported metal particles, experimental studies of particle growth mechanisms can determine the type of ripening. Generally, studies on supported noble metallic catalysts at elevated temperatures ($>500^\circ\text{C}$) indicate atomic diffusion from smaller metal particles across the surface of the support to

larger particles (Wynblatt and Gjostein 1975). The following paragraphs review some of the models and experimental data applied to supported metal particles.

In supported metallic systems, in the atomic migration model, the simplified steps are: diffusion and migration of the metal-atom species along the support surface and capture by larger particles which thus grow at the expense of smaller particles, giving in effect a 'bimodal' particle size distribution (PSD) (figure 2.9). As described earlier, this mechanism is known as Ostwald ripening and the rate of Ostwald ripening may depend on many factors: rate of surface migration of atomic species or their capture, and metal loading. Various metal-particle studies have suggested that the predominant sintering mechanism between 500–800 °C is Ostwald ripening. In any event, experimental conditions are often complex, leading to complicated sintering mechanisms and accurate determinations of the predominant mechanism have often been difficult. For example, in the mathematical models, surface reduction or changes due to catalysis are not considered. Under oxidation in Pt/alumina, PtO₂ monomers may be formed.

5.5 Experimental studies by electron microscopy

5.5.1 Sintering of Pt/alumina

As mentioned earlier, TEM sintering studies of model metal-particle catalyst systems supported on carbon-filmed TEM grids provide better insights into the coarsening phenomena. However, their applications to real catalyst systems may not be straightforward because of the differences in the model and real systems outlined in the earlier sections. To avoid this difficulty in preparing TEM samples of real catalyst samples, a new technique for preparing commercial Pt/alumina catalysts has been described by Harris *et al* (1983) using a sol-gel method. In this method, an aqueous tetramine platinum chloride is used with (η) alumina sol to dip-coat the TEM grid. After drying, calcining and reducing thin films of the real catalyst are readily obtained for EM. Other examples (e.g. ceria gels) using such methods have also been described in the literature. Catalysts thus obtained are then subjected to a series of heat treatments at ~600 °C. Following the method in Flynn and Wanke (1974), PSDs are developed by dividing the particle size range into 10 Å increments. A population of ~1000–2000 particles from different areas on both a heat-treated and a fresh sample are measured. For each heat treatment, an average particle diameter d_A and surface average diameter d_S are measured. n_i is the number of particles in diameter increment with a mid-point of d_i Å (following Adams *et al* 1962):

$$d_A = \sum n_i d_i / \sum n_i \quad \text{and} \quad d_S = \sum n_i d_i^3 / \sum n_i d_i^2$$

where d_S is the average value. If all the particles are assumed to be spherical, this would produce the observed surface area and is therefore the key to relating the number of particles to surface area measurements. The surface area of the

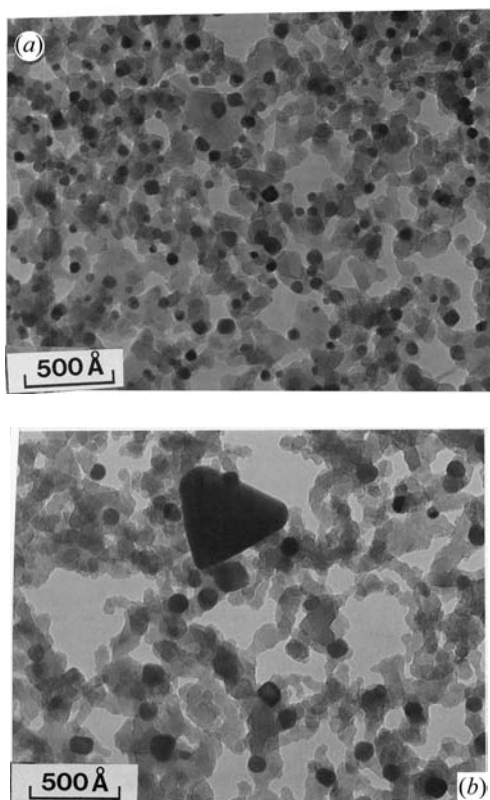


Figure 5.2. (a) Fresh Pt particles on alumina support and (b) catalysts reacted for 24 hr. (After Harris *et al* 1983.)

fresh catalyst samples is measured in air at 600 °C for 2, 8 and 24 hr. The sample reactor tube is flushed with H₂ at 500 °C for 1 hr, followed by Ar at 500 °C, 1 hr (TEM indicates no sintering under these conditions). After the sample is cooled to room temperature under Ar, 0.1 ml slugs of H₂ are injected and the experiment repeated several times. The surface areas are calculated assuming spherical particle geometry and an adsorption stoichiometry of unity and a Pt surface density of 1.12×10^{15} atom cm⁻². This gives d_s which can then be related directly to the TEM measurements.

Experimental TEM images show that the particle shapes are spherical for sizes less than 5 nm and increasingly faceted above this. The growth of Pt particles in the fresh sample and in the sample which has been reacted upon for 24 hr, respectively, is shown in figures 5.2(a) and (b). The corresponding PSDs are shown in figures 5.3(a) and (b). Table 5.1 shows the average particle size as a function of sintering time. Analyses of PSDs may help to interpret particle

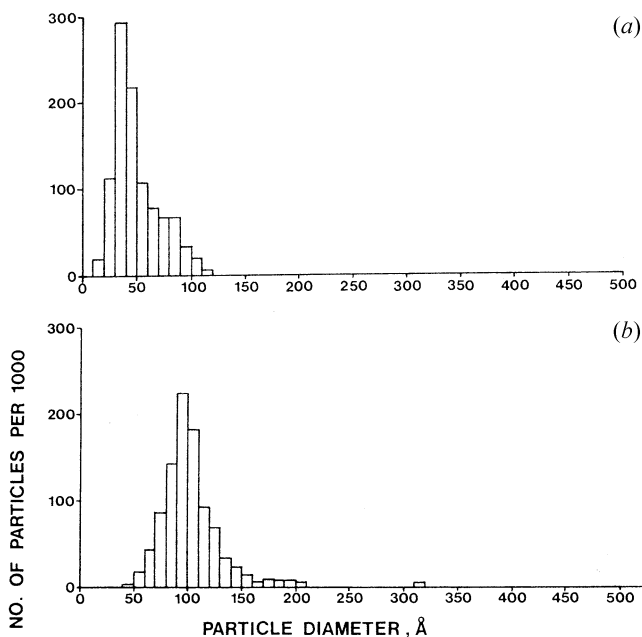


Figure 5.3. Particle size distribution of particles in figure 5.2: (a) fresh; (b) after 24 hr. (After Harris *et al* 1983.)

Table 5.1. Average particle sizes for the supported Pt catalysts heated in air at 600 °C.

Sintering time (hr)	Number average diameter d (Å)
0	49.8 ± 1.0
0.5	66.0 ± 1.6
2.0	73.5 ± 1.6
8.0	95.3 ± 2.0
16.0	103.0 ± 3.0
24.0	109.0 ± 3.0

sintering mechanisms. As described earlier, Wynblatt and Gjostein have shown that the particle growth kinetics can be represented by the expression:

$$n \log[R/R_0] = \log t + \text{constant}$$

where R_0 and R are the particle radii of the fresh sample and of the sample at time t , respectively. Thus a plot of $\log[R/R_0]$ versus $\log t$ gives a value of n , giving the sintering order ($n + 1$). Figure 5.4 shows this plot. It can be seen that the sintering order changes from ~ 14 to ~ 7 after 2 hr. This may indicate a change in

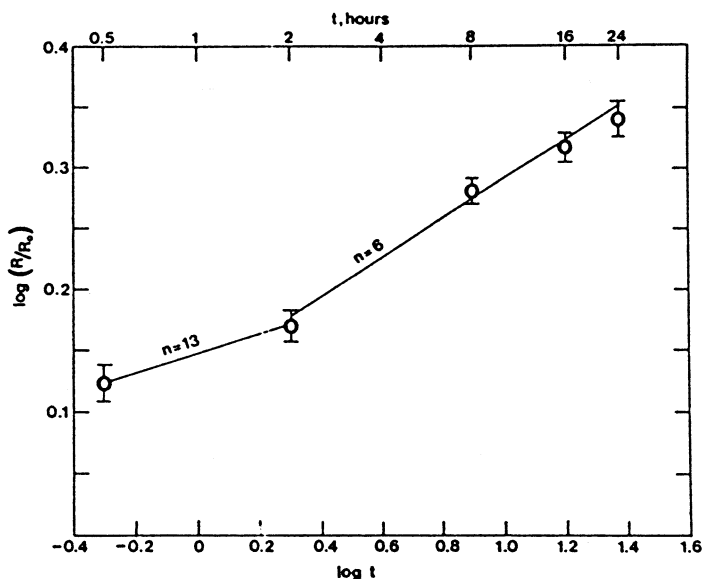


Figure 5.4. Interpretation of catalyst sintering: plot of $\log R/R_0$ versus $\log t$ (R_0 and R are the radii of the fresh and reacted catalyst particles at time t , respectively. (After Harris *et al* 1983.)

Table 5.2. Surface average diameter determined by TEM and H₂ adsorption.

Sintering time (hr)	d_S (Å): TEM	d_S (Å): H ₂ adsorption
0	68.2 + 2.4	60.0 ± 6.0
2.0	98.6 + 4.9	90.0 ± 9.0
8.0	119.0 + 6.0	122.0 ± 12.0
24.0	174.0 + 9.0	164 ± 16.0

the sintering mechanism from particle migration and coalescence mechanism, to an interparticle transport mechanism. The surface average diameter measured by TEM and H₂ adsorption in table 5.2 show excellent agreement.

5.5.2 Re-dispersion phenomena

Generally, as we have discussed earlier, catalytic reactions at elevated temperatures lead to a loss of metal surface area and catalytic activity. Under certain gas treatments it is shown that 're-dispersion' of sintered or deactivated metal particles is possible. Both published and patent literature cite examples of particle regeneration (e.g. Nakayama *et al* 1984). For example, in Pt/alumina

catalysts, the deactivated catalyst is shown to be regenerated (whereby the original catalytic activity is restored or improved), by treating the catalyst up to 500 °C in an inert gas stream with up to 2% oxygen.

Re-dispersion mechanisms are complex and a better understanding is becoming possible by the advances in dynamic ETEM for direct observations of re-dispersion phenomena in gaseous environments (described in section 5.11) and by HRTEM studies of metal particles on different supports.

5.6 Small particles in HRTEM

HREM methods are powerful in the study of nanometre-sized metal particles dispersed on ceramic oxides or any other suitable substrate. In many catalytic processes employing supported metallic catalysts, it has been established that the catalytic properties of some structure-sensitive catalysts are enhanced with a decrease in particle size. For example, the rate of CO decomposition on Pd/mica is shown to increase five-fold when the Pd particle sizes are reduced from 5 to ~2 nm. A similar size dependence has been observed for Ni/mica. It is, therefore, necessary to observe the particles at very high resolution, coupled with a small-probe high-precision micro- or nanocomposition analysis and micro- or nanodiffraction where possible. Advanced FE-(S)TEM instruments are particularly effective for composition analysis and diffraction on the nanoscale. ED patterns from particles of diameter of 1 nm or less are now possible.

HRTEM imaging of structural transformations induced by electron beam current densities have been reported in the literature. For example, morphological transformations of Au particles supported on silicon monoxide have been followed by real-time HRTEM imaging to extract the relative probabilities and preferred structures of different particle morphologies and size effects (Iijima *et al* 1986). In this system, it is suggested that single-crystal morphology dominates in the particle-size regime of 2–8 nm, with icosahedral and decahedral multiply twinned particles associated with the increase in size. However, the methods used for synthesis greatly influence the particle structure and morphology. In the following sections, we show that single-crystal particles of about a nanometre can be obtained by a single-step sol-gel process.

5.6.1 Supported metal-particle catalysis

Some of the important problems concerning composite metal/support catalyst systems are: the chemical reactivity and interfacial interactions between the metal and the support under working conditions, particle migration, coarsening and diffusion mechanisms, stoichiometry of the support oxide, and the structural and electronic properties of bimetallic and intermetallic systems. Multiply twinned particles (MTP) are described in the following sections. Tauster and Fung (1978) have reported strong metal support interactions (SMSI) for metals on reducible ceramic substrates like titania. Interparticle dispersion and surface coverage in

bimetallic Pt–Rh on silica and alumina supports by STEM have been described by Burkhardt *et al* (1989). Gai and Smith (1990), using *in situ* ETEM, have demonstrated the dynamic behaviour of intermetallic Cu–Pd particle catalysts for the methanol synthesis process. The dynamic studies revealed segregated Pd surface layers in CO, with specific crystallographic faces of only a few ångströms. Particle surfaces and shapes are found to be gas dependent and thus they influence the gas chemisorption. The results indicate that active surfaces and shapes of particles can be engineered using appropriate gaseous conditions.

We first describe the structural properties of small metal particles.

5.7 Experimental and theoretical developments in small metal-particle catalysis using electron microscopy

As described earlier, many EM techniques including *in situ* ETEM, STEM, HRTEM, image analysis and EEELS are being pushed to their limits by researchers to study surfaces and ultrafine particles (or clusters) which are thought to be active species. For catalysis, metal particles are, in general, supported on ceramic substrates. Detection of supported particles less than ~ 10 Å (1 nm) in size is possible by HRTEM; however, caution must be exercised in interpreting the size and surface structure of the metal particles since the surface structure is obscured by the support contrast, as demonstrated by calculations.

5.7.1 Detection and surface structure of very small particles by HRTEM

The detection of very small particles with diameters in the range 1–5 nm or less is difficult in EM instruments which have a limited spatial resolution. In HRTEM, the effect of the support can introduce complications in the interpretation of images of very small particles as we show in the following sections. This new understanding can be used to tailor the catalyst and support structures. Excellent results can be obtained by the use of the newer, ultra high-resolution intermediate voltage (200–400 kV) electron microscopes with which it has been possible to image clusters of metal atoms ~ 0.5 –1 nm in diameter on some ceramic oxide supports. Aberration-corrected EMs offer increased spatial resolution for imaging and analysis.

5.7.2 Image contrast and visibility of supported small metal catalyst particles in HRTEM

Although HRTEM is a very powerful technique for the study of small particles, imaging metal-particle catalysts on supports such as alumina, silica or carbon presents challenges. In order to understand the structure and contrast of very small (<5 nm) supported metal particles which are thought to be the active species in catalysis, key computations of supported small metallic catalysts have been reported by Gai *et al* (1986). Image computations for supported particles, carried

out at both 200 and 400 kV accelerating voltages, at various defoci, support thicknesses and particle sizes and shapes (e.g. cuboctahedron, icosahedron), with and without C_s corrections, have shown that in HRTEM, the particle images are obscured by the support contrast with the loss of surface definition. The computations have revealed better visibility of small cuboctahedron particles which can tolerate thicker supports. They have also shown that higher kV EM is much more favourable for imaging small supported particles. The calculations have demonstrated the need for image simulations for interpreting the image contrast of supported small catalyst particles in HRTEM and that improved resolution is obtained with C_s corrections ($C_s = 0$, ideal EM). In the following paragraphs we illustrate the experimental observations and theoretical developments in interpreting the image contrast from supported small metal particle catalysts.

5.7.3 Examples of image simulations of supported small particles

Energy calculations for small clusters of atoms indicate that a cluster of 55 atoms should be reasonably stable (Mackay 1962, Allpress and Sanders 1970, Hore and Pal 1972). In addition, calculations suggest that the 55-atom cluster will take up an icosahedral structure in preference to the cubic cuboctahedral structure (Hore and Pal 1972).

An experimental diffraction contrast image of model catalysts of Ag/alumina, prepared by evaporation, is shown in figure 5.5(a) at 200 kV. The corresponding EDX spectra from and off the metal particle are shown in figures 5.5(b) and (c), respectively. An HRTEM image of Pt/alumina at 400 kV in figure 5.6.

5.7.4 Theoretical procedures and corrections of spherical aberration

Supported small catalyst particle images are calculated using the dynamical theory of electron diffraction. The following examples show image simulations for model 55-atom cuboctahedral and icosahedral particles (figure 5.7). Calculations are performed at both 200 and 400 kV, at various defoci, with and without the support to understand the effect of the support contrast on the particle visibility. For the computations, particles are oriented along their two-fold axis. The slices along the beam direction (z) are 0.24 nm (Ag/alumina) and 0.23 nm (Pt/alumina) thick. The atomic coordinates for both the amorphous support and the metal particles are sectioned along the beam direction, so that atoms can be placed in large unit cells with dimensions 2.45 nm \times 2.45 nm \times 0.24 nm (for Ag/alumina) and 2.35 nm \times 2.35 nm \times 0.23 nm for Pt/alumina. Arrays 128 \times 128 are used in this study to ensure a real-space sampling of 50 points/nm in the x - and y -directions. The 55-atom particles (which roughly correspond to 1.2 nm diameter particles) are sectioned in five slices. The amorphous layers are simulated by placing 68-Al and 102-O atoms with random x - and y -positions

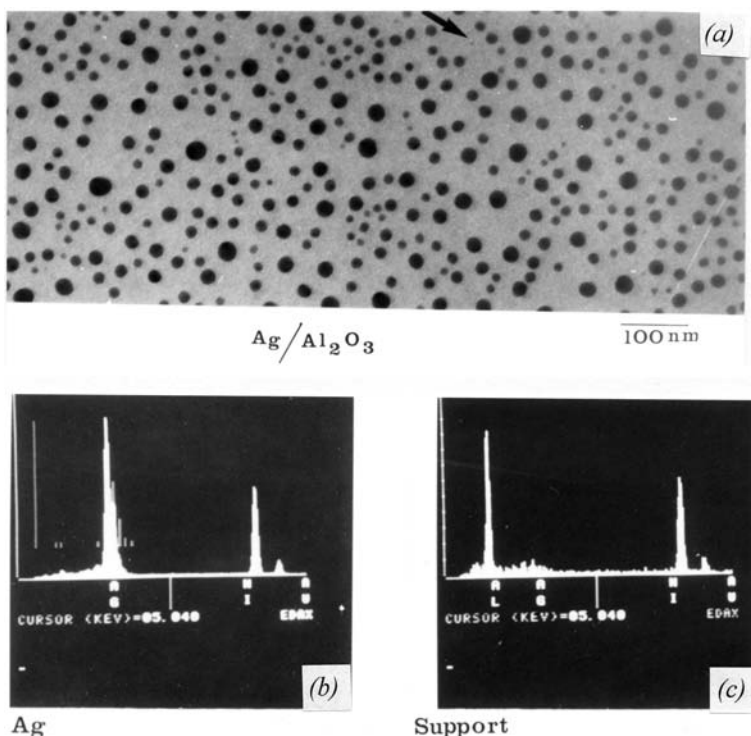


Figure 5.5. (a) TEM image of Ag/alumina catalysts; (b) and (c) are the EDX spectra from and off the catalyst particle, respectively, indicating the Ag metal and the support (sample on Cu-grid).

in the large unit cells, respectively, for Ag and Pt systems, to give a density equivalent to crystalline alumina. Twenty different amorphous slices are used in each case so as to give a good reproduction of the experimental supports. Calculations are carried out for thicknesses ranging from 1 to 20 nm, sizes which are applicable to real catalyst systems. Similarly calculations for Pt on alumina and other supports can be performed. These principles can also be applied to simulate larger particles.

It may be seen that the 55-atom cuboctahedral models are constructed by using silver fcc atomic positions and imposing cuboctahedral faces (figure 5.7(a)). The 55-atom icosahedron (figure 5.7(b)) can be constructed by rearranging the cuboctahedron particle so as to achieve icosahedral faces (Mackay 1962). The atomic coordinates of the icosahedron can then be generated by using the Ag–Ag nearest-neighbour distance.

For the calculations, the following parameters are used for the calculations. For 200 kV HREM, $C_s = 1.2$ mm, the objective aperture radius $R = 0.5 \text{ \AA}^{-1}$,

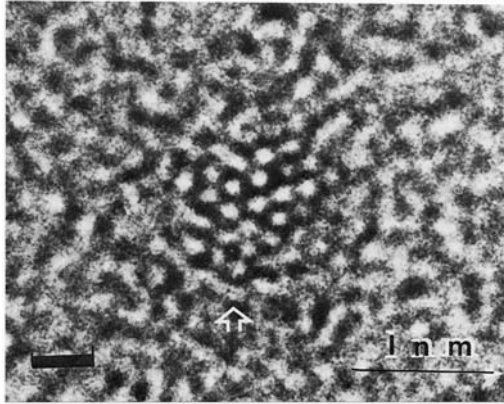


Figure 5.6. An HRTEM image of a Pt nanoparticle/alumina.

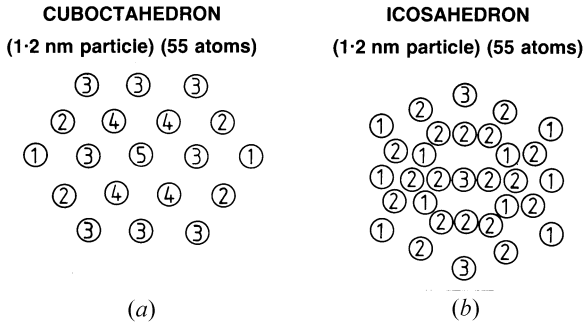


Figure 5.7. Schematic diagrams of 55 atoms (1.2 nm particle): (a) cuboctahedron and (b) icosahedron. The numbers denote the number of atoms on top of each other.

chromatic spread, $FS = 5$ nm and a semi-angular beam divergence of 0.25 mrad; For 400 kV HRTEM: $C_s = 1$ mm, $R = 0.7$ and 1 \AA^{-1} , $FS = 3$ nm and $d = 0.2$ mrad. Micro- and nanodiffraction patterns are also calculated. These are compared with images from an ‘ideal EM’ with $C_s = 0$ (aberration-free) and $R = 1 \text{ \AA}^{-1}$, $FS = 0$ and $d = 0$. HRTEM images are computed at optimum defocus values and at a focus which is at half a Fourier period underfocus from the optimum defocus. A Fourier half-period is given by $\Delta f(1/2) = d^2/\lambda$ (O’Keefe *et al* 1977), where d is the d -spacing of the lattice planes being imaged. This leads to a reversal of the image contrast (dark regions into light regions in an image). Figures 5.8 and 5.9 show the calculated images of an Ag cuboctahedral particle 1.2 nm in size on an alumina support at (a) 200 kV and (b) 400 kV, respectively. Image calculations of a Pt (cuboctahedron) particle on an alumina support at 400 kV are shown in figure 5.10. The calculated image is consistent

with the experimental HRTEM image in figure 5.6. Diffraction contrast images of larger (e.g. 309 atoms) particles show significant changes in the shape of the particle as a function of support thickness and defoci (figure 5.11).

The calculations demonstrate the difficulties in identifying very small supported metal particles and in interpreting their structures only from HRTEM experimental images and that simulations are necessary for image interpretation. The simulations have shown that the bulk structure of the particles, but not their shape, can be identified by diffraction contrast. They further elucidate that cuboctahedron particles have better visibility in HRTEM imaging and can tolerate thicker supports than icosahedral particles. Misaligned particles may create additional problems in imaging and careful orientation of the particles is necessary for them to be clearly visible. The simulations of Gai *et al* (1986) also show that aberration-free EM could be crucial in the interpretation and for new understanding of supported nanocatalysts.

5.8 Structure of small metal particles

5.8.1 Single crystal particles and multiply twinned particles (MTP)

There has been considerable work in the literature on the structure of very small particles and clusters. Interest in this field has been primarily due to Ino's (1966) early experimental studies of normally fcc metals prepared by vapour condensation which showed that a sizable portion of the particles exhibited non-crystallographic structures. These non-crystallographic atomic clusters or polycrystalline nuclei have been observed to consist of pentagonal bi-pyramid or icosahedra form of twinned structures and are known as multiply twinned particles (MTPs). EM studies of supported transition metal catalyst systems have indicated that MTPs sinter faster in catalytic reactions leading to the loss of surface area and are not beneficial to catalysis (Gai 1992). We describe the structure and the role of MTPs in catalysis in the following sections.

MTPs can be considered as five or 20 fcc tetrahedra joined by twin boundaries to yield decahedra or icosahedra (figure 5.12(a)). These tetrahedra do not form a completely space-filling structure and require elastic strains or grain boundaries to do so. An HRTEM image of an Au MTP (including a decahedral particle) is shown in figure 5.12(b). The early experimental results and nucleation theories for the formation of MTPs have resulted in a number of studies aimed at understanding the relative stabilities of small particles. The scope and significant features of these studies have been described by Hoare *et al* (1972), Gillet (1977), Heinemann *et al* (1979), Marks and Smith (1981) and Yacaman *et al* (1992). Most of the theoretical studies have involved potential or surface energy calculations of small particles.

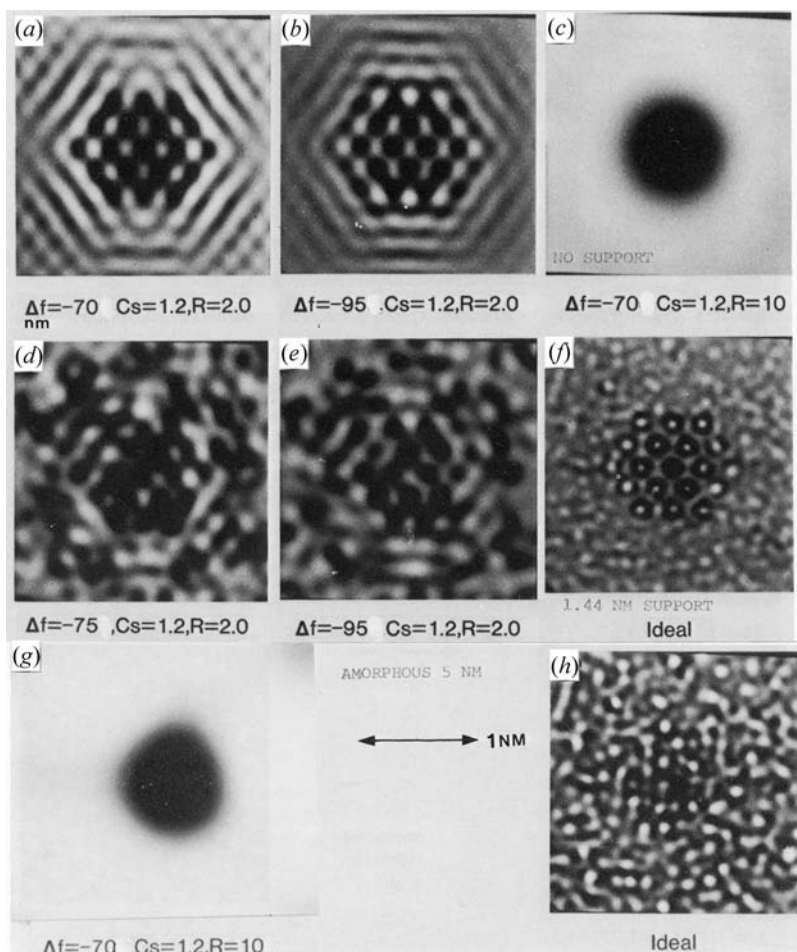


Figure 5.8. Simulated HRTEM images of supported metal-particle catalysts: cuboctahedron, Ag particle (55 atoms, 1.2 nm) at 200 kV. The images are: (a) near optimum defocus (Δ_{opt}), with no substrate; (b) half a Fourier period underfocus from (Δ_{opt}); (c) diffraction contrast image; (d) and (e) with amorphous alumina support of 1.44 nm thick showing that the support contrast obscures particle visibility; (f) ideal EM image with no C_s showing higher resolution. (Simulations also show that particle are just visible with a support thickness of ~ 2 nm but the visibility decreases markedly after that); (g) diffraction contrast image with 5 nm support (particle shape seems to change); and (h) ideal EM image with 5 nm support and $C_s = 0$ (spherical aberration-corrected). (After Gai *et al* 1986.)

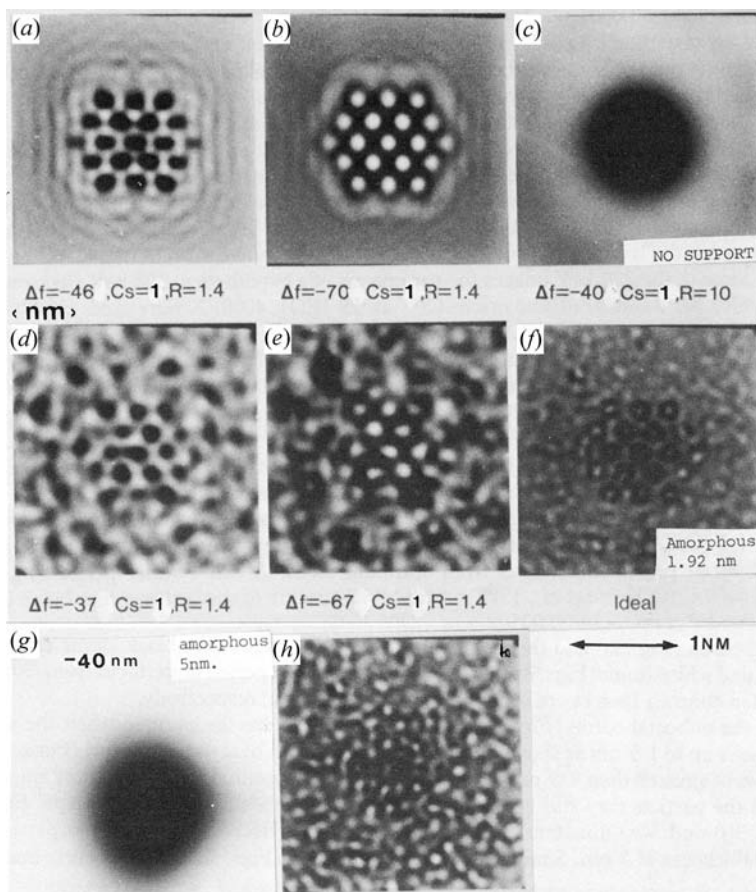


Figure 5.9. Simulated images of 1.2 nm Ag particle/alumina at 400 kV: (a), (b) and (c) are images with no support, near (Δ_{opt}), at half a Fourier period underfocus from (Δ_{opt}), and diffraction contrast, respectively. (d) to (f) are images with amorphous support of 1.9 nm at various defoci. The particle is still somewhat visible. (g) and (h) diffraction contrast and ideal EM images with 5 nm support. (After Gai *et al* 1986.)

5.8.1.1 Defects in MTPs

As described earlier, MTPs are not completely space-filling if considered solely as fcc single-crystal aggregates. For example, a decahedral MTP and an icosahedral MTP configuration leave solid angle deficits of about 0.08π and 0.048π , respectively. Some crystal distortion is therefore necessary to accommodate the deficits. EM (HRTEM and/or STEM nanodiffraction) methods play a key role in determining the nature of such distortions in these nanoscopic particles. Under favourable conditions, HRTEM is useful in elucidating the microstructural details

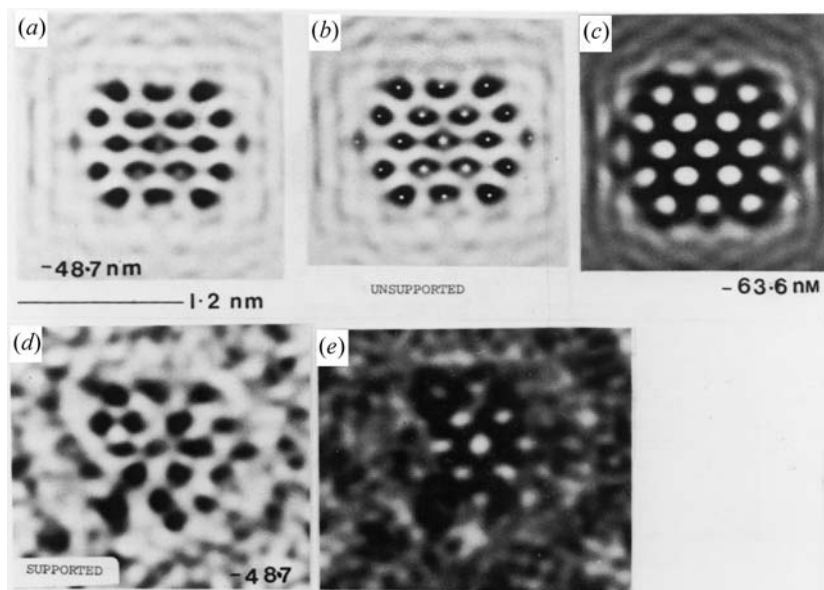


Figure 5.10. Simulations of Pt/alumina (Pt particle: 1.2 nm cuboctahedron) at 400 kV HRTEM. The images are: (a) unsupported particle near (Δ_{opt}); (b) image in (a) with Pt atoms superimposed; (c) white atoms at defocus of -63.6 nm; (d), (e) images with alumina supports 4.6 nm thick at defoci of (d) -48.7 nm and (e) -63.6 nm. The latter is consistent with the experimental HRTEM image in figure 5.6.

in small particles and STEM micro/nanodiffraction mapping provides diffraction information from small local regions. Diffraction contrast techniques (bright- and dark-field weak beam imaging) can also be used to locate defects. The formation and role of such defects are of interest in the sintering of supported metal-particle catalysts used in heterogeneous catalysis.

It is suggested that the favourable surface energies of certain crystal faces (e.g. in fcc, (111)) promote a particular structure consisting of a number of twinned microcrystals (Marks and Smith 1981). In icosahedral MTPs greater than 15 nm in size, the basic defect structure observed in the study consists of a stacking fault parallel with the external surface, terminating on a Shockley partial dislocation or on twin boundaries, with varying defects in the different particles. Lattice rotations are also evident in both larger and smaller particles. These studies indicate that distortions in icosahedral particles are accommodated by inhomogeneous elastic strain in smaller particles and this is combined with dislocations in larger particles. Qualitative defect models exist and these are reviewed as follows.

In icosahedral MTPs, Howie *et al* (1979) correlate the type of distortion with an isotropic inhomogeneous elasticity theory. The type of distortion is first

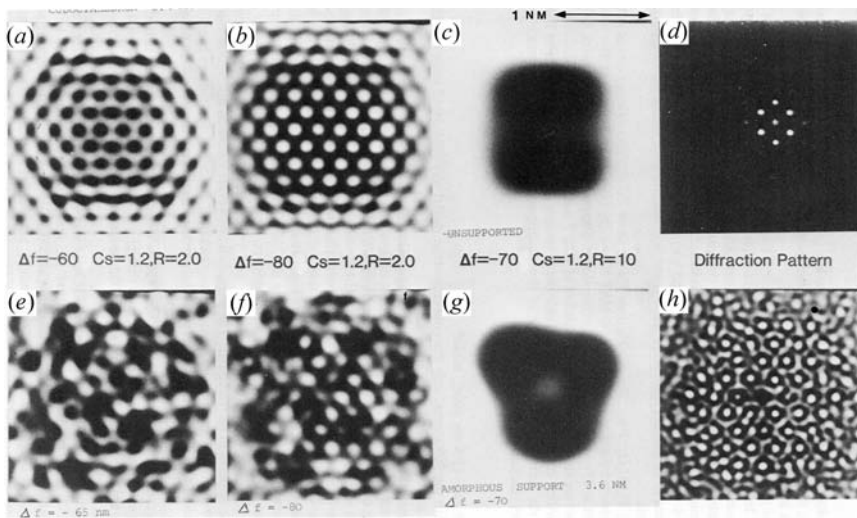


Figure 5.11. Simulations of 309-atom (2.4 nm) cuboctahedron Ag particle/alumina at 400 kV HRTEM. Images with no support in near (Δ_{opt}) and black atoms (a); at defocus -80 nm with white atoms (b); diffraction contrast image (c); and ED (d). Images with supports 3.6 nm thick and different defoci: (e) -65 nm; (f) -80 nm; (g) diffraction contrast image—with change in particle shape; and (h) ideal image with $C_s = 0$. The diffraction contrast images show significant shape changes at higher support thicknesses. (After Gai *et al* 1986.)

considered by applying normal tractions to the twinned faces of the tetrahedral units, which leads to an expansion between the faces. To accommodate this stress, Shockley partial (screw) dislocations may form and expand from the surface via a glide process; Frank partial dislocations may form and expand by the climb process; or there may be a mixture of the glide and climb of a full dislocation. EM has confirmed the presence of Shockley partials ruling out the other two stress-relieving mechanisms. In decahedral MTPs, defects due to twin boundary relaxations and stacking faults are found near twin boundaries. In larger particles (>30 nm), a loss of five-fold symmetry is sometimes observed due to twin boundary migration and stacking fault formation (Marks *et al* 1981). In smaller particles lattice rotations are not observed indicating the absence of inhomogeneous lattice strain.

5.9 EM studies of chemical interactions at metal–support interfaces

Solid–solid interfaces are a key element in many areas of materials technology. In electronics, hybrid circuits and power devices require an increasing variety of

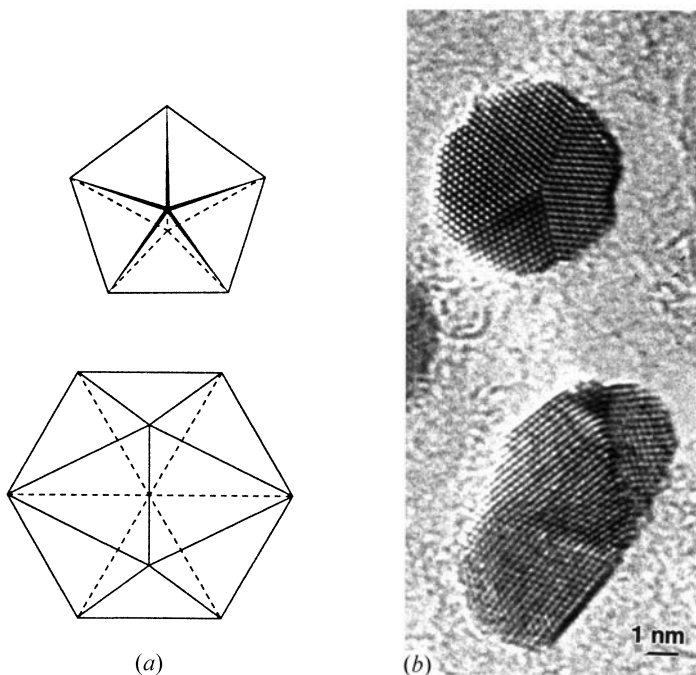


Figure 5.12. Multiply twinned particles (MTPs): (a) decahedral MTP (top) and icosahedral MTP; (b) an HRTEM image of Au MTP. The decahedral MTP is at the top.

stable metal/ceramic supports as well as metal/semiconductor interface contacts. Chemical interactions can contribute to the strength of the metal–ceramic bond and this can be exploited in the catalytic as well as in the electronic sciences. The performance and reliability of metal to ceramic support adhesion or contacts is determined by many factors, for example their synthesis, chemical and material properties. Our understanding of these parameters and their influence on the adhesion (bond) strength is still somewhat limited. HRTEM, electron diffraction from nano-areas (<1 nm in diameter) and EDX microanalysis with (sub)/monolayer sensitivity are helpful in studying the bonding and nature of the chemical interaction at the interfaces at the atomic level. In addition, catalyst deactivation due to changes in the microstructure or microchemistry can be distinguished.

5.10 Metal–support interactions

The chemical and physical interactions between small metal catalyst particles and the support are complex. They may introduce morphological changes in the particles and affect their reactivity. Studies of such modifications of supported

particles are particularly important in reduction–oxidation (redox) cycles and in the regeneration of catalysts to restore their activity. Interactions of metals on reducible (wetting) oxide supports and also on irreducible (non-wetting) oxide supports have recently received considerable attention. The majority of the studies have been static, *ex situ* experiments (samples reacted *ex situ* and examined in EM at room temperature). We examine these studies in the following sections and show that some of the complexities of metal–support interactions can be better understood by observing the interactions directly under dynamic reaction conditions using *in situ* ETEM.

5.10.1 Strong metal–support interactions (SMSI) and electronic structures: *In situ* atomic resolution ETEM

Supported metal catalysts on reducible oxide supports may lead to strong metal–support interactions (SMSI), especially in reductions. SMSI may be characterized by a sharp decrease in chemisorption, thermal sintering and an altered catalyst morphology. Proposed mechanisms include electron transfer from the support and under normally reducing conditions, the support material covering the metal particles which, in some cases, deactivates the catalyst by preventing further gas reaction. Tauster and Fung (1978) observed that the chemisorption properties with respect to H₂ and Co of Group VIII metals (e.g. Pt) are considerably reduced when supported on a reducible transition-metal oxide like TiO₂ at high temperatures (>500 °C). This reduction was accompanied by a decrease in the rates of structure-sensitive reactions. Several noble metal catalysts on TiO₂ and transition metals on TiO₂ (e.g. Ni/TiO₂ and Fe/TiO₂) have shown this behaviour. The role of SMSIs in other reactions such as syngas is also of interest. The combination of materials and the exact conditions are highly specific, for example, the reaction is strongly influenced by the addition of another type of particle, e.g. adding Pt to Ag/TiO₂.

Several mechanisms for SMSI have been put forward to explain the loss of chemisorption and catalytic properties. These include the electronic effect, following the transfer of an electron from Ti to the metal, the formation of covalent bonding and intermetallic compounds, the existence of H₂ spillover and the coverage of the metal by TiO_x suboxide species (Tauster and Fung 1978). Such electron transfer to Pt reduces its d-band vacancies (making it less active), thereby reducing its catalytic activity. Explanations of the physical effects include the extensive migration of TiO_x overlayers on metal particles, thus physically blocking the active metal surface. Sanchez *et al* (1987) discuss the oxygen vacancy model in SMSIs. In this work, the interaction between metal atoms with anion vacancies in the oxide support is considered. The occupancy of vacancies by metal atoms is affected by the type of support. In fluorite oxide supports, the interactions are limited to metal occupancy of surface vacancies due to the diffusion barrier created by support cations. In rutile-type supports, metal diffusion into the support bulk vacancies is possible under reduction, because of

the open framework of the cations.

In Pt/TiO₂, as described in the preceding sections, it is suggested that a metal which is capable of dissociating H₂ (e.g. platinum) introduces SMSIs under appropriate reaction conditions at elevated temperatures. There is evidence for reduced oxide phases being involved in this system and in those with other noble metals (Tauster *et al* 1978, Baker *et al* 1979, Harris *et al* 1983, Bradford *et al* 1998, Logan *et al* 1989): migration of suboxides TiO_x over Pt particles: for example, at ~500 °C, white Pt/TiO₂ changes to a grey 'Pt/Ti₄O₇' non-stoichiometric compound and suppression of chemisorption is observed. However, more work is required to understand the precise mechanisms of the nanoscale overlayer formation in gas environments and the migration of support species at moderate temperatures.

In situ atomic-resolution ETEM is providing the most direct evidence of the nature of the SMSI phenomenon at the atomic level (Gai 1998). Figure 5.13(a) shows a fresh Pt/TiO₂ powder synthesized from the reaction of TiO₂ with a Pt chloride solution, consisting of finely dispersed Pt in titania. Figures 5.13(b) and (c) show dynamic atomic-resolution ETEM images of the Pt catalyst particle P during *in situ* H₂ reaction at 300 and 450 °C, respectively. The atomic lattice of the particles is clearly visible under gas environments and at high temperatures. A Ti-oxide overlayer (confirmed by EDX) of ~6 Å covers the particle in H₂ (figure 5.13(c)). The atomic level dynamic studies further illustrate that there is no epitaxial relation between the overlayer and particle morphology/orientation. The image shows the simultaneous emergence of single nanocrystals of Pt with ~0.2 nm lattice spacings, (arrowed). Analysis of the dynamic surface atomic structure of supported metal catalysts is therefore very important. In addition, the cathodoluminescence technique in the EM is expected to play a key role in improving our understanding of the nature of electronic structural changes in both the metal and the support in SMSI.

EM is also playing a key role in understanding the mechanisms in reduction, interface interactions and the regeneration of supported metal-particle catalytic systems under different reaction conditions. Suppression of CO chemisorption on noble metals supported on titania is also thought to result mainly from SMSI, based on studies in which the chemisorption ability is found to be restored at least partially by heating the reduced catalysts in O₂ and then reducing at 250 °C (Li *et al* 1989). In these static *ex situ* EM studies, it is found that the effect of SMSI on the hydrogenation of adsorbed CO differs from one noble metal to another. These studies indicate that the nature of SMSI is complex and more work is needed to understand its role in specific catalytic reactions better. Studies on transition metals such as Ni/TiO₂ at different temperatures show spreading or extension of particles (probably NiO) in oxygen followed by contraction in H₂, e.g. at 700 °C. At 730 °C in H₂ the formation of pits has been observed (Baker *et al* 1979). Ni is thought to facilitate the reduction of TiO₂ to Ti₄O₇ which migrates over the metal particles. Alternate changes in crystallite morphology are observed in Ni/TiO₂ in H₂ at 500 and 700 °C (Ruckenstein and Lee 1984, 1987). These are thought to

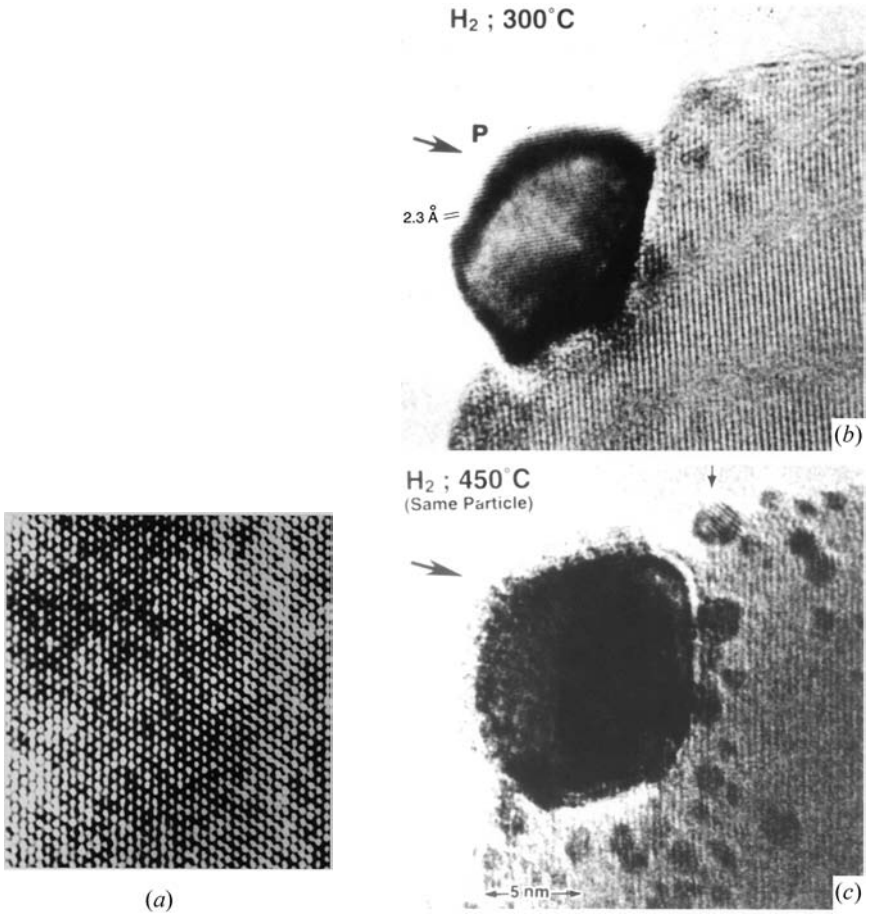


Figure 5.13. *In situ* atomic-resolution ETEM image of Pt/titania catalyst: (a) finely dispersed Pt particles; (b) *in situ* real-time dynamic activation in hydrogen imaged at $\sim 300^\circ\text{C}$. The 0.23 nm (111) atomic lattice spacings are clearly resolved in the Pt metal particle, P; and (c) the same particle imaged at $\sim 450^\circ\text{C}$, also in H_2 . SMSI deactivation with a growth of a Ti-oxide overlayer (C), and the development of nanoscale single-crystal clusters of Pt, with atomic resolution (arrowed). (After Gai 1998.)

be associated with the extension and contraction of particles. (From these studies SMSI in Ni/TiO₂ is shown to be more pronounced in oxygen.) In these studies, the extension of Ni particles over TiO₂ in H₂ is attributed, for example, to the decrease in interfacial free energy between substrate and crystallite, γ_{ce} , caused by SMSI between TiO_{2-x} and Ni. In contrast, in O₂, extension is a result of the lower surface free energy of oxide compared to that of the metal and of the lower interfacial free energy between the metal and the substrate caused by the reaction

between oxidized crystallite and substrate.

SMSI is also thought to affect methanation catalysts (normally transition metal or noble metals supported on alumina), which are used in the production of substitute natural gas (SNG). In general, heating in H₂ causes sintering on alumina and silica supports and heating in O₂ or steam can cause dispersion and particle coalescence at ~200 °C (Rukenstein and Lee 1984, 1987, Nakayama *et al* 1984). The data have been based on *ex situ* EM studies. Here EM methods, especially under dynamic reaction conditions, can provide a wealth of new insights into metal–support interactions under reaction conditions.

In the following example, we examine the role of different gases and metal–support interactions in metal-particle catalysts supported on the so-called non-wetting or irreducible ceramic oxides by dynamic EM. The direct observations provide powerful insights into the role of gas environments in catalytic reactions and in the regeneration of supported metallic catalyst particles.

5.11 *In situ* ETEM studies of metal–irreducible ceramic support interactions

In situ ETEM permits direct probing of particle sintering mechanisms and the effect of gas environments on supported metal-particle catalysts under reaction conditions. Here we present some examples of metals supported on non-wetting or irreducible ceramic supports, such as alumina and silica. The experiments are important in understanding metal–support interactions on irreducible ceramics.

5.11.1 Copper/alumina systems in different gas environments

The following examples describe *in situ* studies of copper metal catalysts supported on alumina in different gas environments.

The dynamical behaviour of metal particles or films deposited on ceramic surfaces is of great importance in heterogeneous catalysis and in other areas of materials science such as metal brazing of ceramics and microelectronics. The dynamic nature of metal–ceramic interactions which is a function of the environment and temperature is crucial in determining the extent of deactivation and dispersive regeneration mechanisms in metal-particle catalysts supported on high surface area ceramic oxides (and in interfacial bonding in microelectronic devices). The existing understanding of metal-particle sintering is primarily based on static room temperature *ex situ* studies, which have considered only the surface spreading of the metal on the support as described in the previous sections (e.g. Nakayama *et al* 1984). *In situ* ETEM of copper/alumina and other metal/ceramic oxide systems under controlled environments have provided the first direct evidence for the diffusion of metal particles through the bulk of an irreducible ceramic substrate (Gai *et al* 1990).

Previous studies of metal dispersion in oxidative environments on irreducible ceramic oxides (e.g. Wang *et al* 1981, Burkhardt *et al* 1989) have not incorporated

the contribution from the bulk diffusion through the support preceding surface spreading to form a thin film. Studies of metals on irreducible oxides (including γ -alumina) and strongly interacting reducible oxides like titania (Tatarchuk *et al* 1981) have been performed *ex situ* under static conditions (cooling samples to room temperature after reactions and removing them from reaction environments for characterization), which may not represent the dynamic reaction conditions accurately as described earlier. This makes it difficult to obtain insights into the reaction sequences. *In situ* ETEM experiments from the same regions of the catalyst sample in controlled gas environments provide insights into the dynamic nature of the metal–ceramic interaction. They are described in the following sections. The relative contributions of the surface and bulk diffusion of metal catalysts correlated with electron spectroscopy for chemical analyses (ESCA) and SEM, elucidate the nature of dynamic metal–support interactions.

Copper/alumina is a commercially important system. It is used in catalysts for the synthesis of methanol by the hydrogenation of carbon monoxide at $\sim 250^\circ\text{C}$ (Madix *et al* 1982) and is of interest in water–gas shift reactions (Bond 1987). It is also an important candidate for the fabrication of microelectronic devices. In the following example, Cu catalysts supported on alumina are prepared by electron-beam evaporation ($\sim 50 \text{ \AA}$ Cu) on an alumina substrate $\sim 200 \text{ \AA}$ thick. High-quality non-porous amorphous alumina is prepared by anodic oxidation of aluminum and the structure is confirmed by HRTEM. For comparison, other metals (transition and noble) (e.g. Ni, Ag, Pd, and Pt) and bimetallic systems (e.g. Cu–Pd, Cu–Ni, Cu–Ru) on alumina and silica (and also carbon) are also prepared using the same procedures and examined to understand the effects of different metals and substrates, thickness, gas environment, temperature and time on metal–irreducible support interactions. Figures 5.14(a) and (b) show examples of dynamic ETEM observations of Cu/alumina catalyst particles recorded in real time at $\sim 200^\circ\text{C}$ from the same area of the sample in CO and in O₂ environments, respectively. Gas pressures of $\sim 0.2 \text{ atm}$ are used and the catalysts are reacted for $\sim 1 \text{ hr}$. The oxygen gas is introduced after outgassing CO. The particles demonstrate quite different behaviour in the different gas environments. Figure 5.14(b) shows particle spreading and complex wetting in oxygen gas and EDX reveals that the lighter regions are devoid of Cu metal. The data are quantified by SEM of both the top and bottom surfaces of the sample showing Cu diffusion through the support and also by ESCA (XPS) depth profiling. ESCA confirms bulk Cu-diffusion through the irreducible alumina substrate (figure 5.15). In ESCA, alumina is deposited over Cu and oxidation studies are performed at $\sim 200^\circ\text{C}$. Depth profiles are obtained with an Ar ion beam. Before oxidation, the results show two layers of material, with Cu below the alumina/Cu interface (i_s in figure 5.15). After $\sim 1 \text{ hr}$ oxidation, copper oxide is observed in alumina through i_s analysed as bulk diffusion of Cu²⁺ species into the substrate.

The spread in oxygen is the result of surface energy effects. As described previously, under equilibrium conditions, $\sigma_{\text{sg}} - \sigma_{\text{ms}} = \sigma_{\text{mg}} \cos \theta$ (where the σ

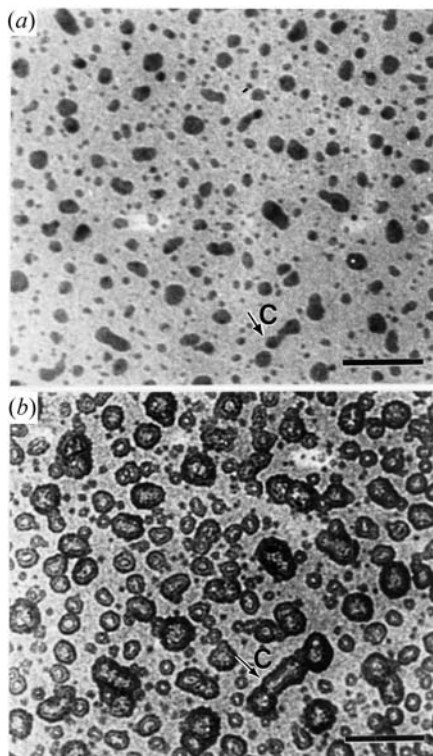


Figure 5.14. *In situ* ETEM studies directly probing a dynamic Cu/alumina catalyst in different gas environments (scale bar is 100 nm). Dynamic images are recorded from the same area of the sample at ~ 200 °C in 0.2 atm gas pressure: (a) in CO gas and (b) in O₂ gas. Complex wetting and spreading is observed in (b). (After Gai *et al Nature* **348** 430.)

are the surface energies between pairs of metal (m), support (s) and gas (g) and θ is the contact angle between the metal particle and the support.) In oxidation σ_{mg} is lowered which decreases θ , leading to an apparent increase in particle radius. It is believed that the resultant volume change upon oxidation and the reduction of σ_{mg} contribute to the driving force for bulk diffusion. Both bulk and lateral diffusion of metal particles are also observed in other metal systems on alumina and silica (and carbon) under dynamic conditions. The results indicate that both the surface and bulk diffusion processes should be considered in the treatment of oxidative dispersion. These discoveries of metal–irreducible ceramic substrate interactions in oxidative environments at moderate temperatures by EM provide a better fundamental understanding of the redispersion and regeneration phenomena of supported metal-particle catalysts. They are leading to a radical revision of the fundamental processes in regeneration catalysis.

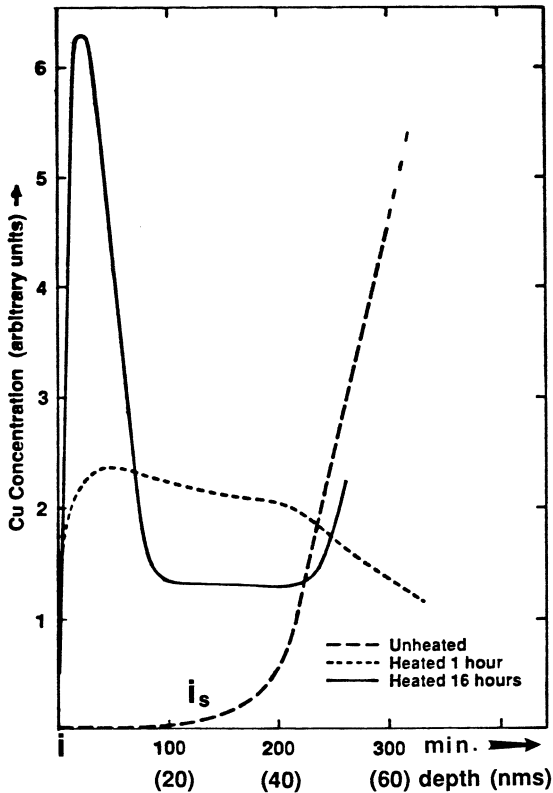


Figure 5.15. ESCA depth profile of Cu diffusion through an alumina substrate following oxidation at $\sim 200^\circ\text{C}$. The sample is etched from the alumina edge (i), towards the alumina/Cu interface i_s . (After Gai *et al Nature* 348 430.)

5.11.2 Ag/alumina

The state of cupric ions dispersed on alumina supports has been described in the previous section. $\text{Ag}/\text{Al}_2\text{O}_3$ is a well-known catalyst for the epoxidation of ethylene to ethylene oxide. The mode of adsorption of oxygen on the surface of Ag particles determines catalyst selectivity and activity. Metal sintering studies on the surfaces of model Ag/alumina using low-voltage SEM are shown figures 5.16(a) and (b) at room temperature and 200°C , respectively, revealing important morphological changes. The sintering behaviour of model silver particles on non-porous alumina has also been examined by TEM. Recently, the Eastman Chemical Co. has announced the vapour phase epoxidation of butadiene over an Ag-based catalyst. Detailed investigations are needed to understand the loss of active metal surface area due to sintering at different temperatures.

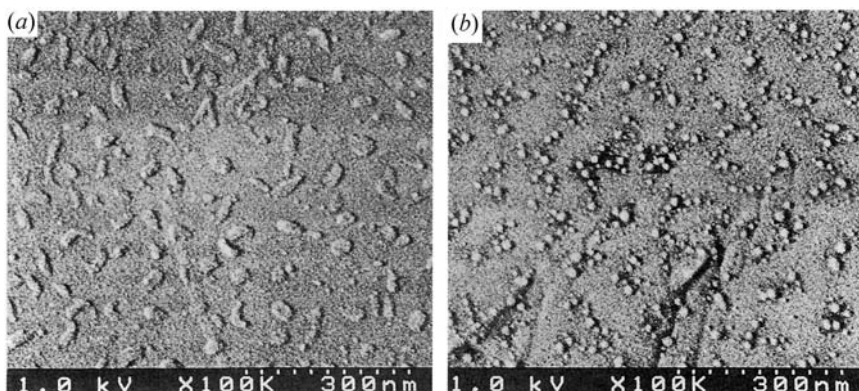


Figure 5.16. *In situ* LVSEM image of (a) the as-deposited Ag/alumina catalyst and (b) when it is dynamically heated at ~ 200 °C.

5.11.3 Pd/alumina and thermal sintering

Supported Pd-based catalysts are used in a multitude of catalytic processes. Here we describe a couple of examples and highlight typical issues in a catalytic process using these catalysts.

Pd/Al₂O₃ catalysts are employed in a number of manufacturing processes including the hydrogen peroxide (H₂O₂) process. Uses of H₂O₂ include as a bleaching agent and an oxidant in some fuels. The loss of catalyst activity in the process is one of the issues. Treatment in a halogen-rich environment is a common redispersal technique for Pd or Pt bearing catalysts on alumina substrates, for which the main deactivation process is often the growth and agglomeration of particles under exothermic reaction conditions. These processes modify the catalyst's microstructure and reduce the surface area available for catalytic reaction, while changes in the microchemistry can modify the activity of particles by blocking some of the surface sites available for the reaction. In some cases, the processes may be combined, and may involve strong metal–support interactions leading to the formation of a new compound or to the incorporation of the metal particles into the ceramic substrate. In either of these cases, the availability of chemically active sites on the surface of the metal may be reduced significantly, with a corresponding deactivation of the catalyst and a reduction in the selective yield of the desired product.

In order to examine the detailed structure, microstructure and microchemistry of the supported catalyst, the powders are dispersed on carbon-film grids for EM studies, using conventional diffraction contrast, HRTEM, STEM and high-precision EDX methods. EDX chemical analyses, for example in a 100 kV FEG STEM, have a high lateral resolution, but the data are averaged through a thin catalyst sample, typically ~ 500 Å thick, and there may be some limited

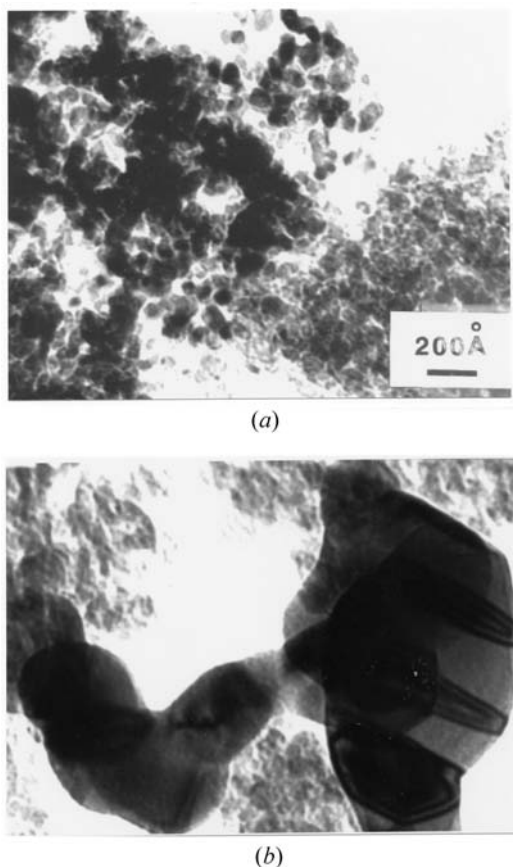


Figure 5.17. TEM image of (a) fresh Pd/alumina catalyst and (b) used catalyst in the H_2O_2 process, showing sintered twinned particles.

broadening of the electron beam as it proceeds through the sample. As discussed in chapter 2, in the novel 2–2–2 200 keV FE(S)TEM, EDX analytical resolution (and therefore the sensitivity of the analysis), can approach atomic resolution for metal catalysts under optimum conditions (Boyes *et al* 2001). In heterogeneous systems such as supported metal catalysts, discrete data from individual selected areas of the sample, for example from an individual particle, are possible using EM methods. (As described earlier, other diffraction techniques such as XRD and neutron diffraction, integrate the information from large volumes of material and thus the data are averaged over many particles). Both types of data may be required in some cases for an adequate description of heterogeneous samples; however, for this type of heterogeneous supported nanoscopic catalyst materials, EM methods are essential.

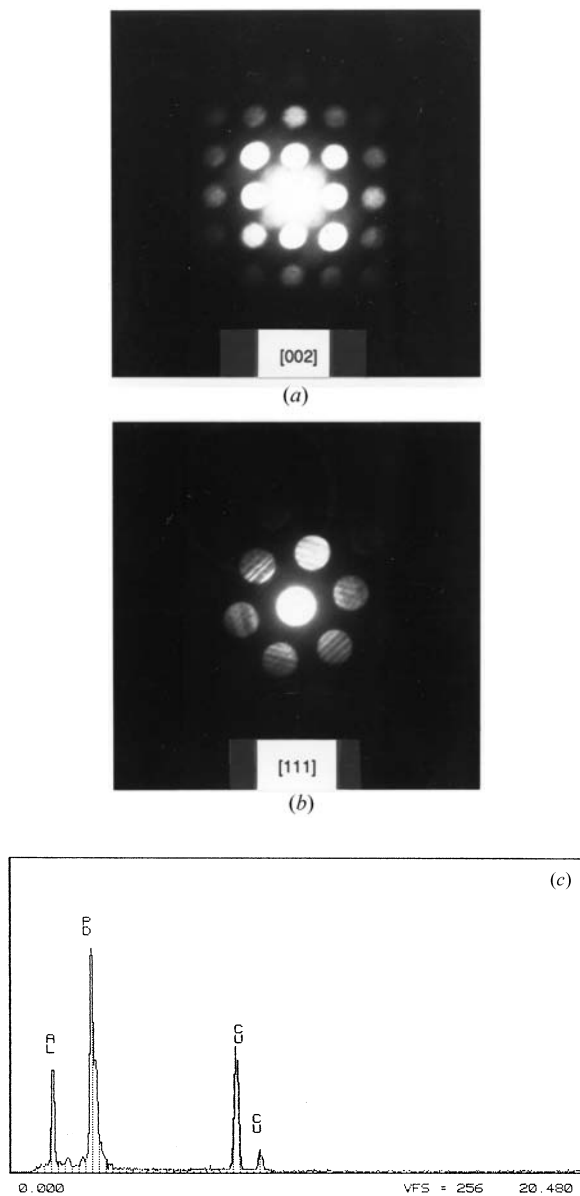


Figure 5.18. (a) and (b) show convergent-beam ED (CBED) patterns in the [001] and [111] zone-axis orientation with the lattice constants confirming that the particles are pure Pd. (c) EDX image from Pd + support in (b). The Cu line is due to fluorescence from the Cu support grid for the sample.

The basic characteristics of the microstructure of a fresh and used catalyst established by TEM are shown in figures 5.17(a) and (b), respectively. They show a uniform dispersion of fine particles in the fresh catalyst. However in the used material shown in (b), there is a significant growth in the average size of the particles through extensive combination of individual particles into polycrystalline agglomerates and a correspondingly drastic reduction in the active surface area. The presence of twins in Pd particles in the H_2O_2 reaction is found to be unhelpful to catalysis. (This indicates that twins provide sites for agglomeration. This leads to metal sintering and a substantial reduction in the free surface available for reaction), confirming work on MTPs described earlier. In principle, informative data on PSDs and shape functions are available from EM methods. However, in practice, real powder catalyst samples may present challenges in determining their PSDs because of the very small particles on supports with complex morphology. LVSEM is playing a major role in addressing this issue of separating chemical/structural and topographic/morphological contrasts (Boyes 2000). The use of polished cross-section samples in the SEM is a powerful method for separating the chemical/structural information and topological/morphological contrasts, for example, in the Pd/alumina case described here, by suppressing the contribution of the latter to the image and analysis. The identification of the main particles as crystals of fcc Pd metal is confirmed by complementary diffraction in (S)TEM (figures 5.18(a) and (b)), and by direct EDX chemical analysis (figure 5.18(c)). The presence of the Cu peak in the spectrum is due to the use of a copper support grid for the sample, and the Al peak is due to the inclusion in the analysis volume of some of the support alumina material. The results confirm that the particles are essentially pure Pd. In modern EM instruments all the structural and complementary chemical information can be obtained from the same local area of a catalyst sample.

The heavily agglomerated particles in the used samples are much larger than the pores or particles in the support. X-ray mapping of the material (after embedding in epoxy resin and polished) to determine the gross distribution of the Pd and Al distribution indicates long-range segregation (and coarsening) of Pd to the outside of the agglomerate of alumina particles. High-precision EDX confirms that the centre is completely free of the Pd. Such detailed analyses indicate that deactivation of the catalyst particle during the operation is microstructural, rather than microchemical, in origin. TEM studies demonstrate a large-scale agglomeration of the particles leading to a reduction in the catalyst's surface area, together with macroscopic segregation of Pd (which produce areas depleted in active Pd). They provide powerful insights into working catalysts and enable appropriate remedial procedures. These include the addition of a second metal to inhibit sintering.

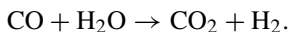
Similarly, the addition of Ag in Pd–Ag alloy catalysts with Ag on the surface changes the selectivity in acetylene polymerization.

5.12 Methanol synthesis and oxidation reactions

Methanol synthesis is the subject of extensive research in heterogeneous catalysis. This is because methanol can be easily transformed into a source of fuel. The synthesis is carried out using synthesis gases, namely by the hydrogenation of carbon monoxide ($2\text{H}_2 + \text{CO} \rightarrow \text{CH}_3\text{OH}$ or from $\text{H}_2/\text{CO}/\text{CO}_2$ reactions) over catalysts. Most of the current catalysts are based on the $\text{Cu}/\text{ZnO}/\text{Al}_2\text{O}_3$ system; however, other catalyst systems are also being tested (Klier 1982). It is generally believed that the alumina acts as a structural stabilizer. However, the nature of the active sites and the role of the individual components in the complex catalyst system in the catalytic process are not fully understood. Some of the suggestions are that the activity is related to the Cu surface area. Chemical reaction studies of CO_2/H_2 with reduced $\text{Cu}/\text{ZnO}/\text{SiO}_2$ catalyst at $\sim 120^\circ\text{C}$ show copper formate and other species (produced from the hydrogenation of interfacial bidentate carbonates) at the interfaces of Cu and ZnO, influencing the methanol synthesis. The addition of CO to the stream is shown to result in the decrease of such species (Millar *et al* 1992). Modifications of the structural and electronic properties of the particle and support surfaces as well as the interactions of the metals with supports clearly play a key role on the catalytic performance. EM studies on model systems provide insights into the active surfaces and some examples are described here.

5.13 Monometallic nanocatalyst systems: copper nanocatalysts supported on silica (Cu/SiO_2)

The mechanism for methanol synthesis from mixtures of H_2 , CO and CO_2 over supported Cu catalysts have been studied extensively in the literature using a number of chemical methods (Bell *et al* 1995). One of the key issues has been the role of CO and CO_2 in maintaining the carbon supply for methanol synthesis or interconversion between the two via the water–gas shift reaction:



Unpromoted Cu/SiO_2 is found to have a low activity for methanol synthesis from H_2/CO mixtures, whereas an increased activity from H_2/CO_2 . Alkali metal promotion increases the activity for methanol synthesis from the H_2/CO mixtures, probably due to the increase in surface OH groups engaged in the formation of the formate species which are the precursors to the methanol. Cu/SiO_2 powder catalysts (with ~ 5 wt% Cu) can be prepared by ion exchange of silica with $\text{Cu}(\text{NO}_3)_2$ in aqueous solution, followed by calcination and reduction. Such preparations contain very fine Cu particles (~ 0.5 nm) on a powdered silica support as revealed by HRTEM.

5.14 Bimetallic or alloy systems: atomic structure and composition

Following pioneering studies by Sinfelt (1985), it is now well established that alloying an active metal catalyst with another metal (which may not be catalytically active), can produce catalytic properties, which are often unobtainable with the individual components of the binary system. The resulting changes in electronic behaviour, the surface and their relationship with the bulk geometry and composition play a critical role in catalytic reactions. Bimetallic/intermetallic and multimetallic catalyst nanoparticles on multiple supports are being increasingly employed in the chemical industries, in particular in the control of vehicle exhaust emissions and in petroleum reforming. Advances in synthesis and characterization are taking place enabling the design of optimal catalysts. EM is playing a major role in understanding and designing such complex catalysts. The role of EM is particularly important since bulk phase diagrams and bulk diffraction techniques cannot be applied to derive the phases, structures and compositions (including the surface enrichment of one metallic specie over the other) of such nanosized catalyst particle systems accurately. In the following sections we address some of the issues using examples of model and practical 'bimetallic' systems and highlight the role of EM in their development.

Intermetallic compounds of transition metals with rare earths (RE), e.g. Cu-RE-based intermetallics, are employed in methanol synthesis (Owen and Lambert 1987) and other reactions described here. The thermal stability and sintering properties in different gas environments greatly influence the catalytic activity. Exposure to oxygen and CO₂ also affect the catalytic activity and regeneration processes. Both these environments are found to decrease the synthesis activity. Pre-treatment in hydrogen appears to activate the precursors toward better methanol synthesis. However, EM studies on working bimetallic and intermetallic catalysts and understanding of active sites are limited. Here we describe some recent EM studies on transition metal-noble metal compounds which provide insights into these characteristics. The studies show that catalysts can be manipulated during the reaction to produce compositions with desirable catalytic properties. Insights gained from model systems can then be used to understand complex practical bimetallic or multimetallic catalysts.

5.14.1 Cu-Pd alloy system: structure, phase stability and catalysis

Supported Cu-Pd catalysts have the potential to provide new alternatives to conventional commercial methanol synthesis catalysts (based on the Cu-ZnO-alumina system). Cu-Pd catalysts are also of industrial interest in hydrogenolysis and CO oxidation (Bulatov 1995). To interpret the catalyst behaviour and selectivity, including CO hydrogenation, a fundamental understanding of the structure, surface structure and stability of the phases in this system is required. The Cu-Pd phase diagram indicates that at temperatures greater than 600 °C, Cu

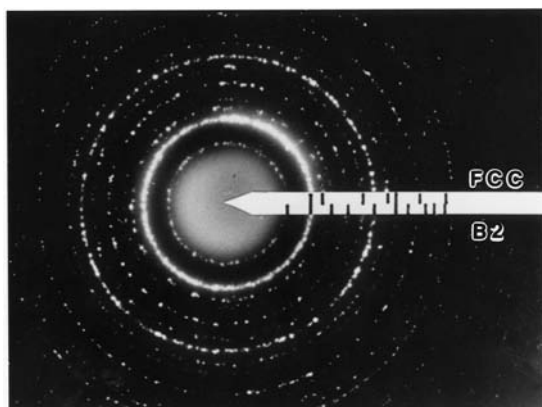


Figure 5.19. ED image of model Cu–Pd intermetallic catalyst system on the carbon support of interest in methanol synthesis showing the presence of both fcc and bcc phases.

and Pd form a continuous solid solution of fcc alloys. Below 600 °C ordered phases are obtained with the structural formulae Cu_3Pd (the α -phase) and CuPd (the β -phase). β -CuPd has the CsCl (B2) type structure (chapter 1), with a lattice parameter 2.988 Å. The lattice parameter for the fcc phase is 3.76 Å which corresponds to a Cu:Pd ratio of ~50%. (It varies depending on the ratio of Cu:Pd.) Chemical studies of Cu–Pd-based catalysts in acetylene hydrogenation reaction (Guzi *et al* 1985) and *in situ* ETEM studies for the system in methanol synthesis ($2\text{CO} + \text{H}_2 \rightarrow \text{CH}_3\text{OH}$) (Gai and Smith 1990) have been reported. The addition of excess Cu has been found to inhibit the hydrogenation of ethylene ($\text{C}_2\text{H}_4 + \text{H}_2 \rightarrow \text{C}_2\text{H}_6$) but to increase the activity in the hydrogenolysis of pentane. The mechanisms involved in these processes are not clearly understood, but modifications of the structural and electronic properties as well as the metal–support interactions are thought to play a key role in controlling the catalytic activity. Adsorption of the reducing gases onto single-crystal Cu–Pd surfaces have shown that the maximum desorption temperature of CO from $\text{PdCu}(111)$, which is a fcc phase, is lower than that from $\text{Pd}(111)$, i.e. it is less tightly bound to the alloy surface, whereas H_2 is desorbed at the same temperature indicating that a similar binding energy is required in both cases (Noordeemer *et al* 1986). Surface energy calculations have been performed to predict the nature of surface segregation (e.g. either Cu or Pd) in the related compounds (van Langeveld 1983) but experimental studies in reaction environments are limited. There have been a number of studies on the nature of phase transformations in the alloys by several authors and EM is playing a leading role in understanding these and the orientation relationships between the fcc and B2 phases. The following examples elucidate the structural transformations in model Cu–Pd intermetallic systems supported on carbon in reaction environments.

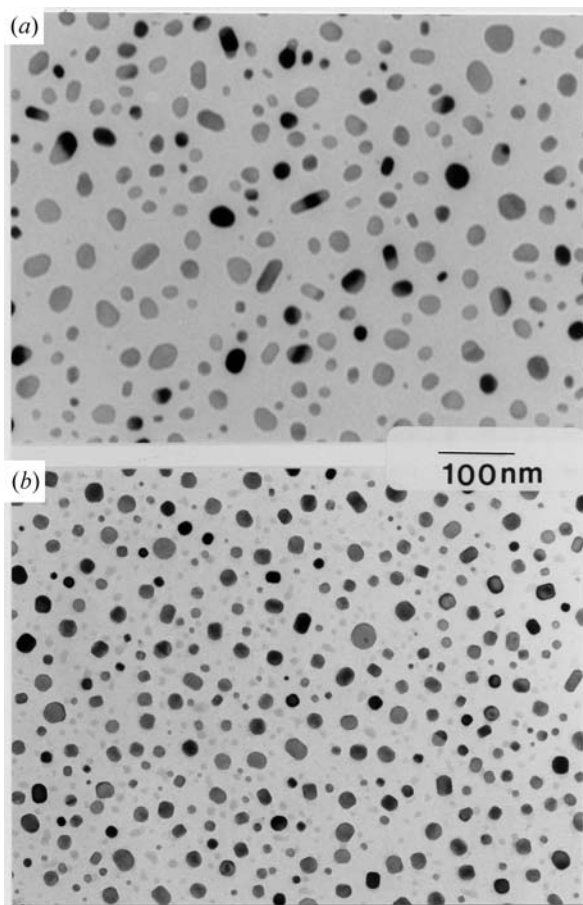


Figure 5.20. Real-time *in situ* ETEM image of the role of gas environments on Cu–Pd/C: (a) H₂ gas, (b) CO. The nature and shape of particles are different. (After Gai *et al* 1990.)

The samples described here are prepared in an evaporator using a double ingot system containing the two metals as described in chapter 3. The rate of deposition and the final composition of the films can be controlled with this method. In the following examples, the Cu:Pd ratio is $\sim 1:1$ and the samples are examined by ED and ETEM. Before heating, the films appear amorphous. After heating, the films rupture to form islands which gradually equilibrate to form faceted crystallites. The ED pattern in figure 5.19 shows the presence of both the fcc and B2 phases in the system. The dynamic behaviour of the particles by *in situ* ETEM at $\sim 250^\circ\text{C}$, in the component gases, H₂ and CO (at gas pressures of ~ 100 torr), after ~ 1 hr is shown in figures 5.20(a) and (b), respectively. The data reveal that the catalyst particles are well faceted and more regular in CO than

in H_2 . In CO, most particles are found to be B2 in (100) orientations and are dominated by (100) surfaces. In H_2 , a mixture of mostly (110) and (111) faces, with some (100), is observed for the B2 particles and the particles sinter faster, as shown in figure 5.20(a). Faster sintering can result in the loss of available metal surface area as discussed earlier. The different surface structures and particle morphology in CO and H_2 indicate that the stability and chemical nature of the surfaces is gas dependent and chemisorption effects are significant. They further indicate that active surfaces and shapes of particles can be engineered in a catalyst system using appropriate gaseous conditions. CO is known to bind more tightly to Pd than to Cu (heats of adsorption ($-\Delta H$) values are 36 and 18 kcal/mole, respectively). The heats of adsorption of H_2 on Pd and Cu are low. In the B2 structure, the (100) faces contain only one type of atom. At 250 °C, the sintering appears to be primarily by Ostwald ripening in this system. The formation of Pd-hydrides in H_2 is ruled out on the basis of the known instability of hydrides at these temperatures, and by ED.

Dynamic *in situ* studies in a mixture of CO + H_2 environments show that a mixture of these faces is obtained with a larger number of (100) faces. However, the sintering reactions can be complex because of the possibility of surface methoxy groups. The methanol synthesis is an exothermic reaction: the large $-\Delta H$ of CO could be expected to favour Pd to be on top, and may well be the driving force for the observed predominantly (100) surfaces in both CO and CO/ H_2 gas environments, with the possibility of preferential segregation of Pd to the surfaces. It is also possible that small amounts of CO_2 formed from CO/ H_2 reaction may interact with the catalyst, leading to oxides. The dynamic behaviour in oxygen is significantly different: sheet-like particles covering smaller particles are observed. EDX and ED show elemental decomposition in an oxygen atmosphere, with larger Cu sheets covering smaller Pd-rich (some Pd-oxides) particles. This has implications for the catalyst regeneration mechanism and subsequent activity. Cu–Pd supported on silica shows a complex sintering behaviour.

5.14.2 Diffuse scattering in essentially perfect B2 catalyst particles and Ewald sphere

Particles with the B2 structure are observed to be essentially defect-free perfect crystals (figure 5.21(a)) but intense diffuse streaks appear in the microdiffraction image (figure 5.21(b)). In contrast, extensive faulting is sometimes observed in fcc particles (figure 5.21(c)) leading to faint superlattice reflections (figure 5.21(d)). Dark-field imaging and HRTEM of B2 do not reveal a contrast indicative of local disorder/stacking faults. Streaks can also arise because of modifications to the shape of the reciprocal lattice due to crystal-shape effects, i.e. they run through each reciprocal lattice point because of the relaxation of the Laue condition along the beam direction produced by the crystal's shape. However, the streaks in B2 only appear along certain crystallographic directions.

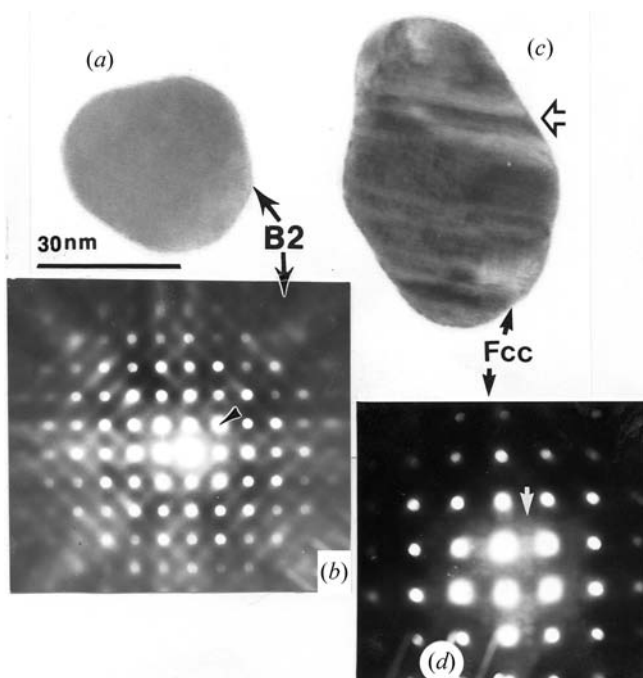


Figure 5.21. Cu-Pd/C: (a) defect-free B2 crystal with (b) the corresponding ED pattern; (c) defective fcc crystal with (d) ED pattern.

These studies, complemented by sample tilting experiments, have shown that shape effects can be ruled out. B2 particles are essentially defect-free ordered single crystals. Walls of similar diffuse streaks have been observed in the related fully annealed β -brass-type systems and have been attributed to directional thermal vibrations incorporating linear chain motion of atoms in close-packed directions (Otsuka and Wyman 1978). The corresponding phonons can be sited either on reciprocal (rel) walls (planes) or rel rods (directions). The existence of a low-frequency acoustic phonon mode giving rise to rel rods has also been suggested. Rel walls run normal to the close-packed directions in real space and the diffuse streaks correspond to the intersections of rel walls with the Ewald sphere. The walls manifest in the ED image as faint streaks along different crystal directions depending on the zone axis. In B2 the strong diffuse streaking present in all the crystallographic zones can be explained by the presence of $\{111\}$ rel walls. However, the extinction of the $\langle 110 \rangle$ streaks in the $[110]$ ED pattern does not rule out the presence of additional $\langle 110 \rangle$ rel rods. These thermal vibrations may indicate an inherent instability in the B2 catalyst structure. The effect of these planes (or directions) on any phase transformations during catalysis remains

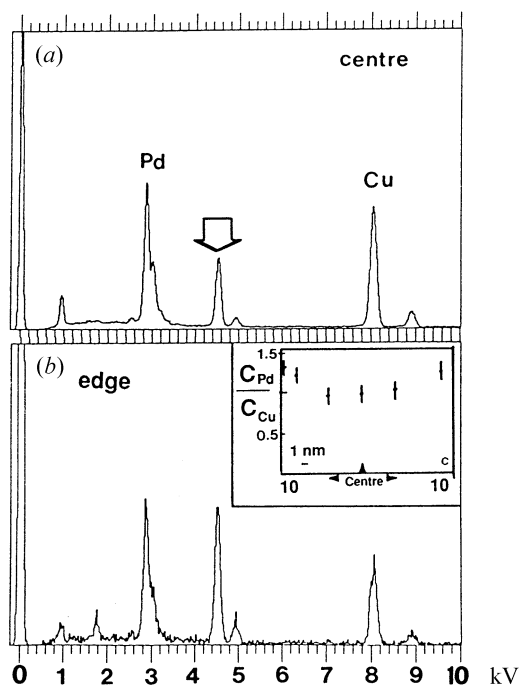


Figure 5.22. EDX of Cu–Pd crystals (a) from the centre and (b) from the edge. Inset: Composition profile from the centre to the edge indicating Pd segregation to the surface.

to be explored in detail. So far, no direct evidence of any structural relationships between B2 and the fcc phases has been reported.

5.14.3 State of the active catalysts

AEM of the individual nanoparticles in the catalyst system provides novel chemical information. EDX spectra for composition profiles from the centre and edge regions show surface enrichment of Pd (figure 5.22) in a (100) B2 particle of Cu–Pd reacted in CO. This is confirmed by HRTEM and image simulations (figure 5.23(a)). Calculations are performed using an extended unit cell (figure 5.23(b)) to generate a large number of structure factors to minimize wrap-around effects. This method allows up to 5000 structure factors and a large number of beams to be created for multi-slice simulations. In H_2 -reacted samples with mainly (110) and (111) faces, no such surface segregation is observed, indicating that both metals are present at the surface. In addition, when the single particle is exactly on-axis, extra peaks can be observed in EDX, which are not due to elemental peaks (Gai *et al* 1990). For example, if the particle is tilted, these peaks would move to new positions. They also shift as a function of the incident

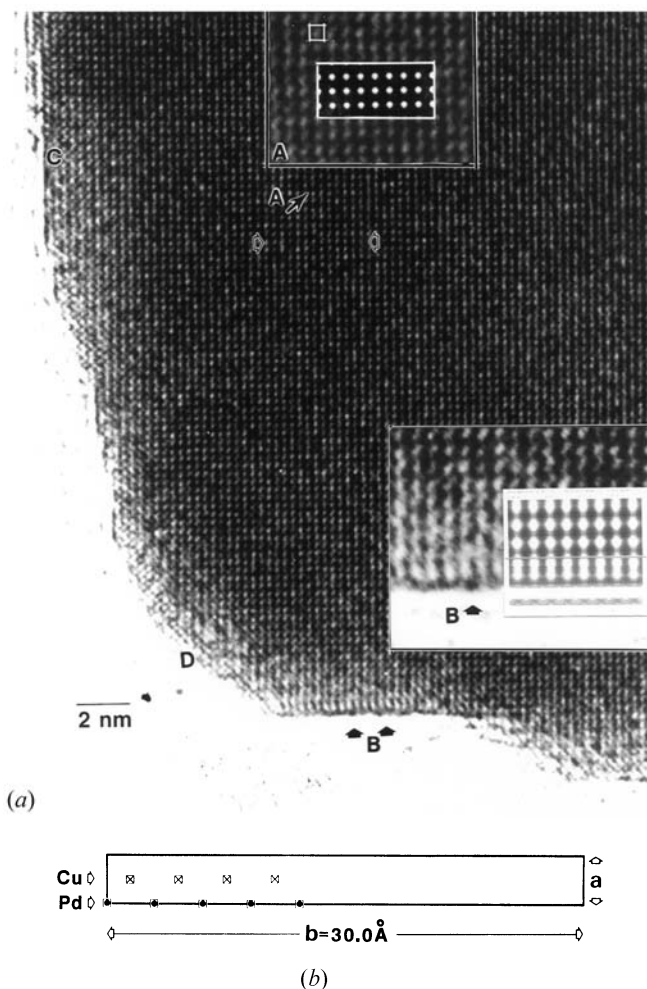


Figure 5.23. (a) HRTEM profile image of a CO-reacted Cu–Pd particle indicating a Pd surface. Inset: Pd surface with simulated image. The flat surfaces (at B) are (100); the stepped ones (D) are (110). Away from the surface the structure has equal Cu and Pd (inset: enlarged area A with image simulation). (b) ‘Extended unit cell’ model used for image simulations. ($a = 0.3 \text{ nm}$.) It minimizes wrap-around effects.

beam energy (figure 5.24).

This phenomenon of peak energy being dependent on the crystal zone-axis orientation and beam energy is characteristic of coherent bremsstrahlung (CB). The effect is well known in x-ray diffraction. As described in previous chapters in EDX from crystals, some background may arise as a result of CB. The CB

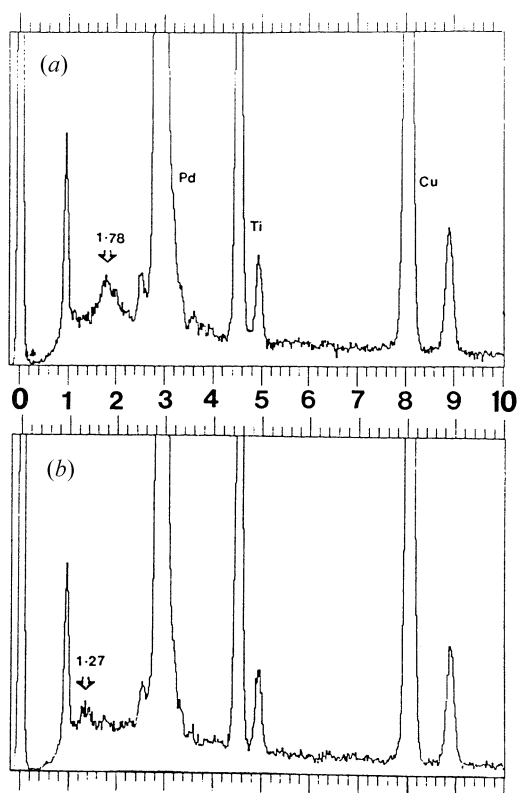


Figure 5.24. Coherent Bremsstrahlung (CB) observed from individual Cu–Pd nanoparticles: (a) [100] zone axis and (b) [110]. The CB energies are 1.78 and 1.27 kV, respectively. (Plots are peak intensity vs kV.)

x-rays result as accelerating electrons traverse through the periodic lattice and are characterized by the accelerating voltage, Bragg reflection by lattice planes normal to the beam direction and geometries of the sample and the x-ray detector. The lattice periodicity causes a coherence effect for certain CB wavevectors. Watson *et al* (1982) have reported the existence of CB peaks in studies of semiconductors and gold, using very high energy 1–3 MV electrons. From figure 5.24, the energies E of CB x-rays for [100] and [110] are 1.78 and 1.27 kV, respectively. This is one of the early reports of CB from nanometal particles at low incident electron voltages. These experimental energies are in quantitative agreement with theory, using a relationship between E and lattice spacings in the beam direction, given by

$$E = 12.4(vc)/(g \cdot n) - 1(1 + (v/c) \sin \theta)$$

where g and n are the reciprocal lattice vector and unit vector in the beam direction, respectively, v the velocity of the electrons and θ the take-off angle in the EDX detector (Spence *et al* 1983). The doubling of the recorded CB energy (2.17 keV) for [111] is actually due to the stronger second-order [222] reflections. Thus it may be possible to use CB spectra to measure the orientation of small metal catalyst particles.

Dynamic studies of the alloy system in CO and H₂ demonstrate that the morphology and chemical surfaces differ in the different gases and they influence chemisorption properties. Subnanometre layers of Pd observed in CO and in the synthesis gas have been confirmed by EDX analyses. The surfaces are primarily Pd-rich (100) surfaces generated during the syngas reaction and may be active structures in the methanol synthesis. Diffuse scattering is observed in perfect B2 catalyst particles. This is attributed to directional lattice vibrations, with the diffuse streaks resulting primarily from the intersections of {111} reciprocal lattice (rel) walls and $\langle 110 \rangle$ rel rods with the Ewald sphere.

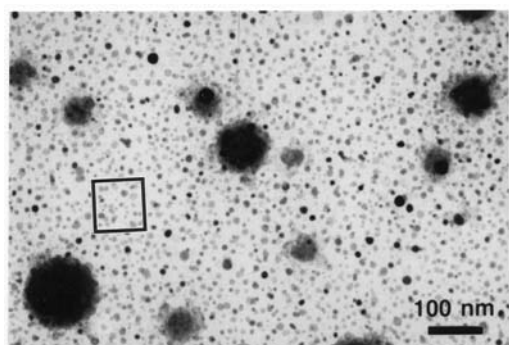
5.14.4 Cu–Ru system

In ‘bimetallic’ catalysts, Cu–Ru is an important system. Combinations of the Group Ib metal (Cu) and Group VIII metal (Ru)-based catalysts are, for example, used for the dehydrogenation of cyclohexane to aromatic compounds and in ethane hydrogenolysis involving the rupture of C–C bonds and the formation of C–H bonds (Sinfelt 1985). Here we elucidate the structural characteristics of supported model Cu–Ru systems by EM methods, including *in situ* ETEM.

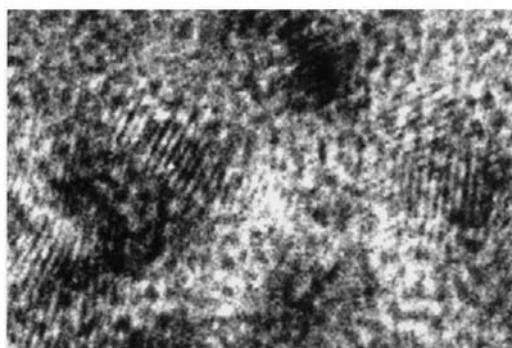
The Cu–Ru system is not known to form any alloy phases in the bulk. The literature reports of Auger spectroscopy data have indicated that hydrogen chemisorption by Ru decreases rapidly with the addition of only a few atomic % Cu, with Cu enriching or coating of the Ru surfaces (Sinfelt 1985). Based on the data a model has been proposed, whereby small particles are said to be bimetallic clusters consisting a Ru-core coated with a monolayer of Cu. However, XRD has shown the existence of a hexagonal close-packed structure characteristic of the Ru metal and not of the fcc structure of Cu. Earlier EM studies (Prestridge *et al* 1977) have suggested the bimetallic clusters to be ‘rafts’. Each raft was thought to be a layer of Ru covered by a layer of Cu. However, tilting experiments on metallic particles in the EM have not confirmed this suggestion.

Vickerman and Ertl (1983) have studied H₂ and CO chemisorption on model Cu-on-Ru systems, where the Cu is deposited on single-crystal (0001) Ru, monitoring the process using LEED/Auger methods. However, the applicability of these studies carried out on idealized systems to real catalyst systems has not been established. Significant variations in the electronic structure near the Fermi level of Cu are thought to occur when the Cu monolayer is deposited on Ru. This implies electron transfer from Ru to Cu. Chemical thermodynamics can be used to predict the nature of surface segregation in real bimetallic catalyst systems.

HRTEM, *in situ* ETEM, ED and EDX are powerful methods to provide



(a)



(b)

Figure 5.25. Cu–Ru/C catalyst in H₂: (a) sintered larger Cu particles; Ru nanoparticles remain stable; (b) enlarged area in the square showing Ru nanoparticles (with lattice spacings of 0.27 nm).

insights into surface and bulk effects, including chemisorption, ensemble and ligand effects in Cu–Ru systems. EM studies on both model and real-life Cu–Ru systems have been reported (Smith *et al* 1986, 1994). The general procedures described in these studies can be used to prepare and study bimetallic catalysts in the system. Cu is fcc with $a = 3.65 \text{ \AA}$. Ru is hexagonal with $a = 2.7 \text{ \AA}$ and $c = 4.28 \text{ \AA}$. A model Cu–Ru system can be prepared using double ingots containing Cu and Ru in an evaporator. The real catalysts are prepared by coprecipitating copper nitrate and ruthenium chloride solutions. Both silica and carbon supports are used for model and real systems. Several Cu:Ru compositions can be prepared and the precursor is dried and treated in H₂ for several hours.

The behaviour of a model Cu–Ru catalyst on carbon, in CO and H₂ in ETEM show sheet-like Cu particles and smaller Ru particles in CO, whereas primarily larger spherical Cu particles and smaller Ru ones are observed in H₂ (figure 5.25),

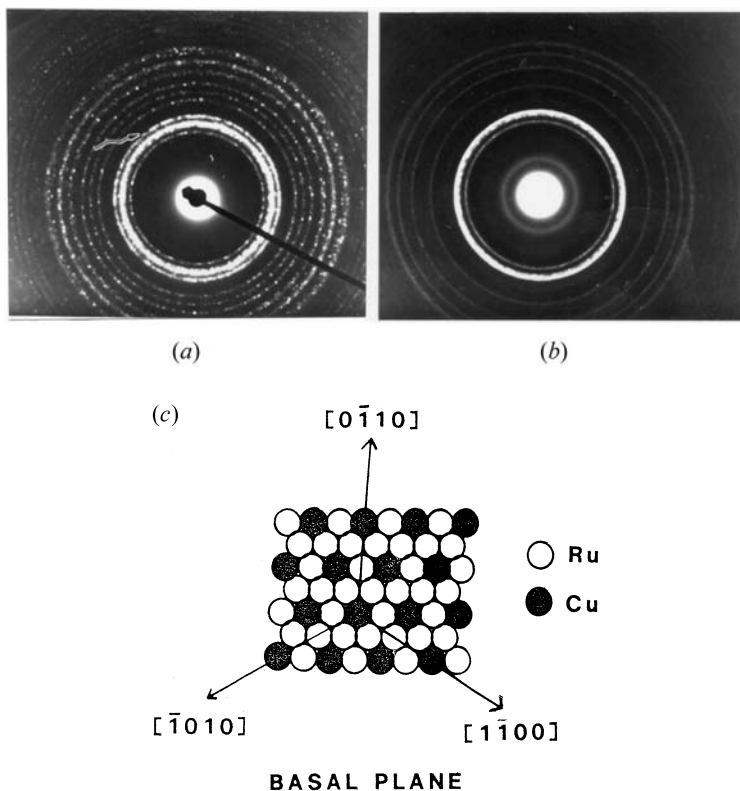


Figure 5.26. *In situ* ethane reaction and dynamic ED patterns: (a) Cu–Ru/C catalyst (room temperature); (b) $\sim 300^\circ\text{C}$ with extra rings; (c) model of CuRu_3 structure observed in dynamic ED. (After Smith *et al* 1994.)

illustrating the role of gas environments. In both H_2 and ethane reduction, the dynamic reduction of the catalyst indicates the presence of extra rings in the ED patterns from intermediate metastable phases of the particles. Figures 5.26(a) and (b) show dynamic ED patterns of the catalyst reacting in ethane at room temperature and at 300°C , respectively. These extra rings in figure 5.26(b) are not due to Cu, Ru or either of the oxides and can be indexed as $\frac{1}{3}$ (0112) and $\frac{1}{3}$ (0004) reflections. EDX indicates a Cu:Ru ratio of $\sim 1:3$. These spacings correspond to a tripling of some lattice spacings in the Ru lattice. The way this can be achieved is shown in figure 5.26(c). The data indicate that the new structure is a superlattice with a CuRu_3 structure and exists in small concentrations, consistent with the XRD data. It is possible that this alloy phase forms at the surface. This superlattice appears to be common in hexagonal lattices. In general, EDX

indicates the presence of largely elemental Cu and Ru particles and a small amount of the alloy formation in a reacting catalyst. More EM studies are required to understand the role of the surface in the catalytic reactions.

The studies reported in the literature have suggested that the surface tension of Cu depends on its surrounding environment: it is higher in vacuum and varies as vacuum > H₂ > CO. Well-rounded particles are likely to form when the surface tension is low. In CO, the surface tension is lowered to the extent that the Cu prefers to spread out as sheets rather than as three-dimensional spherical particles. Experiments carried out on real (practical) powder catalysts are consistent with the data from the model systems. As in the model systems, sintering by Cu particles is dominant, the particles growing to several tens of nanometres. The type and extent of sintering depend on the exact composition of the bimetallic catalyst. For Cu > Ru, ETEM studies show the sintering of Cu to be primarily by particle coalescence.

5.14.5 Promoted Pt catalysts in pollution control

Promoters are added to Pt catalysts because the promoted catalyst with modified electronic properties leads to a decrease in the activity for coke formation and also in the rate of metal sintering. Several promoted systems have been reported in the literature including for environmental pollution (vehicle exhaust emission) control and some are summarized here.

Pt–Ir catalysts supported on alumina are of interest in several catalytic reactions. Sinfelt (1985) has demonstrated that the incorporation of Pt into Ir clusters decreases the oxidative agglomeration of Ir, and leads to the segregation of Ir from the bimetallic system. The separation of Ir phases has been detected by various techniques including TEM (Huang *et al* 1989). Interactions between Pt and Ir have been found to exist in freshly impregnated Pt–Ir/Al₂O₃ catalysts. The incorporation of Pt into Ir clusters is shown to decrease the coking tendency of the catalysts. These aspects are used in enhancing benzene selectivity. In Pt–Rh/SiO₂ (with particle sizes of 2–20 nm) which is of interest in vehicle exhaust control catalysts, EM studies (Chojnacki and Schmidt 1989) show that heating in N₂ produces only alloy particles. In air, at 400 °C however, an Rh₂O₃ layer around each particle is observed. This alloy system differs from the Pt–Pd system in which PdO crystallites are thought to nucleate at the side of the metal crystallites (probably due to the different nucleation and growth processes for Rh₂O₃ and PdO). The studies list melting points (MPs) and oxide decomposition (OD) temperatures for the various metals. The MPs are: Pt (1769 °C), Rh (1966 °C) and Pd (1551 °C). They form the following solid oxides: PtO₂ (hexagonal with OD at 280 and 450 °C); Rh₂O₃ (rhombic with OD of 990 and 1100 °C), RhO₂ (tetra with OD at ~1030 °C); and PdO (tetragonal with OD at 700 °C). (In addition, oxides of Ni and Cu are NiO and CuO (or CuO₂), respectively and are of interest.) In Pt–Rh/SiO₂ in H₂ at ~600–1000 °C for example, a two-phase structure (a combination of cubic and twinned phases) is thought to exist. The cubes have

100 faces with (100) planes. In contrast, in O₂ and N₂, polyhedral or spherical particles are observed. Data on the diffusion coefficient of the metals are very limited and much work needs to be carried out in this area. Nevertheless Chojnachi and Schmidt (1989) have suggested that since Rh has the highest MP, it might be expected to have the lowest diffusion coefficient. Diffusion through oxides could therefore be important in determining the difference in behaviour between Rh and Pd.

Pt–Rh/Al₂O₃ catalysts are widely used in automotive-exhaust emission control. In these systems, Pt is generally used for the oxidation of CO and hydrocarbons and Rh is active for the reduction of nitric oxide to N₂. HRTEM and AEM show two discrete particle morphologies and Pt–Rh alloy particles (Lakis *et al* 1995). EM studies aimed at understanding the factors leading to deactivation, surface segregation of one metal over the other and SMSI are limited. There are great opportunities for EM studies, in particular, of surface enrichment, and defects and dislocations in the complex alloy catalysts as sites for SMSI.

From the preceding discussion, it can be seen that in multi-metal systems during catalytic reactions, the ability of each element to form compounds differs. Metals and compounds have different mobilities and interfacial properties. This affects the nature of the gas uptake and chemisorption. The effect of the gas atmosphere and temperature on the particle morphology and compositions is thus paramount in catalytic studies. STEM has been used to obtain microdiffraction patterns from individual nanoparticles in Pd/alumina and Pt/alumina systems (e.g. Boyes *et al* 1994) and in MgO-supported Au–Ru (Cowley and Plano 1987). Imaging of atomic scale restructuring of catalyst surfaces due to adsorbates, promoters and poisons are possible by *in situ* atomic resolution ETEM (Gai 1998, Gai *et al* 1990) and HRTEM. HRTEM has been used to demonstrate restructuring of surfaces of Pt on alumina due to sulfiding (Jefferson *et al* 1988). The fact that one can obtain diffraction and chemical information from individual nanoparticles is a major advance in EM methods. They provide insights into the structural behaviour of nanocatalyst systems.

5.14.6 Different synthesis routes and HRTEM of bimetallic systems

Novel routes for preparing bimetallic and multi-metallic catalysts have been reported in the literature since the time of Faraday (Moeller 1952) who suggested that colloidal particles of Group VIII and IB metals could be prepared by reducing their aquated metal ions. Although alloys are generally prepared by co-impregnation or co-precipitation, Sermon *et al* (1987) have used a colloidal route to synthesize high-dispersion Pt–Ru catalysts with reactivity (activity and selectivity) in hydrocarbon conversions comparable to alloy catalysts prepared by other routes. Pt_{100–x}Au_x bimetallic sols (with x from 0 to 100) are prepared by the reduction of mixed solutions to H₂PtCl₆ and HAuCl₄, with a 1% trisodium citrate solution at 100 °C. HRTEM indicates that the stable colloidal particles are of high crystalline order with no significant segregation of one metal over

the other in a fresh catalyst. This method of mono-dispersed alloy preparation offers scope for fine-tuning the catalytic performance by controlling the extent of alloying.

5.14.7 Wet-ETEM of catalyst–liquid reactions at operating temperatures: catalytic hydrogenation of nitriles in the liquid phase over novel bimetallic nanocatalysts and polymerization

Many commercial processes for the hydrogenation and polymerization of organic molecules are derived from solutions using heterogeneous catalysts and the associated dynamic chemical reactions occur on the molecular scale. Ultrasensitive *in situ* probing of liquid–solid reactions for understanding the molecular dynamics is, therefore, critically important in the development of advanced catalytic processes. Low-temperature catalytic routes for the hydrogenation and polymerization play a crucial role in the chemical sciences and technology. They can be economical and environmentally clean (green).

Hydrogenation of aliphatic dinitriles in the liquid phase is used in the chemical industry to produce diamines which are reacted with adipic acid and polymerized to produce polyamides such as nylon 6,6. Of particular commercial importance is the hydrogenation of adiponitrile (ADN, $\text{NC}(\text{CH}_2)_4\text{CN}$) to hexamethylene diamine (HMD, $\text{H}_2\text{N}(\text{CH}_2)_6\text{NH}_2$), an important intermediate in the manufacture of linear polyamides. The ADN hydrogenation is carried out with the dinitrile in a solvent (e.g. methanol) over Raney Ni¹ and in the presence of hydrogen (de Bellefon *et al* 1994). Novel *in situ* wet-ETEM studies of titania-supported Co–Ru nanocluster catalyst–liquid ADN reactions at the molecular level at operating temperatures demonstrate an alternative heterogeneous hydrogenation process.

The novel nanocatalysts are prepared by a single-step sol–gel process (Bradley *et al* 1978, Gai *et al* 2000). It involves the incorporation of soluble metal components into an alkoxide derived matrix of TiO_2 . Uniform dispersion of nanocatalysts on the support surface is observed in titania-supported Co–Ru and Ru samples. An LVSEM image and the atomic structure of Ru/titania are shown as an example in figures 5.27(a) and (b), respectively. A liquid holder (described in chapter 2) capable of injecting nano/microlitres of liquid is used for wet-ETEM studies. The catalyst immersed in a liquid and H_2 gas is supplied using the gas manifold of the ETEM under flowing conditions. *In situ* wet-EHRTEM of the selective hydrogenation of ADN to HMD over nanoclusters of Co–Ru on titania is demonstrated in figures 5.28(a)–(c). The product is confirmed to be HMD by high-precision mass spectrometry. The liquid–catalyst studies elucidate a very efficient hydrogenation catalyst giving full conversion of ADN and a very high yield of HMD. The studies elucidate that wet-ETEM can be used to

¹ Raney Ni is prepared by forming an alloy of Ni–Al from which Al is leached out using alkali (NaOH). This leaves Ni complexes with a high surface area, containing H_2 . However, waste disposal (of caustic solutions) is an important consideration in the process.

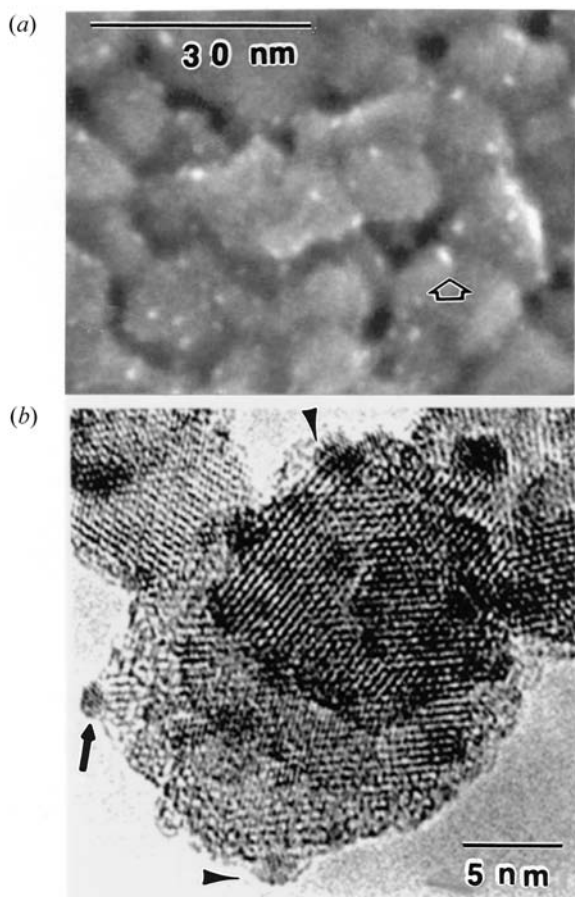


Figure 5.27. Nanocatalysts of Ru/TiO₂: (a) HR LVSEM image illustrating the uniform distribution of Ru (arrowed) on the support surface; (b) atomic structure of Ru/TiO₂ in atomic-resolution ETEM at room temperature. The Ru is in single-crystal clusters in (001) (Ru is hexagonal: $a = 0.27$ nm, $c = 0.428$ nm) and titania exhibits primarily (010) and (110). (After Gai *et al* 2000.)

design a catalytic process. This is confirmed by scaled-up parallel ADN reaction chemistry (figure 5.28(d)). A complete polymerization to the polyamide nylon 6,6 is also observed over the catalysts (in flowing helium gas used to minimize liquid evaporation) (figure 5.29). The wet-ETEM method can be used to probe the formation of a wide range of novel polymers in the solution phase and biological reactions.

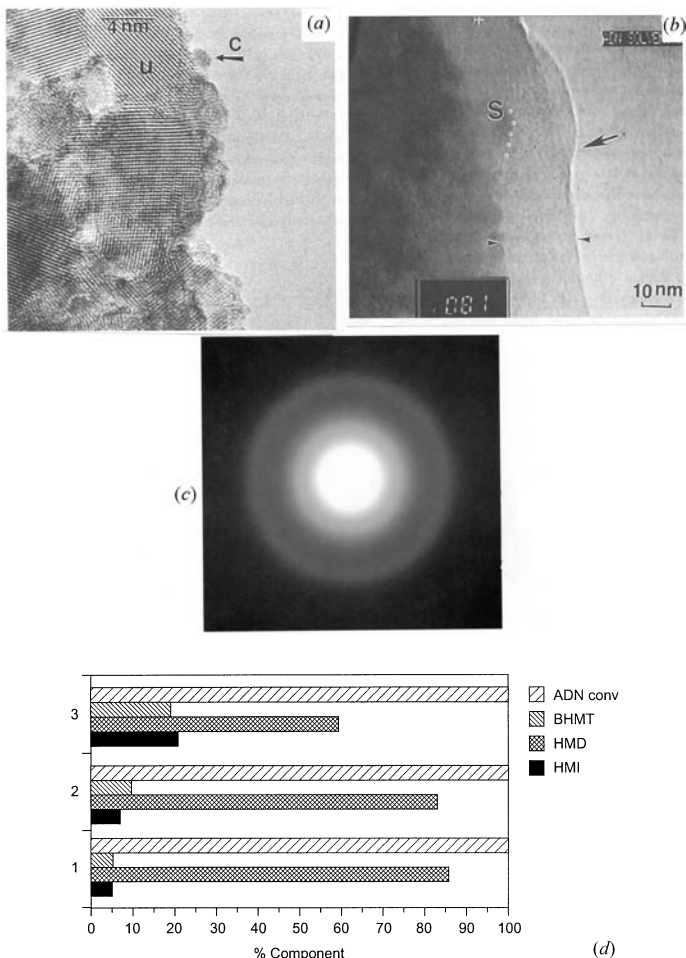


Figure 5.28. *In situ* wet-ETEM of real-time catalytic hydrogenation of nitrile liquids over novel Co-Ru/TiO₂ nanocatalysts. (a) Fresh catalyst with Co-Ru clusters (arrowed at C). The support is marked, e.g., at u. (b) Catalyst immersed in adiponitrile liquid and H₂ gas in flowing conditions; growth of hexamethylene diamine (HMD) layers (at the catalyst surface S in profile, arrowed) at ~81 °C, confirmed by composition analysis and mass spectrometry. (c) ED pattern of HMD in (b) in liquid environments. Further growth is observed at ~100 °C. The studies show that wet-ETEM can be used to design a catalytic process (after Gai 2002). (d) Scaled up reactivity data for novel Co-Ru/TiO₂ nanocatalysts confirming wet-ETEM studies of high hydrogenation activity of the nanocatalyst (2). Plots 1 and 3 are the data for Raney-Ni complexes and Ru/alumina catalysts, respectively.

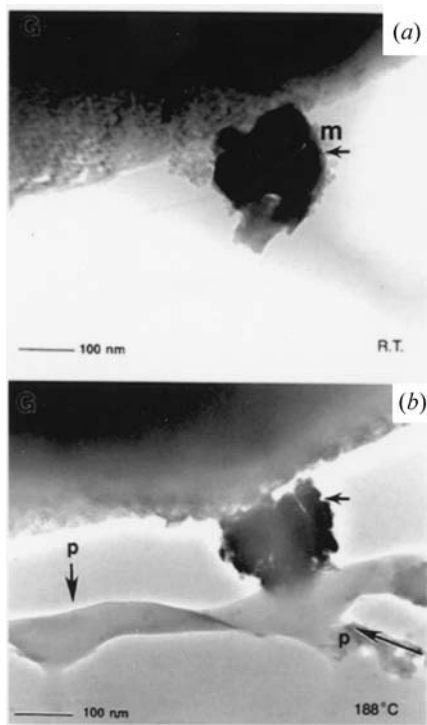


Figure 5.29. *In situ* polymerization in wet-ETEM: (a) Co–Ru/titania catalyst (m) in HMD and adipic acid liquids on support grid (G); (b) *in situ* polymerization to polyamide (p) at 188 °C.

5.15 Fischer–Tropsch and Ziegler–Natta catalysts

Fischer–Tropsch (FT) process is used for the production of hydrocarbon fuels. The process uses synthesis gases CO and H_2O . It is shown that cobalt/alumina-based catalysts are highly active for the synthesis. The process is also used to convert coal to substitute or synthetic natural gas (SNG). The use of Fe-based catalysts is also believed to be attractive due to their high FT activity. HRTEM has played a major role in the study of phase transformations in Fe Fischer–Tropsch during temperature programmed reduction (TPR) using both CO and H_2 (Jin *et al* 2000, Shroff *et al* 1995). $TiCl_x/MgCl_2$ -based (Ziegler–Natta) catalysts are used for polymerization of alkenes (Kim *et al* 2000) and EM is used to study the polymerization (Oleshko *et al* 2002).

Chapter 6

Environmental catalysis and catalyst design

6.1 Perovskite-based catalysts for environmental pollution control: The role of electron microscopy

Simple perovskites, layered perovskites and perovskite–rocksalt intergrowth structures of high-temperature superconducting cuprates (HTSC) are currently finding applications in potential economical routes for the selective oxidation of hydrocarbons and for the decomposition of nitrogen oxides (N_2O and NO) in the environment. In the A_2BO_4 systems, the design of the catalyst depends on (a) the selection of the B-element; (b) valency control by suitable cationic substitutions; (c) the synergistic effect between the elements; and (d) maintenance of an adequate surface area. These criteria are also applicable to substitutions in the ABO_3 perovskites. Recently Misono *et al* (1997) have tested these catalysts for the oxidation of paraffins and for the decomposition of N-oxides using Sr- and Mn-doped $\text{La}^{3+}\text{Co}^{3+}\text{O}_3$ oxides and LaCuO_3 oxides. It was found that the oxygen desorption rate increases with x up to 0.6 in $\text{La}_{2-x}\text{Sr}_x\text{CoO}_3$ and that the synergistic effect between Sr and Co (or Mn and Cu) as well as fine particle sizes are important. LaNiO_3 perovskite shows a unique behaviour in that it exhibits well-defined equilibrium phases in the oxygen-loss curve. Anion vacancy ordering is elucidated by ED in the anion-deficient oxides (Gai and Rao 1975; figure 6.1). Such phases are possible in other related perovskites and the phases may be important in catalysis.

To understand these complex catalysts we describe some basic HTSC (high T_c) oxides and the important role played by EM in elucidating the nanostructure and chemistry of these complex oxides. The redox behaviour of Cu in various oxidation states of HTSC may be important in environmental control catalysis.

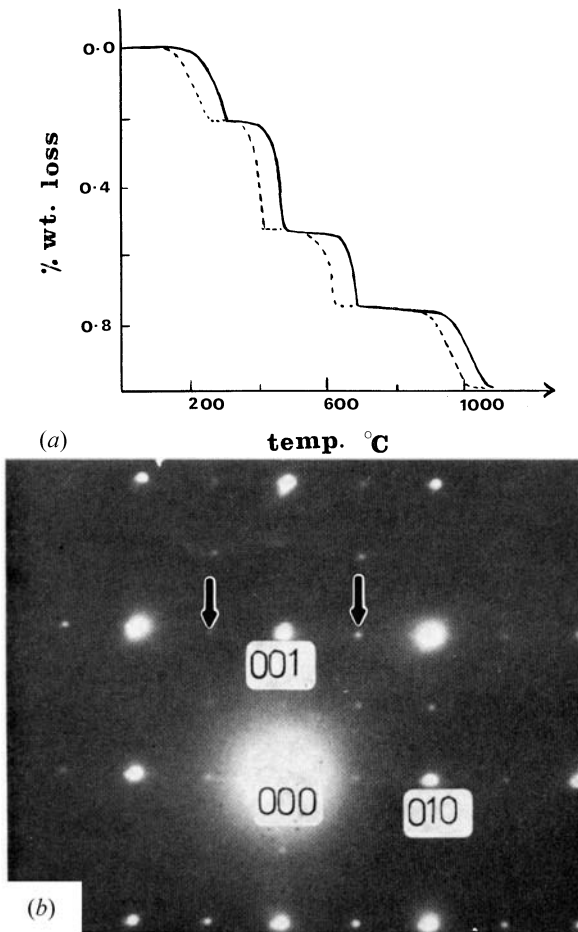


Figure 6.1. (a) Perovskite transformations of LaNiO_3 : thermogravimetric analyses (TGA) data in air (broken curve) and in oxygen; (b) ED of anion-deficient LaNiO_3 in [100], showing superstructure due to anion vacancy ordering arrowed. (After Gai and Rao *Z. Naturforsch.* a **30**).

6.2 High temperature superconducting cuprates (HTSC) as catalysts

The discovery of high T_c superconductivity in $\text{La}_{2-x}\text{M}_x\text{CuO}_4$ ($\text{M} \equiv \text{Ba}, \text{Sr}$) (Bednorz and Muller 1987) based on perovskite and rock-salt structures has led to an international effort in superconductivity research over the last decade. The principles that govern superconducting copper-oxide-based materials have enormous significance in the application of these oxides as potential catalysts

and in synthesizing new catalytic materials. In superconducting materials the current (supercurrent) flows without resistance. EM has played a leading role in the understanding and in the synthesis of cuprate compounds as described in the following sections.

The principal superconducting compounds containing lanthanum, yttrium, bismuth and thallium exhibit high T_c with critical transition temperatures from about 30 to 120 K. All of the copper-based HTSCs possess two-dimensional copper–oxygen (CuO_2) sheets as a common structural unit, which are believed to play a key role in high T_c . The materials are intergrowth structures between rock-salt ($A'O$) layers and perovskite (ABO_3) layers forming composite compounds of the type $(A'O)_n(\text{ABO}_3)_m$ where n and m correspond to the number of intergrowth layers. The perovskite layers are amenable to changes in the stoichiometry and, in particular, to the loss of oxygen. The generally held view is that, in most cases, the charge carriers responsible for superconductivity in these materials are holes that traverse through conducting CuO_2 planes. These copper-oxide-based materials are therefore called ‘hole’ superconductors. In these compounds superconductivity depends on the average formal oxidation state (or the number of electron holes) of the CuO_2 sheets. For the materials to be superconducting, the formal valence of copper should be greater than two; i.e. the copper ions are a mixture of both 2+ and 3+ oxidation states. Generally, the doping of holes in the sheets causes a transition from semiconducting to superconducting behaviour. Doping can be achieved either through oxide ion excess or by substitutional chemistry at the cation site: specifically the substitution of a lower valent cation for a higher valent metal. In the case of a cation vacancy, or substitution, unless a solid solution limit is attained, excess production of holes eventually leads to metallic properties. The metal–insulator transition from antiferromagnetic insulator to metallic behaviour as a function of stoichiometry is of great importance in oxide superconductors and their applications.

EM is playing a major role in understanding the nanostructures and composition which control the properties of the oxides in chemical reactions. The oxides are often non-stoichiometric and extensive nanostructural and compositional variations occur as a consequence. The determination of the local structure and chemistry involving oxygen vacancy ordering, stoichiometric variations, structural modulations, substitutional defects, oxygen interstitials, grain boundary interfaces and observations of coherent intergrowths which have led to the discovery of new materials have all been possible because of EM. In the following sections we examine cuprate HTSC oxides with catalytic properties.

6.2.1 Lanthanum–copper-oxide-based systems

Following the discovery of HTSC in La_2CuO_4 doped with Ba in the lanthanum site (Bednorz and Mueller 1986), work describing HTSC with Sr substitution in the La site was reported. The parent La_2CuO_4 compound (abbreviated to ‘214’) has a distorted K_2NiF_4 structure, with an orthorhombic unit cell ($a =$

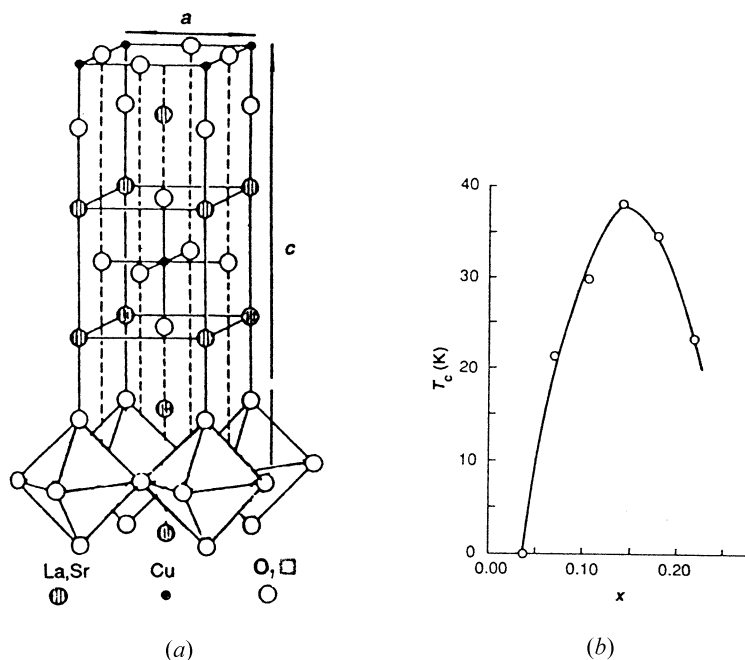


Figure 6.2. (a) $\text{La}_{2-x}\text{Sr}_x\text{CuO}_4$ structure based on the K_2NiF_4 structure. (b) Variation of transition temperature T_c with Sr concentration. Above $x = 0.2$, phase separation may occur. The range of Sr substitution is relevant to catalysis. (After Gai *et al* 1990.)

5.36 Å, $b = 5.41$ Å and $c = 13.17$ Å). The structure consists of corner-shared CuO_6 octahedra intersected by La-O layers forming single $(\text{CuO}_2)^{2-}$ sheets. Partial atomic substitution of, for example, Sr^{2+} for La^{3+} in $\text{La}_{2-x}\text{Sr}_x\text{CuO}_4$ introduces hole carriers oxidizing the CuO_2 layers and raising the average formal copper oxidation state (figure 6.2(a)). Superconductivity is observed for $0.05 < x < 0.25$ (figure 6.2(b)). The variation of transition temperature (T_c) with Sr concentration is shown in figure 6.1(b) which also indicates a narrow range of doping levels in this system for use as a catalyst. The observation of extended glide shear plane defects in this system using EM (Gai *et al* 1990) indicated the presence of anion vacancies in the Cu-O planes which may be important in catalytic reactions (Gai and Hoffmann 2000). The defects increase in density as x is increased up to 0.15, with a phase separation occurring at $x = 0.25$ (figure 6.1(b)).

Doped A_2BO_4 perovskites of the type: $\text{A}_{1-x}\text{A}''_x\text{B}_{1-y}\text{B}''_y\text{O}_4$; and doped ABO_3 perovskites of the type $\text{A}_{1-x}\text{A}''_x\text{B}_{1-y}\text{B}''_y\text{O}_3$ have been attempted where A and $\text{A}'' \equiv \text{La, Sr, K}$ and Cs ; and B and $\text{B}'' \equiv \text{Mn, Co, Cr, Cu, V}$ and Mg . $\text{La}_{2-x}\text{Sr}_x^{3+}\text{CuO}_4$ and $\text{La}_2\text{Cu}_{0.8}\text{Al}_{0.2}\text{O}_4$ have been tested for the decomposition of

N-oxides (Misono *et al* 2001). Substitutions change the Cu's formal oxidation number or state. It is believed that oxygen from N-oxides is adsorbed on the copper surface followed by an electron transfer. However, the mechanism for nitrogen oxide combustion on these oxides is not fully understood.

These mixed layered perovskites have been proved to promote effective soot combustion and NO_x reduction in diesel exhaust gases. Although perovskites are finding increasing applications as active catalysts in the reduction of air pollutants, their thermal stability at high temperatures and loss of surface area present problems. The effects of substitution on the oxygen stoichiometry is not fully understood. Catalyst materials for combustion must be designed to meet the dual requirements of thermal stability and sustained catalytic reactivity and EM methods are set to play a key role in the design of optimum catalysts.

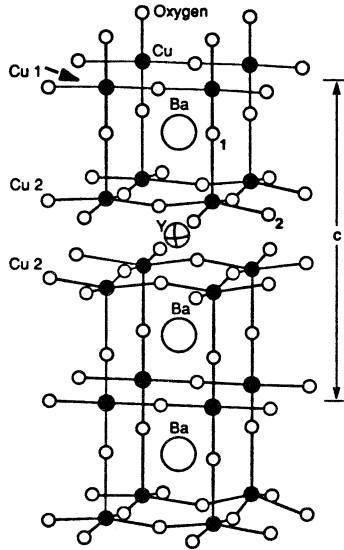
6.2.2 Yttrium–barium–copper oxide systems (Y–Ba–Cu–O)

These compounds with the prototype $\text{YBa}_2\text{Cu}_3\text{O}_7$ are also known as '123' compounds. A schematic diagram of the perfect structure is shown in figure 6.3(a) which shows the O–Cu(1)–O planes and puckering of the median CuO_2 sheets. The tetragonal and orthorhombic phases of the compound exist. The tetragonal $\text{YBa}_2\text{Cu}_3\text{O}_6$ (with $a = 3.87 \text{ \AA}$ and $c = 11.738 \text{ \AA}$) is an antiferromagnetic insulator with random anion vacancies. Below 600°C the transformation of the crystal structure from the tetragonal form to orthorhombic 123 ($a = 3.82 \text{ \AA}$, $b = 3.88 \text{ \AA}$ and $c = 11.87 \text{ \AA}$) results from the ordering of the anion vacancies. The orthorhombic system exhibits a high T_c of 90 K. An HRTEM image of the orthorhombic 123 structure with its ED pattern is shown in figure 6.3(b) and the positions of the Cu, Ba Y atom columns are indicated.

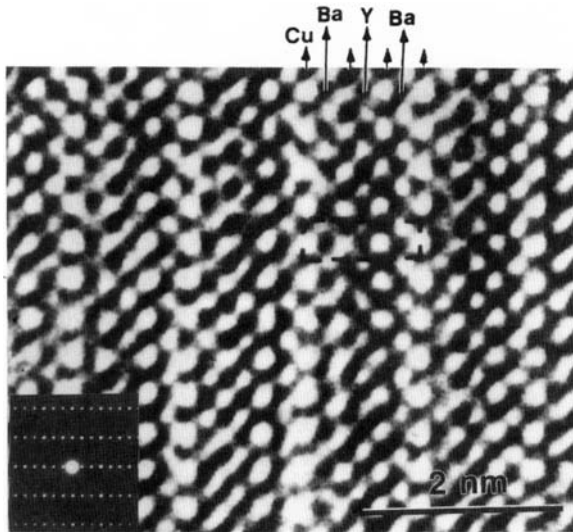
Recently Gao and Au (2000) have reported the synthesis of methanol from the hydrogenation of CO_2 over $\text{YBa}_2\text{Cu}_3\text{O}_7$. The reactions suggest H_2 adsorption at Cu sites and the adsorption of CO_2 at the anion vacancies of the tetragonal phase formed during the catalytic reaction.

6.2.3 Bismuth–copper–calcium based systems

The high temperature superconductivity discovered in the Bi–Sr–Ca–Cu–O system was found to be related to a homologous series of compounds with an idealized formulation $\text{Bi}_2\text{Sr}_2\text{Ca}_{n-1}\text{Cu}_n\text{O}_{2n+4}$ ($n = 1$ to 3 or more). The $n = 1, 2, 3$ phases have T_c values of 10–20, 90 and 11 K, respectively. The presence of superstructure modulations which are, in general, incommensurate with the basic structure was first discovered by HRTEM and ED (Shaw *et al* 1988, Gai *et al* 1988). The periodicity of the modulation is found to be about 4.7 multiplied by the a -lattice parameter. The compounds can be prepared from solid state reactions of the component oxides in stoichiometric proportions and heating between $800\text{--}900^\circ\text{C}$ in air.



(a)



(b)

Figure 6.3. High T_c cuprate superconductors (HTSC) as catalysts: (a) structural schematic diagram of $\text{YBa}_2\text{Cu}_3\text{O}_7$ ('123') HTSC with CuO_2 sheets; (b) HRTEM atomic image of the 123 phase in [010] projection with ED pattern. The image is recorded near the Scherzer defocus. The positions of the Y, Ba and Cu atom columns are indicated. The layer separation is ~ 1.18 nm and the unit cell is outlined. (After Gai and Thomas 1991.)

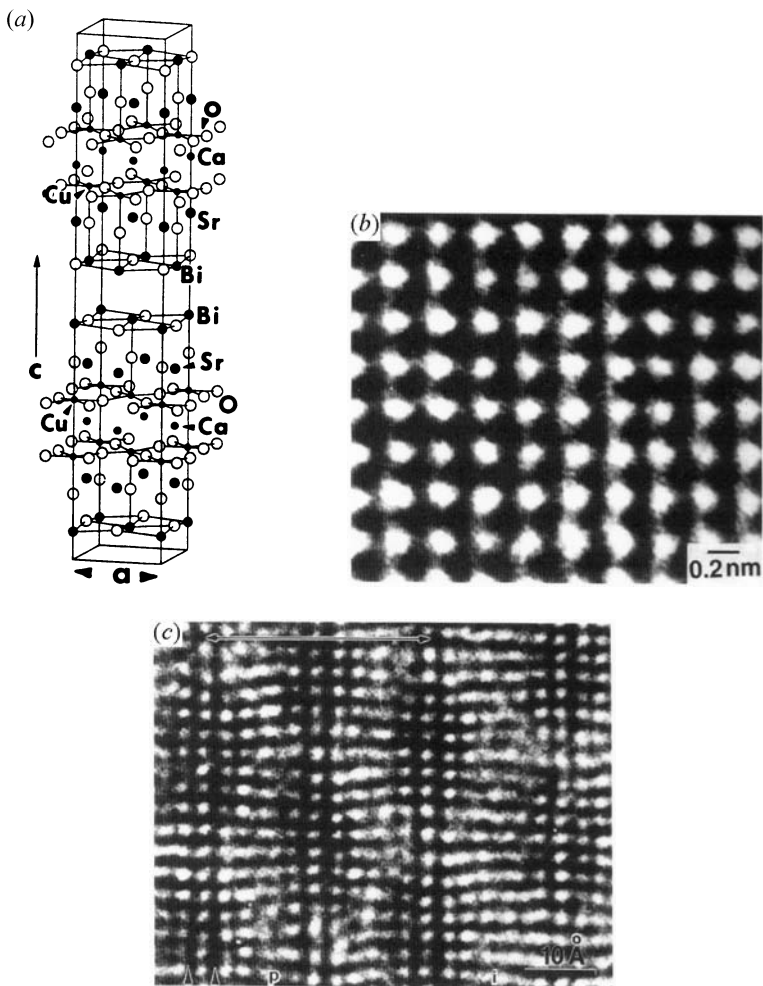


Figure 6.4. (a) Schematic diagram of the structure of idealized Bi₂Sr₂CaCu₂O₈ (2122 structure) HTSC. (b) HRTEM image of 2212 in the (001) orientation and a modulated structure; (c) HRTEM image of the atomic structure in the (010) orientation revealing wavy modulations. The *c*-axis is ~ 31 Å and is indicated by a long arrow. The double Bi layers and the perovskite layers are also indicated by double arrows and p, respectively. The intergrowth (i) is ~ 19 Å and corresponds to the higher 2223 phase. (After Gai 1992.)

The fundamental structure of Bi₂Sr₂CaCu₂O₈ (or the ‘2212’ phase), ignoring the modulations, is orthorhombic, with $a = 5.39$ Å, $b = 5.41$ Å and $c = 30.8$ Å. A schematic diagram of the structure is shown in figure 6.4(a). It consists of a Bi₂O₂ double layer and a perovskite layer containing two CuO₂,

two SrO and one Ca layers. Figures 6.4(b) and (c) show HRTEM images of the atomic structure of the 2212 phase in (001) and (010) crystal projections. Modulations leading to wavy patterns in both the BiO and perovskite layers are clearly visible in this atomic image. Quantified EDX is a powerful technique to obtain cation concentrations, which in turn can provide the formal oxidation state of Cu and the extent of the anion non-stoichiometry. This is also a useful method to deduce cation (non)stoichiometry and, as a consequence, anion stoichiometry in an oxide. Table 6.1 shows the cation concentration in the 2212 system leading, for example, to an Sr cation deficiency of $\sim 16\%$ (and Ca deficiency) in the compound. This non-stoichiometry exerts great influence on the oxide properties. The environmental effects on the oxide nanostructure are important and are elucidated by annealing the samples in different gases at 400°C : samples annealed in O_2 show incommensurate modulations (figures 6.5(a) and (c)), whereas in N_2 , they are commensurate (figures 6.5(b) and (d)). This indicates that the modulations may be intrinsic. Figure 6.5(e) shows the corresponding magnetic flux exclusion and change in the HTSC behaviour. Figure 6.5(f) shows a CBED of (b), giving the c -dimension of the unit cell. The incommensurate modulation period observed in oxygen- or air-treated samples may be related to stoichiometric variations introduced by oxygen interstitials during preparation. The resulting changes in the electronic structure of the compound may play a significant role in catalysis. From the HRTEM (figure 6.4(c)) it may be seen that the intergrowth spacing of $\sim 19 \text{ \AA}$ corresponds to $0.5 c$ -spacing of the next compound in the series $n = 3$, which has an additional CuO_2 and Ca layers with a c -axis of 37 \AA (the 2223 phase). This shows that the intergrowth structures revealed by EM can be used to synthesize novel phases with different widths for the perovskite layers.

The release and uptake of oxygen without essentially changing the basic bulk structure of the oxides are desirable in catalysis (Gai 1993) and efforts are in progress to use these oxides as catalysts in selective oxidation reactions of hydrocarbons.

6.3 Hydrodesulfurization (HDS) catalysis

Layered transition-metal sulfides (with promoters Co or Ni) are increasingly of interest in the petroleum industry to remove sulfur from oil feedstocks. Alumina-supported Ni(Co)W, NiW sulfide catalysts and Co(Ni)-promoted MoS_2 supported on alumina are used for the HDS process (Reinhoudt *et al* 1998). These promoted systems are resistant to poisoning and coking compared to metal oxides such as MoO_3 on alumina supports and metallic catalysts. The catalysts are used for hydrodesulfurization (HDS) in processing heavy residuals, coal-derived liquids and hydrocarbons. The objectives are to prevent poisoning by sulfur compounds in refining processes, to remove the sulfur component from organic molecules, to reduce atmospheric pollution, engine corrosion, and to desulfurize fuels with a

Table 6.1. Quantification of chemical composition analyses: '2212' BiSrCaCuO (oxygen anneal). Spectra normalized to the CuK α peak. The average formula is deduced to be Bi_{1.95(5)}Sr_{1.64(3)}Ca_{0.92(7)}Cu₂O_x with Sr and Ca deficiencies. The standard deviations (in brackets) of the mean ratios, with respect to an assumed Cu stoichiometry of 4.0 per formula unit, are calculated from the variance, $\sigma^2 = [\sum_i (\langle r \rangle - \langle r_i \rangle)^2 / n - 1]$, where $\langle r \rangle$ is the mean, r_i is an individual analysis and (\sum) is the sum over the n values.

Bi/Cu	Sr/Cu	Ca/Cu
1.00	0.845	0.45
0.96	0.785	0.445
0.93	0.80	0.465
0.977	0.78	0.44
0.85	0.74	0.386
0.90	0.71	0.39
0.91	0.82	0.45
1.01	0.78	0.45
1.10	1.09	0.658
1.08	0.806	0.497
0.978	0.87	0.42

higher S-content. However, the operating mechanisms are quite complex and there is only a limited understanding of the HDS process, the dispersion of components, the role of the support and causes of catalyst deactivation. Cruz-Reyes *et al* (1992) have reported HRTEM studies of ($\sim 1\%$) Co-promoted MoS₂ where the preparative methods have been found to be important and mixed sulfides such as Co₉S₈ and MoS₂ can coexist. However, detailed EM studies of dynamic HDS are needed to understand the reaction mechanisms.

6.4 Nanocatalysts in emission control, steam reforming, photocatalysis and fuel cell catalysis

CeO₂-supported noble-metal catalysts such as Pt, Pd and Rh are of interest because of their importance in the so-called three-way converter catalysts (TWC), designed to reduce emissions of CO, NO_x and uncombusted hydrocarbons in the environment and to purify vehicle-exhaust emissions. Such catalysts are also of current interest in steam reforming of methane and other hydrocarbons. Conventional practical catalysts for steam reforming consist of nickel supported on a ceramic carrier with a low surface area and are used at high temperatures of $\sim 900^\circ\text{C}$. This catalyst suffers from coke formation which suppresses the intrinsic catalyst activity. Promoters such as Mo are added to suppress coke formation. Recently, Inui *et al* (1997) have developed a novel Ni-based composite

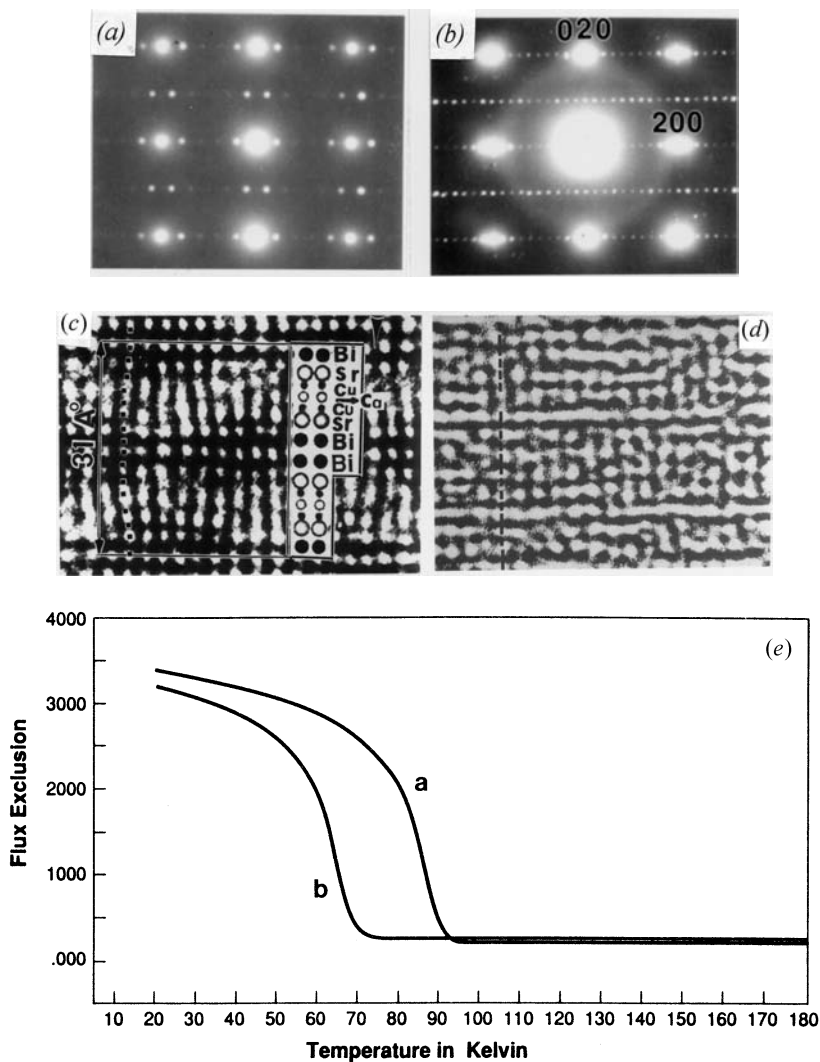


Figure 6.5. ED in (001) of (a) O_2 -annealed 2212 and (c) the HRTEM modulated image—the atom columns are shown with an incommensurate (modulated) structure. (c) N_2 -annealed with 2212. (Temperature of anneal $\approx 400^\circ C$.) (d) its HRTEM image: (b, d) show the commensurate structure. (e) Changes in magnetic flux inclusion: annealed in (a) N_2 ; (b) in oxygen. The resulting changes in the electronic structure due, e.g., to oxygen interstitials, influence the catalytic process. (f) (001) CBED of sample annealed in oxygen. HOLZ is arrowed. (After Gai *J. Solid State Chem.* **104** 119.)

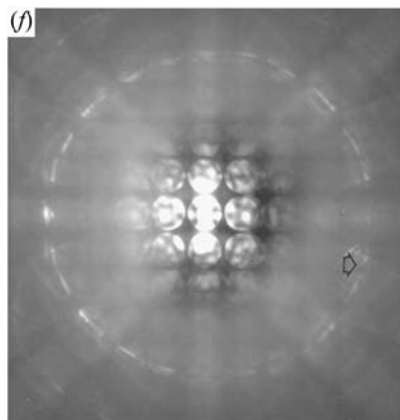


Figure 6.5. (Continued)

catalyst combined with a small amount of ceria and small amounts of Pt and Rh. This catalyst inhibits coke formation due to an evident hydrogen spill-over effect through the precious metals and the reaction temperature is also lower at $\sim 600^\circ\text{C}$. This catalyst also exhibits CO_2 -reforming of methane to syngas ($\text{CO}_2 + \text{CH}_4 \rightarrow 2\text{H}_2 + 2\text{CO}$) even with extremely short contact times for the reaction gas (~ 5 ms). There are opportunities for EM studies to understand the effects of promoters on catalytic activity and on the nature of the carbonaceous deposits.

In environmental catalysis and photocatalysis, TiO_2 (described in chapter 1) is finding important applications. It has a high oxidizing power that is capable of oxidizing organic carbonaceous substances to CO_2 in the presence of water and oxygen. Promoted TiO_2 catalysts are employed in the photocatalytic production of hydrogen from water. EM is particularly useful in studying the particulate structures in TiO_2 .

Fuel cells convert chemical energy into electrical energy at low temperatures and the reactions take place over nanocatalysts. Fuel cell research and technology are rapidly expanding to capture the electrical power market. Different electrochemical reactions are used to produce electricity in fuel cells. Methanol (or H_2) can be used to provide H_2 used as a fuel for the fuel cells. The basic geometry involves an anode and a cathode separated by an electrolyte. Commercialization aspects such as costs are extremely important and EM is playing a key role in understanding and optimizing the nanocatalysts. The methanol oxidation activity, for example, depends strongly on the structure and composition of the nanocatalysts. Pt–Ru and other catalyst systems are being tested as anode materials in several laboratories and much work remains to be performed in understanding the nature of the ‘bimetallic’ phases in the reaction environment. A Pt–Ru nanocatalyst on carbon is shown in figure 6.6.

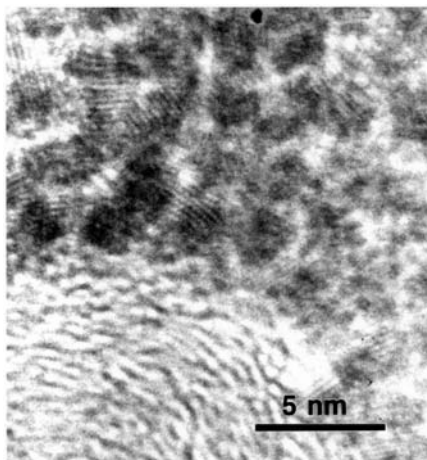


Figure 6.6. Pt–Ru nanocatalyst for fuel cells.

6.5 Nanocatalysts for alternatives to chlorofluorocarbons

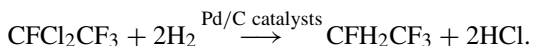
Chlorofluorocarbons (CFCs) are gases or liquids containing chlorine, fluorine and carbon. CFCs have been central to refrigeration, air-conditioning, aerosols and for clean electronics. They have found use in numerous industrial applications around the world accounting for revenues of several tens of billions of dollars. The compounds are colourless, odourless, stable, non-flammable, non-corrosive and have very low toxicity. CFC development began in the 1930s by chemists investigating early refrigeration to replace the more toxic sulphur dioxide and ammonia.

Despite the widespread use and numerous benefits of CFCs, during the 1970s–80s, scientific evidence began to emerge linking fully halogenated CFCs to thinning of the earth's protective ozone layer. Ozone is a form of oxygen containing three atoms (instead of two). The ozone layer is located in the earth's upper atmosphere, the stratosphere, about 10–15 miles above the earth. It acts as a filter to the sun's potentially harmful ultraviolet radiation. Upon release into the atmosphere, CFCs are believed to breakdown, releasing chlorine which harms the ozone molecules, contributing to the depletion of the ozone layer and global warming. The international scientific and technical community is now engaged in addressing the central questions of ozone depletion and finding alternatives to CFCs. Several catalytic processes developed by DuPont, ICI and in Japan are addressing these issues. Alternative products have emerged in the 1990s to enable CFCs to be phased out.

The task facing CFC producers, therefore, is to develop alternatives with all the positive properties associated with CFCs, but with no adverse effect on the ozone layer. The new compounds are hydrofluorocarbons (HFCs). They

breakdown more readily than the CFCs in the earth's lower atmosphere, and thus the potential for ozone depletion is low. In particular, 134a (CH_2FCF_3) is a good alternative for 12 (CF_2Cl_2). 134a can be produced in different ways (Riberio *et al* 1997). There are generally four C_2 feedstocks and several synthetic routes to producing this molecule, one of which is described here.

The hydrodechlorination (HDC) of dichlorotetrafluoroethane (CFCl_2CF_3 , known as CFC-114a) plays a key role in the removal of chlorine from the C-Cl groups in CFC to produce HFC ($\text{CF}_3\text{-CFH}_2$, 134a). A Pd nanocatalyst on carbon is one of the best systems to catalyse this process and EM is providing powerful insights into HDC reactions. The HDC of 114a to 134a can be written as



This reaction gives sufficiently high yields of 134a. However, some by-products, such as undehydrogenated-124 (CH_3CHFCl) and greatly hydrogenated-143a (CH_3CF_3), can also form. EM shows that the catalysts contain Pd clusters and are primarily in (110) orientations (figure 6.7) (Gai 1999b). This is important because this means that most of the metal atoms will be exposed to HDC reactions and are potentially active sites. EDX shows them to be pure Pd. It has been found that the particles are very selective towards HFC 134a with better than 90% selectivity. EM methods also show that the major cause of deactivation is due to thermal sintering of Pd. Catalytic selectivity can, however, be improved by pre-treating the catalyst with an appropriate chlorine source. The mechanism for the HDC reaction is deduced by correlating the nanostructure and reactivity (activity and selectivity) measurements of the hydrodelagogenation of 114a, 124 and 134a. The relative reaction rates for 114a, 124 and 134a are 590:14.4:1, respectively. This suggests that the breaking of the C-halogen bond on the Pd surface is the rate-determining step.

Recently the chemical community, in their search to facilitate attempts to obtain successful 'leads' (and by identifying optimal analogues of such leads), has been attracted towards combinatorial chemistry. It is believed that combinatorial chemistry can offer leads towards discoveries as quickly as possible which can be used to formulate 'candidate' products. This generally involves generating very large arrays of diverse molecules using automated procedures and solid state chemistry. For obtaining 'leads', solid state chemistry of advanced intermediates coupled with selected arrays of informative analogues are being utilized to generate potentially promising structures or compounds for, among other reactions, catalysis.

6.6 Concluding remarks

In this book, we have highlighted the unique contributions of electron microscopy, microanalysis and ED to our understanding of catalysis and the rational design of advanced catalysts at the nano-scale and processes. EM methods, including *in*

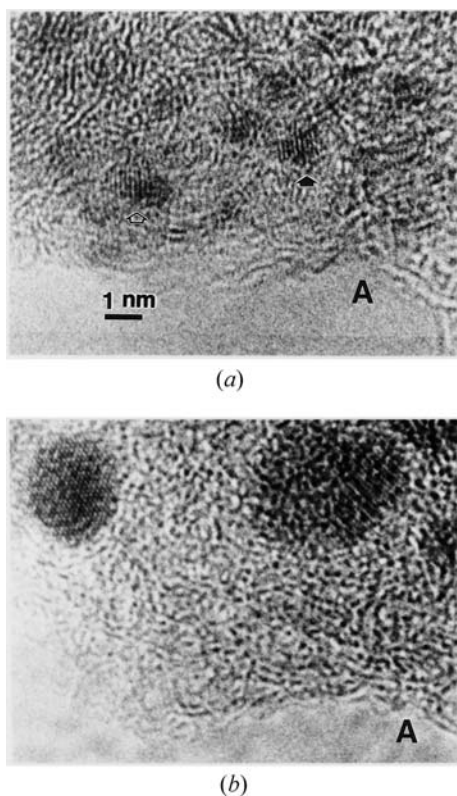


Figure 6.7. Pd nanocatalyst on carbon for CFC conversion to HFC. *In situ* ETEM reaction: (a) room temperature; (b) atomic-scale sintering at $\sim 300^\circ\text{C}$ suggesting Ostwald ripening.

situ dynamic EM during the reaction, combined with defect theories of physics, inorganic coordination chemistry and thermodynamics provide powerful insights into the active sites and surface state of the reacting catalyst. Our study has also established the viability and power of EM in elucidating changes in complex working catalysts. A new understanding of point and extended defect structures has emerged from dynamic EM studies, which impacts on the heterogeneous catalytic process. EM has revealed a novel glide shear mechanism which plays a crucial role in the release of structural oxygen and the preservation of anion vacancies associated with active Lewis centres in oxidation catalysis, without collapsing the bulk catalyst structure. Defect phenomena at the reacting catalyst surface underpin the solid state chemistry of non-stoichiometric compounds, including high-temperature superconducting oxides. The understanding of which microstructure makes catalysts function and which defects can block their operation may lead to the design of novel catalysts. Mechanisms for metal-

particle wetting on ceramic oxide substrates have a wider fundamental interest in metal-oxide adhesion, microelectronics and heteroepitaxy. The introduction of lattice imperfections (point defects) in catalytic materials is now of active interest for catalyst activation, e.g. by neutron bombardment in radiation catalysis. More systematic studies are, however, necessary to characterize the imperfections.

New advanced catalysts for the direct conversion of methane hydrocarbons to methanol (and syngas), for generating economical energy sources, for fuel cell technology, for the direct decomposition of nitrogen oxides (NO) in environmental pollution control, for the dehydration of alkanes, for H₂O₂ process, novel and economical heterogeneous catalysts for the hydrogenation of dinitriles from solutions (for the manufacture of novel polymers) are being actively sought at present with important implications for society. The defect, atomic and electronic structures will all play a critical role in the catalytic properties of such systems and thus there are tremendous new opportunities for EM in the design of catalyst systems to meet these global challenges. Understanding the dynamics of the defects and the complex synthesis involving chemical modifications at the atomic level, are some of the exciting challenges in these areas. *In situ* atomic-resolution ETEM, atomic-resolution analytical FSTEM with Z-contrast, FESEM with its high precision analysis, wet-E TEM for liquid-catalyst reactions and high-resolution cathodoluminescence are powerful tools for probing the dynamic atomic structure, chemistry and electronic structure of catalysts. They are providing insights into the behaviour of catalysts. To create advanced materials and processes for use in catalysis which forms an integral part of national economy and society, new ultrasensitive electron microscopy and ED techniques will continue to emerge to probe the working catalyst surface at an ever increasing pace.

References

- Adams D M 1974 *Inorganic Solids* (New York: Wiley)
- Adams R and Jennings T R 1969 *J. Catal.* **3** 549
- Adams R C *et al* 1962 *J. Catal.* **1** 336
- Agar A W 1982 *Proc. 7th Int. Congress on EM* **115**
- Allpress J G 1969 *J. Solid State Chem.* **1** 66
- Allpress J G and Saunders J V 1973 *J. Appl. Cryst.* **6** 165
- Amelinckx S *et al* 1978 *Diffraction and EM I* (Amsterdam: North Holland)
- Anderson J R 1975 *Structure of Metallic Catalysts* (London: Academic)
- Anderson J S 1973 *J. Chem. Soc. Dalton Trans.* 1107
- 1970 *Non-stoichiometry in Solids* ed A Rabenau (Amsterdam: North-Holland)
- 1971 *Rev. Pure Appl. Chem.* **21** 67
- 1977 *J. Physique Col.* **C7** C1
- Anderson J S and Hyde B G 1967 *J. Phys. Chem. Sol.* **28** 1393
- Anderson J S *et al* 1973 *Nature* **243** 81
- Anderson J S *et al* 1977 *Proc. R. Soc. A* **352** 303
- Andersson S, Mumme W G and Wadsley A D 1966 *Acta Cryst.* **21** 802
- Andersson S and Wadsley A D 1966 *Nature* **211** 581
- Andersson S *et al* 1974 *J. Solid State Chem.* **9** 92
- Anstis G R, Lynch D F, Moodie A F and O'Keefe M A 1973 *Acta. Cryst. A* **29** 138
- Aso I *et al* 1980 *J. Catal.* **64** 29
- Audier M *et al* 1981 *Carbon* **19** 99
- Bachmann H *et al* 1961 *Z. Krist.* **115** 110
- Baker R T K and Chludzinski J 1981 *Carbon* **19** 75
- Baker R T K *et al* 1979 *J. Catal.* **58** 293
- Bakker M and Hyde B G 1978 *Phil. Mag.* **38** 615
- Balandin A 1969 *Adv. Catal.* **19** 1
- Batist P A 1967 *J. Catal.* **7** 33
- Batson P E 1979 *Ultramicroscopy* **3** 367
- Bednorz J G and Muller K A 1986 *Z. Phys. B* **64** 189
- Bell A T and Clarke D B 1995 *J. Catal.* **154** 314
- Bernal S *et al* 1997 *J. Catal.* **169** 510
- Bernau E *et al* 1990 *J. Catal.* **151** 23
- Black J, Clayden N, Serwicka E, Gai P L and Goodenough J B 1987 *J. Catal.* **106** 1
- Blanchin M, Bursill L A, Hutchinson J L and Gai P L 1981 *J. Physique C* **3** (suppl. 6) 95
- Blasse G 1966 *J. Inorg. Nucl. Chem.* **28** 1124
- Bond G C 1987 *Het. Catalysis* (Oxford: Oxford University Press)

- Bordes E 1987 *Catal. Today* **1** 499
- Boyes E D 1983 *Nature* **304** 289
- 1986 *Proc. XI ICEM (Kyoto)* p 383
- 1993 *IOP Conf Ser.* **138** 495
- 1994 *Proc. ICEM-13 (Paris)* **1** 51
- 1998 *Adv. Materials* **10** 1277
- 2000 *Microsc. Microanal.* **6** 307
- 2001 *Microsc. Microanal.* **7** 392
- 2001 *Inst. Phys. (IOP, London, UK) Conf. Ser.* **168** 115
- Boyes E D and Gai P L 1981 *Analytical EM* ed R Geiss (San Francisco Press) p 71
- 1997 *Ultramicroscopy* **67** 219
- Boyes E D, Gai P L and Hanna L 1996 *Mat. Res. Soc.* **404** 53
- Boyes E D, Gai P L and Warwick C 1985 *Nature* **313** 666
- Boyes E D *et al* 1982 *J. Microscopy* **127** 321
- Boyes E D *et al* 1986 *Jeol News E* **24**
- Boyes E D, Ringnald J, van der Stam M A, Flievoet T F and van Cappellen E 2001 *Microsc. Microanal.* **7** 232
- Boyes E D, Watanabe E, Skarnulis A J, Hutchison J, Gai P L, Jenkins M L and Naruse M 1980 *Inst. Phys. (IOP, London, UK), Conf. Ser.* **52** 445
- Boudart M 1981 *Catal. Rev. Sci. Eng.* **23** 1
- Bradford M C and Vannice M A 1998 *J. Catal.* **173** 157
- Bradley M *et al* 1978 *Metal Alkoxides* (New York: Academic)
- Breck D W 1974 *Zeolites and Molecular Sieves* (New York: Wiley)
- Briscoe N and Hutchison J L 1984 *IOP Conf. Ser.* **68** 249; 1985 *Ultram.* **18** 435
- Brunauer S, Emmett P H and Teller E 1938 *J. Am. Chem. Soc.* **60** 309
- Brydson R, Sauer H, Engel W, Thomas J M and Zeitler E 1989 *J. Chem. Soc. Chem. Commun.* **15** 1010
- Burkhardt J T and Schmidt L D 1989 *J. Catal.* **116** 240
- Burrington J D, Kartisek C T and Grasselli R 1983 *J. Catal.* **81** 489
- Bursill L A 1969 *Proc. R. Soc.* **311** 267
- Bursill L A and Hyde B G 1972 *Prog. Solid State Chem.* **7** 177
- Bursill L A 1983 *Rad. Effects* **74** 253
- Burrington J D, Kartisek C and Grasselli R 1983 *J. Catal.* **81** 489
- Butler E P and Hale K F 1981 *Dynamic Experiments* (Amsterdam: North Holland)
- Buttrey D, Jefferson D A and Thomas J M 1986 *Phil. Mag.* **53** 897
- Catlow C R A and James R 1978 *Nature* **272** 603
- Centi G (ed) 1993 *Catal. Today* (special volume) 1
- Chen H 1979 *Mat. Res. Bull.* **21** 19
- Chen J *et al* 1994 *J. Phys. Chem.* **98** 10 216
- Chen M and Schmidt L 1978 *J. Catal.* **55** 348
- 1979 *J. Catal.* **60** 380
- Choi K and Vannice M A 1991 *J. Catal.* **131** 36
- Chojnacki T and Schmidt L D 1989 *J. Catal.* **115** 473
- Chung J S, Miranda R and Bennett C O 1988 *J. Catal.* **114** 398
- Christian J W 1975 *The Theory of Transfn in Metals and Alloys* (New York: Pergamon)
- Cliff I and Lorimer G 1975 *J. Microscopy* **103** 203
- Collingues R 1992 *Progr. Cryst. Gr.* **25** 203
- Cormack A N *et al* 1982 *J. Solid State Chem.* **44** 174

- Cottrell A H 1971 *Introduction to Metallurgy* (London: Arnold)
- Cotton F A and Wilkinson G 1962 *Adv. Inorg. Chem.* (New York: Wiley)
- Coulson C A 1937 *Trans. Faraday Soc.* **33** 111
- 1961 *Valence* (Oxford: Oxford University Press)
- Cowley J M 1981 *Diffraction Physics* (Amsterdam: North-Holland)
- Cowley J M and Moodie A F 1957 *Acta Cryst.* **10** 609
- Cowley J M *et al* 1972 *Z. Naturforsch.* a **27** 445
- Cowley J M and Smith D J 1987 *Acta Cryst.* A **43** 737
- Crewe A V, Wall J and Langmore J 1970 *Science* **168** 1338
- Crewe A V, Isaacson M and Johnson D E 1971 *Rev. Sci. Instrum.* **42** 411
- Crozier P, Sharma A and Datye A 1998 *Microsc. Microanal.* **4** 228
- Crozier P A and McCartney M 1996 *J. Catal.* **163** 245
- Cruz-Reyes J *et al* 1992 *J. Catal.* **137** 232
- Chung J S, Miranda R and Bennett C O 1988 *J. Catal.* **114** 398
- Danilotos G D 1990 *J. Microscopy* **160** 9
- 1997 *In situ Microscopy in Materials Research* (Dordrecht: Kluwer Academic) p 13 on ESEM
- Datye A and Smith D J 1992 *Catal. Rev. Sci. Eng.* **34** 129
- Daulton T 2001 *Microsc. Microanal.* **7** 134
- De Bellefon C and Fouilloux P 1994 *Catal. Rev. Sci. Eng.* **36** 359
- De Broglie L 1925 *Ann. Phys.* **3** 22
- Delmon B 1993 *Catal. Lett.* **22** 1
- Dent-Glasser L S, Glasser F P and Taylor H F W 1962 *Quart. Rev. London* **16** 343
- Deroune E, Chludznski J and Baker R T K 1984 *J. Catal.* **85** 187
- Donald A M 2000 *ESEM: Proceedings of EUREM 12 Congress* **1** 515
- Doole R C *et al* 1991 *IOP Conf. Ser.* **119** 161
- Dresselhaus M S, Dresselhaus G and Eklund P 1996 *Science of Fullerenes and Carbon Nanotubes* (London: Academic)
- Double D *et al* 1978 *Proc. R. Soc. A* **359** 435
- Dufour L C 1984 *Surf. Sci.* **147** 396
- Eddington J W 1975 *Practical Electron Microscopy* (London: MacMillan)
- Egerton R 1981 *Ultramicroscopy* **6** 93
- Ellingham H J T 1930 *J. Soc. Chem. Ind. Trans.* **63** 125
- Erikson H W and Klug A 1971 *Proc. R. Soc. B* **261** 105
- Faraday M 1857 *Phil. Trans. R. Soc.* **147** 145
- Firment L and Ferretti A 1983 *Surf. Sci.* **129** 155
- Flynn P C and Wanke S C 1974 *J. Catal.* **34** 390
- Frank F C 1950 *Proc. R. Soc. A* **201** 586
- 1951 *Phil. Mag.* **42** 351
- Freel J. 1972 *J. Catal.* **25** 139
- Friedel J 1964 *Dislocations* (Oxford: Pergamon)
- Fryer J and Smith D J 1986 *J. Microsc.* **141** 3
- Fujita H (ed) 1985 *In situ Experiments with HVEM* (Osaka: Osaka University Press)
- Gabor D 1948 *Nature* **161** 777
- Gai P L 1981 *Phil. Mag.* **43**(4) 841
- 1983 *Phil. Mag.* **48**(3) 359
- 1983 *J. Solid State Chem.* **49** 25
- 1985 *J. Catal.* **89** 545

- 1992 *Chem. of supercond. Materials* ed T Vanderah (New Jersey: Noyes)
- 1997 *Acta Cryst. B* **53** 346
- 1998 *Adv. Materials* **10** 1259
- 1999a *Topics in Catal.* **8** 97
- 1999b *Solid State Mater. Sci.* **4** 63
- 2001 *IOP (UK) Conf. Ser.* **168** 401
- 2001 *Solid State Mater. Sci.* **5** 371
- 2002 *Microsc. Microanal.* **8** 21
- Gai P L (Gai-Boyes P L) 1992 *Catal. Rev. Sci. Eng.* **34** 1
- 1993 *J. Solid State Chem.* **104** 119
- Gai P L and Anderson J S 1976 *Acta Cryst. A* **32** 157
- Gai P L, Bart J C and Boyes E D 1982 *Phil. Mag. A* **45** 531
- 1981 *IOP (London) Conf. Ser.* **61** 215
- Gai P L, Billinge B H M and Brown A M 1989 *Carbon* **27** 41
- Gai P L 1982 *Proc. 3rd Climax Internat. Congr. on Mo* ed P C H Mitchell (Climax)
- Gai P L and Boyes E D 1997 *In situ Microscopy in Materials Research* (Dordrecht: Kluwer) p 123
- Gai P L, Clayden N, Black J and Goodenough J B 1983 *IOP Conf. Ser.* **68** 253
- Gai P L and Day P 1988 *Physica C* **152** 335
- Gai P L *et al* 1980 *IOP (London) Conf. Ser.* **52** 317; 1983 **68** 253
- Gai P L, Goringe M J and Barry J C 1986 *J. Microscopy* **142** 9
- Gai P L and Goringe M J 1979 *Kristall. Technik* **14** 1385
- Gai P L and Goringe M J 1981 *Proc. 39th El. Micr. Soc. America* (San Fransisco Press) p 68
- Gai P L and Hoffmann R 2000 Private communication
- Gai P L and Howie A 1974 *Phil. Mag. A* **30**(4) 939
- Gai P L and Hutchison J L 1975 *IOP (London) Conf. Ser. EMAG* **75**
- Gai P L, Jacobson A J and Rao C N R 1976 *Inorg Chem.* **15**(2)
- Gai P L and Kourtakis K 1995 *Science* **267** 661
- Gai P L, Kourtakis K, Coulson R and Sonnichsen G C 1997 *J. Phys. Chem.* **101** 9916
- Gai P L, Kourtakis K and Ziemecki S 2000 *Micrsc. Microanal.* **6** 335
- Gai P L and Labun P A 1985 *J. Catal.* **94** 79
- Gai P L and McCarron E 1990 *Science* **247** 553
- Gai P L and Rao C N R 1975 *Z. Naturforsch. a* **30** 1092
- Gai P L and Rao C N R 1975 *Mat. Res. Bull.* **10** 787
- Gai P L (Gai-Boyes P L), Salzburg M and Vega A 1993 *J. Solid State Chem.* **106** 35
- Gai P L, Smith B C and Owen G 1990 *Nature* **348** 430
- Gai P L, Subramanian M A, Gopalakrishnan, J and Boyes E D 1989 *Physica C* **159** 801
- Gai P L and Smith B C 1990 *Ultramicroscopy* **34** 17
- Gai P L (Gai-Boyes P L), Thomas J M, Wright P A, Jones R H, Natarajan S, Chen J and Xu R 1992 *J. Phys. Chem.* **96** 8206
- Gai P L and Torardi C C 1996 *Mater. Res. Soc. USA* **404** 61
- Gai P L *et al* 1997 *Catalyst Materials for High Temp Processes* ed K Ramesh, M Misono and P L Gai (American Ceramic Society) 127
- Gai P L and Thomas J M 1991 *Supercond. Ceramics* **1** 1
- Gai P L and Thomas J M 2002 *Topics in Catalysis*
- Gai P L, Webb A E, Humphreys C J, Pyke D R and Bart J C J 1980 *IOP (London) Conf. Ser.* **52** 317

- Gai *et al* 1980 *Proc. 7th Euro. Congress on EM (The Hague)*
- Gao L Z and Au T 2000 *J. Catal.* **189** 1
- Gates B C *et al* 1979 *Chem. of Catal. Processes* (New York: McGraw Hill)
- Gibson J M, Howie A and Pennycook S 1982 *Phil. Mag.*
- Gillet M 1977 *Surf. Sci.* **67** 139
- Goldstein J I, Newbury D, Echlin P, Joy D C, Fiori C and Lifshin E 1984 *SEM and X-ray Microanalysis* (Oxford: Plenum)
- Gorbusnova Yu E and Linde S A 1979 *Dokl. Acad. SSSR* **245** 584
- Goringe M J *et al* 1996 *Farad. Disc.* **105** 85
- Guczzi L *et al* 1985 *Kinet. Catal. Lett.* **27** 147
- Haber J, Janas J, Shiavello M and Tilley R J D 1983 *J. Catal.* **82** 395
- Haber J *et al* 1975 *Ber. Bunsenges. Phys. Chem.* **79** 970
- Haber J and Zilkovski J 1973 *Proc. 7th Symp. React. Solids* (Chapman and Hall)
- Haber *et al* 1997 *Catal. Today* **33** 119
- Haggin J 1995 *Chem. Eng. News (American Chem.Soc.)* **73**(30) 39
- Hansen T W *et al* 2000 *Proc. 12th Euro. Congr. EM Czech EM Soc.* **2** 537; 2001 *Science* **294** 1508
- Harris P J F, Boyes E D and Cairns J A 1983 *J. Catal.* **82** 127
- Hashimoto H, Naiki T, Eto T and Fujiwara K 1968 *Japan. J. Appl. Phys.* **7** 946
- Hearne G W and Furman K 1961 US Patent 2,991,320
- Heinemann K, Avalos-Borja M, Poppa H and Yacamán M J 1979 *J. Cryst. Growth* **47** 117
- Heinemann K and Poppa H 1985 *Ultramicroscopy* **17** 213
- Hirsch P B, Howie A, Nicholson R, Pashley D and Whelan M J 1985 *Electron Microscopy of Thin Crystals* (New York: Krieger)
- Hirth J P and Lothe J 1968 *Theory of Dislocations* (New York: McGraw-Hill)
- Hoare M and Pal P 1972 *J. Cryst. Growth* **17** 77
- Howie A 1979 *J. Microscopy* **117** 11
- 1980 *Charact. Catalysts* ed J M Thomas and R Lambert (New York: Wiley)
- 1982 *Ultramicroscopy* **8** 163
- 2002 *Microscopy Today* **10**(4) 5
- Howie A and Marks L D 1979 *Phil. Mag.* **A 49** 95
- Howie A and Whelan M J 1962 *Proc. R. Soc. A* **267** 206
- Hull D 1965 *Dislocations* (London: Butterworths)
- Hutchison J L and Lincoln F J 1976 *Phys. Stat. Sol.* **a 17** 169
- Iijima S 1973 *Acta. Cryst.* **A 29** 18
- Iijima S and Ishihashi T 1986 *Phys. Rev. Lett.* **56** 616
- 1991 *Nature* **354** 56
- Ino S 1966 *J. Phys. Soc. Japan* **21** 346
- Inui T *et al* 1997 *Catal. Mater. for High Temp Processes* ed K Ramesh, M Misono and P L Gai (American Ceramic Society) p 39
- Issacson M 1975 *Ultramicroscopy* **1** 33
- Issacs A *et al* 1984 *Concise Science* (Oxford University Press)
- Itoh H and Sinclair R 1984 *Proc. MSA* **3**
- Jain S C and Hughes A E 1978 *J. Mat. Sci.* **13** 1611
- Jacoby M 2002 *Chem. Eng. News (American Chem. Soc.)* **80**(31) 26
- Janisek J R *et al* 1987 *Opt. Eng.* **26** 692
- Jefferson D and Harris P F 1988 *Nature* **333** 617
- Jin Y and Datye A 2000 *J. Catal.* **196** 8

- Jiru P and Novakova J 1963 *Coll. Czech. Chem. Commun.* **28** 1
- Jones H A *et al* 1923 *J. Phys. Chem.* **27** 623
- Keggin J F 1934 *Proc. R. Soc. A* **144** 75
- Kennedy M J and Bevan S C 1974 *J. Less Common Metals* **36** 23
- Kiely C *et al* 1996 *J. Catal.* **162** 31
- Kihlborg L 1963 *Arkiv Chemi* **21** 443
- Kim S H and Somorjai G A 2000 *Catal. Lett.* **68** 7
- Klier K 1982 *Adv. Catal.* **31** 243
- Kobayashi T *et al* 1984 *Acta. Cryst. B* **40** 263
- Koch F and Cohen J B 1969 *Acta. Cryst. B* **25** 275
- Kofstad P 1972 *Non-stoichiometry, Diffusion and Binary Oxides* (New York: Wiley)
- Kratschmer W *et al* 1990 *Nature* **347** 354
- Krivanek O and Swann P R 1981 *Qua. Micr. at High Res.* (London: The Metals Society) p 136
- Kroto H *et al* 1985 *Nature* **318** 162
- Kubaschewski O and Hopkins B E 1962 *Oxidation of Metals* (London: Butterworths)
- Lakis R E, Lyman C E and Stenger H 1995 *J. Catal.* **154** 261
- Lee T C, Dewald D, Eades A, Robertson I M and Birnbaum H K 1991 *Rev. Sci. Instrum.* **62** 1438
- Lewis G N 1923 *Valence and Structure Of Atoms and Molecules* (New York: Chem. Catal. Co)
- Lichte 1981 *Scanning* **6** 433 (SEM Inc)
- Liu J 2000 *Microsc. Microanal.* **6** 388
- Logan A D, Braunschweig E, Datye A and Smith D J 1988 *Langmuir* **4** 82
- Lucas J and Waugh K C 1981 *J. Chem. Soc. Faraday Trans.* **1** 77
- Mackay A L 1962 *Acta. Cryst.* **15** 916
- Madix R J and Bowker M 1982 *Surf. Sci.* **102** 542
- Magneli A 1951 *Acta. Cryst.* **4** 447
- 1953 *Acta. Cryst.* **6** 495
- A 1970 *Chemistry of Extended Defects* ed L Eyring and M O'Keefe (Amsterdam: North-Holland) p 148
- Marks L D and Smith D J 1981 *J. Cryst. Growth.* **54** 425
- 1983 *Nature* **303** 316
- Matsuura I, Schuit R and Harakawa K 1980 *J. Catal.* **63** 150
- McCain C, Gough G and Godin G W 1963 *Nature* **198** 989
- McComb D W and Howie A 1990 *Ultramicroscopy* **34** 84
- Menter R 1952 *Proc. R. Soc. A* **236** 119
- Merritt R R and Hyde B J 1973 *Phil. Trans. R. Soc. A* **274** 627
- Midgley P, Wheland M, Thomas J M and Johnson R 2001 *J. Chem. Soc. Chem. Commun.* 907
- Migeley P, Wheland M, Thomas J M, Gai P L and Boyes E D 2002 *Angew. Chemie.* at press
- Millar G, Rochester C, Bailey S and Waugh K 1992 *Chem. Soc. Faraday Trans.* **88** 2085
- Minoda H and Yagi K 1997 *In situ Microscopy in Materials Research* ed P L Gai (Dordrecht: Kluwer) p 201
- Misono M and Mizuno 1997 *Catalyst Mat. For High Temperature Processes* ed K Ramesh, M Misono and P L Gai (American Ceramic Society) p 67
- Misono M 2001 *Solid State Mater. Sci.* ed P L Gai and M W Anderson **5** 381

- Moeller T 1952 *Inorganic Chemistry* (New York: Wiley)
- Mollenstedt G and Duker Z 1956 *Z. Phys.* **145** 377
- Moore W J 1950 *Phys. Chemistry* (Longmans)
- Nakayama T, Arai M and Nishiyama Y 1984 *J. Catal.* **87** 108
- Nathan H D 1993 *Chemistry (Cliff Notes)*
- Noordermeer A, Kok G A and Neiuwenhuys B 1986 *Thin Solid Films* **172** 349
- Natta G *et al* 1959 *Adv. Catal.* **11** 1
- O'Keefe M A 1973 *Acta. Cryst.* A **29** 389
- O'Keefe M A, Spence J and Kolar H 1977 *Optik* **49** 307
- O'Keefe M and Hyde B G 1976 *Acta. Cryst.* B **32** 2973
- Oleshko V, Crozier P, Cantrell R and Westwood A 2002 *J. Ele. Micr.* **51** 527
- Otsuka K and Wyman C M 1978 *Phys. Stat. Sol.* a **9** 1075
- Owen G, Nix R and Lambert R M 1987 *Appl. Catal.* **33** 405
- Ozkaya D *et al* 1999 *Catal. Lett.* **60** 113
- Pan M and Crozier P 1992 *Ultramicroscopy* **48** 332
- Parsons D F *et al* 1974 *Science* **186** 174
- Pashley D W *et al* 1964 *Phil. Mag.* **10** 127
- Peacor D R 1973 *Z. Krist.* **138** 274
- Pennycook S J *et al* 1983 *J. Mol. Catal.* **20** 345
- 2000 *Microsc. Microanal.* **6** 343
- Pernicone N J 1974 *J. Less Common Metals* **36** 289
- Perrota A J *et al* 1989 *J. Am. Ceram. Soc.* **72** 441
- Ponec V 1977 *Catal. Rev. Sci. Eng.* **11** 1
- Poppa H and Heinemann K 1975 *Optik* **56** 183
- Postek M T, Howard K S, Johnson A H and McMichael K L 1980 *Scanning EM*
- Prestridge E B *et al* 1977 *J. Catal.* **50** 115
- Rao C N R and Subba Rao G V 1974 *Transition Metal Oxides* US Department of Commerce
- Rao C N R, Gai P L and Ramasesha S 1976 *Phil. Mag.* **33**(2) 387
- Rao C N R and Goopalakrishnan J 1986 *New Directions in Sol. St. Chem.* (Cambridge)
- Reinhoudt H *et al* *J. Catal.* **179** 443
- Reller R, Thomas J M, Jefferson D A and Uppal M K 1984 *Proc. R. Soc. A* **394** 223
- Riberio F H *et al* 1997 *Catal. Lett.* **45** 149
- Rideal E K 1951 *Disc. Faraday Soc.* **11** 9
- Rodriguez N M *et al* 2001 *J. Catal.* **197** 365
- Roth W L 1960 *Acta Cryst.* **13** 140
- Ruckenstein E 1981 *Growth of Metal Clusters* ed J Bourdon (Amsterdam: Elsevier) p 57
- Ruckenstein E and Lee S 1984 *J. Catal.* **86** 457
- 1987 *J. Catal.* **104** 259
- Ruhle M *et al* (ed) 1994 *Ultramicroscopy* **56** 1
- Sachtler W M and Van Santen R A *Adv. Catal.* **69** 197
- Saka H 1997 *In situ Microscopy in Materials Research* ed P L Gai (Dordrecht: Kluwer) p 173
- Saltzberg M A *et al* 1992 *J. Am. Ceram. Soc.* **75** 89
- Sanchez M G and Gazquez J L 1987 *J. Catal.* **104** 120
- Schwab G M *et al* 1977 *Z. Phys. Chem.* **107** 109
- Scherzer O 1949 *J. Appl. Phys.* **20** 20

- Sermon P A, Keryou K, Thomas J M and Millward G R 1987 *Mater. Res. Soc. Boston (USA)*
- Shannon R D 1986 *Acta. Cryst. A* **32** 751
- Sharma R and Crozier P 1999 *El. Micr. Anal.* **569**
- Shaw T M *et al* 1988 *Phys. Rev. B* **37** 9856
- Shewmon P G 1963 *Diffusion in Solids* (New York: McGraw Hill)
- Shroff M *et al* 1995 *J. Catal.* **156** 185
- Shuman H *et al* 1981 *Ultramicroscopy* **6** 163
- Sinclair R, Yamashita T and Ponce F 1981 *Nature* **290** 386
- Sinfelt J H 1985 *Bimetallic Catalysts* (New York: Wiley)
- Sleight A W 1977 *Adv. Mat. in Catal.* ed J Burton and R Garten (London: Academic); 1979 *Proc. 3rd Climax Internat. Congr. on Mo* ed P C H Mitchell
- Smalley R E *et al* 1996 *Science* **275** 483
- Smith B C and Gai P L *Proc. XI Internat. Congr. EM (Kyoto)* 983
- Smith B C and Gai P L (Gai-Boyes P L) 1994 *J. Phys. Chem.* **98** 9335
- Smith D J and Marks L D 1986 *Ultramicroscopy* **16** 101
- Smith D J and Marks L D 1981 *J. Crystal Growth* **54** 433
- Smith K C A *et al* 1977 *SEM (IIT Res. Inst. Chicago)* 49
- Snyder T P and Hill G C 1989 *Catal. Reviews. Sci.-Eng.* **31** 43
- Sorensen O T (ed) 1981 *Non-stoichiometric Oxides* (London: Academic)
- Spence J C 1988 *Experimental HREM* (Oxford)
- Spence J C H, Reese G, Yamamoto Y and Kurizki G 1983 *Phil. Mag.* **48** 39
- Spencer N D 1988 *J. Catal.* **109** 187
- Steeds J W 1979 *Introduction to AEM* ed J Hren *et al* (Oxford: Plenum)
- Steinmetz B *et al* 2000 *Mater. Chem. Phys.* **201** 21
- Stone F S 1975 *J. Solid State Chem.* **12** 271
- Stoneham A M 1981 *J. Am. Ceram. Soc.* **64** 54
- Sushumna I *et al* 1985 *J. Catal.* **94** 239
- Swalin R A 1962 *Thermodynamics of Solids* (New York: Wiley)
- Swann P R and Tighe N 1971 *Jernkont. Ann.* **155** 251
- Tanabe K and Yamaguchi T 1994 *Catal. Today* **20** 185
- Tanaka M and Terauchi M 1985 *CBDP* (Jeol Ltd)
- Tatarchuk B J and Dumesic J 1981 *J. Catal.* **70** 308
- Taylor J M, Cheetham A K and Gai P L 1986 *Proc. III Euro. Solid State Chem. (Germany)*
- Tauster S, Fung S and Garten R L 1978 *J. Am. Chem. Soc.* **100** 170
- Thomas J M 1974 *Phil. Trans. Roy. Soc. A* **277** 251
- Thomas J M 2001 *Stud. Surf. Sci. Catal.* **141** 1
- Thomas J M and Raja R 2001 *Chem. Record* **1** 448
- Thomas J M and Thomas W J 1967 *Intro. to Het. Catal.* (London: Academic); 1997 *Principles of Het. Catal.* (VCH)
- Thomas J M, Terasaki O, Gai P L, Zhou W and Gonzalez-Calbet J 2001 *Acct. Chem. Res.* **34**(7) 583
- Thoni W, Gai P L and Hirsch P B 1977 *Phil. Mag.* **35** 781
- Tilley R J D 1970 *Mater. Res. Bull.* **5** 813
- 1979 *Chem. Scripta* **14** 147
- Tonomura A 1997 *In situ Microscopy in Materials Research* ed P L Gai (Dordrecht: Kluwer)
- Torardi C C and Calabrese J C 1984 *Inorg. Chem.* **23** 1308

- Treacy M M J and Howie A 1980 *J. Catal.* **63** 265
- Treacy M M J, Howie A and Wilson C J 1978 *Phil. Mag.* A **38** 569
- Treacy M M J *et al* 1988 *Mater. Res. Soc.* **111** 117
- Trifiro M 1979 *J. Catal.* **79** 2
- Tsang S C, Daniels J, Green M L H, Hill H A O and Leung Y C 1995 *J. Chem. Soc. Chem. Commun.* **17** 1803
- Van den Elzen A F and Rieck G D 1973 *Acta Cryst. B* **29** 433, 2436, 2433
- 1975 *Mater. Res. Bull.* **10** 1163
- Van Langeveld A G *et al* 1983 *Thin Solid Films* **109** 179
- Van Landuyt A *et al* 1997 *In situ Microscopy in Materials Research* (Dordrecht: Kluwer)
- Vaughan D E *et al* *Recent Advances in Zeolites* ed D Barthameuf (New York: Plenum)
- Venables J A 1980 *Ultramicroscopy* **5** 11
- Vickerman J C, Ertl G and Christman K 1983 *Surf. Sci.* **134** 367
- Volta J C *et al* 1985 *J. Catal.* **93** 467
- Von Adrenne M 1938 *Z. Phys.* **109** 553
- Wadsley A D 1964 *Non-stoichiometric Compounds* ed L Mendelcorn (New York: Academic) p 98
- 1967 *Helv. Chim. Acta* (Werner Centenary) 208
- Wadsley A D and Andersson S 1970 *Perspectives in Structural Chemistry* ed J G Dunitz and J A Ibers (New York: Wiley)
- Wang T and Schmidt L D 1981 *J. Catal.* **70** 187
- Watson J E and Koehler J 1982 *Phys. Rev. B* **25** 3000
- Wells O C 1979 *Scanning* **2** 199
- Westamacott K H and Dahmen U 1984 *Decomposition in Alloys* ed P Haasen *et al* (Oxford: Pergamon)
- Williams D W and Carter C B 1996 *Transmission EM* (New York: Plenum)
- Willis B T M 1964 *J. Physique* **25** 431
- Wilson S T, Lok B M, Messina C A, Cannan T and Flanigen E M 1982 *J. Am. Chem. Soc.* **104** 1146
- Wolkenstein T 1960 *Adv. Catal.* **12** 139
- Wright A F and Leadbetter A J 1975 *Phil. Mag.* **31** 1391
- Wright P A, Natarajan S, Thomas J M, Bell R G, Gai-Boyes P L, Jones R H and Chen 1992 *J. Angew. Chemie. Int. Ed. Engl.* **31**(11) 1472
- Wright P A, Natarajan S, Thomas J M and Gai P L (Gai-Boyes P L) 1992 *Chem. Mater.* **4** 1053
- Wynblatt P and Gjostein N A 1975 *Prog. Solid State Chem.* **9** 21
- Yacaman M J *et al* 1992 *Catal. Rev. Sci. Eng.* **34**
- Yagi K 1985 *Thin Solid Films* **126** 95
- Yagi K *et al* 1979 *Surf. Sci.* **86** 174
- Yang B L *et al* 1991 *J. Catal.* **130** 52
- Zeisse U *et al* 2000 *Microsc. Microanal.* **6** 1148

Index

- Activation energy, 4
- Active sites, 4
 - by *in situ* EM, 61, 115
- Activity, 3, 4
- Acrolein, 99, 102
- Acrylic acid, 125, 126
- Adsorption, 3
- Alkanes and alkenes, 11
- Alumina, 17
- Aluminum phosphates, 147
- Al-silicates, 141
- Ammonoxidation, 97, 98
- Amplitude, 54
- Analytical EM, 58
- Anion vacancies, 27, 82
- Anisotropy, 51
- Antimony-tin oxides, 129
- Arrhenius equation, 4
- Atomic resolution, 52
- Atomic structure, 52
- Avogadro number, 7

- Back scattered electron imaging,
 - BSE, 71
- Band theory, 11
- Bimetallic catalysts, 154
- Binding energies, 8
- Biological sciences, 67
- Bismuth molybdate catalysts, 101
- Bismuth cuprate superconductors, 210
- Blank calibration experiments, 65
- Bonds, 8
- Bremsstrahlung, 59

- Bright field (bf) imaging, 49
- Bronsted acid, 12
- Burgers (displacement) vector, 52
- Butane, 11

- CaF₂ structure, 28
- Carbon, 18
- Catalytic reactivity, 3
- Cathodoluminescence method, 74
- Ceria, 131
- Chemisorption, 3
- Chemical state, 2, 18
- Chromium, 26
- Chlorofluorocarbons, 217
- Climb, 88
- Clusters, 51, 201
- Cobalt doped catalysts, 201
- Combinatorial chemistry, 218
- Commercial catalysts, 82
- Contrast transfer function, 56
- Convergent beam diffraction, 61
- Copper based supported metal catalysts, 63, 180
 - Cu, 63
 - Cu–Pd, 189
- Copper carbonates, 127
- Correlation studies, 98
- Covalent bonding, 8
- Cracking catalysts, 141
- Cristobalites, 135
- Crystallographic shear, 29

- Deactivation, 4
- Dealumination, 149
- Debye–Waller factors, 139

- Deceleration, 59
Deformation, 49
Defects, 49
Depth profiling, 181
Diffraction, 45
Diffusion, 93
Dislocations, 49
 edge, 51, 52
 Frank, 175
 Frenkel, 25
 partials, 53
 Shockley, 174
 screw, 51
Disorder, 117
Dynamic catalytic studies, 65
Dynamical theory of contrast, 51
- Elasticity, 85
Electron, 45
Electron diffraction, 49
Electron holography, 78
Electron Microscopy, EM, 45
 analytical EM, 58
 atomic resolution-ETEM, 66
 high resolution TEM, HRTEM,
 52
 in situ Environmental TEM
 (ETEM), 61
 scanning EM, SEM, 70
 STEM, 75
 transmission EM, 49
Electron spectroscopy for chemical
 analysis (ESCA), 183
Electron tomography, 76
Elongation, 109
Emission control, 206
Energy, 9, 206
Enthalpy, 9
Energy dispersive x-ray
 spectroscopy (EDX), 58
Electron energy loss spectroscopy
 (EELS), 60
Entropy, 9
Environmental catalysis, 206
Environmental cell (ECELL), 62
Exothermic, 183
- Faujacite, 141
Feedstock, 2
Ferric molybdate catalysts, 109
Fe-oxides, 109
Fe-Sb catalysts, 123
Filaments, 22
Fischer-Tropsch catalysts, 206
Formaldehyde, 109
Fuel cell catalysts, 214
- Gallium-niobium oxides, 36
Gas chromatography, 79
Gas environmental effects, 180, 189
Glide Shear mechanism, 40, 110
Glide plane, 110
Graphite, 18
Growth,
 CS planes, 85
 defects, 85
 particles, 162, 184
- Halogen, 217
Heat of adsorption, 9
Helium, 85
Heteropolymolybdates, 125
High angle annular dark field
 (HAADF), 75
High temperature superconductors,
 207
Hydrocarbons, 10
Hydrodesulfurization, 213
Hydrofluorocarbons, 217
Hydrogenation, 190
- Image simulations, 57
Imperfections, 24
Infinitely adaptive structures, 36
Injection, 78
Intensity, 49
Intergrowths, 39
Iron oxides, 109
Irreducible supports, 180

- In situ* Electron microscopy studies, 61
gas-catalyst reactions at the atomic level, 66
in situ atomic-resolution ETEM development, 66
liquid-catalyst reactions, 67
liquid-gas catalysts, 202
- Island growth, 157
- Jahn-Teller effect, 15
- Joule, 10
- Kinetics, 180
- KCl, 206
- Lanthanum-based materials, 208
- Lewis sites, 12
- Life of catalysts, 43, 124
- Ligands, 8
- Liquid environments, 67
- Low voltage SEM, 73
- Lowry nomenclature, 13
- Maleic anhydride, 110
- Mass spectrometry, 79
- Methacrolein, 125
- Methanol synthesis, 109
- Microreactor, 61, 79
- Microstructure, 52
- Misfit defects, 84
- Mole, 93
- Mordenite, 143
- Molybdenum trioxide, 83
- Multiply twinned particles, 171
- Multislice simulations, 57
- Multiwalled nanotubes, 20
- Naphtha, 2
- Nanocatalysts, 151, 214
- Nanoclusters, 99, 214
- Nickel, 26, 177
- Nitrogen, 109
- Nitrogen oxides, 206
- Non-stoichiometry, 24, 26
- Nucleation, 83
- Optic axis, 49
- Ostwald ripening, 162
- Oxidation, 41, 82
- Oxidation state, 7
- Oxide catalysts, 14, 82
- Palladium based catalysts, 20
- Particle size distributions, 158
- Perovskites, 206
- pH, 12
- Photocatalysis, 214
- Platinum based metal catalysts on supports, 165
Pt, 165
Pt-bimetallic/alloy catalysts, 200
- Point defects, 26
- Polymers, 24
- Polytypes, 135
- Pore sizes, 3
- Propylene, 11, 91
- Pyrochlores, 16
- Quantification, 59
- Quartz, 135
- Rafts, 171
- Raney catalysts, 202
- Reactivity, 3
- Reaction chemistry, 79, 202
- Reflection EM, 78
- Reforming catalysts, 214
- Real-time, 61
- Redox reactions, 82
- Reduction, 82
- Resins, 125
- ReO₃, 15
- Rutherford scattering, 76
- SAPO catalysts, 147
- Scanning EM, 70
- STEM, 75
- Selectivity, 3
- Shape selective catalysts, 143

- Shear structures,
 crystallographic shear based, 41
 glide shear based, 40, 109
- Silica, 135
- Silicalites, 144
- Sintering, 162
- Single wall nanotubes, 20
- Spreading, 180
- Stabilization, 135
- Stacking faults, 49
- Static studies, 31, 61
- Strong metal–support interactions,
 177
- Surface area, 4, 162
- Surface profile imaging, 57
- Supersaturation, 93
- Synergy, 151
- Syngas, 189
- Tamann temperature, 162
- Thermodynamics, 9
- Thermogravimetric analysis, 207
- Titania, 15
- Topotactic transformations, 109
- Transition metals and oxides, 83
- Transmission EM, TEM, 49
- Tungsten oxides, 93
- Tungsten-niobium oxides, 34
- Turn over frequency (TOF), 4
- Twinning, 28, 40
- Ultra high vacuum, 64
- Uranium oxides, 26
- Vacancies, 26
- Vacuum, 62
- Valence, 7
- Vanadium oxides, 91
 V_2O_5 , 92
 VO, 26
- V–P–Oxide catalysts, 110
 VHPO, 110
 $(VO_2)P_2O_7$ (VPO), 110
- Vernier structures, 37
- Video imaging, 65
- Weak beam, 49
- Weak phase object, 51
- Wet-ETEM for liquid–catalyst
 reactions, 67
- Wetting, 156
- X-ray diffraction, 123, 136
- X-ray spectroscopy, 59
- YAG crystals, 57
- Young's equation, 156
- Z-contrast, 76
- Zeolites, 141
- Ziegler–Natta catalysts, 205
- Zirconia catalysts, 131
- Zone axis, 49